Heterostructures of C_{60}/C_{70} and Rotation of C_{70}-Au Magic Number Clusters on Au(111) and Highly Oriented Pyrolytic Graphite

by

Yitao Wang

A thesis submitted to The University of Birmingham for the degree of Doctor of Philosophy

Nanoscale Physics Research Laboratory

School of Physics and Astronomy

University of Birmingham

January 2020

UNIVERSITY OF
BIRMINGHAM

University of Birmingham Research Archive

e-theses repository

This unpublished thesis/dissertation is copyright of the author and/or third parties. The intellectual property rights of the author or third parties in respect of this work are as defined by The Copyright Designs and Patents Act 1988 or as modified by any successor legislation.

Any use made of information contained in this thesis/dissertation must be in accordance with that legislation and must be properly acknowledged. Further distribution or reproduction in any format is prohibited without the permission of the copyright holder.

Abstract

In this thesis, the nucleation, growth and mixing of C_{60} and C_{70} molecules are investigated on Au(111) and HOPG. The properties of $(C_{70})_m$-$(Au)_n$ magic number clusters on Au(111) are also studied.

Similar to C_{60} molecules, C_{70} molecules form close-packed multilayers on Au(111), but with a different lattice constant. C_{70} molecules within the molecular layers are able to rotate freely at room temperature. Several azimuthal orientations have been found for C_{70} layers giving rise to the R30°, R0° and R14° domains. When C_{70} molecules are deposited on top of a C_{60} layer, C_{70} molecules occupy the three-fold hollow site and form a two dimensional (2-D) lattice matching that of C_{60}. When C_{60} molecules are deposited on top of a C_{70} layer, the C_{60} molecules tend to form a close-packed layer and that forces the underlying layer of C_{70} to stand up. At elevated temperatures, significant molecular diffusion takes place leading to mixing of C_{60} and C_{70} from different layers.

The stable magic number $(C_{70})_m$-$(Au)_n$ clusters on the Au(111) substrate are fabricated in ultrahigh vacuum. These clusters are observed displaying unpredictable rotational movements characterised by sudden change followed by long interval of inactivity. During rotation, these clusters can maintain certain configurations associated with structural polymorphism. The time durations between two successive rotations of magic number clusters such as $(C_{70})_{10}$-$(Au)_{35}$ and $(C_{70})_{12}$-$(Au)_{49}$ can range from minutes to hours.

Abbreviation

AFM	Atomic Force Microscopy
CCI	Constant Current Imaging
CFM	Chemical Force Microscopy
CHI	Constant Height Imaging
CPC	Connector Plate Cryostat
DLs	Discommensuration Lines
EFM	Electrostatic Force Microscopy
FCC	Face Centred Cubic
FEL	Fast Entry Lock
HCP	Hexagonal Closed Packed
HOMO	Highest Occupied Molecular Orbitals
HOPG	Highly Oriented Pyrolytic Graphite
HRHAS	High Resolution Helium Atom Scattering
HTC	High Temperature Cell
K-cell	Knudsen Cells
LDOS	Local Density of State
LEED	Low Energy Electron Diffraction
LUMO	Lowest Unoccupied Molecular Orbitals
MBE	Molecular Beam Epitaxy
MoS2	Molybdenum Disulfide
NND	Nearest Neighbour Distances
OMBE	Organic Molecular Beam Epitaxy
PBN	Pyrolytic Boron Nitride
PPM	Push Pull Motion
PVD	Physics Vapor Deposition

RHEED	Reflection High Energy Electron Diffraction
RT	Room Temperature
SAM	Self-assembled Monolayers
SC	Simple Cubic
SEM	Scanning Electron Microscopy
STM	Scanning Tunnelling Microscopy
STS	Scanning Tunnelling Spectroscopy
TEM	Transmission Electron Microscopy
UHV	Ultra-high Vacuum
VT	Variable Temperature
XPS	X-ray Photoelectron Spectroscopy
XRD	X-ray Diffraction

Acknowledgement

I would like to express the deepest gratitude to all the people who helped me in my Ph.D. projects and writing. First and foremost, I would like to show my sincere thanks to my main supervisor Dr Quanmin Guo, without his valuable guidance and warm encouragement, it would be impossible for me to finish all my projects. Thank you for providing me with an excellent research environment and facilities and showed to me his great patience during the four years. I learned lots of valuable skills in and out of the laboratory from you, which, I believe, are giving great help in my future career. I also want to show my sincere thanks to my second supervisor Dr Wolfgang Theis. Thank you for spending your precious time training me in operating STEM in person and appointed me as the manager of STM laboratory. Thank you for trusting in my ability.

I would like to express my special appreciation to Dr Marhoo Rokni Fard who trained me VT-STM, introduced me how to design and conduct experiments and correct the fault I made blamelessly every time. I will never forget the days collaborating with you. I want to also show my deepest thank to Dr Dogan, Kaya, who spent the whole summer time training my academic presentation and teaching me how to conduct single molecular manipulation. It cannot be more wonderful to have teachers and friends like you in life. I also want to show my thanks to Prof Jianzhi Gao, who recommended me to study here and always give me strong support during these years.

I also want to express my gratitude to my friends and colleagues currently working in NPRL group. Firstly I wish to show my gratitude to Miss Rihan Wu. I will always treasure the precious friendship. I also want to send thanks to Mr Patrick Harrison, Mr Ross Griffin, Mr Megan Grose and Mr Alexander Pattison. Thank you for proof reading my thesis and offering me necessary help during the past few years. I will always treasure the friendship and memories in mind and wish to have chances of working with you again if possible.

I want to send my special thanks to my friends in London, Dr Brian Smith and Dr Kevin Walsh. Thank you for being my friends and helping me when I need it most.

Finally, honourable mention goes to my lovely and beloved family for their understanding, support, belief and prayer from a thousand miles away for me.

Table of Contents

Abstract i

Abbreviation ii

Acknowledgement iv

1. Introduction 1

References 6

2. Literature Review 9

2.1 Surface Structure of Au(111) 9

2.1.1 The Features of Au(111) Surface 9

2.1.2 The ($\mathbf{22 \times \sqrt{3}}$) Unit Cell 11

2.1.3 Monoatomic Step Edges on Au(111) 14

2.1.4 Elbow Sites and Rotational Domains 16

2.2 Metal Adsorption on Au(111) 19

2.3 Highly Oriented Pyrolytic Graphite (HOPG) 24

2.3.1 Structure of HOPG 24

2.3.2 Surface Electronic Structure of Graphene and HOPG 28

2.3.3 Molecules Deposited on HOPG 30

2.3.4 Gold Atoms Deposited on HOPG 32

2.4 C_{60} Molecule 35

2.4.1 Temperature Dependent Rotational Dynamics of C_{60} Molecules 38

2.4.2 Close-packing Structures of C_{60} on Au(111) 39

2.5 C_{70} Molecule 42

2.5.1 Temperature Dependent Rotational Dynamics of C_{70} 44

2.5.2 Structures of Close-packed C_{70} on Ag(111) 45

2.6 Election Properties of C_{60} and C_{70} Molecules 47

2.7 Magic Number $(C_{60})_m$-$(Au)_n$ Clusters 52

2.8 The STM Apparatus 56

2.8.1 1-dimensional Model 57

2.8.2 Two Scanning Modes of Scanning Tunnelling Microscopy....64
2.9 Solution and Vacuum Deposition 65
References 69
3. Experimental Procedure....78
3.1 Scanning Tunnelling Microscopy 78
3.2 Heating and Cooling System.... 81
3.2.1 Radiative Heating and Direct Current Heating....83
3.2.2 Sample Cooling 83
3.3 ISE 5 Ion Gun.... 84
3.4 Tip Preparation.... 85
3.4.1 Electrochemical Etching....85
3.4.2 Tip Insert and Heating 87
3.5 Source Evaporator of Fullerene.... 89
3.6 Sample Preparation and Cleaning.... 91
References 93
4. Nucleation and Growth of Close-packed C_{70} Molecules on Au(111).....94
4.1 Introduction.... 94
4.2 Experimental Procedure.... 94
4.3 Growth of C_{70} with Different Coverages on Au(111).... 95
4.4 R0°, R30° and R14° Close-packed C_{70} Structures.... 98
4.5 Changes of the Close-packed Fullerene Layer Due to Thermal Annealing..... 100
4.6 Multi-layer C_{70} Islands.... 102
4.7 Summary 110
References 111
5. Two-component Molecular Layers (C_{60}/C_{70}) Assembled on Au(111)....112
5.1 Introduction.... 112
5.2 Experimental Procedure.... 113

5.3 Results and Discussion 113
5.3.1 Mixed C_{60} and C_{70} on Au(111) At Room Temperature 113
5.3.2 Mixed C_{60} and C_{70} on Au(111) at 573 K 116
5.3.3 0.65 ML C_{60} Deposited on 1 ML C_{70} 120
5.4 0.65 ML C_{70} Deposited on 1 ML C_{60} 124
5.5 Change of Bias Voltage for The Mixed C_{60} and C_{70} 128
5.6 Summary 132
References 134
6. Orientational Epitaxy of Van der Waals Molecular Heterostructures . 136
6.1 Introduction 136
6.2 Experimental Procedure 136
6.3 1.2 ML of C_{60} (C_{70}) on HOPG 137
6.4 Deposition of 0.2 ML C_{70} (C_{60}) on 1.2 ML C_{60} (C_{70}). 140
6.5 Thermally Activated Structural Evolution 145
6.6 Summary 157
References 158
7. $(C_{70})_m$-$(Au)_n$ Hybrid Magic Number Clusters 160
7.1 Introduction 160
7.2 Experimental Procedure 160
7.3 Structure of $(C_{70})_m$-$(Au)_n$ Magic Number Clusters on Au(111) 161
7.4 Branching Ratio of $(C_{70})_m$-$(Au)_n$ Clusters 164
7.5 Stick-Sudden-Rotation of $(C_{70})_m$-$(Au)_n$ Magic Number Clusters 169
7.5.1 Rotation of $(C_{70})_{10}$-$(Au)_{35}$ Clusters At Room Temperature 171
7.5.2 Rotation of $(C_{70})_{10}$-$(Au)_{35}$ Clusters At Low Temperatures 183
7.5.3 Rotation of Other Hybrid Clusters 185
7.6 Cluster Shifting and Merging At Room Temperature 192
7.7 Summary 196
References 197

8. Summary and Future Work 198

Appendix 202

1. Introduction

Materials with multi-components have a wide range of properties [1-4]. There are vast diversities of their properties with different synthesis procedure, component and structure [5,6]. With the simplest structures, binary and ternary colloidal crystals are introduced by Denkov *et al*. firstly [7,8]. A layer-by-layer assembly method is used, and layers of two types of particles with a high degree of accuracy are deposited alternately to grow colloidal crystals [9-11]. When two particles with different sizes and shapes are mixed, the mixture is expected to have a complex structure. In binary colloidal crystals, most nanospheres and nanorods prefer to have phase separation. A particular case is the mixture of Fe_3O_4 nanospheres and $NaYF_4$ nanorods investigated by Ye *et al.*, in which a lamellar phase, a bulk separating phase, and an AB_2 binary nanocrystal shape alloy (BNSA) co-existed. Among them, the BNSAs are stabilized mainly because of short-range attractions [12]. However, in the previous research, building blocks with sizes of the order of about one nanometer has rarely been studied. It is due to the technological challenges in producing size-selected particles at this scale and difficulty in operating the small particles with the conventional assembly methods based on a colloidal suspension.

Fullerene molecules such as C_{60} and C_{70} can be roughly treated as the smallest type of "colloidal particles" because of the speciality in their geometric structures. One C_{60} molecule has a spherical shape with the van der Waals diameter of 1 nm. Each carbon atom of the molecule is bonded covalently with its three neighbouring ones, and the bonding formed can be divided into two types: The double bonds existing between two hexagons (6:6 bonding) and the single carbon bonds existing between one pentagon and one hexagon (6:5 bonding). C_{70} has a geometric shape of ellipsoid and more complex structures. Based on the calculation of Hartree-Fock model, there are eight types of carbon-carbon bonding existing in an C_{70} molecule, of which the bond lengths range from 1.356

Å to 1.475 Å. The average bonding energy of carbon atoms in an C_{70} molecule is 7.42 eV/C, which is slightly larger than the 7.40 eV/C of an C_{60} [13-15]. However, as ten extra carbon atoms are required to form an C_{70}, C_{60} are still more stable and are easier to be produced compared with C_{70}. One C_{70} molecule involves eight types of carbon bonding Unlike the two types of carbon-carbon bonding, There are Interaction between these molecules is dominated by van der Waals force. Thus layers of molecules form closed packing structure in the corresponding molecular crystals, which is similar to the hard-sphere packing mode in colloidal crystals of larger spheres [16,17]. C_{60} and C_{70} are thus good candidates to illustrate the binary mixtures of small-sized particles. Several experiments of the mixtures of C_{60} and C_{70} in solid solutions have been conducted by Sauvajol *et al*., where the mixing of the molecules suppressing the orientation transition temperatures of the whole system are observed [18,19]. Investigations of C_{60} and C_{70} mixed crystals have found that the $(C_{60})_{1-x}(C_{70})_x$ alloys tend to form several bulk phases but maintain isolated single crystals of C_{60} or C_{70}. Between the two phases, a miscibility gap can be observed [20,21].

Due to its strong ability of imaging surfaces with atomic resolution, Scanning tunnelling microscopy (STM) has been used widely to study the self-assembly as well as the interaction of atoms and molecules on various substrates, such as noble metals (Ag, Au, Cu) [22], molybdenum disulfide (MoS_2) [23] and highly oriented pyrolytic graphite (HOPG) [24]. As one of the allotropes of carbon, HOPG is a useful solid-state material which consists of stacked graphene layers. Interaction between the two adjacent graphene layers is rather weak. Within each graphene layer, the carbon atoms are connected with the neighbouring ones by strong bonding and weak π bonding [25-28]. The ` of HOPG leads to a weak interaction with other materials [28]. Hence HOPG is an ideal substrate to illustrate self-assembly of atoms and molecules. When C_{60} (C_{70}) molecules are introduced into close-packed layers of C_{70} (C_{60}) on HOPG, the C_{60} molecules are

expected to disturb the interactions between their neighbouring C_{70} molecules and result in the new properties of the mixed layer. On the Au(111) surface, the adsorption of fullerene molecules such as C_{60} has been well studied [29-39]. There is a strong tendency for the molecules to assemble into close-packed layers on Au(111). Several types of phases can co-exist in the close-packed layer depending on their azimuthal orientations [30,31,36]. Compared with gold atoms, adsorbed C_{60} or C_{70} molecules are more electronegative, which results in charge transferring from the substrate to the molecules. Different from HOPG, the gold substrate has a relatively stronger interaction with close-packed C_{60} and C_{70}, and hence the interaction in C_{60}/C_{70} is more complicated. Up to now, packing structures and orientation and direct interaction close-packed layers of the two types of fullerene molecules have rarely been studied on HOPG or Au(111) in UHV. Hence how this type of bilayer accommodates the strain at the molecular interface is an interesting problem and deserved to be investigated.

As one of the major pathways for the coarsening of homoepitaxial submonolayers on metal substrates [40,41], Ostwald ripening can be described as the expansion of large-sized clusters at the cost of small-sized ones. It is triggered by the variation in the chemical potential of different sized clusters [42-44]. As have been studied before, when gold atoms are deposited on Au(111) at low coverage, they prefer to form two dimensional clusters with irregular shapes and monolayer in height [45,46]. At low temperatures, most of the gold atoms nucleate at elbow sites on the reconstructed gold surface [47]. Triggered by Ostwald ripening, clusters at bulged elbows ripen slowly at the expense of the ones at pinched elbow sites. This preferred type of ripening pathway is termed biased-Ostwald ripening [46].

Mass transport during clusters coarsening is also affected by thermal activation and can be modified by the presence of guest molecules [48,49]. When certain amounts of C_{60} molecules are added on the substrate before the increase of

temperature, these molecules tend to decorate the existing gold atoms and form stable $(C_{60})_m$-$(Au)_n$ magic number clusters at 110 K, which has been reported by Xie *et al*. [50]. On Au(111), the aggregated C_{70} molecules take upright orientation with their long axis perpendicular to the substrate, leading to the weak interaction between gold substrate and adsorbed C_{70} molecules. Formed on the same Au(111) substrate, the $(C_{60})_7$-$(Au)_{19}$ clusters are stable up to 400 K, while most of the $(C_{70})_7$-$(Au)_{19}$ clusters break apart after being annealed to 350 K. It indicates the weaker thermal stability of $(C_{70})_m$-$(Au)_n$ clusters compared with $(C_{60})_m$-$(Au)_n$ clusters. The gold islands as well as C_{70} molecules inside this type of clusters can reshape or change their occupied positions more easily.

In chapter 2, detailed review of the literature including the properties of the substrate (Au(111) and HOPG), fullerene molecules (C_{60} and C_{70}) and metal-organic clusters ($(C_{60})_m$-$(Au)_n$) are introduced. It is followed by self-assembly nucleation and aggregation of several metals, organic molecules on the substrate of gold and graphite in UHV. In the end, working principles of variable temperature scanning tunnelling microscopy (VT-STM) and the two methods of deposition are introduced.

In chapter 3, experimental equipment and sample preparing techniques used in my experiments are introduced in detail. It includes the components of a variable temperature scanning tunnelling microscopy, evaporators used for in-situ deposition of molecules and atoms, and several sample cleaning methods in our laboratory.

Chapter 4 and 5 mainly includes the experimental studies of self-assembled nanostructures formed by fullerene molecules and gold atoms on the substrate such as Au(111) and Highly Oriented Pyrolytic Graphite (HOPG). Various amounts of pure C_{70} molecules are deposited onto the Au(111) surface at room temperature, forming the R0° (In-Phase), R14° and R30° phases. It is then followed by a co-deposition of C_{60} and C_{70} molecules. Both the two types of

molecules form close-packed layers with different lattice constants. At room temperature, the close-packed molecules have freedom of rotating. When C_{60} molecules are deposited onto a monolayer of C_{70}, these molecules can merge into C_{70} and force C_{70} molecules around them to stand with their long axis is perpendicular to the interface. Significant interlayer diffusion takes place at elevated temperatures. When C_{70} molecules are added to a monolayer of C_{60}, there is a little evidence of C_{70} moving into the layer of C_{60}. Instead, most C_{70} sit on top of the first layer and form a lattice-matched structure by taking a uniform upright orientation.

In chapter 6, the nucleation and growth of C_{70} molecules at room temperature on HOPG have been introduced. Interaction between the substrate and molecules are rather weak. When C_{70} molecules are deposited onto a monolayer of C_{60}, the strain at the interface can be minimized when all the C_{70} molecules stand upright. When a layer of C_{60} molecules is placed upon a monolayer of C_{70} molecules, orientation of the C_{70} molecules within a close-packed layer can be steered by contacting the C_{60} below. This phenomenon is potentially useful for exploring the epitaxial growth of multilayer van der Waals molecular heterostructures.

In chapter 7, C_{70} molecules and gold atoms are co-deposited onto the Au(111) surface at 110 K, in ultrahigh vacuum (UHV) environment. Magic number $(C_{70})_m$-$(Au)_n$ clusters are formed at elbow sites or attached to step edges on the gold surface. We introduce a type of clusters rotation mechanism which demonstrates the self-reorganization and balance between metal bonding, metal-organic coordination and van der Waals force between molecules. On the Au(111) substrate at room temperature, thermal fluctuation results in the rapid diffusion of gold atoms at the edges of islands inside clusters. These disturbed clusters keep their overall shapes and change their azimuthal orientations after thermal agitation, instead of disintegrating. Many of the orientations are not aligned with primary crystallographic directions of the Au(111) surface. During

the process, the metal-fullerene, metal-metal and fullerene-fullerene interactions coordinate to maintain clusters stable. External factors such as clusters' adsorption sites, the bias voltage applied to the scanning tip, as well as the temperature of the substrate affect the reshaping of clusters.

In chapter 8, the summaries of my research as well as the possible future work can be done further will be introduced.

References

[1] D. V. Talapin, C. B. Murray, Science **310**, 86 (2005).

[2] J. M. Weissman, H. B. Sunkara, A. S. Tse, S. A. Asher, Science **274**, 959 (1996).

[3] A. Dong, J. Chen, P. M. Vora, J. M. Kikkawa, C. B. Murray, Nature **466**, 474 (2010).

[4] S. Kim, S. Ishii, R. Yagi, Y. Kuwahara, T. Ogata, S. Kurihara, RSC Adv. **7**, 51978 (2017).

[5] S. Ding, Y. Liu, Y. Li, Z. Liu, S. Sohn, F. J. Walker, J. Schroers, Nat. Mater. **13**, 494 (2014).

[6] H. Furukawa, K. E. Cordova, M. O'Keeffe, O. M. Yaghi, Science **341**, 1230444 (2013).

[7] N. Denkov, O. Velev, P. Kralchevski, I. Ivanov, H. Yoshimura, K. Nagayama, Langmuir **8**, 3183 (1992).

[8] G. Singh, S. Pillai, A. Arpanaei, P. Kingshott, Adv. Funct. Mater. **21**, 2556 (2011).

[9] Y. Lvov, K. Ariga, I. Ichinose, T. Kunitake, J. Am. Chem. Soc. **117**, 6117 (1995).

[10] N. I. Kovtyukhova, P. J. Ollivier, B. R. Martin, T. E. Mallouk, S. A. Chizhik, E. V. Buzaneva, A. D. Gorchinskiy, Chem. Mater. **11**, 771 (1999).

[11] J. J. Richardson, J. Cui, M. Björnmalm, J. A. Braunger, H. Ejima, F. Caruso, Chem. Rev. **116**, 14828 (2016).

[12] X. Ye, J. A. Millan, M. Engel, J. Chen, B. T. Diroll, S. C. Glotzer, C. B. Murray, Nano Lett. **13**, 4980 (2013).

[13] M. S. Dresselhaus, G. Dresselhaus, P. C. Eklund, Science of Fullerenes and Carbon Nanotubes: Their Properties and Applications (Elsevier, 1996).

[14] K. Hedberg, L. Hedberg, D. S. Bethune, C. A. Brown, H. C. Dorn, R. D. Johnson, Science **254**, 410 (1991).

[15] D. R. McKenzie, C. A. Davis, D. J. H. Cockayne, D. A. Muller, A. M. Vassallo, Nature **355**, 622 (1992).

[16] C. S. Yannoni, P. P. Bernier, D. S. Bethune, G. Meijer, J. R. Salem, J. Am. Chem. Soc. **113**, 3190 (1991).

[17] P. A. Heiney, J. E. Fischer, A. R. McGhie, W. J. Romanow, A. M. Denenstein, J. McCauley, P. John, A. B. Smith, D. E. Cox, Phys. Rev. Lett. **66**, 2911 (1991).

[18] A. R. McGhie, J. E. Fischer, P. A. Heiney, P. W. Stephens, R. L. Cappelletti, D. A. Neumann, W. H. Mueller, H. Mohn, H.-U. ter Meer, Phys. Rev. B **49**, 12614 (1994).

[19] J. L. Sauvajol, Z. Hricha, N. Coustel, Z. Zahab, R. Aznar, J. Phys. Condens. Matter **5**, 2045 (1993).

[20] D. Havlik, W. Schranz, AIP Conf. Proc. **67**, 779 (1999).

[21] M. Sai Baba, T. S. L. Narasimhan, R. Balasubramanian, N. Sivaraman, C. K. J. Mathews, Phys. Chem. **98**, 1333 (1994).

[22] E. Ganz, K. Sattler, J. Clarke, Surf. Sci. **219**, 33 (1989).

[23] M. Sakurai, H. Tada, K. Saiki, A. Koma, H. Funasaka, Y. Kishimoto, Chem. Phys. Lett. **208**, 425 (1993).

[24] M. Drechsler, J. J. Métois, J. C. Heyraud, Surf. Sci. **108**, 549 (1981).

[25] H. P. Schultz, J. Org. Chem. **30**, 1361 (1965).

[26] H. W. Kroto, J. R. Heath, S. C. O'Brien, R. F. Curl, R. E. Smalley, Nature **318**, 162 (1985).

[27] H. P. Boehm, A. Clauss, G. O. Fischer, U. Hofmann, Zeitschrift für Anorg. und Allg. Chemie **316**, 119 (1962).

[28] J. Ma, X. Yu, Phys. Exp. **28**, 1. (2008).

[29] E. I. Altman, R. J. Colton, Surf. Sci. **295**, 13 (1993).

[30] G. Schull and R. Berndt, Phys. Rev. Lett. **99**, 226105 (2007).

[31] J. A. Gardener, G. A. D. Briggs, and M. R. Castell, Phys. Rev. B **80**, 235434 (2009).

[32] S. Guo, D. Fogarty, P. Nagel, S. A. Kandel, J. Phys. Chem. B **108**, 14074 (2004).

[33] C. Rogero, J. I. Pascual, J. Gomez-Herrero, A. M. Baro, J. Chem. Phys. **116**, 832, (2002).

[34] X. Zhang, F. Yin, R. E. Palmer, Q. Guo, Surf. Sci. **602**, 885 (2008).

[35] L. Tang, X. Zhang, Q. Guo, Y. N. Wu, L. L. Wang, H. P. Cheng, Phys. Rev. B **82**, 125414 (2010).

[36] L. Tang, Y. C. Xie, Q. Guo, J. Chem. Phys. **135**, 114702 (2011).

[37] Y. C. Xie, L. Tang, and Q. Guo, Phys. Rev. Lett. **111**, 186101 (2013).

[38] D. Kaya, D. Bao, R. E. Palmer, S. Du, Q. Guo, Nano Lett. **17**, 6171 (2017).

[39] Y. C. Xie, M. Rokni Fard, D. Kaya, D. Bao, R. E. Palmer, S. Du, Q. Guo, J. Phys. Chem. C **120**, 10975 (2016).

[40] W. Ostwald, Lehrbuch der Allgemeinen Chemie (Engelmann, Leipzig, Germany, 1896).

[41] M. Von Smoluchowski, Z. Phys. **17**, 557 (1916).

[42] L. Ratke, P. W. Voorhees, Coarsening and Growth: Ostwald Ripening in Materials Processes (Springer, Berlin, 2001).

[43] M. Zinke-Allmang, L. C. Feldman, M. H. Grabow, Surf. Sci. Rep. **16**, 377 (1992).

[44] I. M. Lifshitz, V. V. Slyozov, J. Phys. Chem. Solids **19**, 35 (1961).

[45] J. W. Evans, P. A. Thiel, M. C. Bartelt, Surf. Sci. Rep. **61**, 1 (2006).

[46] M. Rokni-Fard, Q. Guo, J. Phys. Chem. C **122**, 7801 (2018).

[47] J. V. Barth, H. Brune, G. Ertl, R. J. Behm, Phys. Rev. B **42**, 9307 (1990).

[48] A. R. Layson, J. W. Evans, V. Fournée, P. A. Thiel, J. Chem. Phys. **118**, 6467 (2003).

[49] J. B. Hannon, C. Klünker, M. Giesen, H. Ibach, N. C. Bartelt, J. C. Hamilton, Phys. Rev. Lett. **79**, 2506 (1997).

[50] Y. C. Xie, L. Tang, Q. Guo, Phys. Rev. Lett. **111**. 186101 (2013).

2. Literature Review

2.1 Surface Structure of Au(111)

Lattice arrangement such as face centred cubic (FCC) and hexagonal close-packed (HCP) have high efficiency of packing [1]. Bulk gold is known as the only face centred cube (FCC) metal with herringbone reconstruction on its (111) surface. Before the invention of scanning tunnelling microscopy, surface with crystallographic orientations such as (100) and (111) have been already studied by reflection high-energy electron diffraction (RHEED) [3], high-resolution helium atom scattering (HRHAS) [4], low energy electron diffraction (LEED) [5,6] and transmission electron microscopy (TEM) [7-10]. The first high-resolution electron micrograph achieved by TEM intuitively identifies a 6.3 nm long-range corrugation on the (111) reconstructed gold surface, which shows a significant difference with the unreconstructed (1×1) gold surface [3,5]. When STM was introduced into the research of the Au(111) surface, the real-space images with atomic resolution have been observed [11,12].

2.1.1 The Features of Au(111) Surface

The Au(111) surface is one of the most studied metal substrates because of its inertness and unique surface reconstruction [1]. Fig. 2-1 indicates a unit cell in the FCC stacking gold crystal. The gold atoms occupying the corner sites of a unit cell is represented by the grey balls, while the six atoms at the centre of each face (or called face atoms) are represented by red balls. The grey triangular plane marked in the unit cell represents the (111) plane of gold, which goes through three face gold atoms and three corner atoms. To illustrate the adsorption sites on this plane, a low index crystalline axes on this plane as well as the ball model are demonstrated in Fig. 2-2.

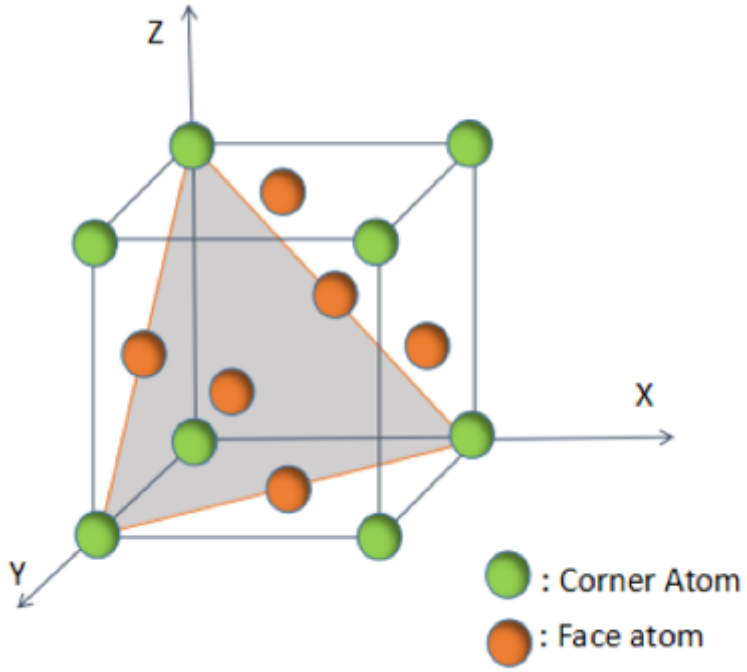


Fig. 2-1 Schematic showing the bulk lattice structure of FCC crystal. In one unit cell, the atoms sitting at the corners and in the centre of faces are marked with green and red colours respectively. The triangular grey plane linked by three corner atoms represents the (111) gold surface.

A diagram of the (111) plane together with the major crystallographic directions is shown in Fig. 2-2 (a), in which six yellow spheres represent the gold atoms in the top-most layer. The close-packing directions of Au atoms, shown by three yellow solid double-headed arrows, are along one of the three equivalent <110> directions. The dashed black line points to the <112> directions, which are perpendicular to the atoms' directions. The three-fold hollow sites appearing at the interspace between three close-packed gold atoms can be divided as the hexagonal closed-packed (HCP) and the face centred cubic (FCC) hollow sites. The two types of hollow sites are marked with blue and green circles, respectively.

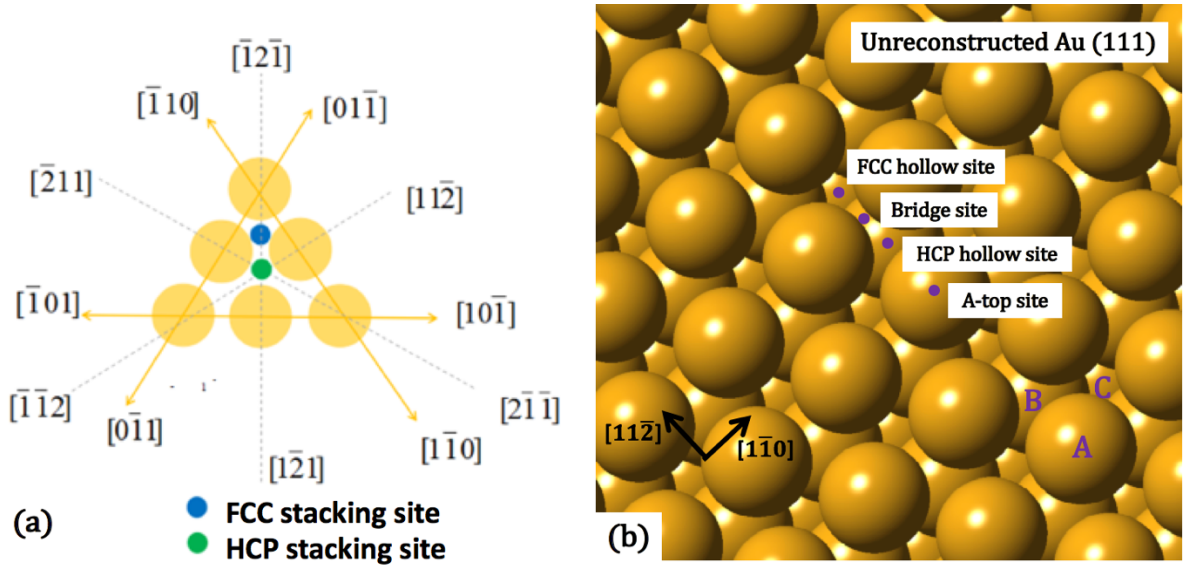


Fig. 2-2 (a) Low index crystalline axes of the Au(111) surface, in which the major crystallographic directions and two types of hollow sites are shown. (b) Ball model showing the (1×1) Au(111) surface. An FCC hollow site, an HCP hollow site, a bridge site and a top site on the unreconstructed gold surface are marked with purple circles. Gold atoms in the crystal can be divided into three types, marked as A, B and C respectively.

A ball model of the unreconstructed (111) gold surface is demonstrated in Fig. 2-2 (b), on which the four major adsorption sites are marked with purple spheres. On the gold surface, FCC hollow sites appear slightly deeper than HCP ones. Right over each close-packed gold atom in the top-most layer, there is an A-top site. The purple sphere marked in Fig. 2-2 (b) represents one of the most common bridge sites on the surface. Any sites located between the other three types of adsorption sites could be named as bridge sites collectively [2].

2.1.2 The $(22 \times \sqrt{3})$ Unit Cell

Fig. 2-3 (a) shows a unit cell on the Au(111) surface described by the Frenkel-Kontorova model [14], of which the ground state has been calculated by F. C. Frank *et al.* [7]. In this model, the surface gold atoms are compared to the connected springs. In the upper part, corrugation of the gold surface in the z

direction is shown. The HCP and FCC regions have similar heights and are marked as the region A and C, respectively. Gold atoms in between the two regions sit on the bridge sites of the layer below and form the incommensurate regions. In the STM images, these atoms are taller than the ones sitting on hollow sites.

Spheres and crosses in the lower part of Fig. 2-3 (a) represent the gold atoms in the first and the second layer respectively, which correspond to the successive small wrinkles shown in the upper part. Gold atoms in the region A stack with the model of ABABA (HCP stacking), while gold atoms in the region C show the stacking model of ABCABC (FCC stacking) [15], which is in agreement with the stacking-fault model interpreted by Hove *et al*. in 1981 [2]. A unit cell marked in a black rectangle includes one FCC region, one HCP region and two transition regions in between them. In the unit cell, 23 gold atoms occupy the total 22 bulk lattice positions in each line. It results in a 4.55 % uniaxial contraction of gold atoms along one of the <110> directions. As shown in Fig. 2-3 (b), the DLs are always perpendicular to the close-packing directions of gold atoms.

Fig. 2-3 (c) shows the Au(111) surface with atomic resolution. A unit cell is highlighted in a blue box. The nearest neighbour distance (NND) of the surface gold atoms is measured between 2.7 Å to 2.9 Å. It agrees with the previous theoretical simulations, which showed a value of 2.7744 Å [16]. Following the close-packing directions, the lateral displacement of atoms is measured as 0.9 Å. It achieves a good agreement with the theoretical result of 0.83 Å. Due to the difference of the occupation sites, gold atoms in the transition regions are brighter than the ones in the FCC or HCP regions. The bright patterns formed by these atoms on the (111) gold surface are known as the well-known herringbone reconstruction, which is also named as discommensuration lines (DLs). The DLs run in the directions of <112> and are always perpendicular to the close-packing directions of the gold atoms.

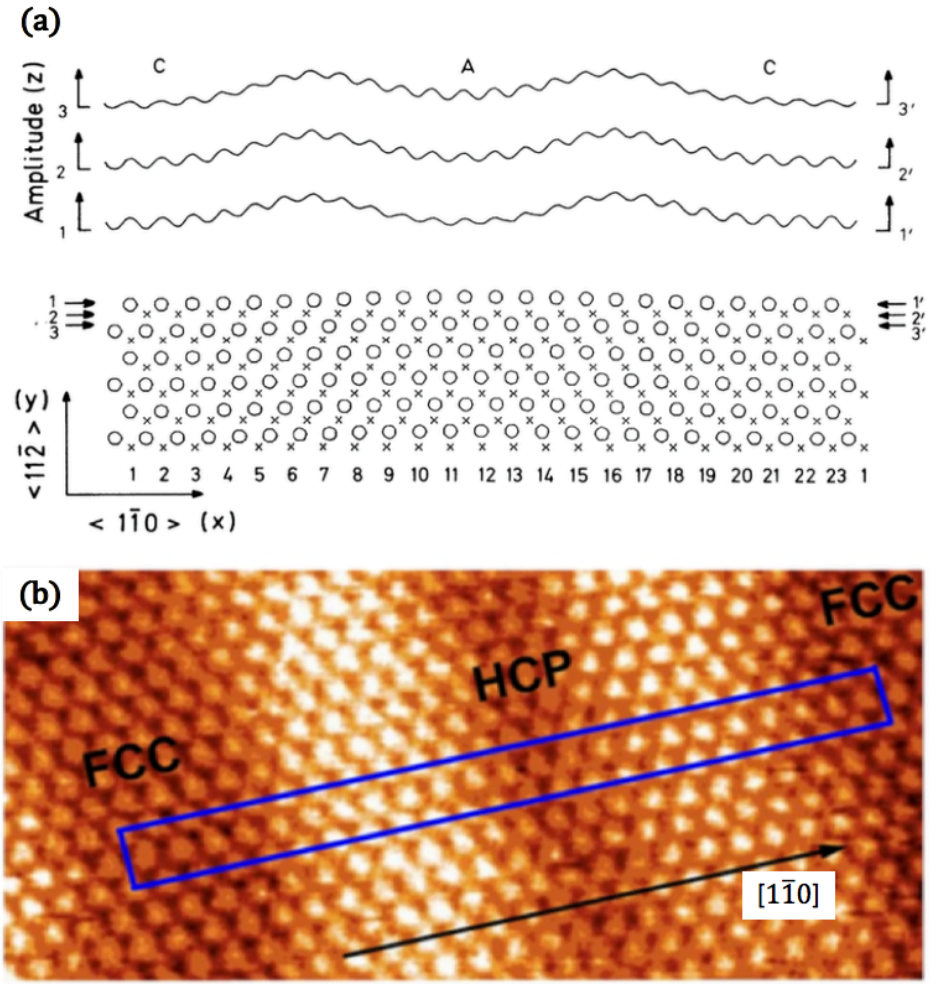


Fig. 2-3 (a) Upper part: corrugation in the z-direction for 1, 2 and 3 sections. The amplitude is enhanced proportionally. Bottom part: an atomic structural model of the Au(111) surface, in which the $(22 \times \sqrt{3})$ unit cell is marked with a black rectangle. The circles and crosses refer to the surface layer atoms and the second layer atoms, respectively. Gold atoms at the transition regions occupy the bridge sites [4]. (b) STM image of the Au(111) surface with atomic resolution, the $(22 \times \sqrt{3})$ unit cell is marked with the blue rectangle. The black arrow indicates the $[1\bar{1}0]$ direction [16].

Marked in the blue box of Fig. 2-3 (b), each $(23 \times \sqrt{3})$ unit cell includes two DLs, which separate one HCP region and two half FCC regions. Width of the HCP and FCC regions on both sides of the DLs are measured as 22 Å and 44 Å respectively. The difference of the width suggests a variation in the binding energies of the two regions [15].

The stressed domains on the (111) gold surface result from the long-range elastic interaction force [17]. Gold atoms in the top-most layer of Au(111) has a lower coordination number compared with those stacking in bulk and thus become unstable. Due to the soft atomic potential in the crystal, surface gold atoms are allowed to reduce atomic spacing by having a short distance shift from their original positions. Meanwhile, these surface atoms still tend to occupy the three-fold hollow sites. It results in the majority of atoms occupying the three-fold hollow sites (FCC and HCP hollow sites) but some others occupying the transition regions. For releasing the stress, the DLs bend periodically to make the gold surface anisotropic. When atoms or molecules are deposited onto the gold surface, the adsorbate-substrate interaction could change the surface elastic force and lift the herringbone reconstruction [18,19].

2.1.3 Monoatomic Step Edges on Au(111)

Two types of monoatomic steps consisting of close-packed Au atoms on the Au(111) surface are identified and are named as the A and B steps, respectively. These steps influence the local surface strain and change DLs' patterns. Type A steps ascend along the $[11\bar{2}]$ azimuth (or the equivalent $[\bar{2}11]$ or $[1\bar{2}1]$ azimuths) and present a {100} microfacet. The B steps descend along the $[11\bar{2}]$ azimuth and present a {111} microfacet. Both the microfacets of the {111} and {100} type steps are illustrated in Fig.

Fig. 2-4 (a) shows the stacking model of the gold atoms at the two types of the steps on the Au(111) surface. One {111} and one {100} types of steps exist directly opposite the hexagonal close-packed island along the $[\bar{2}11]$ azimuth. One step is ascending while the other is descending. The microfacets {100} and {111} in the figure are marked in a blue box and a blue triangle, respectively. Gold atoms at a {100} step edge sit on the bridge sites of the layer below, while the

atoms at a {111} step edge sit on the hollow sites. Compared with the {100} facet step, the {111} step has higher atomic density and thus lower step energy [19,20]. 2-4 [20].

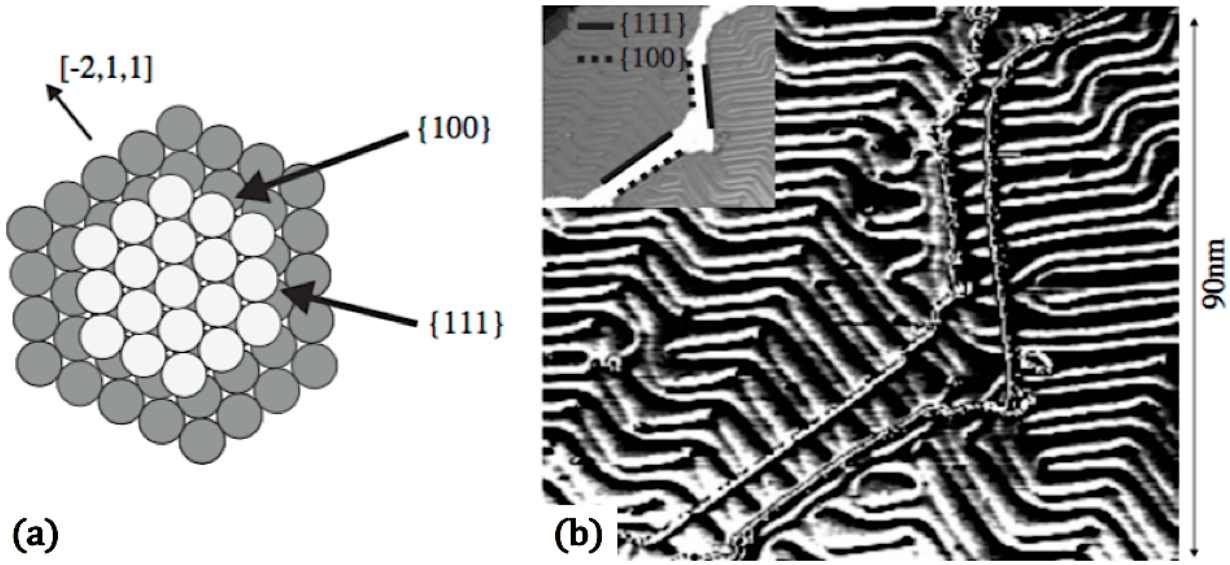


Fig. 2-4 (a) Schematic top view of the two kinds of close-packed gold steps: one with {100} microfacet (A step) and another with {111} microfacet (B step). Along the [$\bar{2}11$] azimuth, the B step is descending while the A step is ascending [20]. (b) STM image showing the two types of step edges on Au(111). A long plateau passes from the lower-left to the upper-right part of the image. In the inset, the {100} and {111} type of steps are marked with the dashed and dashed lines, respectively. Herringbone reconstruction close to the two types of steps have different shapes [20].

As shown in Fig. 2-4 (b), patterns formed by the DLs on the Au(111) surface are different around the two types of step edges. The DLs can run across a {111} step without being interrupted. Atoms under the plateau stack with the unreconstructed FCC structure, which allows the two layers' atoms at step edges to compress synchronously. When the DLs approach to the step edge, atoms in the transition regions tend to switch to the FCC stacking. It behaves as an expanding of FCC regions and a shrinking of the HCP regions globally. Therefore, the DLs pass over the upper terrace of the {111} step instead of

interrupting. On the contrary, when the DLs approach to a {100} step, they turn back with a “U” shaped end. The FCC regions on the lower terrace of the {100} step are sealed by an extra DL growing parallel to the step, which guarantees all the gold atoms close to the step edges have the FCC stacking.

2.1.4 Elbow Sites and Rotational Domains

A typical topography of the reconstructed Au(111) surface is present in Fig. 2-5 (a), in which the periodic fluctuations shown as zigzag patterns are picked out by STM. The pairwise DLs separate the narrow HCP and wide FCC regions, making them arrange on the gold surface alternatively.

Marked by the white dashed lines, a pair of DLs on the two sides of one commensuration (FCC or HCP) region maintain parallel between the two adjacent bending points. In some previous research, heights of DLs are measured between 0.02 nm and 0.08 nm [21,22].

In our scanning image, surface fluctuation along the black solid line AB is shown in the line profile of Fig. 2-5 (b). It indicates that the DLs are measured ~ 0.2 Å higher than the unreconstructed regions, which corresponds to the previous research. The DLs on the Au(111) surface bend systematically with a period of 25 nm, and the zigzag patterns are well known as the herringbone reconstruction. Therefore, the Au(111) surface can also be divided into three types of domains with the orientations differing in 120°. In each type of the domains, there is a uniaxial contraction along one of the <110> directions [23].

Fig. 2-6 (a) shows the bending points of the DLs on Au(111). The DLs on the gold surface can be divided into the type x and the type y DLs based on the different elbow sites they contain. Elbow sites of the type x DLs have pointed shapes, while elbows of the type y DLs have a more smooth shape. The pointed

elbow sites on one type x DLs could either bend in the adjacent FCC or the HCP regions.

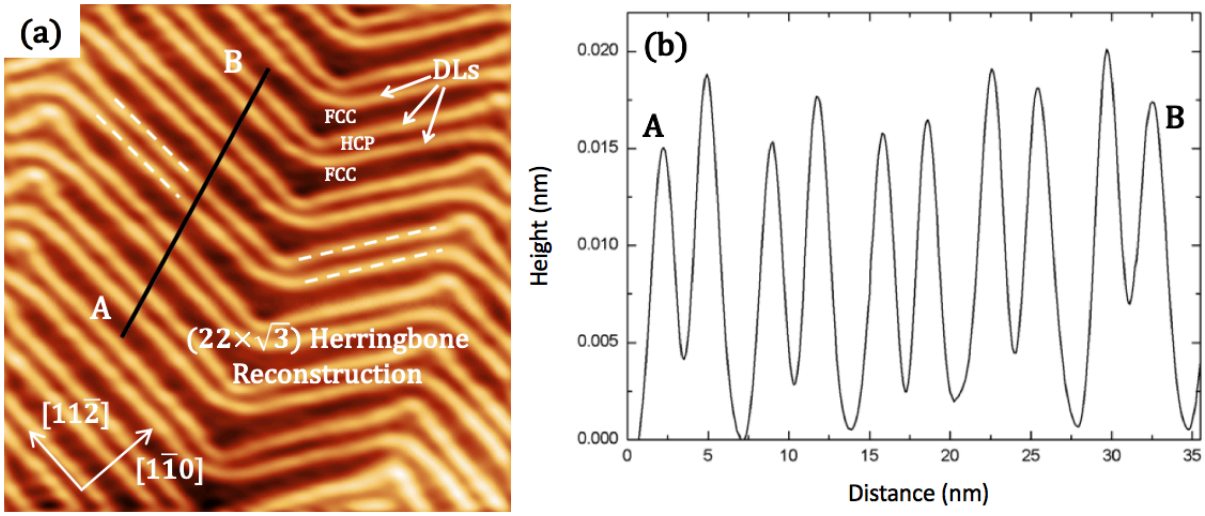


Fig. 2-5 (a) STM image showing the DLs on the Au(111) surface. (-1.61 V, 0.04 nA. 60 nm × 60 nm). These DLs separate the gold surface into the wide FCC regions and the narrow HCP regions. (b) A line profile along AB showing the height differences between the FCC regions, the HCP regions and the DLs on the Au(111) surface.

Marked in the yellow boxes in Fig. 2-6 (a), a series of pointed elbow sites bend into the adjacent FCC commensuration regions on the Au(111) surface, which are called bulged elbow sites. Meanwhile, the elbow sites called pinched elbow sites are marked in the green boxes. These elbow sites bend into the adjacent HCP regions [18]. Along the yellow or green arrow, it can be found that either the bulged or pinched elbows pack in rows on the Au(111) surface.

The sketch image in Fig. 2-6 (b) indicates the atomic structures of the pointed and rounded elbow sites in detail. As mentioned before, gold atoms in the DLs sit on the bridge sites [4].

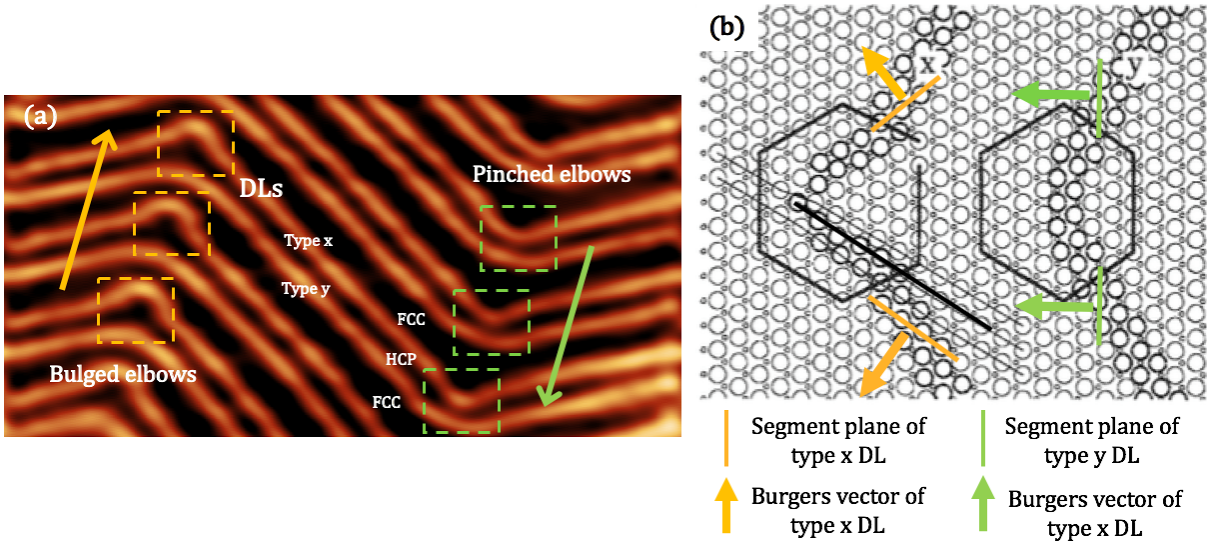


Fig. 2-6 (a) Higher resolution of the DLs on the Au(111) surface. The bending points of the DLs have either pointed or rounded shapes. The bulged and pinched elbow sites with the pointed shape are marked with orange and green dashed boxes respectively (V = -2.0 V, I = 0.05 nA, 30 nm × 60 nm). (b) Sketch showing a possible atomic lattice of the pointed and rounded elbow sites. Gold atoms on the two sides of the type x DLs occupy bridge sites with different orientations, while the gold atoms in the type y DLs occupy bridge sites with the same orientations [18].

For investigating the atomic lattice and the defects of the elbow sites, here the Burgers vectors are used to mark the close-packing of the gold atoms on the two sides of an elbow. Each Burgers vector is perpendicular to a corresponding segment plane. Due to the different pointing directions of two vectors, Burgers circle of type x DLs is opened. Marked with the orange arrows, the Burgers vectors on the two sides of a bulged elbow point in two different directions. It indicates the different orientations of the gold atoms on the elbow's two sides. The edge dislocation in this area results from an extra row of gold atoms terminating at the pointed elbows. The extra row of gold atoms are marked with a solid black line in Fig. 2-6 (b). At the terminal of this DL, one gold atom is observed having reduced coordination compared with the adjacent ones. It thus works as a single atom defect. However, on the two sides of a rounded elbow site,

the two Burgers vectors point in the same direction. Therefore, gold atoms in the type y DLs orient in the same directions. It results in a closed Burger circle of the type y DLs and the smooth shape of the elbow sites. Compared with the pointed ones, the rounded elbows on the gold surface are less strained.

2.2 Metal Adsorption on Au(111)

As introduced, the (111) gold surface has long-range periodicity and rich structural features. It hence can be taken as an ideal substrate for the growth of different kinds of nanostructures. In UHV, a series of metal atoms' epitaxial growth on the reconstructed Au(111) surface have been characterized by STM [24-31].

There are mainly two types of nucleation behaviours of these metal atoms on the Au(111) substrate at low coverage. In the first type, adsorbed atoms prefer to nucleate epitaxially and grow as three-dimensional clusters at the herringbone elbow sites. Due to the long-range periodicity of DLs, highly ordered arrays of hexagonal clusters can be observed on the surface of gold.

Element	Surface free energy (eV)	Heat of sublimation (eV)
Ag	0.50	2.95
Al	0.56	3.39
Cu	0.69	3.51
Au	0.72	3.79
Ni	0.90	4.45
Co	0.94	4.40
Fe	0.96	4.32

Table 2-1 The surface free energy and heat of sublimation for the metals Ag, Al, Au, Ni, Co and Fe. Data is obtained from [24].

In the second type, metal atoms nucleate as irregular islands and attach to the gold step edges. When the coverage of atoms increases, growing of these islands in the FCC regions are astricted by the herringbone reconstruction on the two sides. The two kinds of nucleation can be explained by the different surface free energy of atoms as well as heat of sublimation.

Surface free energy and heat of sublimation of some metal materials are shown in table 2-1. On the surface of Au(111), metals such a Ni [24,25], Pd [26] and Mo [27] have lower surface free energy and heat of sublimation than gold and prefer to nucleate as islands and ripen at the elbow sites. However, metals such as Al [28], Ag [31] have higher surface energy and heat of sublimation compared with Au. After being deposited onto the gold surface, these atoms prefer to nucleate as irregular islands and ripen on the flat terraces instead of nucleating at elbow sites [24].

As introduced in Fig. 2-6 (b), the single atom defects at the pointed elbow sites of DLs are easier to be replaced by the adsorbed metal atoms. Introduced by Meyer *et al*., the nucleation and ripening of the metal atoms on Au(111) can be divided into two steps. In the first step, some atoms firstly land on the gold surface replace the gold atoms working as single defects. Then, these atoms work as the new centres of nucleation and are able to capture the later deposited atoms.

As shown in Fig. 2-7 (a), 0.25 ML nickel atoms are deposited on the Au(111) surface, most of which nucleate epitaxially as truncated triangular islands [24,25]. Due to the periodic reconstruction on the substrate, these islands are uniformly spaced with similar distances and pack as highly ordered arrays on the gold surface.

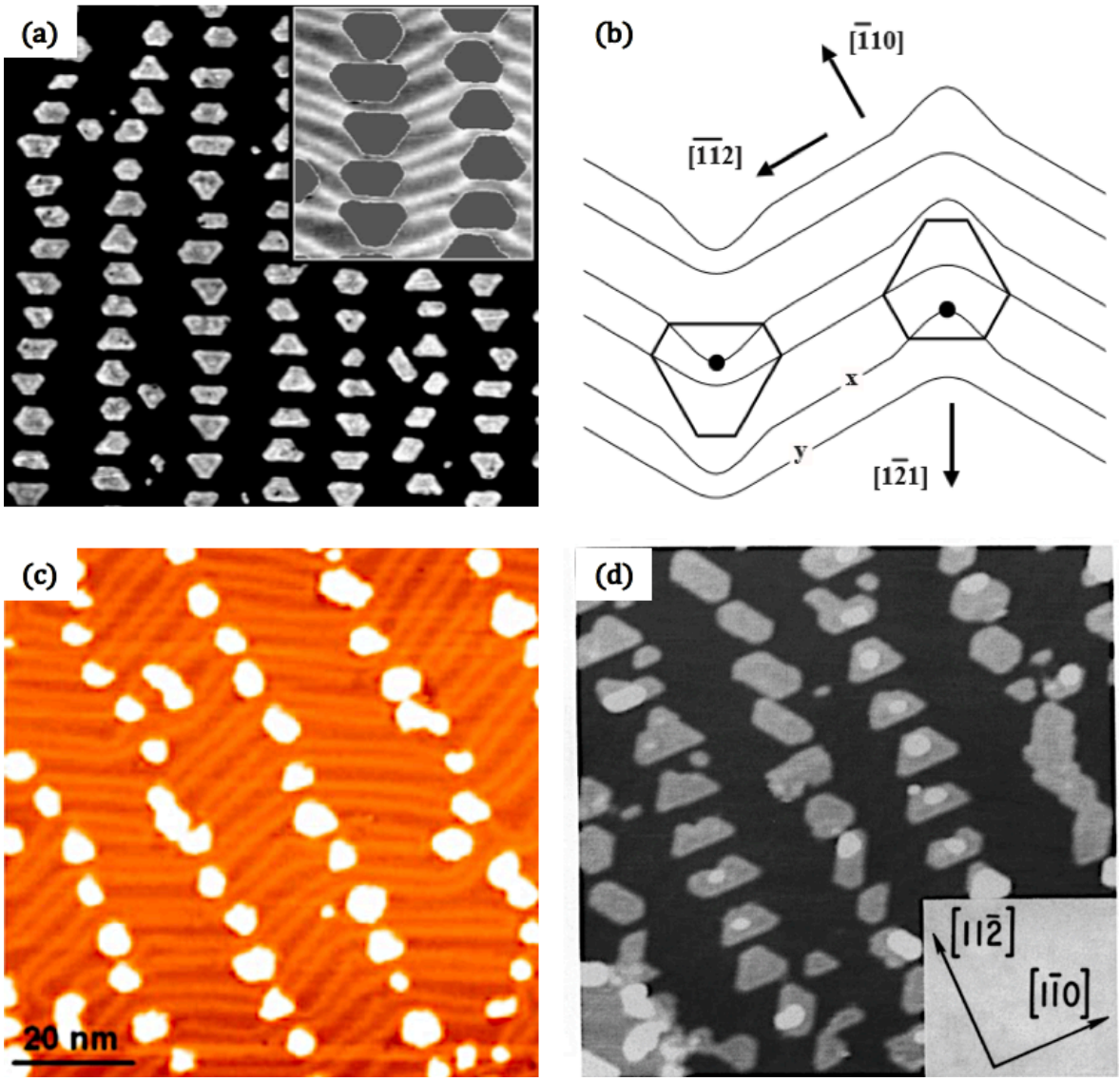


Fig. 2-7 STM images showing the nucleation of the Ni, Pd and Fe adatoms on the Au(111) surface. These atoms occupy the periodic elbow sites and form the monolayer islands in highly ordered arrays. (a) 0.25 ML Ni atoms are deposited on the gold surface at 300 K (V = -0.4 V, I = 1.0 nA, 99 nm × 90 nm) [25]. (b) Schematic of 2-D Ni islands showing the crystallography, the nucleation places of islands as well as the orienting relationship between the two Ni islands sitting at two adjacent elbows [25]. (c) 0.14 ML Pd on the Au(111) surface at room temperature (90 nm × 90 nm) [26]. (d) 0.25 ML Fe atoms on the Au(111) surface at room temperature (80 nm × 80 nm) [30].

At higher coverages, the second layers of Ni appear even before the isolated islands in the first layer merge and ripen as the larger ones. The Ni islands at the

bulged elbow sites or the pinched elbow sites have similar sizes and shapes. After being heated to 570 K for one hour, the free energy of the Ni atoms in the islands is commonly enhanced. Some of them can replace gold atoms below and merge into the substrate, forming a special Ni-Au alloy at the interface [29].

Schematic in Fig. 2-7 (b) shows the growing direction of the Ni islands as well as the relationship between the islands sitting at bulged elbows and pinched elbows. There is a polygonal Ni island occupying a bulged elbow site on the right side of the image. The most preferred growing direction of the island is $[\bar{1}2\bar{1}]$. Main part of these islands occupy the FCC regions, while in the islands there are also a few atoms observed sitting in the adjacent HCP regions and attaching to the pinched elbow sites. The DLs on the surface do not affect the epitaxial growth of Ni atoms. On the left side, another island originally nucleating at a pinched elbow site has its most preferred growing direction of $[1\bar{2}1]$. Some atoms of this island are also observed sit in the adjacent FCC and HCP regions. Co-existing of the two types of islands results from the energy difference required for forming the two kinds of island's steps [25]. Part of the DLs underlying the adsorbed Ni islands has been lifted as there is no fluctuation on islands' surface observed in the STM images.

Apart from Ni atoms, elbow sites are also the preferential adsorption sites for other atoms. Islands formed by 0.14 ML Pd [26] and 0.25 ML Fe [30] on the Au(111) surface are respectively shown in Fig. 2-7 (c) and (d), where the islands also have similar sizes and truncated polygonal shapes and almost occupy all the elbows on the gold terrace. Some of these islands at adjacent elbows have combined and appear as short chains.

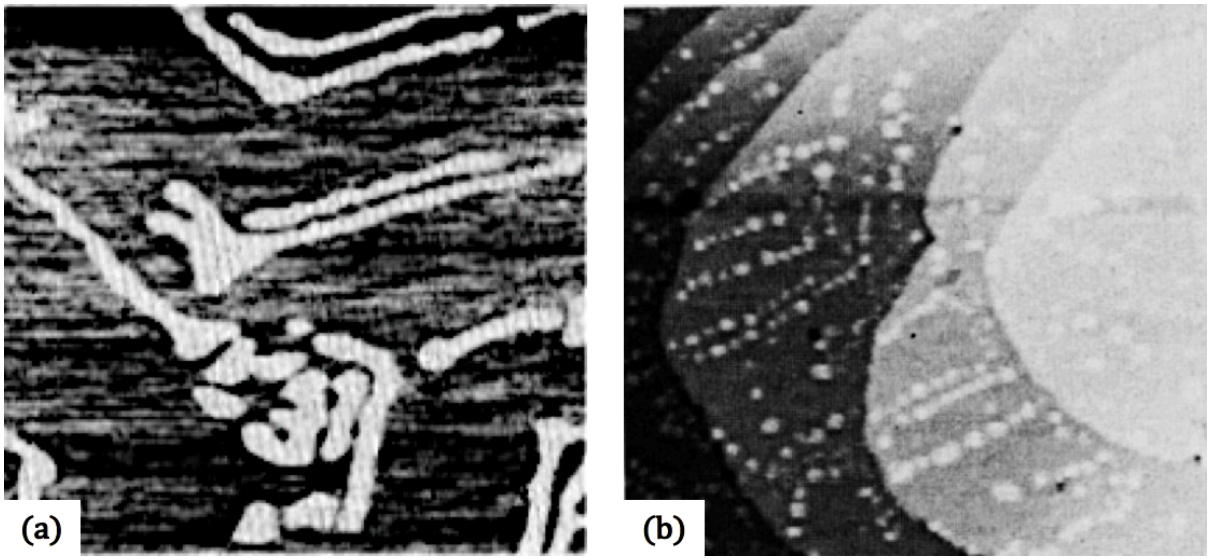


Fig. 2-8 (a) STM image showing 0.25 ML Ag atoms deposited on the surface of Au(111). The narrow Ag islands are defined by the herringbone reconstruction and extend along the DLs (115 nm × 115 nm) [31]. (b) STM image showing 0.1 ML Au atoms forming the alignments of islands on the Au(111) surface (115 nm × 115 nm) [33].

0.25 ML Ag on the Au(111) surface is demonstrated in Fig. 2-8 (a), in which atoms initially nucleate as finger-like clusters and attach to the step edges. As the coverage increases, Ag islands then ripen as long and narrow islands, gradually growing onto the gold surface. Most of these islands prefer to pack in the FCC regions and are defined by the parallel DLs on both the two sides [31,32]. When gold is chosen as the deposited sediment, its adsorption mechanism on the gold surface is affected by both the atoms' deposition flux and surface diffusion rate. As indicated in Fig. 2-8 (b), 0.1 ML Au form small atomic layer islands at elbows sites on Au(111). Different from the islands of Ni, Pd and Fe, the size distribution of these gold islands is not uniform. In STM images, most of the gold islands have a preference of sitting in FCC regions [18,33].

2.3 Highly Oriented Pyrolytic Graphite (HOPG)

2.3.1 Structure of HOPG

Highly oriented pyrolytic graphite (HOPG), belonging to lamellar materials, can be treated as a highly ordered form of synthetic graphite. It has high purity and is crystallographically stacked by the two-dimensional carbon films with atomic layers. These films are well aligned with each other and are known as graphene [34,35]. Diameters of the individual crystallites in HOPG are commonly thinner than 10 μm [36]. Similar to other lamellar materials such as mica and molybdenum disulphide, the force between the two adjacent layers of HOPG is rather weak. Fig. 2-9 (a) shows the basic physical appearance of a HOPG crystal with the dimensions of $10\ \text{mm} \times 10\ \text{mm} \times 1\ \text{mm}$. Its purity level can be controlled on the order of 10 ppm ash. With high quality and less roughness of the surface, and a smaller number of atomic steps appear on a freshly cleaved surface under the microscopic.

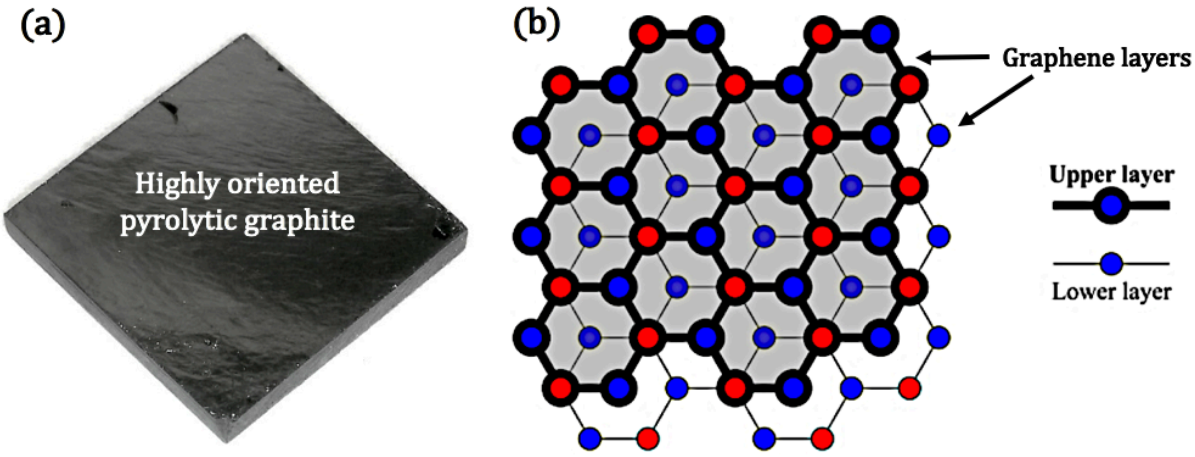


Fig. 2-9 (a) Physical appearance of one HOPG crystal. It has high purity and offers a flat surface under the microscopic [37]. (b) Schematic illustrating the stacking structure of a bilayer graphene in HOPG crystal. Carbons in the upper and lower layer are marked with dark and light colours respectively. In each layer, the carbon atoms in blue sit directly over another atom in the adjacent layer, while the carbon atoms in red sit over the centre of a hexagonal ring [34].

High-quality graphene is known as a kind of material with rich properties. zero bandgap material with strong thermal and electrical conductivity along the certain directions [40,41]. It's applied in a various fields [41], e. g., supercapacitors [42], solar cells [43], and light-emitting diodes [44]. Graphene can be described as chicken wire patterns formed by atomic-scale carbon atoms [38]. Each carbon atom forms strong equivalent covalent bonds to its three neighbouring ones. Therefore all the carbon atoms in graphene are equal to each other [39,40].

Once two or more graphene are overlaid and form bilayers or multilayers, carbon atoms in a single layer are not necessary for the same environment anymore. Here the most basic case is discussed. Packing structure of two layers graphene in HOPG crystals is shown in Fig. 2-9 (b). For being distinguished conveniently, carbon atoms in the upper and lower layers are represented by the spheres with dark and light colours, respectively. Inside the upper layer of graphene, carbon atoms could be divided into the A and B types averagely. The two types of carbon atoms are represented by the red and blue spheres, respectively. In HOPG, each type A atom with red colour stands directly over another type A atom in the beneath layer, while type B stands over the centre of a hexagonal ring formed by six atoms. In graphene, the two types of atoms are equivalent to each other in the same layer.

The lattice structure of graphene is illustrated on the left side of Fig. 2-10, in which one carbon atom has three lateral coordination. Each type A (type B) carbon atoms forms strong covalent bonds (or called σ bonds) with its three coordinated type B (type A) atoms. In graphene, the NND of two carbon atoms (one type A and one type B atoms) is ~ 2.46 Å.

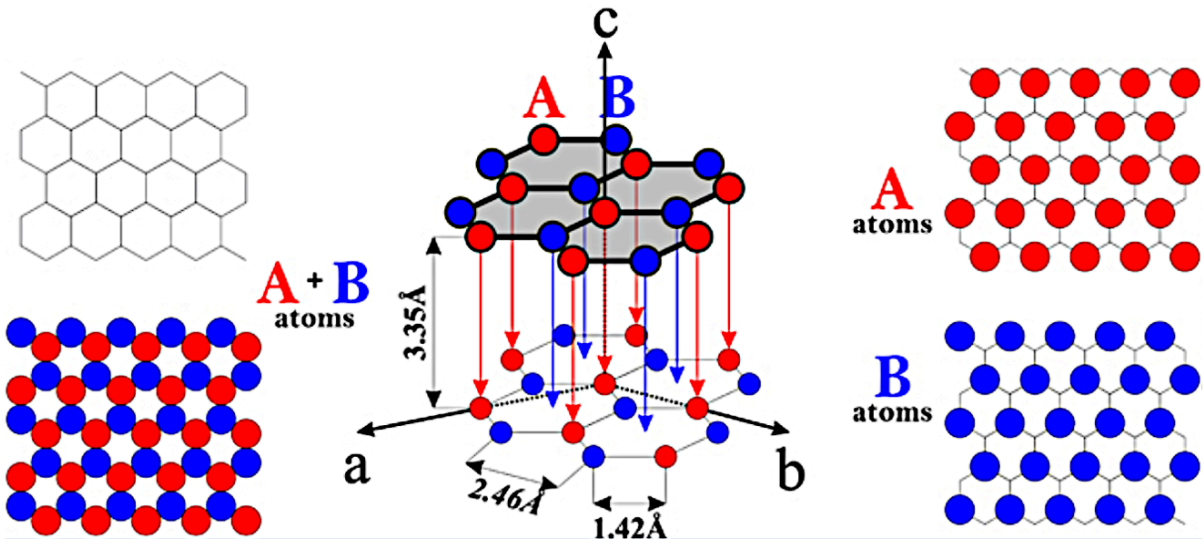


Fig. 2-10 Schematic showing the crystal structure of HOPG. Left side: top view of the basal plane of graphene. The schematic showing its surface structure packed by carbon atoms. Middle: half of the HOPG's unit cell. The dashed lines in the middle part represent the axes of the bulk unit cell. Right side: Type A and B carbons in the same layer graphene represented by the red and blue spheres [34].

By separating the two types of carbon atoms, a whole lattice of graphene consists of two equivalent sublattices, and one sublattice can be treated with a rotation of 120° to the other. The NND of the same type atoms (type A or type B) is ~ 1.42 Å [45,46]. Half of the HOPG's unit cell is shown in the middle of Fig. 2-10 [34], in which the dashed lines in the middle part represent the axes of the bulk unit cell. Introduced by Bernal *et al.*, the carbon atoms in HOPG stack in the model of ABABAB [34]. The spacing between two adjacent carbon layers is measured as 3.35 Å [47]. The large distance between layers results from the interlayer van der Waals force, which is much weaker compared with the bonds. According to the Raman scattering data observed by Nicklow *et al.*, the average force constant for a pair of carbon atoms is measured as 900 N/m in the x-y plane while only 14 N/m in the z direction [48]. It makes HOPG a freshly cleavable material.

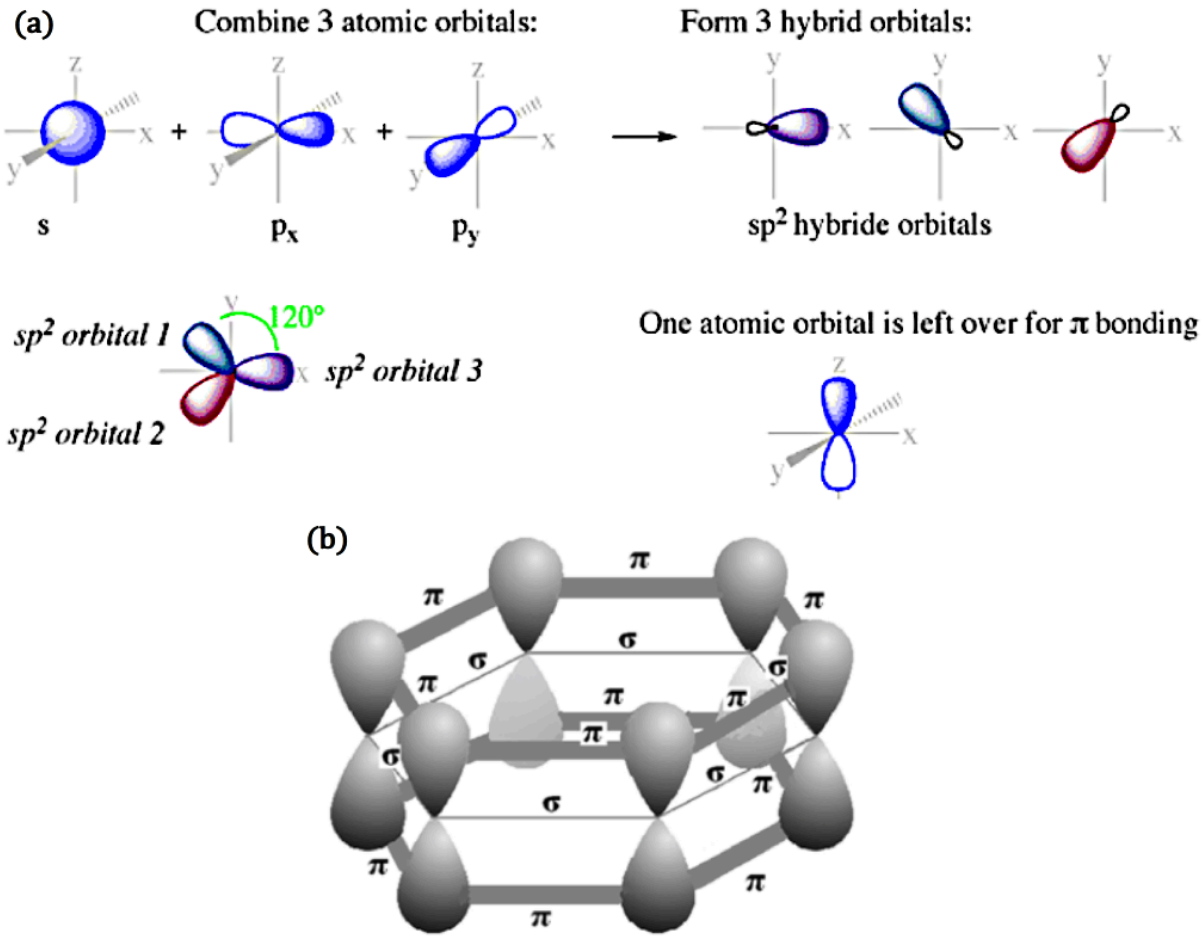


Fig. 2-11 (a) sp^2 hybridised electron orbitals in one carbon atom. Three atomic orbitals s, p_x, p_y in one carbon atom combine as three new sp^2 hybrid orbitals. One atomic orbital p_z is left for forming π bonds above and below carbon rings [50]. (b) σ and π bonds existing in a hexagonal carbon ring [49].

Both the carbon bonding existing in HOPG and graphene are featured by the sp^2 hybridisation. Fig. 2-11 (a) introduces the sp^2 hybridisation of carbon atoms in HOPG. Each carbon atom contributes four valence electrons for forming chemical bonding with its neighbouring ones. Due to the Pauli exclusion principle, any two electrons of one atom are prohibited from having the same set of quantum states. In an isolated carbon atom, two of its valence electrons occupy the 2s orbital while the other two occupy the $2p_x$ and $2p_y$ orbitals respectively. When the 2s orbital is combined with the $2p_x$ and $2p_y$ ones, three new hybrid

orbitals are formed in XY plane and have a 120° to each other. When the two isolated carbon atoms have extremely small spacing, each atom donates one of the three sp^2 orbitals out. Then wave functions of the two orbitals overlap and form a covalent σ bond with a length of 1.42 Å. This type of bonding is able to lock the two carbon atoms tightly [45,51]. In HOPG, all the carbon atoms in the same layer connect their adjacent ones by the stable σ bonds and establish the "honeycomb" patterns. Accompanying with each σ bond, a weak antibonding state (or called the σ^* bond) will also occur and work for preventing the combination of the two atoms and reducing the charge density between carbon atoms. A pair of σ and σ^* bonds exist at the two sides of a carbon atom but point to the opposite directions.

When the stable σ bonds have been formed between carbon atoms in each atomic layer of HOPG, the left $2p_z$ orbitals of carbon atoms are donated out to create a particular type of dangling bond, known as the π bond. It exists above and below each graphene layer and enhances the charge density between carbon atoms [52]. Each π bond also has a corresponding antibonding state (or called π^* bond). It exists at the mirror position of the π bond if the carbon layer is taken as a reference, and tends to offset the change of atoms' charge density when multilayer graphene stack together and form HOPG [45]. Fig. 2-11 (b) demonstrates one hexagonal carbon ring consisting of six atoms, in which σ bonds and π bonds are built.

2.3.2 Surface Electronic Structure of Graphene and HOPG

Colour contract presented in the STM images reflects the difference of local electron densities commonly on samples' surface [54]. When an STM tip scans over carbon atoms in the top-most layer of HOPG, carbon atoms with higher electron densities lead to a higher tunnelling current between the sample and tip,

which makes these atoms bright. On the contrary, the atoms with low electron densities appear as dims in the scanning image [55]. One atomic image of graphene is shown in Fig. 2-12 (a). Due to the variation in electron densities, all the atoms are equal to each other and appear as the bright spots in the image, while the voids of the carbon rings appear as dims in the image [53,56,57]. It matches graphene's "honeycomb" structure perfectly. It is compared with the surface of HOPG scanned by STM with the same bias voltage and the tunnelling current.

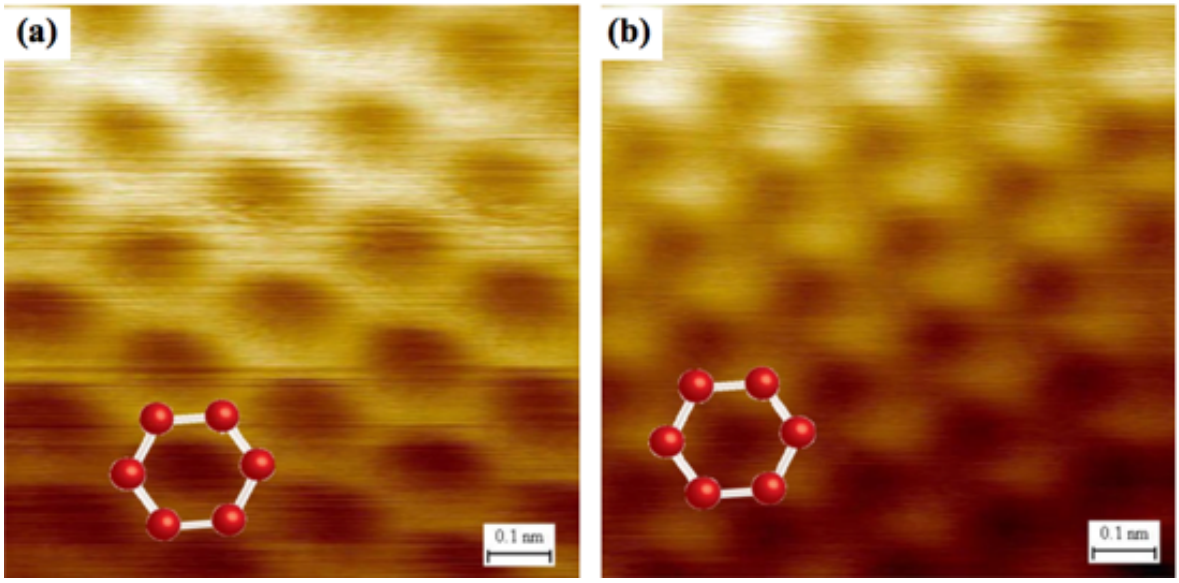


Fig. 2-12 (a) Surface electronic structure of (a) the graphene and (b) the HOPG recorded by scanning tunnelling microscopy (STM), respectively. A "honeycomb" pattern and a three-fold symmetry pattern are observed on the surface of graphene and HOPG, respectively. A model of the underlying atomic structure is illustrated inside two images [53].

A three-fold symmetry pattern formed by the on HOPG surface in Fig. 2-12 (b), in which the dims and bright spots in the image represent the type A and B carbon atoms respectively. Distance between the two adjacent bright spots or dims is also identical to the lattice constant of graphene. As already mentioned in Fig. 2-9, a type A carbon atom sits over another same type atom in HOPG, then its p_z orbital

overlaps with the orbitals in the adjacent two layers. It reduces the local electron density around this atom.

On the contrary, since each type B atom stands over a void of the lower layer, local electron densities around these atoms are less reduced. In the same scanning image, the type B atoms look brighter compared with the type A ones. In the real process of producing HOPG crystals, the grain boundaries [58] and superlattices [42,44,59] are able to be observed on the graphite surface occasionally. The superlattice in the STM image appear as large bright spots and have a common periodicity of 38 Å. Due to the surface deformation, some π bonds above carbon atoms interact with each other, which changes the local charge density states of HOPG [43]. For achieving the flat terraces with fewer atomic steps and less contamination, graphite can be taped several times in air firstly before being used.

2.3.3 Molecules Deposited on HOPG

Due to the smooth surface and lower surface energy, HOPG is widely used as an ideal solid substrate for studying the self-assembled metal atoms, molecules and metal-organic frameworks. Compared with the materials such as mica and molybdenum disulphide, HOPG guarantees the examined intact of both adsorbed sediments and substrate during STM scanning [60-62]. The surface of HOPG can maintain unchanged up to 300 ℃ in UHV. The high thermos-stability of HOPG allows the adsorbed materials to be tested or analysed under a wide range of temperatures.

In the ultrahigh vacuum chamber, sizes and distribution of diverse metal particles [63,64] or metal-organic complexities [65,66] are already studied by STM at a variety of temperatures on the HOPG surface. Especially when the aromatic molecules with long chains are deposited, their orientations and the close-packing packing structures are affected by the π bonds over the graphite surfaces [67,68].

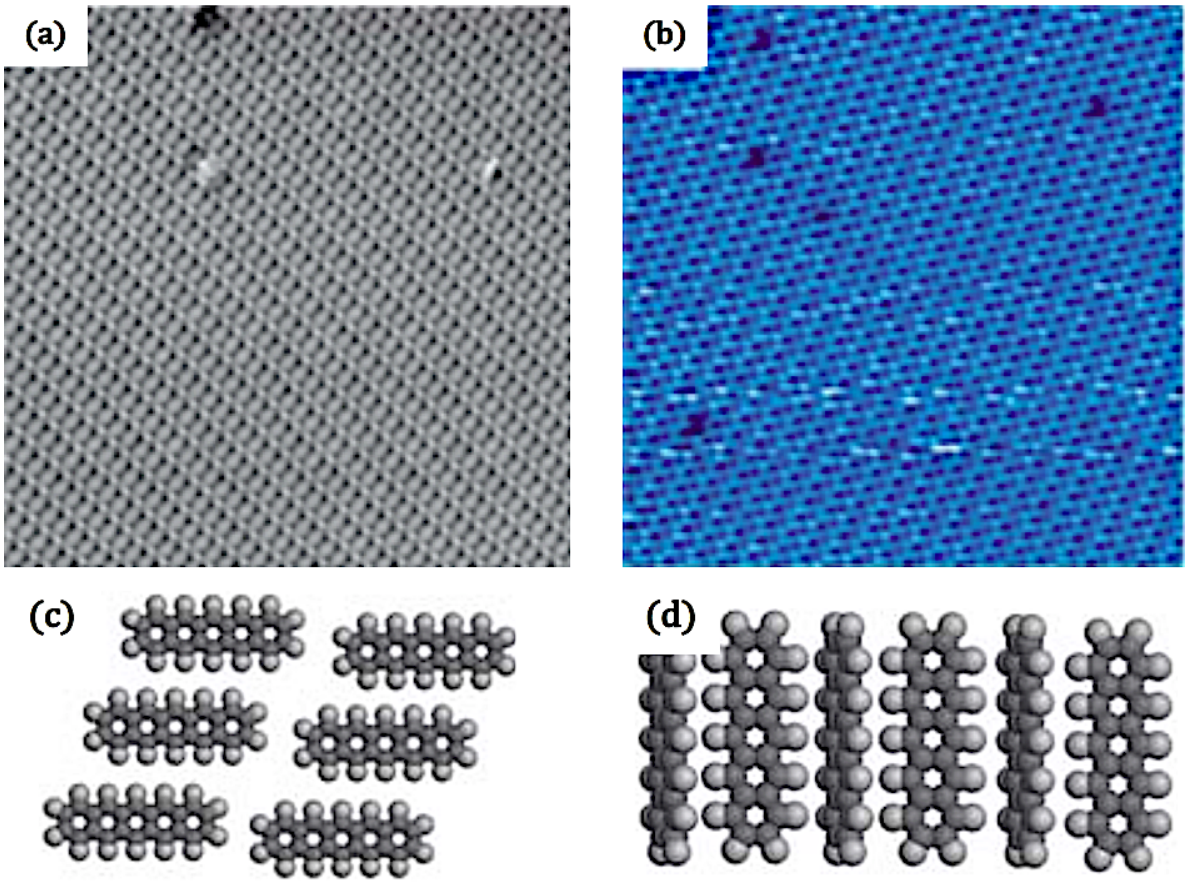


Fig. 2-13 (a) STM image showing the lying-down monolayer of pentacene deposited on HOPG surface (V = 2.0 V, 30nm × 30nm) [68]. (b) STM image showing the pentacene layer on HOPG surface. Each molecule stands upright with its long axis perpendicular to the substrate (V = 0.8 V, 20nm × 20nm). Schematic showing the packing structure of (c) lying-down and (d) standing-up pentacene on HOPG, respectively [68].

Fig. 2-13 (a) shows a well-ordered packing structure formed by a monolayer of close-packed pentacene on the HOPG surface. At low coverage, some pentacene molecules lie down with an π-π stacking mode, where all the molecules' benzene rings are parallel to the substrate [68]. Molecules look like small disks in the scanning image. The proposed packing structure of the lying-down pentacene are shown in Fig. 2-13 (c). In this stacking mode, molecules' packing status are dominated by the interfacial dispersion force between pentacene and HOPG. A unit cell of this long-range supramolecular structure can be easily measured in the scanning image.

However, when the coverage of pentacene is more than 1 ML, most of the pentacene molecules on the substrate take a uniform head-on configuration. Influenced by both the intermolecular dispersion force and the attractive intermolecular electrostatic force, most molecules form stable benzene-dimmers. It gives rise to the repeated T-shaped patterns on the graphite surface. Under this stacking mode, the interaction between the pentacene molecules and graphite becomes dramatically weak.

2.3.4 Gold Atoms Deposited on HOPG

In the previous research, nucleation of the gold clusters on air-cleaved or vacuum-cleaved HOPG has been studied with the help of the techniques such as scanning electron microscopy (SEM) and transmission electron microscopy (TEM) [64]. After being deposited on the HOPG surface, most metal atoms nucleate and aggregate to 3D crystals with a three-fold symmetry [64,69-72]. Particularly, the gold and silver atoms commonly stack with FCC structure and have their (111) plane face up for achieving the lowest surface energy [62].

A series of TEM images in Fig. 2-14 shows the growth of the gold crystals on the air-cleaved graphite with the average thickness of 1.0 Å, 7.8 Å, 99 Å and 250 Å. Deposition rate of the atoms is fixed at 0.1 Å/s. Since the average thickness reaches 1.0 Å, plenty of small gold particles with irregular shapes have occurred on the substrate. These particles then merge with the neighbouring ones and form elongated islands, containing (111) nuclei and fibre textures [62].

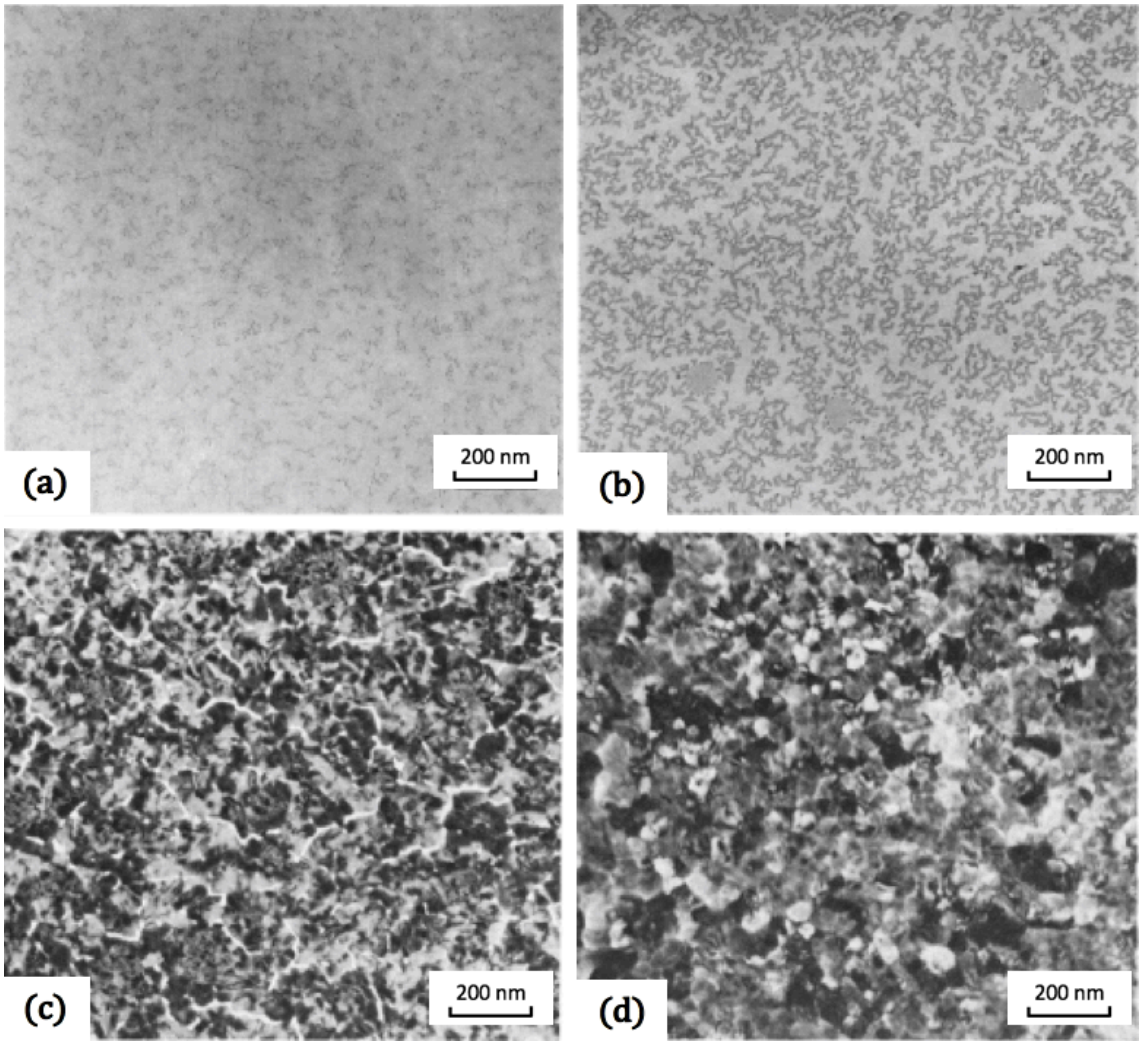


Fig. 2-14 TEM images showing the growth of gold films with a deposition rate of 0.1 Å/s on the air-cleaved graphite. Average thicknesses of gold films are: (a) 1.0 Å, (b) 7.8 Å, (c) 99 Å, (d) 250 Å [62].

As the coverage of gold atoms increases, the isolated gold islands tend to have larger sizes before ripening with higher thickness. It takes a longer time for them to recrystallize and leads to the gold islands' sequential coalescence. It corresponds to the previous investigation did by Stowell *et al*. [73]. Instead of directly joining in the existing large islands, the gold atoms deposited latter on the graphite choose to fulfil the gaps between islands, which increases the diversity of atoms' packing orientations.

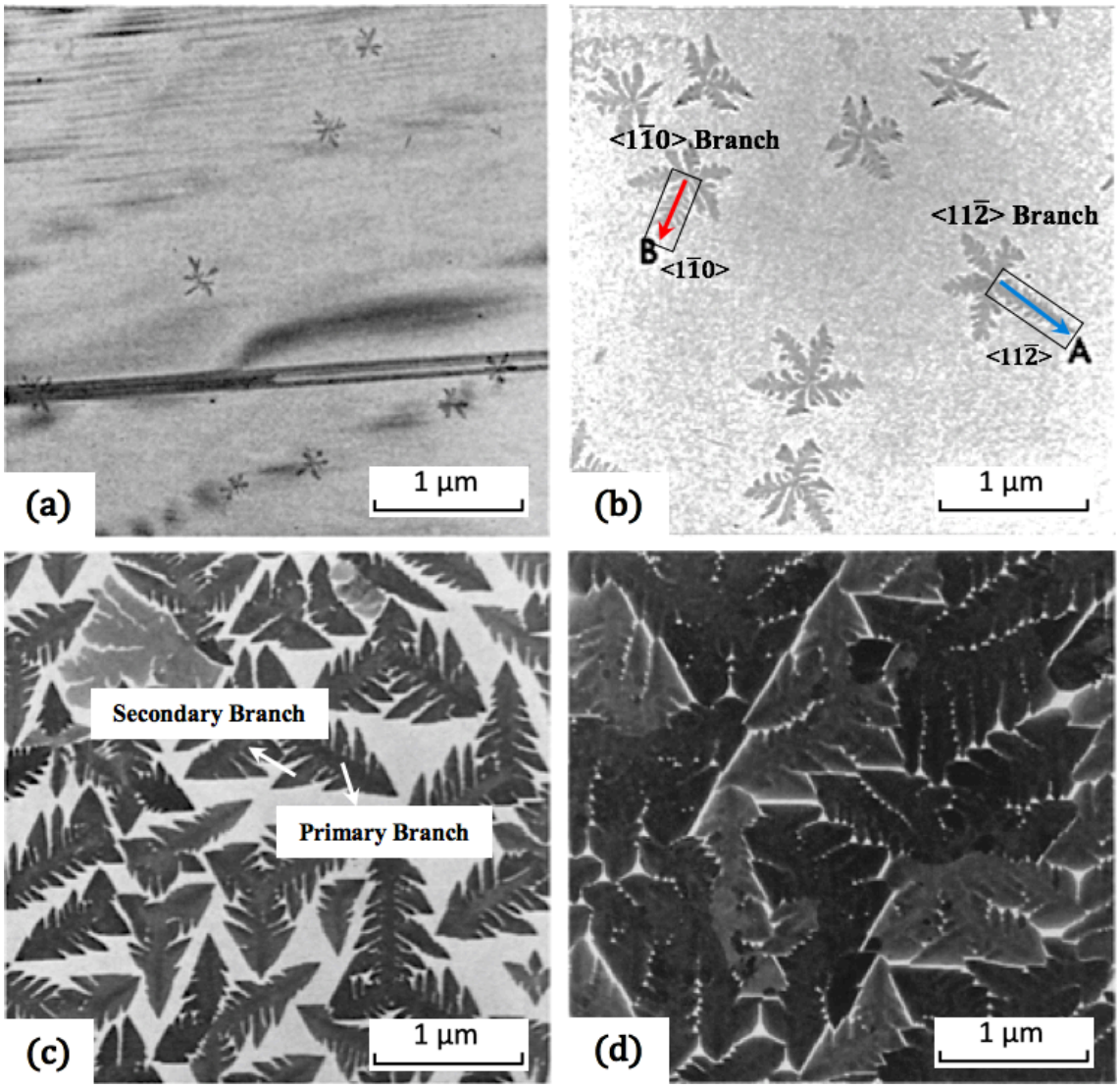


Fig. 2-15 TEM images showing the nucleation and aggregation of gold films on vacuum-cleaved HOPG with a deposition rate of 0.1 Å/s. The average thickness of gold from (a) to (d) are measured as 1.0 Å, 7.8 Å, 99 Å and 248 Å respectively [62].

Fig. 2-15 (a) - (d) illustrate the growth of gold crystals on the vacuum-cleaved graphite, in which h the average thicknesses of gold are kept the same as on the air-cleaved one. For the vacuum-cleaved graphite, less contamination on the substrate surface encourages the Ostwald ripening of gold atoms and thus leads to the extremely low densities of the gold islands [62,74-77]. The small gold islands then ripen as larger ones and have dendrite branches emanating the initial nuclei. On the two sides of the primary branches, there are also smaller and

shorter secondary branches growing out. Gold dendrite branches on graphite are divided into two types, named as the type A and type B branches respectively. As shown in the right side of Fig. 2-15 (b), a type A dendrite branch marked by the blue arrow has its primary branches lying along one of the <11$\bar{2}$> directions. Its secondary branches grow out from the primary branch and direct roughly towards the dendrite centre. Therefore, this type of branches are also referred to as <11$\bar{2}$> branches. In the left side of Fig. 2-15 (b), a type B dendrite branch is marked by a red arrow. The axis of the primary branch lies along one of the <1$\bar{1}$0> directions while the secondary branches point away from the dendrite centre. Under different conditions, gold atoms have a mainly special favour to the two types of branches. For example, the formation of the type B branches is restrained, and most of the gold branches orient in <11$\bar{2}$> directions when the substrate temperature increases from room temperature to 373 K [62,78]. At higher rates of deposition, dendrite branches belonging to the type B ones and growing in the directions of <1$\bar{1}$0> on the graphite surface can be observed easily. When the average thickness of gold films increases from 7.8 Å to 99 Å, both the size and the number of dendritic branches in Fig. 2-13 (c) have a noticeable rise. These large islands maintain isolated from their neighbouring ones but have a tendency of covering the graphite surface. With a further increase of average thickness, branches of the adjacent islands finally impinge as Au(111) thin films. Long straight or rows of triangular gaps exist between every two merged islands, which could be fulfilled by the latter deposited gold atoms.

2.4 C_{60} Molecule

Fullerene family includes a group of carbon allotropes with the shape such as cages and tubes. Among them, the molecules with the shapes of hollow closed-cages are commonly denoted as C_n, where **n** represent the total number of carbon

atoms a molecule contain. The famous carbon isomers including C_{20}, C_{28}, C_{36}, C_{60}, C_{70}, C_{76} and C_{84} have been obtained of macroscopic quantities by Krätschmer and Diederlich *et al*. from the benzene-soluble materials produced by resistive heating of graphite by the technique of gravity chromatography in inert atmosphere. Atoms inside these molecules donate are connected with their neighbouring ones with covalent single or double bonds, making the molecules fully closed or partially closed meshes with rings of five, six or seven atoms [79,80].

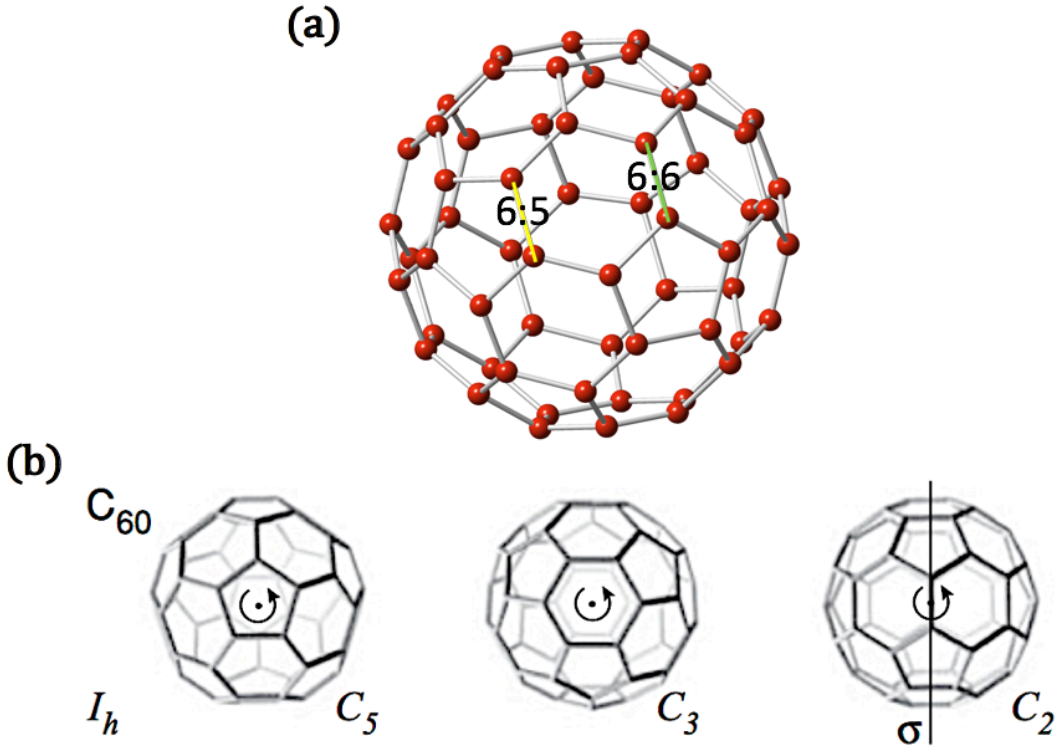


Fig. 2-16 (a) Schematic showing the structure of a C_{60} molecule. (b) DFT models showing the three types of symmetry of a C_{60} molecule: C_5, C_3 and C_2 [90].

As the simplest fully closed fullerene molecules, C_{60} and C_{70} contain the fewest number of carbon atoms and have the simplest molecular symmetries. Apart from the method mentioned above, these two types of molecules were also successfully produced by from the combustion of hydrocarbon by Howard et al. [81]. The two kinds of molecules have a wide range of applications in the fields of optic,

electronics and semiconductor technologies [82,83]. Measured by the X-ray Photoelectron Spectroscopy (XPS), the physical diameter of C_{60} molecules in the crystal is ~ 7.1 Å [84,85] and the molecule's van der Waals diameter is ~ 10.3 Å in the gas phase [86-89].

A C_{60} cage has a sphere shape consisting of 60 carbon atoms [82,91]. A schematic diagram of the C_{60} is shown in Fig. 2-16 (a), which consists of 20 hexagons (six-atom rings) and 12 pentagons (five-atom rings) [92]. Carbon atoms in the hexagons and pentagons are connected by only two types of covalent bonding. A carbon-carbon double bond exists (denoted as 6:6 bonds) between two adjacent hexagons, which is deficient in electrons and has an average bond length of 1.45 ± 0.015 Å. Between a pentagon and a hexagon ring, there is a single carbon bond (denoted as 6:5 bonds) which is rich in electrons. The average length of a single carbon bond is 0.05 Å longer than the double bond [82,93]. The weak interactions between the fullerene molecules have been calculated by Wolf-Dieter's group, where 1D row and 2D layer of single C_{60} molecules within the supercells have been achieved [90,94].

As shown in Fig. 2-16 (b), the structure of an C_{60} molecule belongs to the full icosahedral point group in three dimensions, which is labelled as I_h [95]. It contains the order of 120 and includes a series of subgroups of symmetries and all the symmetries exist on a sphere. It has an I_h symmetry including five-, three- and twofold axes. For the C_5 and C_3 symmetries of a C_{60} molecule, one hexagon and one pentagon ring are observed respectively along the directions of rotation axes. While for the C_2 symmetry, the C_{60} molecule rotates by a mirror plane, which is perpendicular to the three-fold axis and separates the molecule into two equal parts. At room temperature, C_{60} molecules are able to show different orientations sitting on the flat substrate such as HOPG, and the height change during rotation could be ignored [90].

2.4.1 Temperature Dependent Rotational Dynamics of C_{60} Molecules

Solid C_{60} at room temperature commonly present as the small dark pieces of crystals, where the molecules are dominated by van der Waals force. There is a phase transition of C_{60} stacking in crystal if they are annealed gradually and slowly from an ultralow temperature to room temperature.

When the C_{60} crystal is cooled down to 5 K, molecules contain low energy and lose the ability to change orientations. Each electron-deficient phase in one molecule is parallel to the electron rich (6:6) bonds of its neighbouring ones for optimising the stability of all the carbon atoms in crystal.

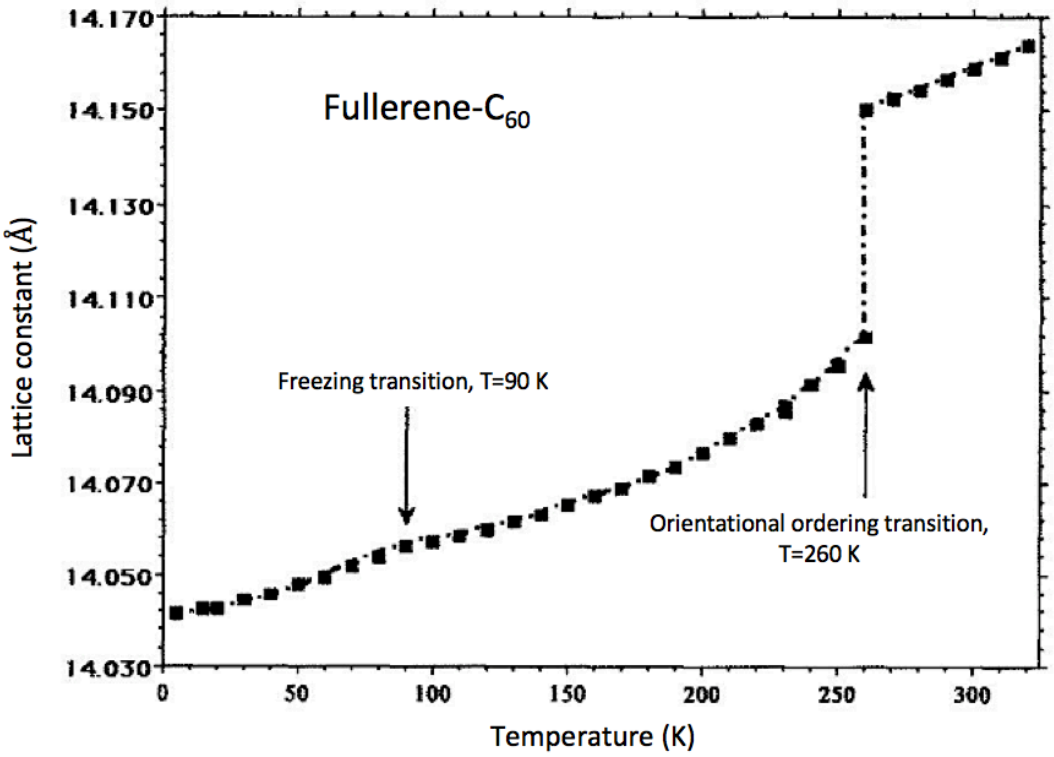


Fig. 2-17 Point profile showing the lattice constant of C_{60} in crystal with respect to the temperatures. There are two phase transitions happening as the temperature increases from 5 K to above 260 K. The freezing transitions happen since the temperature reaches 90 K. At 260 K, there is a sudden increase of the curve due to the phase changing from SC to FCC [96].

All the C_{60} in the phases keep still at their original positions instead of rotating. An overwhelming majority of the C_{60} molecules in crystal form perfect simple cubic (SC) structure. The lattice constant of the C_{60} crystal doesn't have a significant change before being heated to 90 K [84,96-98].

As shown in Fig. 2-17, the freezing transitions appear once the temperature reaches 90 K. From 90 K to 260 K Majority of the C_{60} in crystal still form SC structure. The lattice constant of C_{60} keeps increasing slowly but is always below 14.110 Å. However, some C_{60} molecules can rotate at their positions with an increasing molecular spacing gradually, because the thermal energy gained by molecules beyond their rotational barrier [96]. After being heated up to 260 K, most of the molecules are able to rotate freely. Both the FCC and SC phases coexist in the C_{60} crystal. A sudden jump of the lattice constant as well as the domain boundaries could be observed. When the temperature is above 260 K, all the C_{60} molecules can rotate freely and stack with FCC structure.

2.4.2 Close-packing Structures of C_{60} on Au(111)

When a low coverage of C_{60} molecules are deposited on the Au(111) substrate at RT, several close-packed structures could be formed. Each C_{60} molecule is affected and stabilized by the van der Waals forces from adjacent ones as well as the weak chemical interaction with the gold substrate simultaneously.

When temperature of the gold substrate is high enough, C_{60} molecules diffuse freely on the smooth sample surface before attaching to the step edges or defects. Then, these molecules nucleate as large close-packed islands. At high coverages, C_{60} molecules are assembled by the van der Waals force and stack as multilayer thin films [99].

2.4.2.1 $R0°$ Structure and $(2\sqrt{3} \times 2\sqrt{3})$ $R30°$ Structure

At room temperature, most C_{60} molecules form $R0°$ (or called In-Phase) structure on the Au(111) surface on account of the kinetics of the growth process. C_{60} molecules firstly pack densely as long chains along with the {111} steps and then ripen as large-sized domains. Supposing there is no defect on the substrate, orientations of the C_{60} domains are commonly determined by the types of the gold steps.

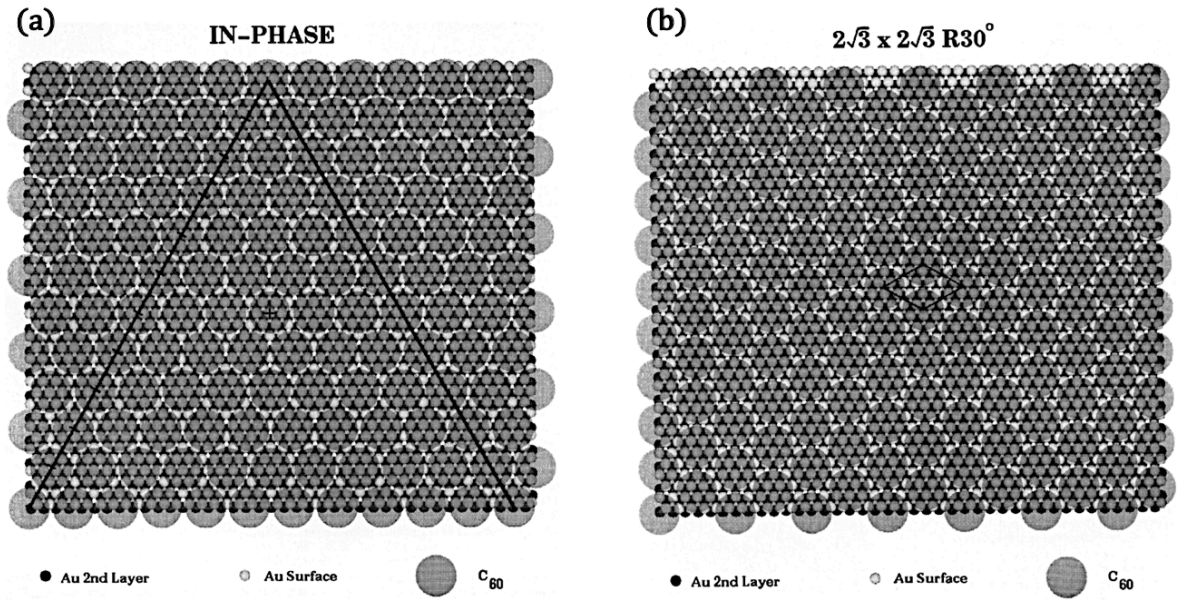


Fig. 2-18 Schematic showing the models of the (a) the R0°and (b) the R30° phase of C_{60} molecules on the unreconstructed the surface of Au(111). (a) Half of the unit cell of R0° phase and (b) the intact unit cell of R30° phase are marked in a solid black triangle and a rhombus, respectively [21].

Model of this packing structure is shown in Fig. 2-18 (a), where the C_{60} molecules pack in the same direction with gold atoms below. Half of a supercell including (38×38) gold atoms or (11×11) C_{60} molecules are marked in a black triangle. This close packing structure is also observed when C_{60} are deposited on the other metal surfaces such as Cu or Ni [99]. The NND of C_{60} molecules in the R0° phase is measured as ~ 1.0 nm, which is not the integral multiple of the

spacing of surface gold atoms [100]. Due to the lattice mismatch, some C_{60} molecules sit on three-fold hollow sites, while some others sit on the bridge or A-top sites.

At high temperature, the C_{60} molecules on the Au(111) surface prefer to sit uniformly on the three-fold hollow sites. It leads to a phase transition from the R0° to the $\left(2\sqrt{3} \times 2\sqrt{3}\right)$ R30° [101]. All the C_{60} molecules in Fig. 2-18 (b) occupy FCC or HCP hollow sites equivalently on the Au(111) substrate, where a stronger interaction between C_{60} layers and gold atoms are built. The close-packed directions of the C_{60} makes an angle of 30° to the gold atoms below, and the NND of molecules is $2\sqrt{3}$ times the spacing of surface gold atoms. The R30° structure is thus more favoured by C_{60} molecules compared with R0° structure thermodynamically. However, the C_{60} molecules on the Au(111) surface can change the gold surface. In the R30° phase, some molecules appear brighter than the others. These brighter molecules have weaker interactions with the gold substrate [91,102].

2.4.2.2 (7×7) $R14°$ Structure and (3×3) $R34°$ Structure

(7×7) R14° and (3×3) R34° C_{60} phases are also able to be observed on the gold substrate occasionally. Structures of the two phases are shown in Fig. 2-19 (a) and (b), where the black crosses represent the surface gold atoms, while the light and dark spheres represent the adsorbed C_{60} molecules. Close-packing directions of the C_{60} molecules in the images are marked with the thick black arrows.

The R14° superstructure has been found firstly by R. Berendt et al., where the C_{60} molecules' close-packing direction rotates 14° to that of the surface gold atoms [102]. Highlighted by the solid black lines, this structure has a very large unit cell, consisting of 49 molecules in total. Molecules in one unit cell sit on the

random sites of the Au(111) surface and form a large (7×7) array. Compared with R14°, the superstructure of R34° are less observed. As shown in Fig. 2-19 (b), this type of structure includes a unit cell of (3×3) molecules, where every third C_{60} molecule sits on the same type of sites on the gold surface [102-104].

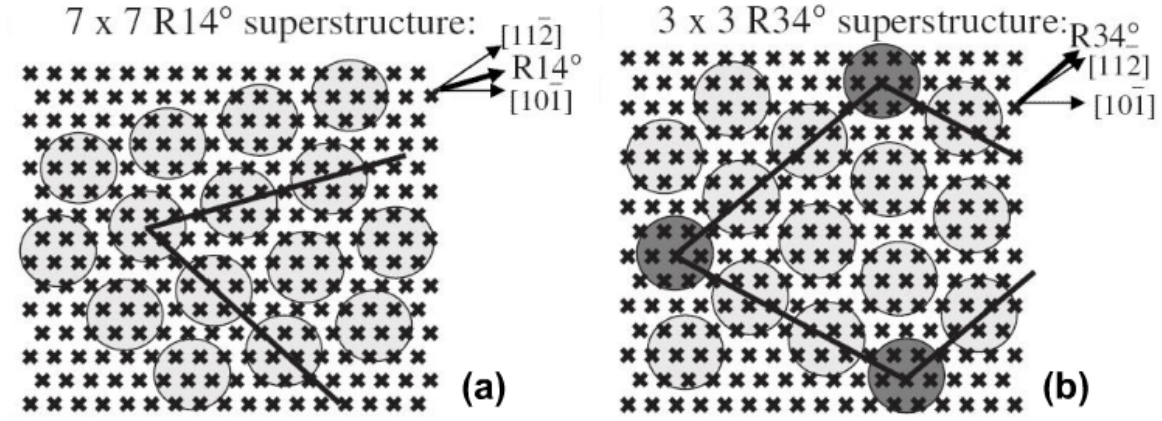


Fig. 2-19 Schematic showing the two superstructure of (a) (7×7) R14° and (b) (3×3) R34°, respectively. The crosses represent gold atoms in the substrate, and the light and dark spheres represent C_{70} molecules. The molecules' close-packing directions in the two types of structures are highlighted by the thick black arrows respectively [102].

Before the development of STM, all the four kinds of structures of C_{60} molecules that have already been studied by the techniques such as X-ray diffraction (XRD) and low energy electron diffraction (LEED) [102]. C_{60} structures such as $\left(2\sqrt{3} \times 2\sqrt{3}\right)$ R30° have also been observed on the other metal surfaces such as Au(100) [21,100,105], Ag(111) [106] and Al(111) [107].

2.5 C_{70} Molecule

One C_{70} molecule consists of 70 carbon atoms. It has an ellipsoidal shape and looks like a "rugby ball" [108]. The carbon atoms connected by covalent bonds form 25 hexagons and 12 pentagons. In C_{70} molecules, the double covalent bonds exist between two hexagons (6:6) while the single bonds exist between the

adjacent hexagons and pentagons (6:5). Compared with C_{60}, the ten extra carbon atoms existing at the equator of a C_{70} molecule make a belt of 5 hexagons, which are marked with the blue spheres in Fig. 2-20 (a). It not only distinguishes the shapes of C_{70} from C_{60} but also riches the diversity of C-C bonding in a C_{70} molecule [101]. In Fig. 2-20 (a), one single bond and one double bond in a C_{70} cage have been highlighted with yellow and green bars respectively. When these bonds are formed, each carbon atom dominates all the electrons to interact with the other three neighbouring atoms [106].

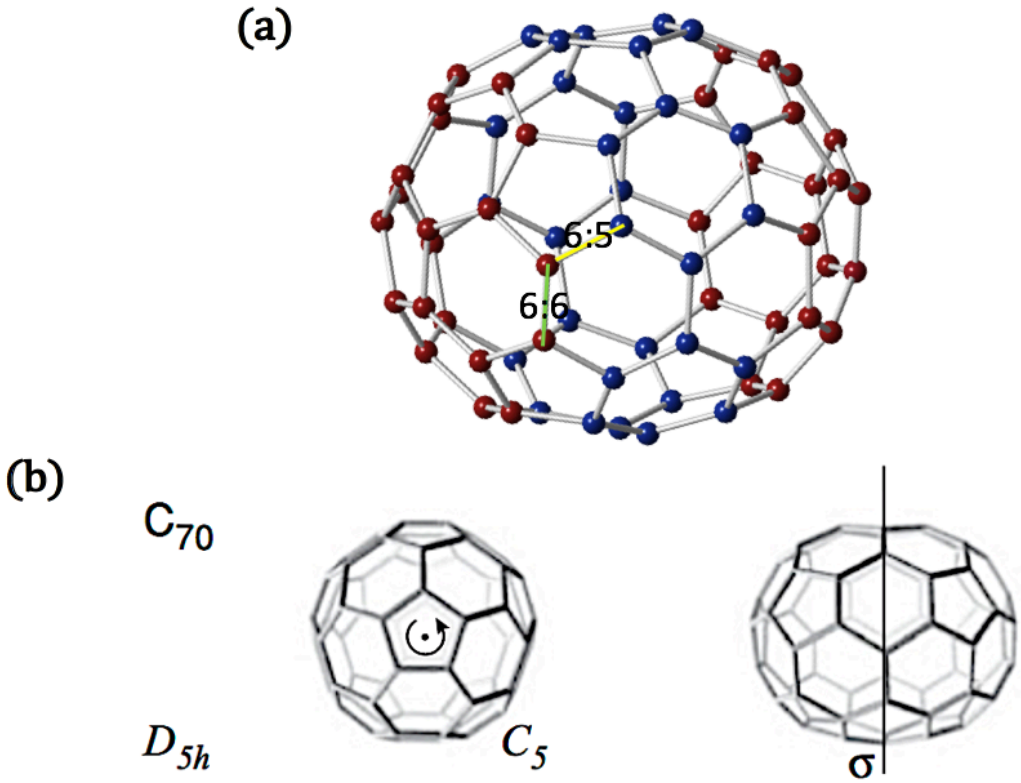


Fig. 2-20 (a) Schematic showing the structure of a C_{70} molecule. 5 hexagons coloured in blue are made up of the carbon atoms at the equator of the molecule. (b) The D_{5h} symmetry of a C_{70} molecule. The molecule has a fivefold axis and an axial plane [90].

Due to the difference of molecular structures and carbon-carbon bonds, there is a significant difference between a C_{70} molecule and a C_{60} molecule in the symmetries. As shown in Fig. 2-20 (b), one C_{70} molecule has the D_{5h} symmetry. The point group D_{nh} includes a five-fold axis of symmetry (C_n), a mirror plane σ,

which is perpendicular to the C_n axis [95]. This mirror plane also includes n two-fold axes (C_2). For the first type of rotation, the molecule rotates by a fivefold axis, which is perpendicular to the two parallel pentagons. On the right side of the figure, a C_{70} molecule rotates symmetrically by an axial plane (σ plane). This plane exists at the molecular waist and separates it into two equal parts. In the crystal, the geometric length of a C_{70} molecule along the directions of the σ plane is measured as 10.4 Å, while its length along the C_5 axis is ~ 0.5 Å longer [100].

2.5.1 Temperature Dependent Rotational Dynamics of C_{70}

Compared with C_{60} molecules, phase transition of C_{70} crystal are more complicated and are mainly studied in the air environment [109]. When the temperature is above 350 K, C_{70} molecules stack in the mode of FCC, and all the molecules in the crystal can rotate freely at their positions and could be treated approximatively as spheres. At the temperature between 270 K and 337 K, some rhombohedral and monoclinic phases are transferred by the FCC ones due to the rotating limitation of molecules.

The FCC, (ideal (c/a=1.63) and deformed (c/a=1.82)) HCP, rhombohedral and monoclinic phases coexist in the C_{70} crystal [110]. The rhombohedral phases contain C_{70} molecules rotating along the fivefold axes and tilting with certain degrees uniformly [111-114]. It commonly appears with some disordered rhombohedral phases, which has unequal vector lengths. When the temperature is lower than 270 K, only the rhombohedral and monoclinic phases remain in crystal, while the FCC and HCP phases have disappeared. With further cooling, the thermal energy of C_{70} molecules is low enough, most of the molecules stop rotating totally and orient in an ordered direction, and the crystal is dominated by the monoclinic phases.

2.5.2 Structures of Close-packed C_{70} on Ag(111)

The close-packing structures of C_{70} molecules on the gold and silver substrates have been studied in the air [115-117] and the liquids [118,119]. Some previous studies have indicated that the majority of C_{70} molecules on the (111) metal substrates form close-packed structures and stack as molecular layers at room temperature. Each molecule stands with its long axis perpendicular to the atoms in the top-most layer of substrate. Molecules in the upper layers have weaker interaction with the substrate compared with the ones in the layers below [117]. In our research, on Au(111), orientations of the C_{70} molecules are found having angles such as 0°, 14° or 30° in respect to that of the surface gold atoms. However, when C_{70} molecules are deposited on Ag(111), $\left(\sqrt{13} \times \sqrt{13}\right) \mathrm{R} \pm 13.9°$ is the most thermal favoured structure.

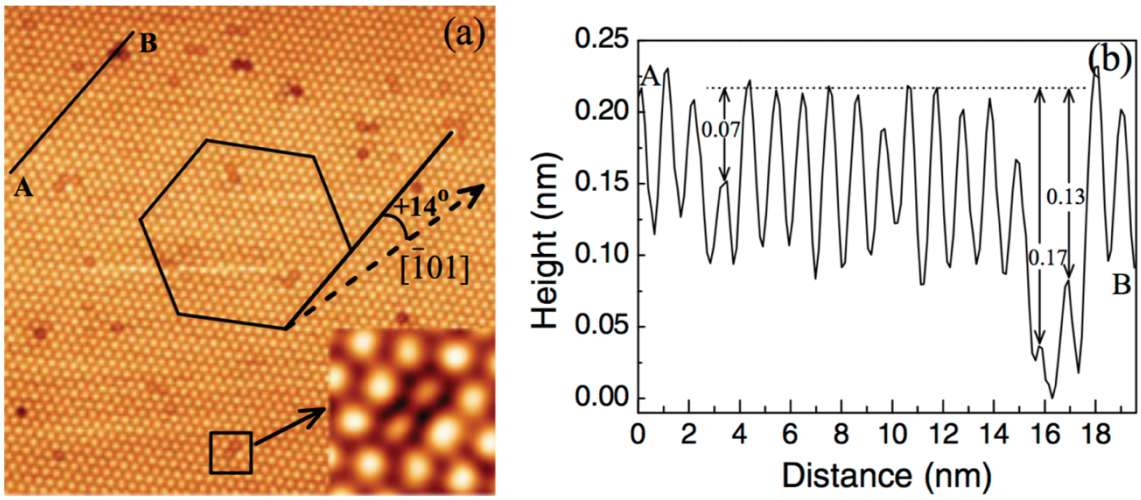


Fig. 2-21 (a) STM image showing the close-packed C_{70} molecules on the Ag(111) surface. The rotational angle of C_{70} lattice is 14° from that of surface atoms. Inset showing the area marked in the black rectangle with higher resolution. (V = 0.76 V, I = 0.04 nA, 50 nm × 50 nm). (b) Line profile along the line AB showing depths of the three types of molecular defects [122].

Fig. 2-21 (a) indicates that the close-packed monolayer of C_{70} on the Ag(111) substrate at room temperature. The sample was heated up to 573 K for 20 minutes and then cooled down to room temperature. Close-packing directions of C_{70}

molecules (marked with the solid line) and the silver atoms below (marked with the dashed line) has an angle of 14°. Some single or dimmer defects with greater depths appear inside the C_{70} domain. These defects can be divided into three types: weak dims (WD), middle dims (MD), and dark dims (DD), which are measured respectively as 0.07 nm, 0.13 nm and 0.17 nm, shown in Fig. 2-21 (b). Under the defects, one-atom or seven-atom atomic pits are created on the silver surface. The inset shows one MD in the black box is shown in the inset with a higher resolution, where the molecular defects show different electronic states compared with the molecules around.

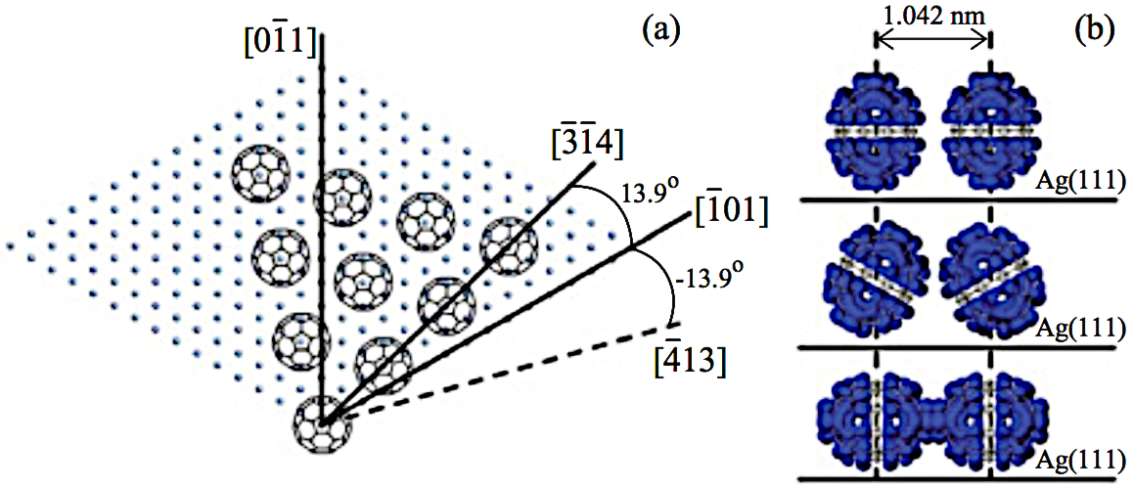


Fig. 2-22 (a) Schematic showing the $\left(\sqrt{13} \times \sqrt{13}\right)$R $\pm$ 13.9° structure of C_{70} molecules on the Ag(111) surface. All the C_{70} molecules take an upright orientation uniformly [122]. (b) Models showing three possible types of molecular orientations on Ag(111). When the two adjacent C_{70} molecules stand upright, their spacing agrees with the measured distance in the STM image [122].

Fig. 2-22 (a) demonstrates a model of $\left(\sqrt{13} \times \sqrt{13}\right)$ R $\pm$ 13.9° structure of C_{70} molecules on the Ag(111) surface, where each blue spot represents a surface silver atom. Each C_{70} molecule in this structure sits directly on top of one silver atom. It is because that the evident charge transferring from the substrate to the adsorbed neutral molecules ($>$ 2.6 e per C_{70}) enhances the Coulomb repulsion

between adjacent molecules dramatically. Therefore, the total energy of the monolayer C_{70} on the Ag(111) surface minimizes even though it requires higher energy for C_{70} molecules sitting on the A-top sites instead of three-fold hollow sites. The models in Fig. 2-22 (b) demonstrates that the two adjacent C_{70} molecules in the phase have three possible orientations. When the two adjacent C_{70} molecules stand upright with their long axes perpendicular to the Ag(111) surface, the calculated molecular spacing is $1.04\ \text{nm} \pm 0.02\ \text{nm}$, which agrees with the NND measured in Fig. 2-20 [122].

For the substrate of Highly Oriented Pyrolytic Graphite (HOPG), each carbon atom in the top-most layer achieves saturated electronic state by forming σ and π bonds with its adjacent ones. When C_{70} molecules adsorb onto substrates, the interaction between the substrate and the adsorbed molecules are rather weak.

2.6 Election Properties of C_{60} and C_{70} Molecules

The electronic properties of C_{60} and C_{70} molecules have been studied. With the help of x-ray photoemission spectroscopy (XPS) [97,114], the gap between the highest occupied molecular orbitals (HOMO) and the lowest unoccupied molecular orbitals (LUMO) of a C_{60} in the crystal is measured as 3.7 eV [103]. It is twice as the one of a C_{70} (1.6 eV) [123]. The C_{60} or C_{70} molecules deposited onto specific noble metal substrates, e.g. Au(111) or Ag(111) are able to work as electron acceptors. It thus leads to a shrink of the molecules' HOMO-LUMO gap. Proved by Modesti et al., fullerene films switch gradually from the metallic to the semiconductor-like characteristic as the thickness increases [124].

As mentioned, the LUMO state localizes in the 6:5 single bonds (sp^2 bonds) of one C_{60}, which appears with a doughnut-like shape in the Fig. 2-23 [106,125]. When a pentagonal ring, a carbon atom or a hexagonal ring of one C_{60} molecule

faces down to the surface of Au(111), the bright patterns with one, two or three-fold symmetry are shown in the STM images at low temperature.

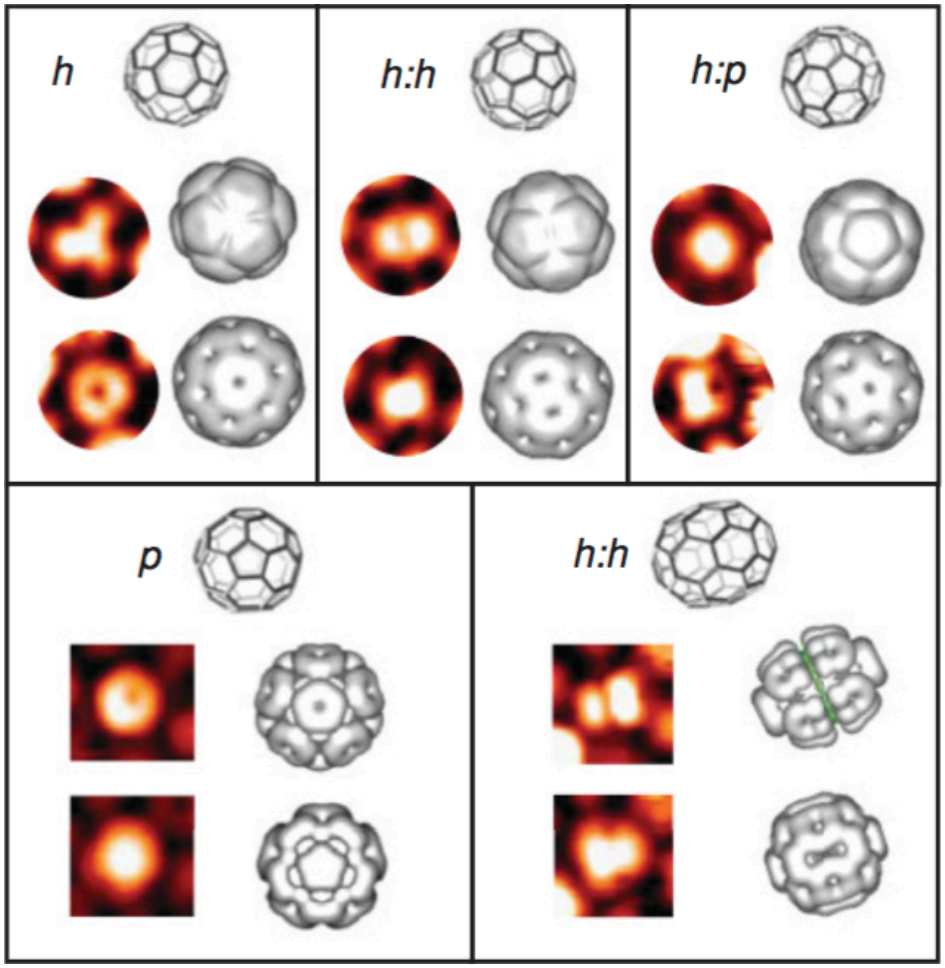


Fig. 2-23 STM topographies and schematic indicating the unoccupied and occupied molecular orbitals of the (a) C_{60} and (b) C_{70} molecules in the surface of the nanocrystals. (a) The top row showing the schematic of one C_{60} facing the scanning tip with a hexagonal carbon ring (h), one 6:6 bond (h:h) and one 6:5 single carbon bond (h:p) respectively; The middle row showing the STM topography and the corresponding DFT calculations of the LUMO orbitals (V = 2V, I = 20 pA); The bottom row showing the showing the STM topography and the corresponding DFT calculations of the LUMO orbitals for the C_{60} molecule (V = -2.8 V, I = 20 pA) (from [90]). (b) The top row showing the schematic of one C_{70} molecule orienting with its pentagonal ring (p), one 6:6 bond (h:h) facing the tip; The middle row showing the STM topography and the corresponding DFT calculations of the LUMO orbitals (V = 3V, I = 20 pA); The bottom row showing the STM topography and the corresponding DFT calculations of the LUMO orbitals for the C_{70} molecule (V = -3 V, I = 20 pA) [90].

When C_{60} or C_{70} molecules are deposited onto the Au(111) surface and nucleate as close-packed domains, the hexagonal carbon rings of one molecule is deficient in electrons and tend to face the electronic-rich 6:6 bond of another molecule. It drives the rotation of C_{60} molecules in the domains and enables the distinguished molecular orbitals to be recorded by STM tip during scanning. The lowest unoccupied molecular orbitals (LUMO) and the highest occupied molecular orbitals (HOMO) state of the C_{60} and C_{70} molecules in the close-packed monolayer on Au(111) have been studied by Dieter et al. using an LT STM [90].

Fig. 2-23 indicates the LUMO and HOMO of one C_{60} molecule when a hexagonal carbon ring of carbon, two hexagons and one 6:5 single carbon bond face up to the STM tip. The corresponding models of these orbital states calculated by the density functional theory (DFT) are put to the right of the image. At the same bias voltage and tunnelling current, the electron-rich and electron-deficient regions of a molecule appear bright and dark in the scanning image, respectively.

Fig. 2-24 demonstrates a redistribution of interfacial charge densities when one C_{60} sits on the Au(111) and Ag(111) surface. Electrons transfer from the gold atoms to the 6:6 carbon bonds of the molecule. The regions in the figure with a more significant number of the charge density are marked with blue colour, while the regions with a decrease of charge density are marked in red

Sitting on Au(111), the C_{60}-Au bonding mechanism could be treated as a “charge-neutral” polarization and belong to the metal-ligand interactions [90]. The C_{60} molecule in Fig. 2-24 (a) faces to the Au(111) surface with one of its carbon hexagons. Only a few numbers of carbon atoms close to the substrate have been charged, while most atoms of the molecule still maintain as neutral. Under this circumstance, the charge density at the surface-adsorbate interface has a significant increase [126].

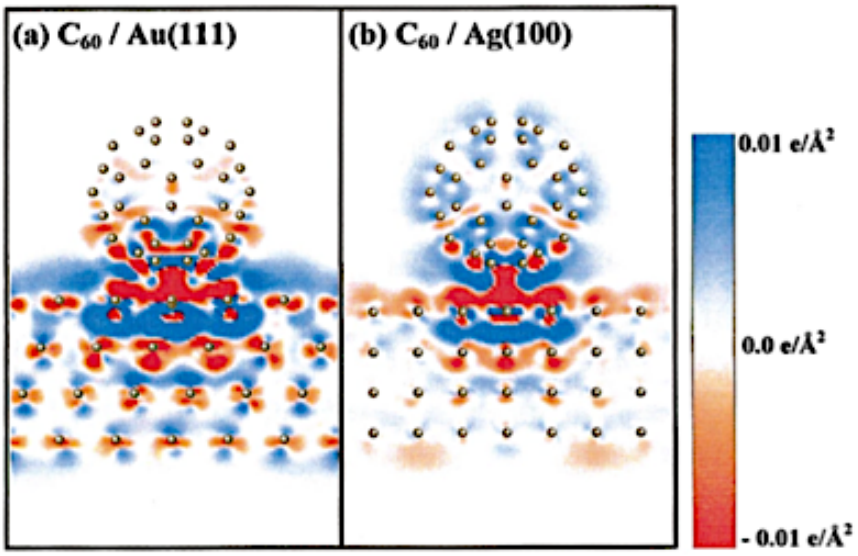


Fig. 2-24 DFT models showing the differential charge densities of C_{60} molecule sitting on (a) the Au(111) and (b) the Ag(100) surfaces, respectively. The regions coloured in blue have an increase in the electron density while the regions having a decrease of electron density have been marked with red colour [126].

The C_{60}-Ag bonding mechanism behaves more like a combination of ionization and polarization. As shown in Fig. 2-24 (b), when a C_{60} molecule is adsorbed on the Ag(100) surface, a net of electrons contributed by the silver atoms in the substrate transfer to the adsorbed C_{60} molecule directly, making the molecule charged. At the interface of the molecule and silver atoms, the interface polarization also appears. The difference between the two metal-molecule systems could results from the lower work function of the Ag(100) surface compared with that of Au(111) [127]. When the change of electron affinity is ignored, the LUMO state of the C_{60} molecules adsorbed on Ag(100) are reduced and close to E_F compared with on Au(111), which makes it easier for charge transfer from the silver substrate to the adsorbed molecules. If C_{60} molecules are deposited onto a more active metal substrate with a further lower working function, molecular ionization would be more evident while the interface polarization would be further limited [128,129]. Apart from the surface energy,

the intramolecular Coulomb force also plays an essential role in influencing the electronic properties of the adsorbed C_{60}.

Most of the C_{70} molecules on the surface of Au(111) prefer to stand with their long axes perpendicular to the substrate, and face up to the STM tip with their pentagonal carbon rings, while a small number of C_{70} keep their long axis parallel to the gold substrate. Two hexagonal rings of these molecules face up to the tip during scanning. HOMO and LUMO of both the two types of C_{70} are recorded [90]. Due to the variation in schematic structure and bond types, electronic states of two hexagons in a C_{70} and a C_{60} molecule are different at the same bias voltage and tunnelling current constant.

Interaction type	**Energy range**	**Bonding length**	**Nature**
van der Waals	$\sim 0.02 - 0.1$ eV	< 1nm	Non-selective
Hydrogen bonding	$\sim 0.05 - 0.7$ eV	≈ 0.15 nm $- 0.35$nm	Selective and directed
Ionic	$\sim 0.05 - 2.5$ eV	Up to several nm	Non-selective
Dipole-dipole	$\sim 0.1 - 0.5$ eV	≈ 0.2 nm $- 0.3$nm	Directed
Metal-ligand interactions	$\sim 0.5 - 2.0$ eV	≈ 0.15 nm $- 0.35$nm	Selective and directed
Reconstruction mediated	≈ 1eV	System dependent	Covalent

Table 2-2 Typical interactions with the different interaction energies, bonding length and character [90,91].

Table 2-2 exhibits the most typical interactions along with their energy range, bonding lengths and characters used to study the different molecular structures on metal surfaces [90]. Among them, hydrogen bonding, dipole-dipole force and van der Waals dispersion force belong to intermolecular interactions. Van der Waals forces exist between uncharged molecules and commonly have lower energy and longer bonding lengths compared with the other two interactions. Metal-ligand interactions exist between the interface atoms and one molecule or

a group of molecules and the charge transfer is directed [90,91]. Compared with van der Waals forces, this type of interactions have higher energy and lower bonding lengths.

2.7 Magic Number $(C_{60})_m$-$(Au)_n$ Clusters

In an ultrahigh vacuum chamber, when C_{60} molecules and gold atoms are co-deposited, at 110 K with a ratio of $\sim 1:2$, gold atoms create arrays of clusters at the elbow sites of the Au(111) surface. The molecules fully or partially encapsulate the Au islands via surface diffusion. When the sample is brought up to room temperature, performed by STM, quite a number of the C_{60} molecules around the gold islands have moved away or desorbed from the substrate, leaving the rest gold islands and molecules to reorganise and form a series of well-defined $(C_{60})_m$-$(Au)_n$ magic number clusters. These clusters consist of specific numbers of close-packed C_{60} molecules, which sit around or on top of the single atomic layer gold islands [130,131]. The smallest type of magic number clusters $(C_{60})_7$ only includes seven molecules in total, where the six C_{60} molecules encircle a 19-atom island while another one sits on the island's top. A simplified Formation process of this type of magic number clusters in the ultrahigh vacuum is demonstrated in Fig. 2-25.

Apart from the magic number clusters, there are some large gold islands with circular shapes on the gold substrate, of which the edges are decorated by C_{60} molecules. However, there is no molecule sitting on the top of the islands. This type of clusters is named as ring clusters. Fig, 2-25 (b) demonstrates the magic number clusters and ring clusters scanned by STM. The magic number clusters can be divided into different types according to their unique shapes, sizes and the included molecules. As marked in the orange box of Fig. 2-25 (b), a row of $(C_{70})_7$ magic number clusters located in the FCC regions and next to the elbow sites. In

one of these clusters, the central C_{60} molecule sitting on top of the gold island is measured ~ 0.21 nm taller than the six surrounding molecules and thus appears brighter. For the magic number clusters with larger gold islands, two or more C_{60} molecules sit side-by-side on the top of the island.

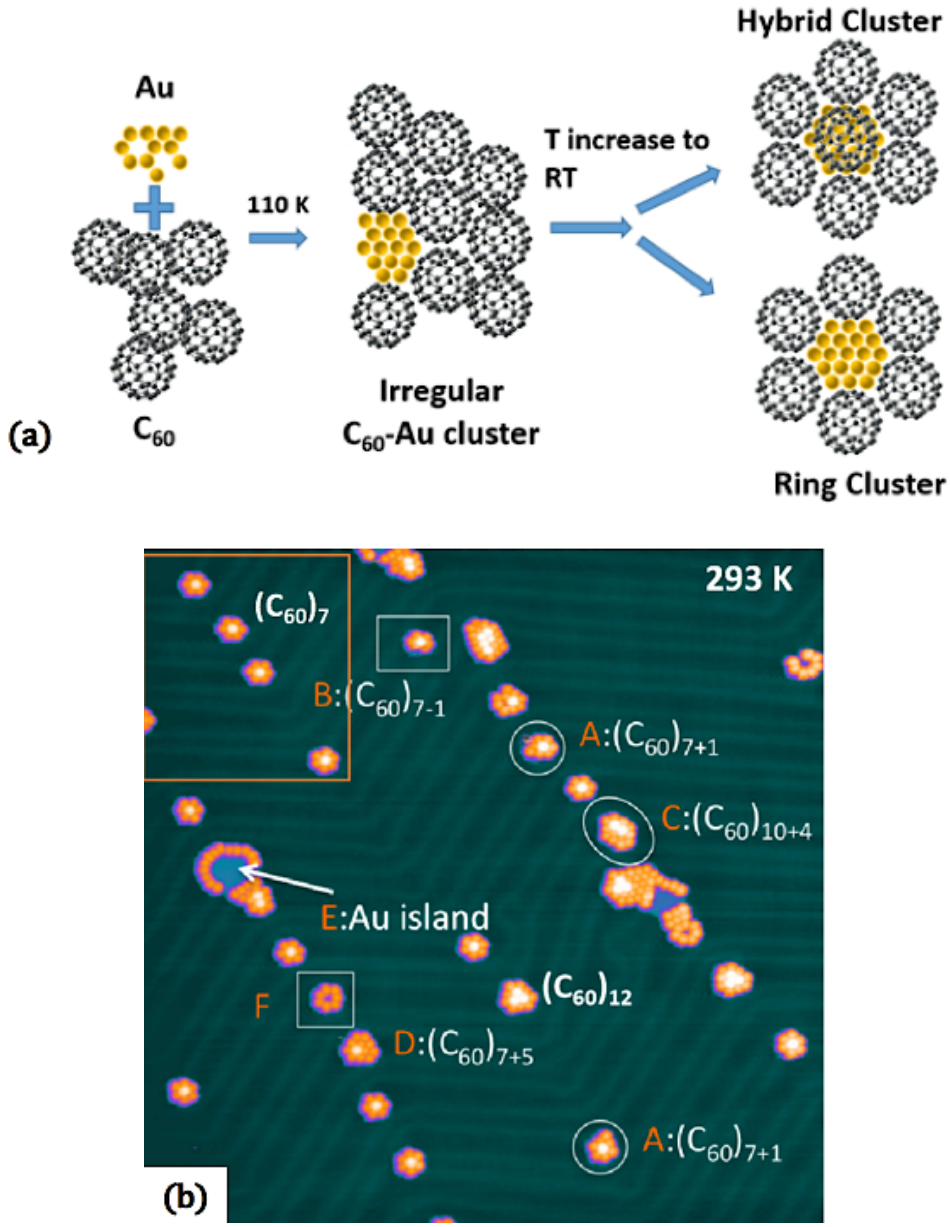


Fig. 2-25 (a) Schematic showing the formation process of a $(C_{70})_m$ magic number cluster and a ring cluster on the Au(111) substrate. Gold atoms and C_{60} molecules were co-deposited at 110 K, and the sample was then heated up to room temperature. (b) STM image showing $(C_{70})_m$-$(Au)_n$ magic number clusters, ring clusters and other clusters sitting on the Au(111) substrate. All the clusters sit in the FCC regions and close to elbow sites (V= -1.8 V, I= 0.03 nA, 105 nm × 105 nm) [131].

Close to these $(C_{70})_7$ clusters, a large size gold island of the ring cluster occupies two adjacent elbow sites simultaneously. Its steps are decorated by a chain of close-packed C_{60} molecules. The B and F type (or called $(C_{60})_{7\text{-}1}$) clusters are marked in the white boxes, which are similar to the $(C_{60})_7$ ones but have one C_{60} molecule lost. Since the gold island is not covered by any molecule, the F type cluster also belongs to a ring cluster. At room temperature, some perfect $(C_{60})_7$ magic number clusters are able to capture diffusing C_{60} molecules. Marked in the white circles and ellipse, A, C and D types can be treated as a $(C_{60})_7$ clusters adding one, four and five other C_{60} molecules.

The model in Fig. 2-26 (a) shows a single atomic layer of the gold island inside a $(C_{60})_7$-$(Au)_{19}$ cluster. The island consists of 19 close-packed gold atoms and has a hexagonal shape. All the atoms in the island occupy the three-fold hollow sites on the Au(111) surface. The seven C_{60} molecules in the clusters are added in Fig. 2-26 (b). Six of the molecules are located at the hollow sites on the substrate and sit close to the island's step. There is one molecule sitting directly over the central gold atom in the island.

In this system, interaction between the C_{60} molecules and gold substrate achieve a great balance with the intermolecular forces and result in high stability of this cluster. Considering the space of molecules measured in the STM images, C_{60} molecules in one magic number cluster are found packing with $\left(2\sqrt{3} \times 2\sqrt{3}\right)$ R30° structure on the Au(111) surface [102,104,132].

In this model, gold atoms at the step edges have the distance of ~ 0.25 nm with the nearest carbon of a C_{60} molecule, which agrees with the calculated value [133].

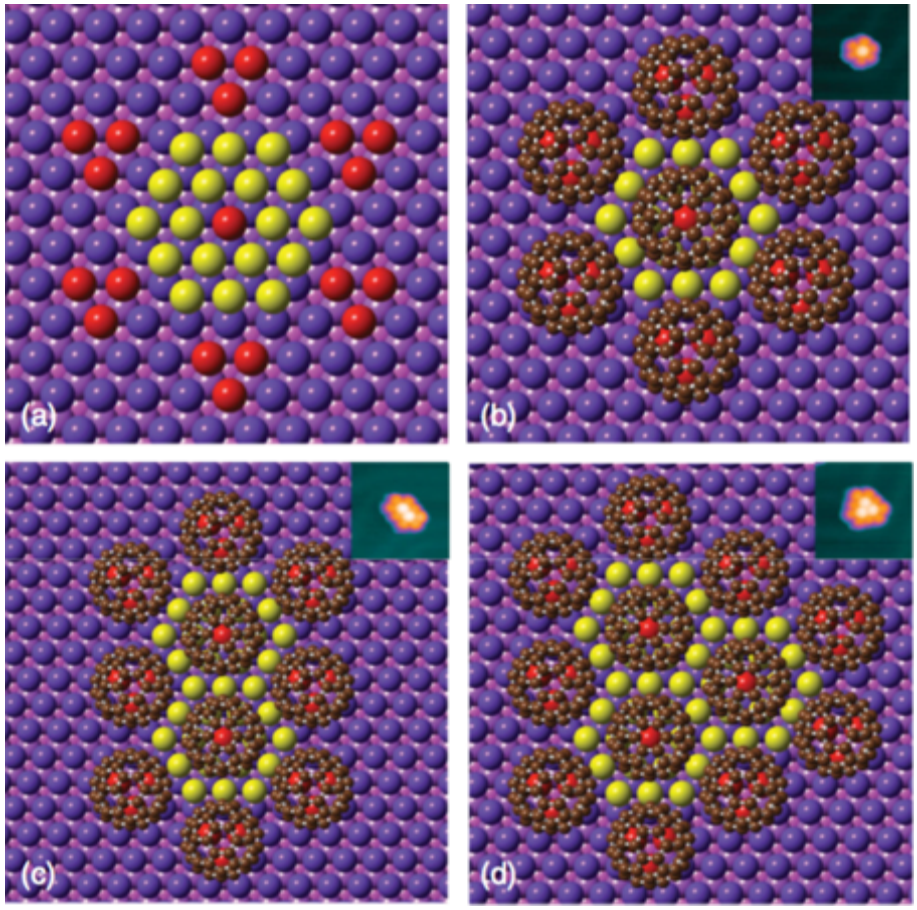


Fig. 2-26 (a) Ball models showing a single atomic layer gold island inside a $(C_{60})_7$-Au_{19} magic cluster consisting of nineteen gold atoms. The yellow spheres and one red sphere in the centre represent the gold atoms in the island, while the dark purple spheres represent the surface gold atoms of the Au(111) substrate. The gold atoms having a direct contact with seven C_{60} molecules are marked in red [134]. (b) Ball models of $(C_{60})_7$-Au_{19} cluster consisting of both the gold island and C_{60} molecules. One C_{60} molecule sits on the island's top, and the other six attach to the island's edges. Ball models showing the atomic structures of (c) a $(C_{60})_{10}$-Au_{35} and (d) a $(C_{60})_{12}$-Au_{49} cluster, where two and three molecules sit side-by-side on the gold island. Inset in (b), (c) and (d) show the corresponding magic number clusters scanned by STM [134].

In a magic number cluster, the gold-carbon distances are decided by the types of gold steps. When a C_{60} molecule sits close to a {111} or {100} gold facet, there is a small discrepancy in the space and bonding energy between the edge atoms and molecules [131]. Therefore, a global optimization process inside a magic number cluster irons out the difference in the distance by allowing some

molecules and atoms to change their positions from the theoretically predicted ones. In UHV, one $(C_{60})_7$-$(Au)_{19}$ cluster can maintain stability up to 400 K, while a pure 19-atomic gold island disintegrates beyond 200 K [134]. It indicates that the molecules play a role in enhancing the stability of the atomic island and prohibiting Ostwald ripening of gold atoms.

Fig. 2-26 (c) and (d) demonstrate the models of another two magic number clusters: $(C_{60})_{10}$-$(Au)_{35}$ and a $(C_{60})_{12}$-$(Au)_{49}$, respectively. The two types of clusters consist of more atoms and molecules and thus have larger sizes compared with $(C_{60})_7$-$(Au)_{19}$. In a $(C_{60})_{10}$-$(Au)_{35}$ cluster, eight C_{60} molecules surround a twin-hexagonal island consisting of 35 gold atoms. The island is large enough to accommodate two molecules on its top simultaneously side by side.

A $(C_{60})_{12}$-$(Au)_{49}$ cluster includes 12 molecules, in which three molecules can sit on top of the monolayer gold island. However, the bonding conditions between molecules and atoms in the two types of clusters are more complexed compared with that of a $(C_{60})_7$-$(Au)_{19}$ cluster. For example, in one $(C_{60})_{12}$-$(Au)_{49}$ cluster, there are three C_{60} molecules interacting with V-shaped step edges instead of the straight ones [134]. Hence these larger-sized magic number clusters have weaker stability.

2.8 The STM Apparatus

The first STM in the world was produced by G. Binnig *et al*. at the IBM Zürich Research Laboratory in 1981 [135]. It provides real-space atomic resolution images of material surfaces. Binnig and Rohrer were awarded the Physics Nobel Prize in 1986 for their contribution.

STM was initially used for achieving the surface topography and electronic structure of the conducting samples. The technique of scanning tunnelling

spectroscopy (STS) was then introduced to study the information about the surface's local electronic structure.

After STM, some other microscopy techniques, including atomic force microscopy (AFM), electrostatic force microscopy (EFM) and chemical force microscopy (CFM) have been developed in succession and used for surface analysis. Most of my research work is conducted with the help of a VT-STM.

2.8.1 1-dimensional Model

STM works by detecting the tunnelling current between the two electrodes (sample and tip). It works based on a quantum mechanics phenomenon, which is also known as electron tunnelling. The concept of electron tunnelling is demonstrated by a 1-dimensional model. Fig. 2-27 shows 1-dimensional energy model of the tip-barrier-sample junction.

In the 1-Dimensional model, there are two electrodes separated by a finite energy barrier, of which the potential is U. For simplify, the two electrodes are assumed to be are made of the same material. The work function of electrode is represented as Φ. The Fermi levels of the tip and the sample are marked by the solid black lines while the potential barrier has the width of z. In classical mechanics, the Fermi levels of two electrodes are equal to each other when there is no applied bias voltage, and the electrons in the electrodes are confined under their Fermi levels. In quantum mechanics, electrons have wave-like properties and thus can be described by a wave functions $\Psi(z)$.

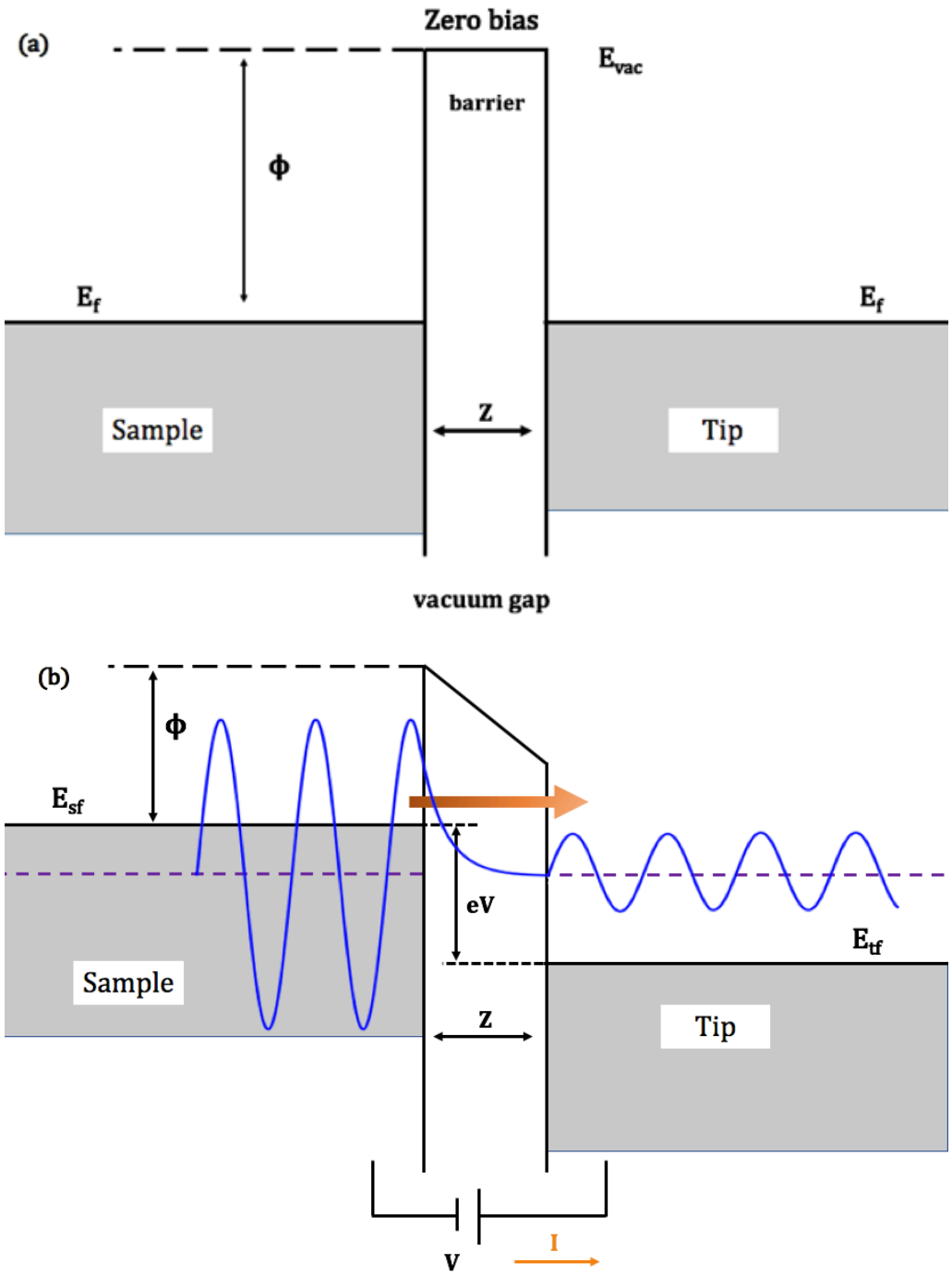


Fig. 2-27 Schematic showing 1-dimensional energy model of the tip-barrier-sample junction. (a) Assuming the tip and sample are made of the same material, their Fermi levels are equal when there is no applied bias voltage, and all the electrons in the sample and tip are confined under their Fermi levels. There is no tunnelling current passing through the energy barrier. (b) When a bias voltage applied to the sample, its Fermi level rises by *eV*. Electrons with the energy between the two Fermi levels have the possibility of tunnelling and form the stable tunnelling current.

When the two electrodes approach each other with an extremely short distance, there is a possibility a small number of electrons can tunnel through the energy barrier. When an electron with energy E propagates in the $+z$ direction towards the energy barrier, the Schrodinger equation is used to describe the electron states:

$$-\frac{\hbar^2}{2m}\frac{d^2}{dz^2}\Psi(z) + U(z)\Psi(z) = E\Psi(z) \tag{1.1}$$

As shown in Fig. 2-26, $U < E$ on the left side of potential barrier. Therefore the equation is:

$$-\frac{\hbar^2}{2m}\frac{d^2}{dz^2}\Psi(z) = E\Psi(z) \tag{1.2}$$

the wave function of elections $\Psi(z)$ is written as:

$$\Psi_1(\mathrm{z}) = \mathrm{A}_1\mathrm{e}^{+\mathrm{ik}_1\mathrm{z}} + \mathrm{A}_2\mathrm{e}^{-\mathrm{ik}_1\mathrm{z}} \tag{1.3}$$

where k_1 is wave vector and given by:

$$k_1 = \frac{\sqrt{2mE}}{\hbar} \tag{1.4}$$

Inside the barrier, $U \neq 0$ and $U > E$. The equation becomes:

$$-\frac{\hbar^2}{2m}\frac{d^2}{dz^2}\Psi(z) = (E - U)\Psi(z) \tag{1.5}$$

and the wave function of elections is:

$$\Psi_2(\mathrm{z}) = \mathrm{B}_1\mathrm{e}^{+\mathrm{ik}_2\mathrm{z}} + \mathrm{B}_2\mathrm{e}^{-\mathrm{k}_2\mathrm{z}} \tag{1.6}$$

where k_2 is decay constant and given by:

$$k_2 = \frac{\sqrt{2m(U-E)}}{\hbar} \tag{1.7}$$

On the right side of potential barrier, $U < E$. The wave function of elections is similar to that on the left side of barrier, but there is only transmitted waves. Thus the wave function $\Psi(z)$ is written as:

$$\Psi_3(\mathrm{z}) = \mathrm{C}\mathrm{e}^{\mathrm{ik}_1\mathrm{z}} \tag{1.8}$$

A_1, A_2, B_1, B_2 and C in the equations are the coefficients and in terms of k_1 and k_2. It is due to the wave functions as well as their first order derivative are continuous when the elections pass across the barrier.

At $x = 0$,

$$\Psi_1(0) = \Psi_2(0)$$

$$\left.\frac{d\Psi_1(x)}{dx}\right|_{x=0} = \left.\frac{d\Psi_2(x)}{dx}\right|_{x=0} \tag{1.9}$$

also, $x = z$,

$$\Psi_2(\mathrm{z}) = \Psi_3(z)$$

$$\left.\frac{d\Psi_2(x)}{dx}\right|_{x=z} = \left.\frac{d\Psi_3(x)}{dx}\right|_{x=z} \tag{2.0}$$

then the transmission coefficient T is calculated as:

$$T = \frac{(\Psi_3)^2}{(\Psi_1)^2} = \frac{CC^*}{A_1 A_2{}^*} = \left[1 + \frac{\left(e^{k_2 z} + e^{-k_2 z}\right)}{16(1-\frac{E}{U})\frac{E}{U}}\right] \tag{2.1}$$

When $k_2 z \gg 1$, the result can be written as:

$$T \approx 16(1 - \frac{E}{U})\frac{E}{U} e^{-k_2 z} \tag{2.2}$$

It means that the transmission probability of elections decreases exponentially when the barrier width z increases [136]. The electrons with energy between the two Fermi levels have the same possibility of transferring the vacuum when there is no bias voltage applied, thus there is no net tunnelling current detected under this condition.

In a STM, the scanning tip and sample can work as the two electrodes, of which the Fermi levels are named as E_{Ft} and E_{Fs} respectively, and the vacuum between the tip apex and sample surface works as the energy barrier. For simplify, E_{Ft} and E_{Fs} are equal to each other before the application of a bias voltage. When the

sharp tip is brought extremely close to the sample surface with the distance of ~10 Å, the total number of electrons passing across the barrier is strongly affected by the bias voltage put on the sample or tip [137,138]. As shown in Fig. 2-27 (b), the areas with shadow represent the occupied states of elections in the tip and sample. A specific bias voltage *V* is applied to the sample making its Fermi level an upward shifting of *eV*, where *e* represents the charge of electrons. Elections of the sample with the energy between E_{Ft} to $E_{Ft} + eV$ tunnel through the barrier and form net tunnelling current. The current is given by:

$$I \propto \sum_{E_{Ft}}^{E_{Ft}+eV} |\Psi(z)|^2 \, e^{-2z\sqrt{\frac{2m}{\hbar^2}(\Phi - \frac{e|V|}{2})}}) \tag{2.3}$$

By taking in account of the local density of states (LDOS) $\rho_s(\mathrm{E_{Fs}})$ of the sample surface:

$$\rho_s(E_{Fs}) \propto \frac{1}{eV} \sum_{E_{Ft}}^{E_{Ft}+eV} |\Psi(z)|^2 \tag{2.4}$$

where we can achieve that the tunnelling current *I* is exponentially related to the barrier width *z* [136].

$$I \propto V \rho_s(E_{Fs}) e^{(-2z\sqrt{\frac{2m}{\hbar^2}(\Phi - \frac{e|V|}{2})})} \tag{2.5}$$

where z represents the gap distance between tip apex and the surface atoms of the sample, $\hbar$ represents the Dirac constant and equals to the value of $\frac{h}{2\pi}$, m the effective mass of the electron and Φ represents the work function of the sample.

By detecting the tunnelling current, the tip-sample distance can be achieved sensitively(vice versa). For example, 1 Å difference in tip-sample distance can result in a difference of the tunnelling current by a factor of 10 [139,140]. For an working VT STM in the ultrahigh vacuum environment, the highest image resolution in the depth direction reaches 0.1 Å and the highest resolution in the lateral directions can reach 1 Å [143,144]. Therefore, geometric surface features in real space can be directly obtained with atomic resolution when the tunnelling

current is recorded continuously by STM. It enables scientists to understand their research subjects on an atomic or molecular level.

Apart from the geographic information, an STM can also detect surface electronic contour of the target sample. This technique is called Scanning Tunnelling Spectroscopy (STS) [135]. By taking the derivative on the two sides of the formula with respect to the bias voltage V, (2.5) is written as:

$$\frac{dI}{dV} \propto \rho_s(E_{Fs}) \tag{2.6}$$

For probing the occupied and unoccupied election density states of the sample surface, an I-V curve can be made by sweeping the bias voltage from a minus value to a positive one and recording the corresponding current at the same time. The Fermi-level LDOS are achieved by taking differentiation to a recorded I-V curve [136,141].

As a powerful tool for surface science study, STM has a lot of advantages. It is widely used in studying the three dimensional contours as well as the positions of surface reconstructions and surface defects [144,145]. Before the development of STM, it was known from LEED experiments that the unit cell has a six-fold symmetry and is constructed by the original 49 cells of Si(111). With the help of STM, a clean Si(111) surface with the detailed information of 7×7 reconstruction was obtained. Each unit cell were found including 12 adatoms and a combination of two triangles. Therefore, the unit cell of Si(111) has a three-fold symmetry. What's more, by comparing with the unreconstructed surface, that the original 49 dangling bonds in a unit cell were found reduced to 12 once the surface reconstruction appear [145].

STM are versatile and can be used in ultrahigh vacuum (UHV), air and liquids. The testing material can be scanned at different temperatures and will not be damaged. For the VT STM operated in our laboratory, the variable temperature operated in the microscope stage is in the range of 25 K to 1500K. The STM is

also powerful tool for studying the surface dynamic process and electrochemical reaction process [146,147]. The early studies measured the surface diffusion of clean and oxygen-covered Si(111) surface. The feedback loop of STM was suspended while the tip was kept still over a selected area during scanning. Then, the continuous tunnelling current were recorded and analysed by the power spectrum analyser. Fluctuation of the current caused by diffusion of adatoms through the tunnelling area were separated and used to calculate the diffusion coefficients [146,147].

However, there are also some disadvantages of STM. STM works based on the principle of quantum tunnelling, it requires the testing sample and scanning tip to have conductivity. For the materials of semiconductors or insulators, it is hard for STM to achieve high-resolution of sample surface directly. The lateral developed techniques such as atomic force microscopy (AFM) make up this deficiency effectively. What's more, the fluctuation shown in the scanning images not necessary reflect the real physical height difference. It is because STM collect both the electronic and geometric information at the same time during scanning. The regions of the material surface with strong charge transfer to the tip could appear brighter and be measured higher the areas with weak charger transfer.

The STM is strict with the experimental environment. The tunnelling current created between tip are in the scales of picoampere and nanoampere. It is easier to affected if there is any external noise. The highest resolution STM images of atomic structures typically needs an UHV environment, with the pressure reach -10^{10} mbar. It makes STM fragile and expensive to be built.

Another disadvantage of STM is the limited scanning areas. For the time being, the largest scanning magnifications are commonly micrometres in the x, y and z directions. It only detects the local surface features and cannot be used to study the overall properties of the materials.

2.8.2 Two Scanning Modes of Scanning Tunnelling Microscopy

The two scanning modes of STM are the constant current imaging mode (CCI) and the constant height imaging mode (CHI). Schematic of the two working modes are demonstrated in Fig. 2-28 (a) respectively.

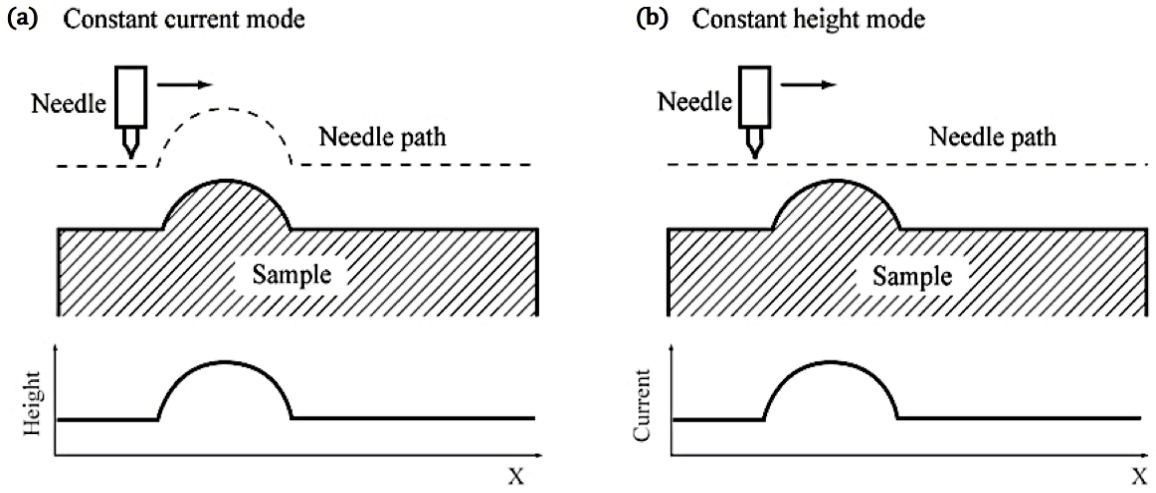


Fig. 2-28 Schematic showing the two working modes of an STM. (a) For the constant current mode (CCI), the tip-sample distance height is adjusted by the feedback circus while the tunnelling current is fixed. (b) For the constant height mode (CHI), the tunnelling currents are recorded by STM as the tip's height is kept constant [148].

In the constant current mode (CCI), the tunnelling current is set as a constant value during scanning [102] while the height of tip is adjusted with the help of a feedback circuit. When the tip scans over an area with protrusions, the sudden shrink of the tip-sample distance leads to the tunnelling current increasing. Once the change of current is detected, a voltage is applied to the piezo. Then the tip retracts back a few distances until the set-point tunnelling current achieves the pre-set value again. In contrast, when the tip scans over the sunken areas, it will move forward a few steps to the sample surface. During scanning, all the tip's motion curves are recorded by STM, and the sample's geometric corrugation is thus achieved. This mode is suitable for materials with rugged surfaces.

On the other hand, the constant height mode (CHI) is introduced in Fig. 2-28 (b). The feedback electric is employed to maintain the tip's height at a constant value. During scanning, fluctuation of the sample surface results in the change of the sample-tip distance as well as the tunnelling current. Hence, the current at each point is recorded by the controller and shows as different contrasts in the STM image. The constant height mode is suitable for scanning a sample having been studied before or already known with a smooth surface. If the sample surface is extremely rough, the tip is easy to crash. In experiments, the two scanning modes are usually combined to study the surfaces with different features [130].

2.9 Solution and Vacuum Deposition

At the laboratory, solution phase and vacuum phase deposition are the most common methods for producing small particles, organic islands and successive thin films on a series of solid substrates. The schematic diagrams in Fig. 2-29 (a) and (b) demonstrate both the two preparation methods. The solution deposition method is suitable for the mass production of MOFs, which have been developed since the successive monolayers of palmitic, stearic and arachidic acids were transferred onto the solid substrate from the liquid surface in the first time [149-154,155].

Compared with other methods, solution phase deposition has the advantage of simplicity and low-costing. The solution with a specific concentration of the target molecules has to be prepared firstly. Then the solid substrate is fully dipped into the liquid repetitively, and the molecules in the solution are possible to transfer onto the solid substrate and form monolayers or thin films. The solution phase method has been used to make Langmuir films or Langmuir-Blodgett films, of which is each molecule consists of a hydrophobic headgroup and a hydrophilic endgroup. The molecules' endgroups in the solution have a specific affinity to

water and attach to the surface of the liquid, while the hydrophobic headgroups prevent all the molecules from lying down on the surface of solution [153,156]. As shown in Fig. 2-29 (c), when a solid substrate is put into the solution, molecules are possible to transfer from the liquid to the solid substrate and contact with their headgroups [150,155]. One of the drawbacks of this deposition method is that the cleanliness of the solution is hard to be fully removed. Apart from the target molecules, some impurities contained in the solution are also able to adsorb on the substrate.

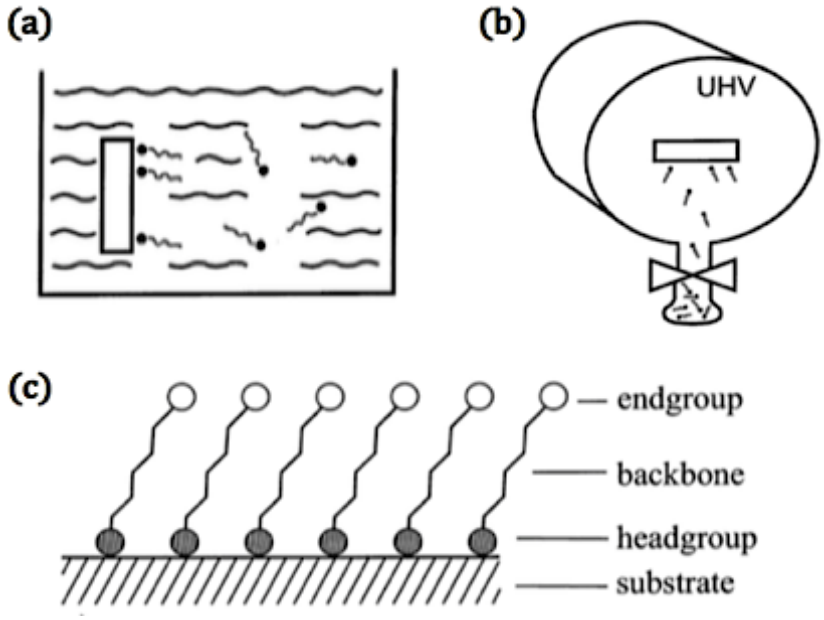


Fig. 2-29 Overview of the two methods for preparing crystalline organic thin films or the self-assembled monolayers (a) in solution or (b) in ultrahigh vacuum. Langmuir films are formed by spreading amphiphilic molecules on the liquid surface. LB films are prepared by transferring Langmuir films onto solid substrates. Organic molecular beam deposition (OMBD) uses evaporation techniques in UHV. (c) Schematic of the self-assembled monolayer. Shaded circles represent chemisorbing headgroups while the open circles indicate endgroups [155].

With the development of ultrahigh vacuum techniques, gas phase deposition has become more popular gradually. The metal crystals working as the substrate can maintain its top-most layers with high purity after being cleaned by ion sputtering and thermal annealing. It offers the potential of building complex and oversized

structures and can be measured by methods such as microscopy [157], spectroscopy [158,159] and diffractions [160-162]. As introduced, fullerene molecules do not have obvious hydrophilic headgroups and do not build a strong chemical binding, but they can also work as electron acceptors after being deposited onto the solid metal surface such as Au(111). These molecules are thus able to have both strong abilities of adsorption and diffusion [157].

In UHV, there are some other deposition methods newly developed, e.g., organic molecular beam epitaxy (OMBE). It is widely used for making aromatic molecular crystals, the homoepitaxial and heteroepitaxial thin films [69,163]. The working principle of this method is similar to molecular beam epitaxy (MBE), which is mainly applied in the nonorganic systems [164].

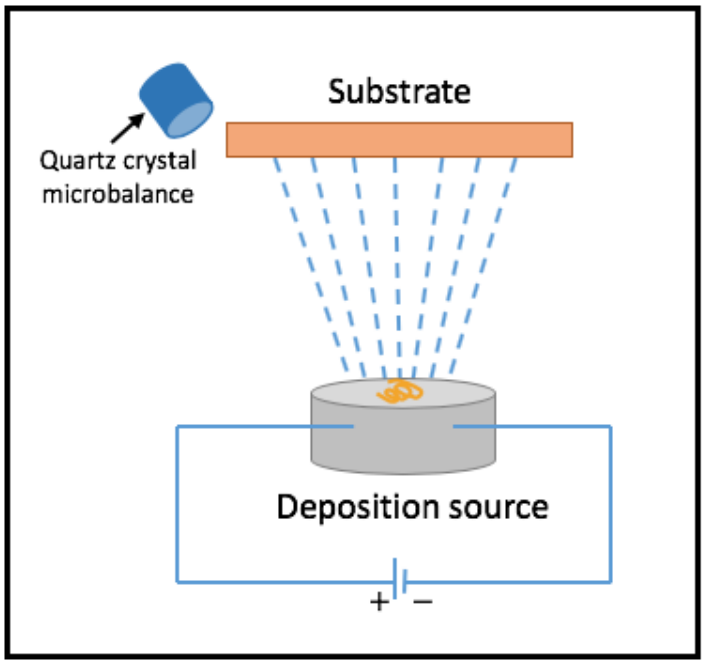


Fig. 2-30 Schematic of the PVD vacuum system with an quartz crystal microbalance (QCM) working for monitoring atomic vapor density and mass flux during thermal evaporation.

All of my experiments have been carried out in the ultrahigh vacuum chamber. The working pressure is always controlled lower than -10^{10} mbar. The testing samples measured in my projects are prepared with the technique of in-situ

physical vapor deposition (PVD). It belongs to the vacuum deposition. Sputtering and thermal evaporation are the two most common process of PVD. Here the latter one are adopted. The schematic of the PVD system used in our lab is shown in Fig. 2-30.

The deposition source is fixed directly under the substrate. When deposition starts, the materials are firstly annealed to their melting points and switch from a condensed phase to a vapor phase. Once the atoms land onto the substrate, they diffuse, nucleate and aggregate as thin films with condensed phase.

An Quartz crystal microbalance (QCM) is fed back of the substrate and used for measuring atomic vapor density and mass flux during deposition [165]. One oscillating piezoelectric quartz crystal is included in the OCM, which is extremely sensitive to the added mass and has high stability of temperature. The crystal resonates at discrete frequencies once a voltage is applied. When the evaporation starts, atoms landing onto the resonating crystal will reduce its resonant frequency [165]. The frequency's change Δf is repeatable and has the relationship with the added mass:

$$-\frac{\Delta f}{f_q} = \frac{M_f}{M_q} \tag{2.7}$$

where f_q and M_q represent the resonant frequency as well the mass of the uncoated quartz crystal respectively. If Δf is smaller than 2% of f_q, the thickness of the deposited thin films, named as d_f, can be obtained by taking into the Sauerbrey equation and written as:

$$d_f = -\frac{\Delta f}{\rho_f}\frac{N\rho_q}{{f_q}^2} \tag{2.8}$$

Where ρ_f and ρ_q represent the densities of thin films and quartz crystal, respectively, while N represents the crystal's frequency constant [165, 166].

References

[1] W. Haiss, D. Lackley, J. K. Sass, and K. H. Besocke, J. Chem. Phys. **95**, 2193 (1991).

[2] M. A. Van Hove, R. J. Koestner, P. Stair, J. P. Bibérian, L. L. Kesmodel, I. Bartoš and G. A. Somorjai, Surf. Sci. **103**, 189 (1981).

[3] H. Melle, and E. Menzel, Z. Naturforsh. Teil A **33**, 282 (1978).

[4] U. Haren, A. M. Lahee, J. P. Toennies, and C. Wöll, Phys. Rev. Lett. **54**, 2619 (1985).

[5] J. Perdereau, J. P. Biberian, and G. E. Rhead, J. Phys. F-Metal Phys. **4**, 798 (1974).

[6] Y. Nakai, M. S. Zei, D. M. Kolb, and G. Lehmpfuhl, Ber. Bunsen-Ges. Phys. Chem. **88**, 340 (1984).

[7] F. C. Frank, and J. H. van der Merwe, Proc. R. Soc, London. **198**, 205 (1949).

[8] Y. Tanishiro, H. Kanamori, K. Takayanagi, K. Yagi, G. Honjo, Surf. Sci. **111**, 395 (1981).

[9] J. C. Heyraud, and J. J. Métois, Surf. Sci. **100**, 519 (1980).

[10] K. Yagi, K. Takayanagi, K. Kobayashi, N. Osakabe, Y. Tanishiro, and G. Honjo, Surf. Sci. **86**, 174 (1979).

[11] C. Wőll, S. Chiang, R. J. Wilson, and P. H. Lippel, Phys. Rev. B **39**, 7988 (1989).

[12] J. V. Barth, H. Brune, G. Ertl, and R. J. Behm, Phys. Rev. B **42**, 9307 (1990).

[13] P. Bak, Rep. Prog. Phys. **45**, 58 (1982).

[14] Y. I. Frenkel, and T. Kontorova, Zh. Eksp. Teor. Fiz. **8**, 1340 (1938).

[15] N. Takeuchi, C. T. Chan, K. M. Ho, Phys. Rev. B **43**, 13899 (1991).

[16] S. Narasimhan, and D. Vanderbilt, Phys. Rev. Lett. **69**, 1564 (1992).

[17] O. L. Alerhand, D. Vanderbilt, R. D. Meade, and J. D. Joannopoulos, Phys. Rev. Lett. **61**, 1973 (1988).

[18] D. D. Chambliss, R. J. Wilson, and S. Chiang, J. Vac. Sci. Technol. B **9**, 933 (1991).

[19] D. D. Chambliss, R. J. Wilson, and S. Chiang, Phys. Rev. Lett. **66**, 1721 (1991).

[20] S. Rousset, V. Repain, G. Baudot, Y. Garreau, and J. Lecoeur, J. Phys-Condens. Matter. **15**, 3363 (2003).

[21] E. I. Altman and R. J. Colton, Surf. Sci. **279**, 49 **(**1992).

[22] Ernst, S. Optimisation of the Preparation Process for Tips Used in Scanning Tunnelling Microscopy. Thesis paper (2006).

[23] K. G. Huang, D. Gibbs, D. M. Zehner, A. R. Sandy, and S. G. J. Mochrie, Phys. Rev. Lett. **65**, 3313 (1990).

[24] J. A. Meyer, I. D. Baikie, E. Kopatzki, and R. J. Behm, Surf. Sci. **365**, L647 (1996).

[25] W. G. Cullen, and P. N. First, Surf. Sci. **420**, 53 (1999).

[26] C. S. Casari, S. Foglio, F. Siviero, A. L. Bassi, M. Passoni and C. E. Bottani, Phy. Rev. B **79**, 195402 (2009).

[27] S. Helveg, J. V. Lauritsen, E. Lægsgaard, I. Stensgaard, J. K. Nørskov, B. S. Clausen, H. Topsøe and F. Besenbacher, Phys. Rev. Lett. **84**, 951 (2000).

[28] B. Fischer, J. V. Barth, A. Fricke, L. Nedelmann, and K. Kern, Surf. Sci. **389**, 366 (1997).

[29] A. G. Trant, T. E. Jones, J. Gustafson, T. C. Q. Noakes, P. Bailey, and C. J. Baddeley, Surf. Sci. **603**, 571 (2009).

[30] B. Voigtländer, G. Meyer, and N. M. Amer, Surf. Sci. Lett. **255**, L529 (1991).

[31] M. M. Dovek, C. A. Lang, J. Nogami, and C. F. Quate, Phys. Rev. B **40**, 11973 (1989).

[32] L. Gao, Q. Liu, Y. Y. Zhang, N. Jiang, H. G. Zhang, Z. H. Cheng, W. F. Qiu, S. X. Du, Y. Q. Liu, W. A. Hofer and H. J. Gao, Phys. Rev. Lett. **101**, 197209 (2008).

[33] C. A. Lang, M. M. Dovek, J. Nogami, and C. F. Quate, Surf. Sci. Lett. **224**, 947 (1989).

[34] http://nanoprobes.aist-nt.com/apps/HOPG%20info.htm.

[35] H. Yang, L. Jones, H. Ryll, M. Simson, H. Soltau, Y. Kondo, R. Sagawa, H. Banba, I. MacLaren, and P. D. Nellist, J. Phys. Conf. Ser. **644**, 012032 (2015).

[36] A. W. Moore, Chem. Phys. Carbon **11**, 70 (1973).

[37] https://www.2spi.com/item/436hp-ab/

[38] F. Cavallo, R. Rojas Delgado, M. M. Kelly, J. R. Sánchez Pérez, D. P. Schroeder, H. G. Xing, M. A. Eriksson and M. G. Lagally, ACS Nano **8**, 10237 (2014).

[39] E. Y. Andrei, G. Li, X. Du, Rep. Prog. Phys. **75**, 056501 (2012).

[40] https://www.merriam-webster.com/dictionary/graphene.

[41] K. I. Ho, M. Boutchich, C. Y. Su, R. Moreddu, E. S. R. Marianathan, L. Montes and C. S. Lai, Adv. Mater **27**, 6519 (2015).

[42] S. R. Snyder, W. W. Gerberich, and H. S. White, Phys. Rev. B **47**, 16 (1993).

[43] W. T. Pong, J. Bendall, and C. Durkan, Surf. Sci. **601**, 498 (2007).

[44] H. Lipson and A. R. Stokes, Proc. R. Soc. Lond. Ser. A **181**, 101 (1942).

[45] N. G. Shang, P. Papakonstantinou, M. McMullan, M. Chu, A. Stamboulis, A. Potenza, S. S. Dhesi and H. Marchetto, Adv. Funct. Mater. **18**, 3506 (2008).

[46] H. Jussila, H. Yang, N. Granqvist and Z. Sun, Optica **3**, 151 (2016).

[47] R. Turton, The Physics of Solids (Oxford University press, New York, 2000).

[48] J. C. Meyer, A. K. Geim, M. I. Katsnelson, K. S. Novoselov, T. J. Booth and S. Roth, Nature **446**, 60 (2007).

[49] http://butane.chem.uiuc.edu/pshapley/genchem1/L12/2.html.

[50] http://www.nanomaterials.pl/graphene; Chemistry land intro, Hybridisation in covalent bonds, <-CHM151 Progress Page.

[51] C. Aaron, Cosmos magazine the coming age of diamond, (2010).

[52] http://www.optigraph.fta-berlin.de/basics.html.

[53] W. T. Pong, and C. Durkan, J. Phys. D **38**, R329 (2005).

[54] P. L. Giunta and S. P. Kelty, J. Chem. Phys. **114**, 1807 (2001).

[55] I. P. Batra, N. Garcia, H. Rohrer, H. Salemink, E. Stoll and S. Ciraci, Surf. Sci. **181**, 126-138 (1987).

[56] E. Stolyarova, K. T. Rim, S. Ryu, J. Maultzsch, P. Kim, L. E. Brus, T. F. Heinz, M. S. Hybertsen and G. W. Flynn, Proc. Natl. Acad. Sci. **104**, 9209 (2007).

[57] R. C. Tatar, and S. Rabii, Phys. Rev. B **25**, 4126 (1982).

[58] J. Červenka and C. F. J. Flipse, Phys. Rev. B **79**, 195429 (2009).

[59] J. C. Charlier, J. P. Michenaud and X. Gonze, Phys. Rev. B **46**, 4531 (1992).

[60] U. Müller, K. Sattler, J. Xhie, N. Venkateswaran and G. Raina, J. Vac. Sci. Technol. B **9**, 829 (1991).

[61] C. Becker, T. Fries, K. Wandelt, U. Kreibig and G. Schmid, **9**, 810 (1991).

[62] T. P. Darby and C. M. Wayman, J. Cryst. Growth **28**, 41 (1975).

[63] R. T. Pötzschke, C. A. Gervasi, S. Vinzelberg, G. Staikov and W. J. Lorenz, Electrochim. Acta **40**, 1469 (1995).

[64] P. Marcus, and C. Hinnen, Surf. Sci. **392**, 134 (1997).

[65] R. Klingeler, G. Kann, I. Wirth, S. Eisebitt, P.S. Bechthold, M. Neeb, and W. Eberhardt, J. Chem. Phys. **115**, 7215 (2001).

[66] M. E. Garah, A. Ciesielski, N. Marets, V. Bulach, M. W. Hosseini, Samori, P. Chem. Commun. **50**, 12250 (2014).

[67] T. Schmitz-Hübsch, F. Sellam, R. Staub, M. Törker, T. Fritz, C. Kübel, K. Müllen, K. Leo, Surf. Sci. **445**, 358 (2000).

[68] W. Chen, H. Huang, A. Thye and S. Wee, Chem. Commun. **36**, 4276 (2008).

[69] S. R. Forrest, Chem. Rev. **97**, 1793 (1997).

[70] O. V. Cherstiouk, P. A. Simonov, E. R. Savinova, Electrochim. Acta, **48**, 3851 (2003**).**

[71] L. Lopez-Salido, D. C. Lim, Y. D. Kim, Surf. Sci. **588**, 6 (2005).

[72] H. Y. Nie, T. Shimizu, H. Tokumoto, J. Vac. Sci. Technol. B **12**, 1843 (1994).

[73] M. J. Stowell, Thin Films **1**, 55 (1968).

[74] D. W. Pashley, M. J. Stowell, M. H. Jacobs, and T. J. Law, Philos. Mag. **10**, 127 (1964).

[75] J. G. Allpress and J. V. Sanders, Phil Mag. **9**, 645 (1964).

[76] J. G. Allpress, and J. V. Sanders, Surf. Sci. **7**, 1 (1967).

[77] T. P. Darby, and C. M. Wayman. Phys. Status solidi (a) **25**, 585 (1974).

[78] C. M. Wayman and T. P. Darby, J. Cryst. Growth **28**, 53 (1975).

[79] F. A. Cotton, Chemical Applications of Group Theory (Wiley, New York, 1963).

[80] M. Bodner, J. Patera, and M. Szajewska, PLoS One **9**, e84079 (2014).

[81] J. B. Howard, J. T. McKinnon, Y. Makarovsky, A. L. Lafleur, and M. E. Johnson. Nature **352**, 139 (1991).

[82] H. W. Kroto, J. R. Heath, S. C. O'Brien, R. F. Curl, and R. E. Smalley, Nature **318**, 162 (1985).

[83] R. D. Johnson, G. Meijer, D. S. Bethune, J. Am. Chem. Soc. **112**, 8983 (1990).

[84] K. Hedberg, L. Hedberg, D. S. Bethune, C. A. Brown, H. C. Dorn, R. D. Johnson, M. De Vries, Science **254**, 410 (1991).

[85] W. Krätschmer, L. D. Lamb, K. Fostiropoulos, and D. R. Huffman, Nature **347**, 354 (1990).

[86] G. Dresselhaus, M. S. Dresselhaus, P. C. Eklund, Science of Fullerenes and Carbon Nanotubes: Their Properties and Application (Academic Press, San Diego, 1995).

[87] C. S. Yannoni, P. P. Bernier, D. S. Bethune, G. Meijer, and J. R. Salem, J. Am. Chem. Soc. **113**, 3190 (1991).

[88] O. Zhou and D. E. Cox, J. Phys. Chem. Solids **53**, 1373 (1992).

[89] P. A. Heiney, J. E. Fischer, A. R. McGhie, W. J. Romanow, A. M. Denenstein, J. P. McCauley Jr, A. B. Smith, D. E. Cox, Phys. Rev. Lett. **66**, 2911 (1991).

[90] F. Rossel, M. Pivetta, F. Patthey, E. Cavar, A. P. Seitsonen and W.-D. Schneider, Phys. Rev. B **84**, 075426 (2011).

[91] M. S. Dresselhaus, G. Dresselhaus and P. C. Eklund, Science of Fullerenes and Carbon Nanotubes (Academic, New York, 1996); A. Kühnle, Curr. Opin. Colloid Interface Sci., **14**, 157 (2009).

[92] C. S. Yannoni, R. D. Johnson, G. Meijer, D. S. Bethune, J. R. Salem, J. Phys. Chem. **95**, 9 (1991).

[93] R. F. Curl and R. E. Smalley, Sci. Am. **265**, 54 (1991).

[94] E. Cavar, M.-C. Blum, M. Pivetta, F. Patthey, M. Chergui, and W.-D. Schneider, Phys. Rev. Lett. **95**, 196102 (2005).

[95] S. L. Altman, and P. Herzig, Point group Theory Tables (Clarendon, Oxford, 1994).

[96] K. Prassides, H. W. Kroto, R. Taylor, D. R. M. Walton, W. I. F. David, J. Tomkinson, R. C. Haddon, M. J. Rosseinsky, and D. W. Murphy, Carbon **30**, 1277 (1992).

[97] W. I. F. David, R. M. Ibberson, T. J. S. Dennis, J. P. Hare and K. Prassides, Europhys. Lett. **18**, 219 (1992).

[98] M. Sprik, A. Cheng and M. L. Klein, J. Phys. Chem. **96**, 2027 (1992).

[99] P. W. Murray, M. Ø. Pedersen, E. Lægsgaard, I. Stensgaard and F. Besenbacher, Phys. Rev. B **55**, 9360 (1997).

[100] T. Chen, S. Howells, M. Gallagher, D. Sarid, L. D. Lamb, D. R. Huffman and R. K. Workman, Phys. Rev. B **45**, 14411 (1992).

[101] D. R. McKenzie, C. A. Davis, D. J. H. Cockayne, D. A. Muller, A. M. Vassallo, Nature **355**, 622 (1992).

[102] J. A. Gardener, G. A. D. Briggs, and M. R. Castell, Phys. Rev. B **80**, 235434 (2009).

[103] G. Schull and R. Berndt, Phys. Rev. Lett. **99**, 226105 (2007).

[104] X. Zhang, F. Yin, R. E. Palmer, and Q. Guo, Surf. Sci. **602**, 885, (2008).

[105] D. Fujita, T. Yakabe, H. Nejoh, T. Sato, and M. Iwatsuki, Surf. Sci. **366**, 93 (1996).

[106] T. Sakurai, X. D. Wang, Q. K. Xue, Y. Hasegawa, T. Hashizume, H. Shinohara, Prog. Surf. Sci. **51,** 263 (1996).

[107] M. K.-J. Johansson, A. J. Maxwell, S. M. Gray, P. A. Brühwiler, and L. S. O. Johansson, Surf. Sci. **397**, 314 (1998).

[108] P. C. Eklund, A. M. Rao, Y. Wang, P. Zhou, K. A. Wang, J. M. Holden, M. S. Dresselhaus, G. Dresselhaus, Thin Solid Films. **257**, 211 (1995).

[109] T. R. Ohno, Y. Chen, S. E. Harvey, G. H. Kroll, J. H. Weaver, R. E. Haufler, and R. E. Smalley, Phys. Rev. B **44**, 13747 (1991).

[110] G. B. Vaughan, P. A. Heiey, J. E. Fischer, D. E. Luzzi, D. A. Ricketts-Foot, A. R. McGhie, Y. W. Hui, A. L. Smith, D. E. Cox, W. J. Romanow, B. H. Allen, N. Coustel, J. J. P. McCauley, A. Smith, B. I. Science **254**, 1350 (1991).

[111] J. H. Weaver, J. Phys. Chem. Solids **53**, 1433 (1992).

[112] C. Christides, T. John, S. Dennis, K. Prassides, R. L. Cappelletti, D. A. Neumann, and J. R. D. Copley, Phys. Rev. B **49**, 2897 (1994).

[113] K. Thirunavukkuarasu, V. C. Long, J. L. Musfeldt, F. Borondics, G. Klupp, K. Kamarás, and C. A. Kuntscher, J. Phys. Chem. C **115**, 3646 (2011).

[114] M. A. Verheijen, H. Meekes, G. Meijer, P. Bennema, J. L. De Boer, S. Van Smaalen, G. Van Tendeloo, S. Amelinckx, S. Muto, and J. Van Landuyt, Chem. Phys. **166**, 287 (1992).

[115] H. N. Aiyer, A. Govindaraj, and C. N. R. Rao, Philos. Mag. Lett. **72**, 185 (1995).

[116] Y. Zhang, X. Cao, and M. J. Weaver, J. Phys. Chem. **96**, 510 (1992).

[117] S. Guo, D. Fogarty, P. Nagel, and S. A. Kandel, J. Phys. Chem. C **5513**, 185 (2004).

[118] N. Katsonis, A. Marchenko, and D. Fichou, Adv. Mater. **16**, 309 (2004).

[119] A. L. Deering and S. A. Kandel, Langmuir **22**, 10025 (2006).

[120] P. Wang, L. Meng, X. B. Wang, Y. J. Li, C. Q. Sheng, J. O. Wang, H. J. Qian, K. Ibrahim, and H. N. Li, J. Phys.: Condens. Matter **23**, 395002 (2011).

[121] X. B. Wang, H. K. Woo, X. Huang, M. M. Kappes, and L. S. Wang, Phys. Rev. Lett. **96**, 143002 (2006).

[122] P. Wang, H. J. Zhang, Y. J. Li, C. Q. Sheng, Y. Shen, H. Y. Li, S. N. Bao, and H. N. Li, Phys. Rev. B **85**, 205445 (2012).

[123] M. P. Marder, Condensed Matter Physics (Wiley, New York, 1999).

[124] S. Modesti, S. Cerasari, and P. Rudolf, Phys. Rev. Lett. **71**, 2469 (1993).

[125] Y. Maruyama, K. Ohno, and Y. Kawazoe, Phys. Rev. B **52**, 2070 (1995).

[126] X. Lu, M. Grobis, K. H. Khoo, S. G. Louie, and M. F. Crommie, Phys. Rev. B **70**, 115418 (2004).

[127] H. B. Michaelson, J. Appl. Phys. **48**, 4729 (1977); M. Uda, A. Nakamura, T. Yamamoto, and Y. Fujimoto, J. Electron Spectrosc. Relat. Phenom. **88**, 643 (1998).

[128] C. Cepek, A. Goldoni, and S. Modesti, Phys. Rev. B **53**, 7466 (1996).

[129] C. Liu, Z. Qin, J. Chen, Q. Guo, Y. Yu, and G. Cao, J. Chem. Phys. **134**, 044707 (2011).

[130] R. Wiesendanger, Scanning Probe Microscopy and Spectroscopy (Cambridge University Press, Cambridge, 1994).

[131] Y. C. Xie, L. Tang, and Q. Guo, Phys. Rev. Lett. **111**, 186101 (2013).

[132] L. Tang, Y. C. Xie, and Q. Guo, J. Chem. Phys. **135**, 114702 (2011).

[133] X. Torrelles, M. Pedio, C. Cepek, and R. Felici, Phys. Rev. B **86**, 075461 (2012).

[134] X. Zhang, L. Tang and Q. Guo, J. Phys. Chem. C **114**, 6433 (2010).

[135] G. Binnig, H. Rohrer, Ch. Gerber and E. Weibel, Phys. Rev. Lett. **49**, 57 (1982).

[136] C. J. Chen, Introduction to Scanning Tunnelling Microscopy (Oxford University Press on Demand, New York,1993).

[137] R. Young, J. Ward, F. Scire, Phys. Rev. Lett. **27**, 922 (1971).

[138] J. A. Stroscio, R. M. Feenstra, A. P. Fein, Phys. Rev. Lett. **57**, 2579 (1986).

[139] C. Joachim, J. K. Gimzewski, A. Aviram, Nature **408**, 541 (2000).

[140] C. Joachim, M. A. Ratner, PNAS **102**, 8801 (2005).

[141] H. Ohnishi, Yukihito Kondo, and Kunio Tkayanagi, Nature **395**, 780 (1998).

[142] J. Bohdansky, J. Roth, and H. L. Bay, J. Appl. Phys. **51**, 2861 (1980).

[143] J. A. Stroscio and W. J. Kaiser, Scanning tunneling microscopy (volume 27. Academic Press, 1993).

[144] F. Besenbacher, Rep. Prog. Phys. **59**, 1737 (1996).

[145] G. Binning, H. Rohrer, Ch. Gerber, and E. Weibel, Phys. Rev. Lett. **50**, 120 (1983).

[146] G. Binning, H. Fuchs, and E. Stoll, Surf. Sci. **169**, L295 (1986).

[147] M. L. Lozano, M. C. Tringides, Europhys. Lett. **30**, 537 (1995).

[148] http://eng.thesaurus.rusnano.com/wiki/article14154.

[149] K. Blodgett, J. Am. Chem. Soc. **57**, 1007 (1935).

[150] K. Blodgett, Phys. Rev. **51**, 964 (1937).

[151] W. C. Bigelow, D. L. Pickett, W. A. Zisman, J. Colloid Interface Sci. **1**, 513 (1946).

[152] L. C. F. Blackman, M. J. S. Dewar, J. Chem. Soc. 162 (1957).

[153] G. L. Gaines, Mixed Monolayers (Interscience, New York, 1966).

[154] A. Ulman, An Introduction to Ultrathin Organic Films (Academic Press, Boston, 1991).

[155] F. Schreiber, Prog. in Surf. Sci. **65**, 151 (2000).

[156] V. M. Kaganer, H. Möhwald, P. Dutta, Rev. Mod. Phys. **71**, 779 (1999).

[157] A. R. Sandy, S. G. J. Mochrie, D. M. Zehner, K. G. Huang, D. Gibbs, Phys. Rev. B **43**, 4667 (1991).

[158] R. G. Nuzzo, D. L. Allara, J. Am. Chem. Soc. **105**, 4481 (1983).

[159] J. Sagiv, J. Am. Chem. Soc. **102**, 92 (1980).

[160] P. Fenter, A. Eberhardt and P. Eisenberger, Science **266**, 1216 (1994).

[161] G. Scoles (Ed.), Atomic and Molecular Beam Methods (Oxford University Press, 1988).

[162] C. E. D. Chidsey, G. Y. Liu, P. Rowntree, G. Scoles, J. Chem. Phys. **91**, 4421 (1989).

[163] E. Umbach, M. Sokolowski, R. Fink, Appl. Phys. A **63**, 565 (1996).

[164] P. Fenter, F. Schreiber, L. Zhou, P. Eisenberger, S. R. Forrest, Phys. Rev. B **56**, 3046 (1997).

[165] V. Matias, and R. H. Hammond, In Situ Characterization of Thin Film Growth (Woodhead Publishing Limited, 2011).

[166] G. Sauerbrey, Z. Phys. **155**, 206 (1959).

3. Experimental Procedure

3.1 Scanning Tunnelling Microscopy

The variable temperature scanning tunnelling microscopy (VT-STM) is fixed inside an ultrahigh vacuum chamber known as the main chamber with the pressure of 2×10^{-10} mbar. A "Fast Entry Lock" (FEL) connected to the main chamber in Fig. 3-1 is used for transferring the tips and samples into the main chamber. Before opening the valve between the two chambers, FEL needs to be pumped down to $\sim 10^{-9}$ mbar to keep the vacuum in the main chamber in the $\sim 10^{-9}$ mbar range during sample transfer [1].

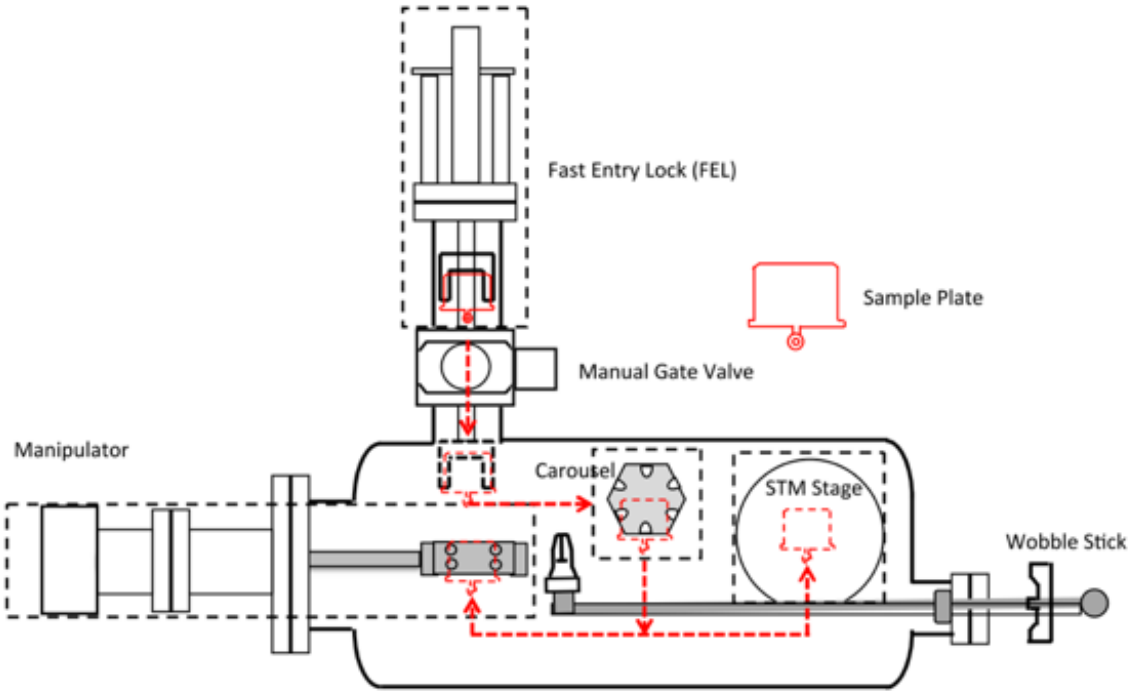


Fig. 3-1 Diagram for the Omicron VT-STM. The manipulator is in the main chamber, which links the Fast Entry Lock on its left side. A carousel stage is put between STM and the manipulator, used for storing the samples and the tips. STM stage is mounted on the right side of the main chamber [1].

In a VT-STM, both the carousel and the manipulator are located in the main chamber. It makes easier for sample transfer. A cryostat system in the chamber is able to change temperature of the testing samples. The samples on the manipulator can be heated to 750 K with resistive heating and 1500 K with direct heating. An Ar^+ ion sputtering system is connected to the chamber for cleaning noble samples such as gold, silver and platinum. By controlling beam energy, the sputtering system can also be used to create atomic defects with certain sizes on the samples like graphite and silicon.

A wobble stick on the right side of Fig. 3-1 is half insert into the chamber. It has a right angle at one of its terminal in the vacuum chamber and can be used to transfer the sample between the STM stage, the manipulator stage and the transfer rod inside the FEL. It can also be used to put samples on the carousel stage for storing.

The STM is extremely sensitive to external vibrations during working. Therefore, the STM has its own damping and vibration isolation system, which are set surrounding the scanning stage. As shown in Fig. 3-2 (a), the scanner is fixed on the eddy current damping stage, which is suspended with four soft springs. The magnets around the STM stage is able to reduce the movement of copper plates based on the damping principle and enhance the stability of the working system. The springs in conjunction with the eddy current damping stage can significantly block external vibrations getting into the STM stage.

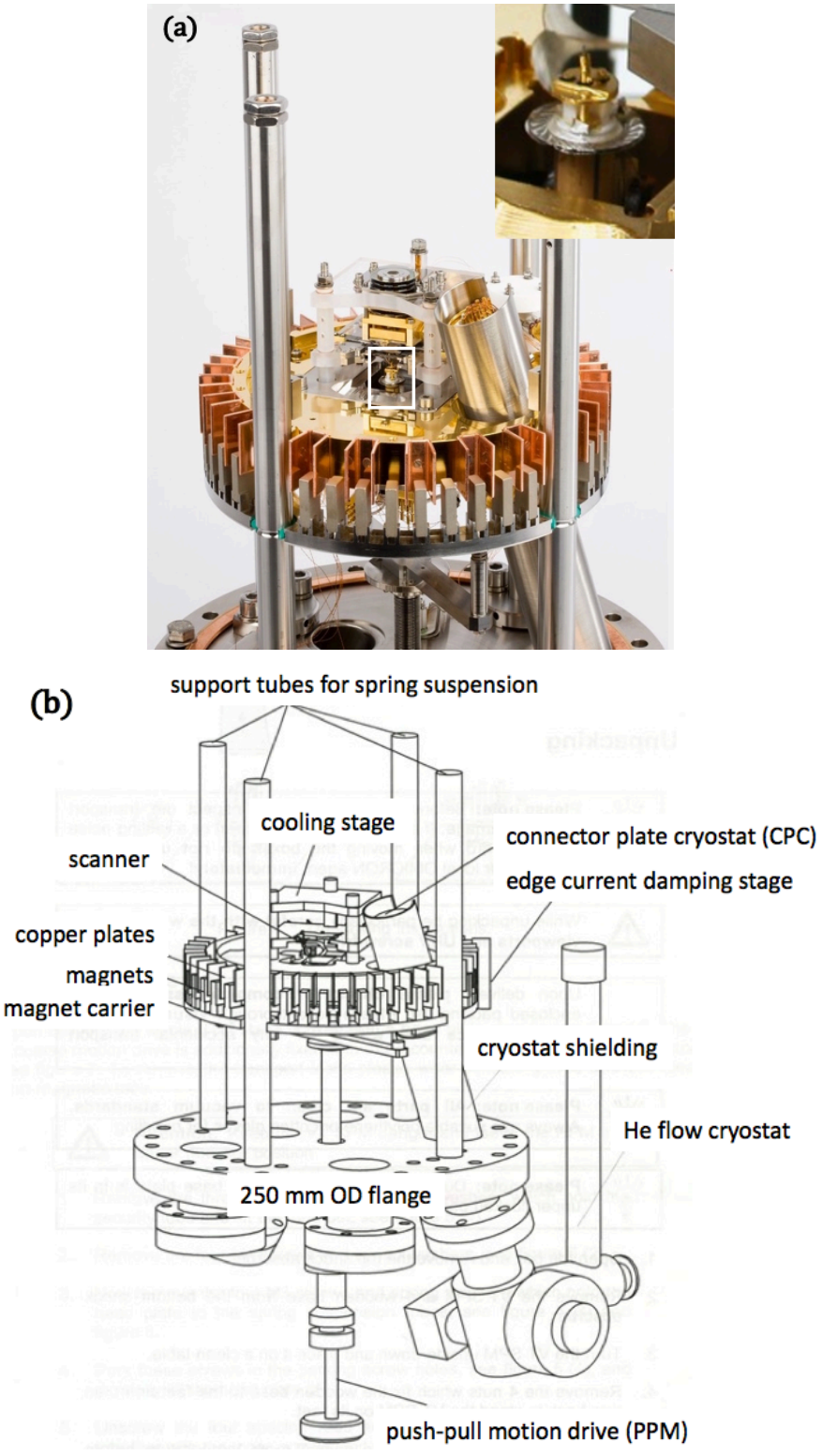


Fig. 3-2 (a) Product picture of a variable temperature scanning tunnelling microscopy (VT-STM) with the eddy current vibration isolation system. The area marked in the black box is magnified and shown in inset [1]. (b) Schematic of the eddy current vibration isolation system. The whole STM stage is mounted onto the main chamber with 250 mm OD flange. A push-pull motion drive under the base plate of STM is used for moving the STM up and down. A

helium flow cryostat is connected to a thermal exchanger running through the flange as well as the base stage. The cooling stage is set just over the sample stage supported by three ceramic bars, in which there is a rectangular copper bar called cooling block. A connector plate cryostat (CPC) is connected to the cooling block via a bunch of highly flexible copper braids. Liquid helium and nitrogen agents can pass through the cryostat to the cooling block. When the cooling block covers the sample, both the block and sample can be cooled down to low temperatures [1].

As demonstrated in Fig. 3-2 (b), before scanning, a cooling block should be moved using a high vacuum screwdriver to press tightly onto the sample holder. This cooling block hangs over the sample stage on STM, which connects to a connector plate cryostat (CPC) via highly flexible copper braids. These copper wires work as the terminal of the heat exchanger by letting the liquid nitrogen or helium agent transfer from external tanks to the cooling block and then reduce the temperature of both the cooling block and the sample. There is a push-pull motion drive (PPM) under the flange, supporting the whole STM stage. When the STM is working, PPM needs to be pulled down, making the stage entirely carried by four springs. After scanning, PPM needs to be pushed upward to park the STM stage. It makes a convenience of the sample transfer and avoids some accidental damage [1].

3.2 Heating and Cooling System

Our VT-STM can change the sample's temperature from 25 K to 1500 K with its heating and cooling systems. Fig. 3-3 (a) shows a specific sample holder used in the VT STM. Its two sides are mounted two molybdenum contact brushes, which touch the contact brushes on the STM stage and allow current to pass through the sample. During the process of scanning, tip approaches from the bottom gradually up to sample surface.

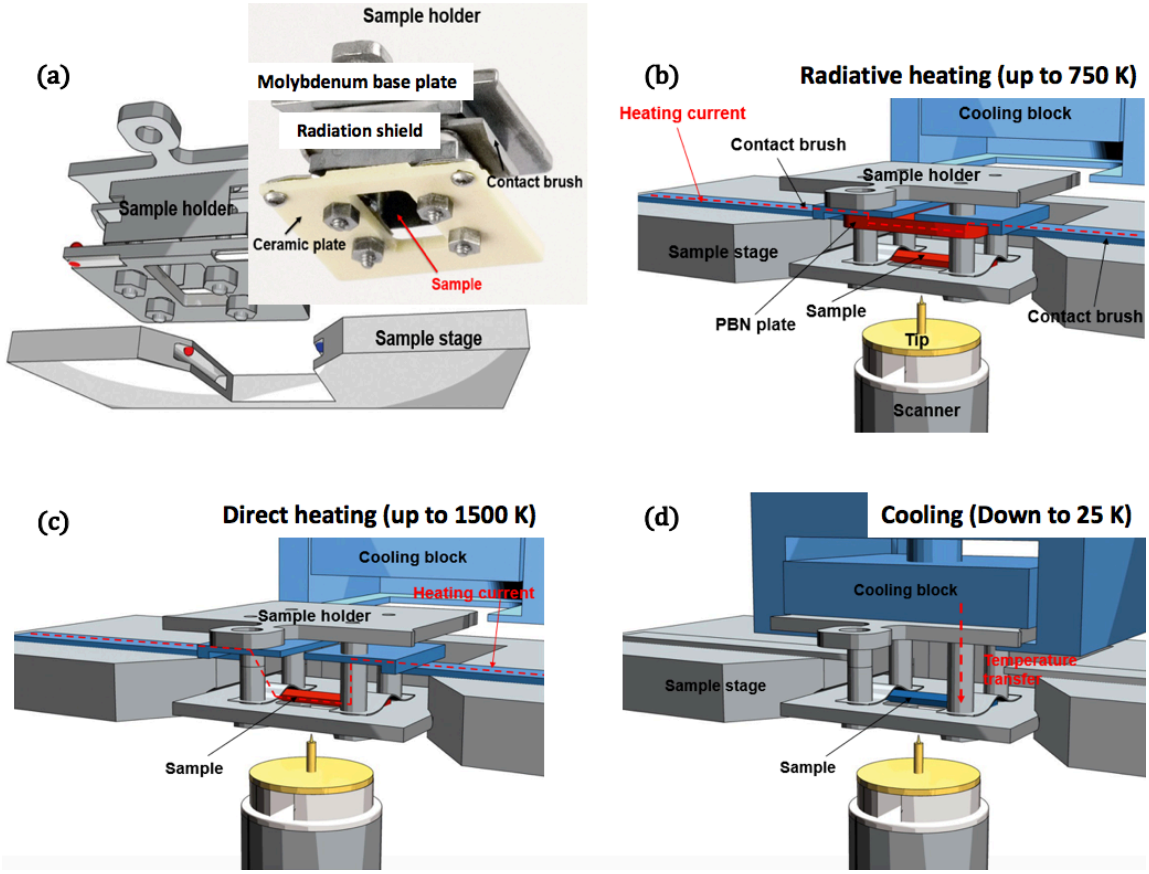


Fig. 3-3 (a) A sample holder is mounted on the sample stage. It is made from a molybdenum plate, a radiative heating shield and a yellow colour ceramic plate working for fixing sample. A pyrolytic boron nitride (PBN) is set inside the radiative heating shield (from [1]). (b) Nonconductive sample can be heated by radiative annealing. The heating current passes through the contact brushes to the pyrolytic boron nitride (PBN) heater inside the sample holder to heat the sample below. During the heating process, the cooling block needs to be away from the top of the sample holder [1]. (c) In the direct annealing setup, the current passes through the sample directly. It requires the sample to be conductive [1]. (d) In the cooling setup, a cooling block is placed on the sample holder to cool down the sample [1].

The inset image in Fig. 3-3 (a) shows the sample plate made for radiative heating to variable temperatures. It includes an additional ceramic plate mainly working as a fixation for testing samples during scanning. Only one side of the ceramic plate is coated with metal to prevent itself from being charged up. It allows this sample holder to be used in applications such as electron spectroscopy. Inside the

metal groove-like radiation shield, there is a small PBN plate which is set just under the sample. Contact brushes fixed on the sample holder, and the STM stage are made of the same materials to prevent local overheating.

3.2.1 Radiative Heating and Direct Current Heating

Omicron VT-STM has two different types of heating systems. One is radiative heating, and the other is direct current heating. Radiative heating mainly relies on the PBN plate integrated inside the metal shield. When a sample is put onto the sample stage, contact brushes on the sample holder and stage touch tightly, which forms a strong closed loop circuit between the sample and the heater. Current passes through and warming PBN as well as the sample above. Under this mode, the temperature of the sample can be increased up to 750 K. Direct current heating mode is appropriate for samples having sufficient electrical conductivity. Samples can be heated up to 1500 K in this mode. The two modes of heating are demonstrated in Fig. 3-3 (b) and (c), respectively.

3.2.2 Sample Cooling

There are lots of advantages of scanning a sample at cryogenic temperatures. Certain molecules can only be imaged at low temperatures because they have low desorption temperatures. Low temperature can also suppress thermal diffusion and lead to more stable images [1].

The sample cooling system works based on a clamping mechanism and is shown in Fig. 3-3 (d). A cooling stage is supported by four spacers over the sample, on which a cooling block is fixed. When the cooling system starts working, this block is pushed down to contact the sample tightly. The cooling block is used to conduct heat away from the sample. Liquid nitrogen or helium is chosen commonly as a cooling agent, which flows through flow cryostat tube, CPC and

finally the cooling block. The sample can be cooled down to 110 K by using liquid nitrogen. A much lower temperature of 25 K can be achieved if liquid helium is used.

3.3 ISE 5 Ion Gun

In UHV, ISE 5 ion gun is used to sputter and clean the sample, where ions of argon are commonly chosen to sputter the sample surface [1]. One ISE 5 ion gun has an optimum working pressure between 5×10^{-6} mbar and 8×10^{-5} mbar. At the working pressure, it can offer beam energy ranging from 250 eV to 5 keV and the maximum discharge current of 1 mA. External view, interior view and operation principle of an ISE 5 ion gun are shown in Fig. 3-4 (a), (b) and (c) respectively.

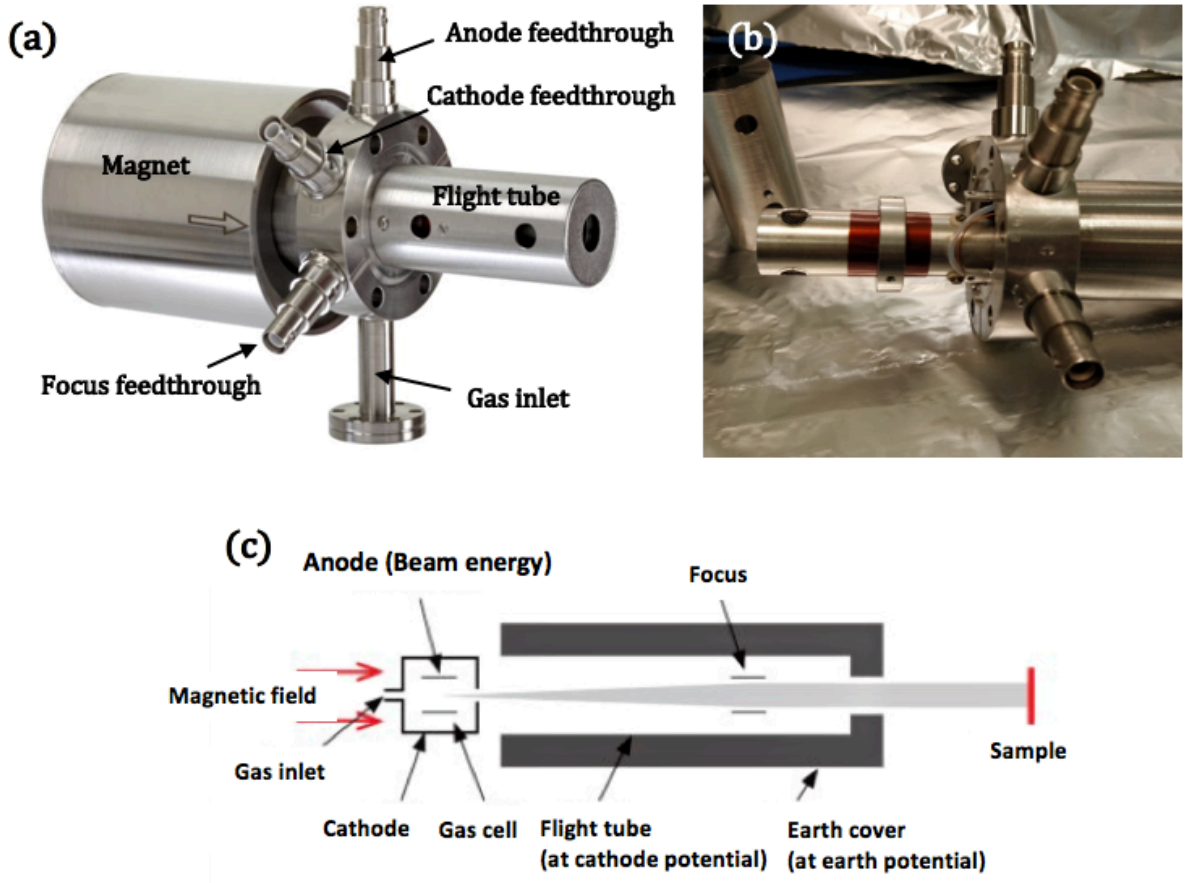


Fig. 3-4 (a) External view of an ISE 5 cold cathode sputter ion gun. It demonstrates the main components including a permanent magnet covering gas cell, feedthrough of the high voltage anode, cathode and beam focus and a gas inlet. (b) Interior structure of the ion gun. Argon gas flows through the white tube inside the earth cover and get into the gas cell. (c) Diagram showing the operation principle of the cold cathode source ion gun. The ion flight tube is at cathode potential while the earth cover outside is at earth potential [2].

Both external and interior view of an ISE 5 sputtering ion gun is shown in Fig. 3-4 (a) and (b), in which a magnet covers the gas cell. The ion flight tube is at cathode potential while the earth cover outside is at earth potential. Argon gas is let into the ion gun via a leaking valve. Then the discharge applied between the cathode and anode makes the noble atoms ionized and confined in the gas cell. The magnet covering the cell offers magnetic field and The size of the ion beam can be controlled and limited by a pair of focus plates [2].

3.4 Tip Preparation

3.4.1 Electrochemical Etching

Quality of the STM tip directly decides whether high-resolution STM images can be achieved. The ideal tip commonly has only one or few atoms at its terminal. The tip is made by electrochemical etching of tungsten wire with a diameter of 0.4 mm and 99.9 % purity. It is made by electrochemical corrosion using 2 M NaOH solution. For making a solution with this concentration, we dissolve 40 g NaOH pellets into the 500 ml distilled water with slow stirring.

Fig. 3-5 (a) and (b) shows a tip etching mount and its basic schematic diagram. A circumscribed electronic control is connected to the etching system, providing and controlling the etching voltage and threshold current. A piece of clean tungsten wire with its one side bent as a circle is put into the solution and the

other side connected to the cathode power supply. Then, another piece of tungsten wire with a length of around 3 cm to 4 cm is cleaned in distilled water several times before being inserted into the tip holder and trapped using clamps on the etching stage. Tip and tip holder are connected to the anode of the power supply. Before etching, we have to make sure the tungsten wire is located over the solution surface and points directly to the platinum ring's centre. Its vertical position can be adjusted by using the handwheel on top of the etching stage.

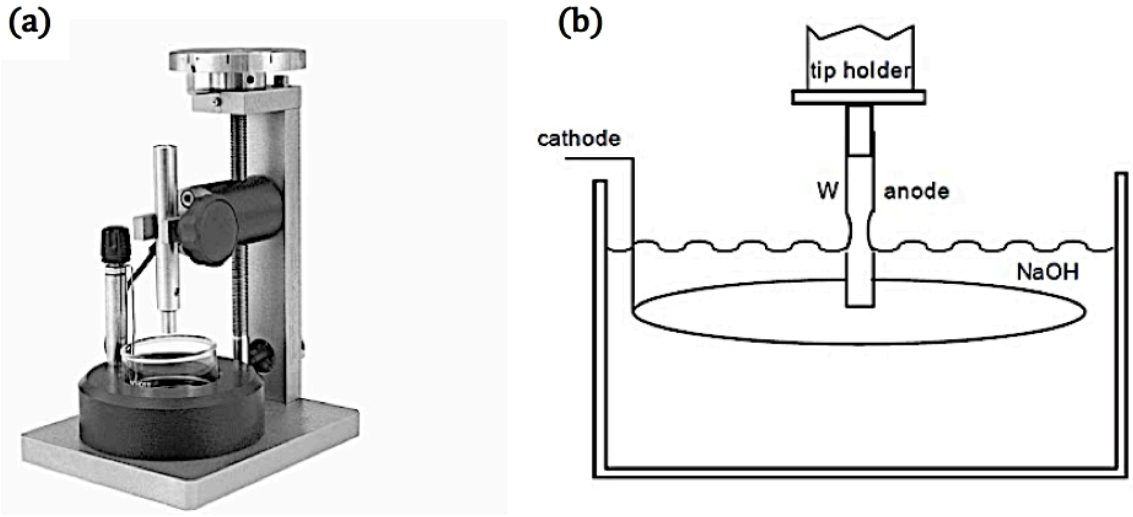


Fig. 3-5 (a) Tip etching mount with adjustable height, etching voltage and threshold current setting [2]. (b) Schematic diagram showing tip etching in a solution of sodium hydroxide. Tungsten fixed on the tip holder is connected to the anode of power supply, and a platinum wire connecting cathode power supply is inserted into solution with its terminal bent as a circle [3].

When the etching process starts, tungsten is immersed into the solution gradually by rotating the handwheel, leaving 2 mm to 3 mm distance between the solution surface and the tip holder. Then, 10 V is applied directly onto the tungsten wire to start chemical etching. The reaction at the anode can be written as:

$$W(s) + 8OH^- \rightarrow {WO_4}^{2-} + 4H_2O + 6e^-$$

During the process, tungsten reacts with OH^- and creates $WO_4{}^{2-}$. Solution surface forms a meniscus at the interface between the wire and the solution. It makes a gradient of OH^- concentrated at this place. Therefore, when etching finishes, the terminal of tungsten wire remaining on the tip holder is sharp with a quasi-circular cone shape. At the cathode, there are H_2 bubbles appearing. The chemical reaction can be written as:

$$6H_2O + 6e^- \rightarrow 3H_{2(g)} + 6OH^-$$

The overall reaction process of tip etching is thus written as:

$$W_{(s)} + 2OH^- + 2H_2O \rightarrow WO_4{}^{2-} + 3H_{2(g)}$$

After the first etching, the power supply needs to be switched off immediately [3,4]. The tip is taken out of the solution and cleaned with distilled water again. The new tip are commonly checked with an optical microscope before being put in the UHV chamber. The tip with a very long terminal results in strong vibrations during scanning. However, when the tip is too short, its terminal would be thick. It leads to a low resolution of the scanning images. In most cases, for achieving a tip with perfect shapes, twice or more times of etching is required. Apart from STM, this device can also be used to make tips for other applications, such as Field Ion Microscopy (FIM) and Field Emission Microscopy (FEM) [3-5].

3.4.2 Tip Insert and Heating

Before scanning, the newly etched tip needs to be heated to over 1073 K for over 1 hour inside an ultrahigh vacuum chamber for removing all the metal oxide, water and NaOH solvent on the tip. These attachments reduce the quality of scanning images as it reduces the stability of the tunnelling current between the tip and the sample. After heat treatment, the tip can be inserted in a tip holder and transferred onto the scanner tube of the STM.

The etched tip is inserted into the chamber and transferred onto the STM stage using a wobble stick. Diagram of a scanning system is shown in Fig. 3-6 (a), in which tip is fixed onto the top of the STM scanning tube with the help of a permanent magnet. Therefore, controlled by the sensors, tungsten tip fixed in the holder can move in x, y, z directions by the scanner tube. The tip holder is magnetically coupled to the scanner tube, making it easy for changing the tip. A round shape radiation shield separates the magnet and scanner tube, aiming at protecting the piezo scanner from being heated radiatively during sample heating.

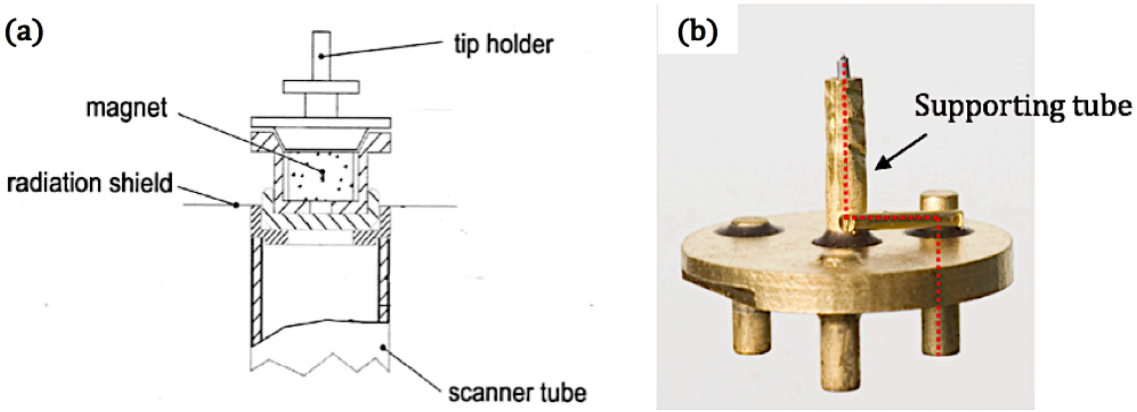


Fig. 3-6 (a) Schematic diagram showing the components of an STM scanner. Tip holder holding a tungsten tip is attracted using a magnet, which is placed on the top of a piezoelectric ceramics scanner tube. A radiation shield is used to protect the scanner tube from being heated during the process of sample annealing (from [1]). (b) Side view of a molybdenum tip holder used in the VT STM. The supporting tube is placed on a large plate working for loading STM tips. The three short bars with magnets inside are stick under the plate, which can be attracted by the large magnet on the scanner tube. One of the three bars is connected to the supporting tube using a short metal bar on the plate, which enables the current detected by the STM scanner [1,3-5].

In Fig. 3-6 (b), an etched tungsten tip is fixed on top of a tip holder, which is made from molybdenum. The tube used for holding the tip (supporting tube) is long and settled on the middle of a round holding plate. Three short bars hold the plate up, and one of them is connected to the supporting tube. It allows the

tunnelling current created between the sample and the tip to be detected and amplified. In each of the three metal bars, there is a piece of permanent magnet. When a tip holder is placed on the magnet shown in Fig. 3-6 (a), it can be attracted tightly and moves with the scanner tube.

For the VT STM, the tip moves near the sample surface with a coarse approaching. The coarse motion device set under the scanner tube has a maximum moving distance of $12\ \mu m \times 12\ \mu m$, in the *x*-*y* plane and $\sim 1.5 \mu m$ in the *z* direction respectively. In the *z*-direction, the motion device has a resolution of better than 0.01 nm, which protects the tip's terminal from crashing on the sample surface. After the coarse approaching, the tip-sample distance is reduced to tens of nanometers. During scanning, the tip is driven by four pieces of piezo electrode on the outer shields of the scanning tube and can travel as far as 10 nm in x, y and z directions. The calibrated resolution of the tip is 0.1 Å [1].

3.5 Source Evaporator of Fullerene

Fig. 3-7 (a) and (b) demonstrates two homemade Knudsen cells (K-cell) containing respectively C_{60} and C_{70} powders. The K-cell is made from tantalum foil of 99.9 % purity. A pair of metal electrodes sitting on the two sides of cells provide direct current heating of the cell. We open a small hole on one side and allow molecules to come out after being heated. The temperature of the cells is measured using thermocouples.

K-cells need to be preheated to $\sim$ 500 K for a short time to remove impurities inside. Then the K-cell is slowly heated to 630 K and the molecules inside are evaporated with a stable flux. At this temperature, C_{60} and C_{70} molecules sublimate directly from solid crystal to molecular gas. By counting evaporation time, the total amount of molecules deposited can be controlled precisely.

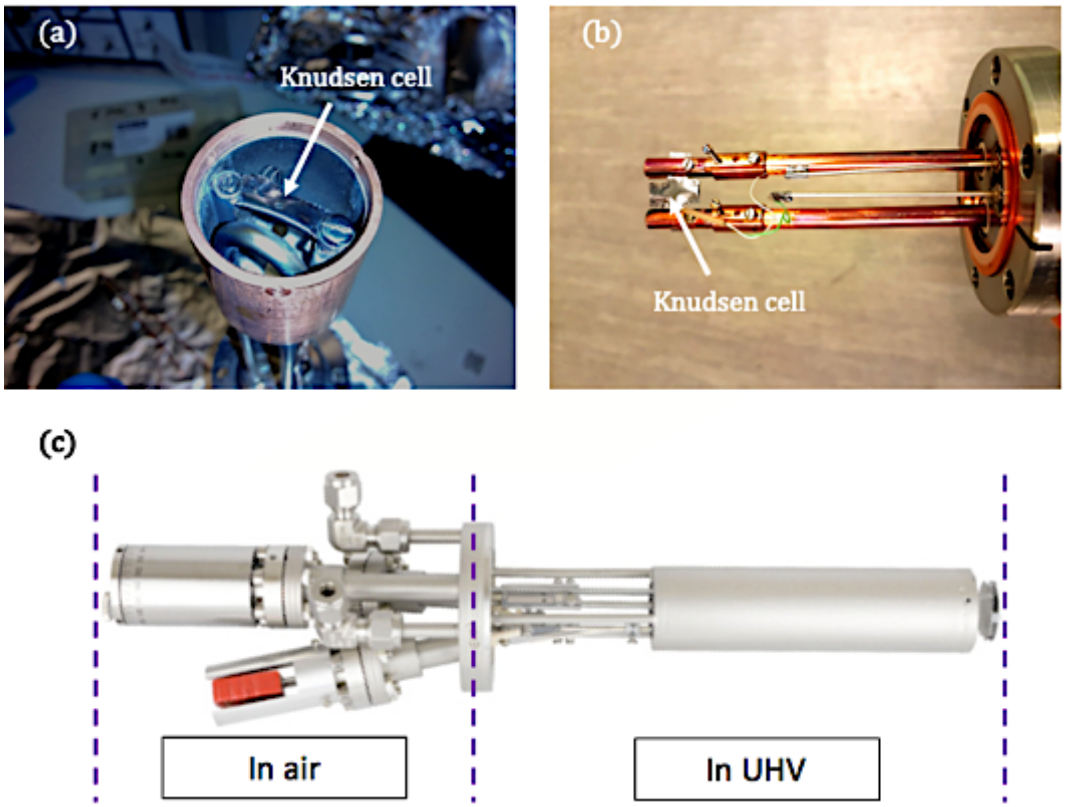


Fig. 3-7 (a) A thermal evaporator is protected by a ceramic cylinder. A flat Knudsen cell (K-cell) made of tantalum foil is fixed on top of the electrodes. It contains pure C_{60} powders inside. There is a small hole in the middle of the cell, which enables C_{60} gas to be evaporated out. The feedthrough of thermocouple attaches the bottom of the cell for measuring temperature. (b) A Knudsen cell containing pure C_{70} powders is trapped by a pair of copper bars working as electrodes. A small leaking hole is opened on the left side of the cell shown in the image. (c) Setup of the high-temperature cell (HTC). It works for evaporating gold atoms in ultrahigh vacuum (UHV) at temperatures up to 2273 K. An Al_2O_3 crucible is used for evaporating metals such as cobalt and gold [6].

For in-situ evaporating gold atoms, a piece of gold wire needs to be cut and put into an effusion cell containing a Al_2O_3 crucible. The gold wire used in our system is of 99.9% purity. As shown in Fig. 3-7 (c), a conventional High-temperature Cell (HTC) working for depositing metals at low vapour pressure such as gold are divided as a UHV section and an air section. The UHV section of the evaporator is protected by a cylinder made from tantalum and tungsten, in which an Al_2O_3 crucible with gold wires is placed. A mechanical shutter is used to open

and close the atomic beam [6]. For removing impurities, the gold wires inside crucible are degassed at 873 K for over 10 minutes before deposition. Then we move the shutter away and let gold atoms evaporated out. The shutter is closed once the evaporation is finished.

3.6 Sample Preparation and Cleaning

The three most common methods for cleaning the substrate in my experiments are cleavage, thermal heating, and ion sputtering. The method of cleavage is suitable for cleaning the samples which grow layer by layer and has weak interactions between the adjacent layers. When the materials such as HOPG and MoS_2 are taped with scotch tapes continually, most impurities adsorbed on their surface could be removed. However, with this method, it is difficult for the sample surface to be touched by the tape evenly. Therefore, some residual debris of the layers removed is possible to remain and result in surface fluctuation.

The Au(111) substrate used in my experiments are created by depositing gold atoms on HOPG with the technique of physics vapour deposition (PVD). HOPG used for supporting gold films is firstly cleaned by cleaving several layers away before being transferred into an ultrahigh vacuum chamber. An evaporating boat holding gold wires are placed just under HOPG. The temperature of the molybdenum boat is raised to 1273 K gradually, which melts gold wire and evaporation starts [1]. The thickness and the depositing rate of gold are measured using an inserted quartz crystal oscillator.

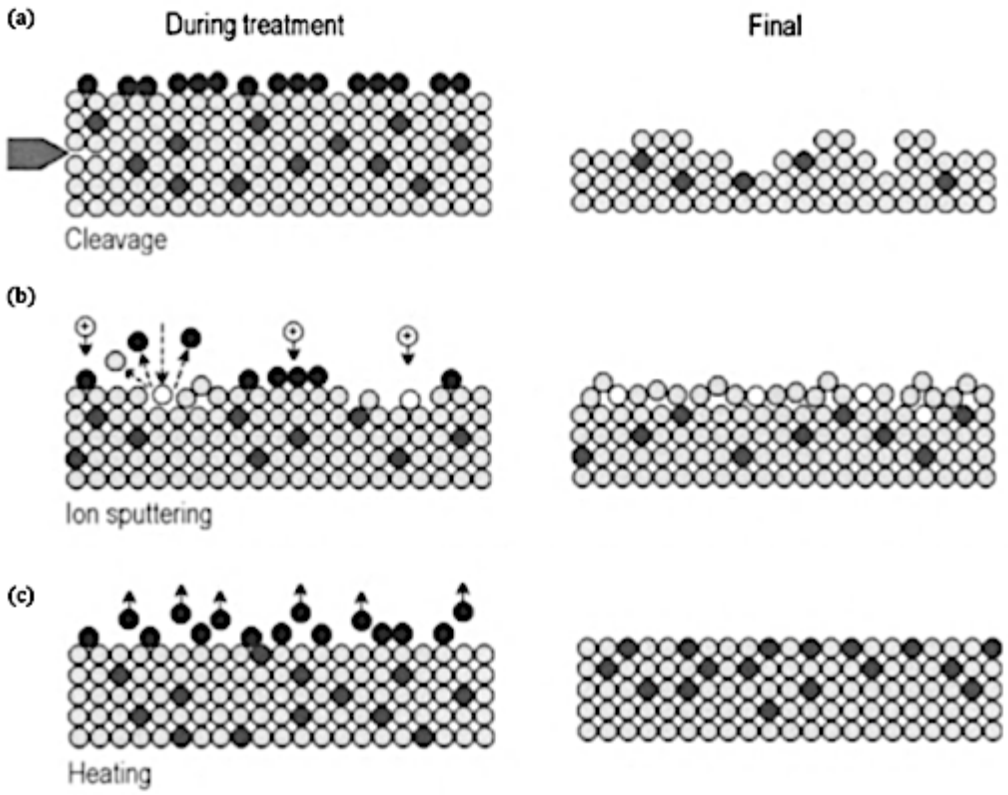


Fig. 3-8 Methods for cleaning substrate used in our research experiments. (a) Cleavage; (b) Ion sputtering; (c) thermal annealing. Light colour spheres are the atoms of sample material while the dark colour ones denote the foreign species mixed in the bulk of sample or adsorbed onto the material surface [7].

The Au(111) surface in UHV can be cleaned with the methods of ion sputtering. As shown in Fig. 3-8 (b), Argon gas is ionized and has high energy inside an ion gun, which hit Au(111) surface with a strong force. During the process, most of the adsorbed impurities, metal oxide and a few layers gold can be removed. After ion sputtering, the gold surface is partly damaged. The sample needs to be heated at 873 K in order to remove the remaining impurities from the surface. Meanwhile, high temperature annealing accelerates the diffusing of the surface atoms, which contributes to the self-healing and smoothing of the sample surface.

References

[1] Omicron's product introduction (Electronics Technical Reference Manual).

[2] Omicron's product introduction (Ion Sources Manual).

[3] C. J. Chen. Introduction to Scanning Tunneling Microscopy. Second Edition, Oxford University Press, Oxford 315 (2008).

[4] C. Weiss, C. Wagner, C. Kleimann, M. Rohlfing, F. S. Tautz, and R. Temirov. Imaging Puali Repulsion in Scanning Tunneling Microscopy. Phys. Rev. Lett. **105**, 086103 (2010).

[5] J. I. MartÍnez, E. Abad, C. González, F. Flores, and J. Ortega. Improvement of Scanning Tunneling Microscopy Resolution with H?Sensitized Tips. Phys. Rev. Lett. **108**, 246102 (2012).

[2] Createc's product introduction (High-Temperature Cell Manual).

[7] K. Oura, V. G. Lifshits, A. A. Saranin, A. V. Zotov and M. Katayama, Surface Science: An Introduction (Springer, Berlin, 2003).

4. Nucleation and Growth of Close-packed C_{70} Molecules on Au(111)

4.1 Introduction

In this chapter, I mainly investigate the nucleation and growth of pure C_{70} on Au(111) in UHV environment. At extreme low coverages, most of the deposited C_{70} molecules pack along the step edges and form narrow single layer islands on the lower terrace. With increasing coverage, C_{70} molecules can grow onto both the upper and lower terraces on both sides of the step edge. When the coverage approaches one monolayer, adsorbed molecules can form large size close-packed domains with a uniform lattice constant of ~ 1.05 nm. The second layer C_{70} islands occur before the gold substrate is fully covered by the first layer. The formation of the second layer does not need step edges.

Then one close-packed monolayer of C_{70} is formed on the clean gold substrate. After being annealed at 673 K for one hour, the close-packed C_{70} domains have R30° structure. By depositing extra C_{70} molecules onto the pre-formed C_{70} monolayer, the isolated second layer islands are formed. On either the R30° phase or R0° phase, these islands show similar sizes, shapes and surface patterns. After being annealed from 423 K to 473 K, molecules are able to jump upward from lower layers and form multilayer islands. When annealing the sample to over 473 K, most of the C_{70} in the upper layers desorb.

4.2 Experimental Procedure

In the first experiment, 0.3 ML, 0.5 ML and 0.8 ML of C_{70} molecules were deposited on Au(111) at room temperature in the UHV chamber. In the second experiment, we first deposited 1.2 ML C_{70} and anneal the sample to 673 K for one hour to create one compact C_{70} monolayer on the gold substrate. An extra

0.65 ML of C_{70} molecules were deposited on top of the monolayer after the sample was cooled to room temperature. The sample was then annealed at 423 K, 473 K, and 523 K respectively for one hour and then scanned by STM in order to study the temperature dependence of the molecular layers.

4.3 Growth of C_{70} with Different Coverages on Au(111)

Fig. 4-1 shows one STM image of the Au(111) sample with 0.3 ML of C_{70} molecules. Long and narrow single layer islands attach to the lower terrace with the step edge as the nucleation site. C_{70} molecules in the image appear as bright spheres and are 0.7 nm above the gold substrate, which is slightly shorter than its real physical size as measured previously [1-3]. Difference of the charge transfer between gold and C_{70} is probably the main reason leading to a reduced apparent height of the molecules.

As marked in the white rectangle of Fig. 4-1 (a), there are two small C_{70} islands sitting on both the upper and lower terraces of the gold step edges, respectively. The gold step edge is contoured by the black dashed lines. C_{70} molecules in the two islands have the same packing structure, which is due to the consistent stacking way of gold atoms on the two sides of the step [4,5].

When 0.5 ML C_{70} molecules are deposited on Au(111), molecular islands sitting on both the upper and lower terraces of the step edges merge as larger ones, as shown in Fig. 4-1 (b). The islands keep capturing and losing the freely diffusing molecules at room temperature. Some isolated molecules are also observed close to island edges, indicating that the island edges keep losing and capturing molecules at room temperature. In addition, the C_{70} molecules can also modify the gold substrate underneath.

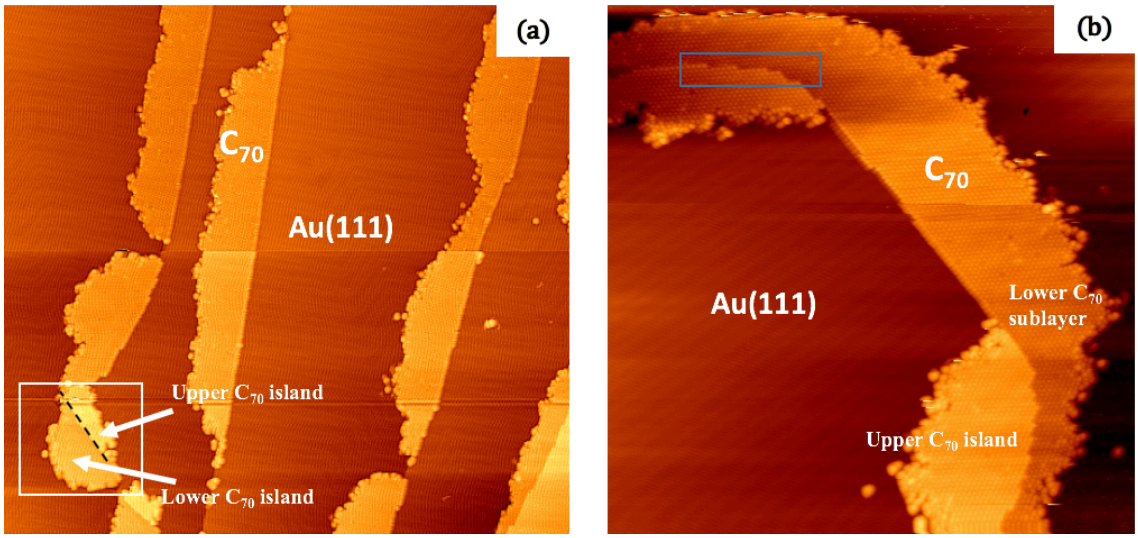


Fig. 4-1 (a) STM image showing 0.3 ML C_{70} molecules deposited on the Au(111) surface at room temperature (255 nm × 255 nm, -2.5 V, 50 pA). C_{70} molecules aggregate to long and narrow single layer islands and attach to gold step edges. (b) STM image showing 0.5 ML C_{70} molecules deposited on the Au(111) surface at room temperature (255 nm × 255 nm, -2.5 V, 50 pA). C_{70} molecules attach to gold steps and form islands on both the upper and lower terraces. The gold step edge marked in the blue rectangle has a zigzag shape due to the modification of C_{70} molecules.

As shown in the blue rectangle in Fig. 4-1 (b), the C_{70} molecules sitting in the vicinity of the step edges tend to keep their packing directions the same as in the islands. The gold steps are thus affected by the molecules and grow in a zigzag form. As introduced in the first chapter, close-packed C_{60} can lift the DLs on the Au(111) surface and drive gold atoms below to form the perfect (1×1) structure [6]. However, the DLs remain unchanged under a single layer of C_{70} fullerene, shown in Fig. 4-2, which suggests a rather weak C_{70}-gold interaction.

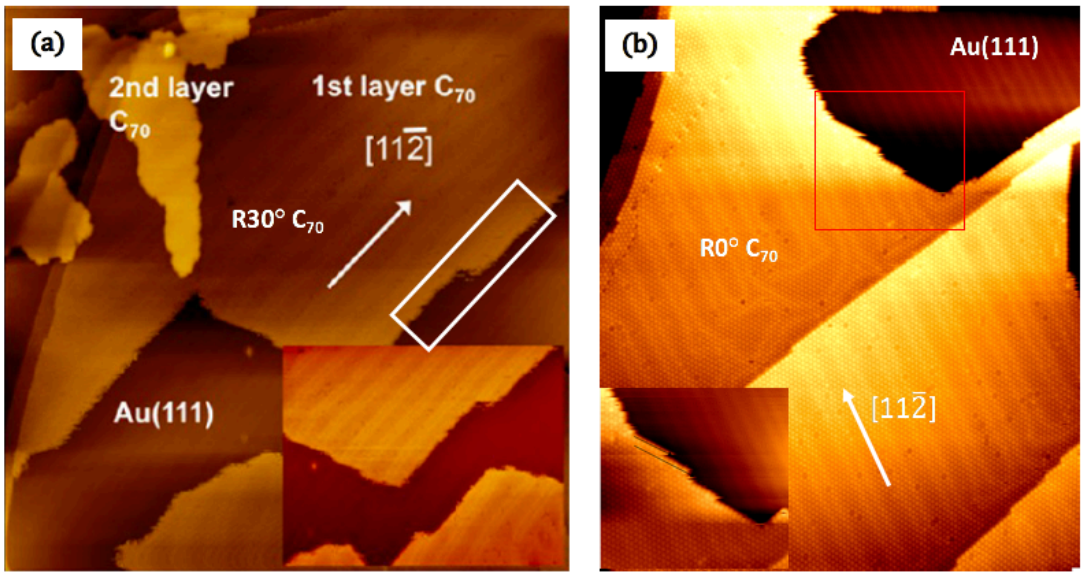


Fig. 4-2 (a) STM image (200 nm × 200 nm, −2.5 V, 80 pA) showing Au(111) covered with 0.8 ML of C_{70} at room temperature, which form R30° C_{70} large domains. One of the C_{70} molecules' close-packing directions is parallel to the discommensuration lines (DLs). The second layer islands appear before the completion of the first layer. One area of the image is treated with contrast enhancement and shown in the insert. (b) 0.8 ML deposited C_{70} forming only R0° C_{70} domains. Inset shows a magnified view of the edges of the R0° C_{70} islands, which is marked in the red rectangle. Neither C_{70} monolayers with R0° or R30° phases on Au(111) lift the herringbone reconstruction underneath.

With the coverage of 0.8 ML, C_{70} molecules aggregate to large close-packed islands and cover most of the Au(111) surface, as shown in Fig. 4-2 (a). There are several C_{70} molecules appearing darker in the molecular islands, which could be attributed to the change of the gold-molecule interface. In the upper left of the image, there are a few patches of second layer C_{70}. The second layer is ~ 0.8 nm taller than the first layer. Edges of the first layer C_{70} are found not as sharp as the second layers. It is due to the freely movement of gold atoms around the islands' edges. Edges of the first layer islands are continually changing by capturing or losing molecules, and there is expected a low concentration of free moving molecules in the vicinity of the edges. For the second layer island, little activity is observed at the edges of the island, indicating a much higher diffusion barrier.

One fraction of Fig. 4-2 (a) is treated with contrast enhancement and demonstrated in the inset. It can be seen that C_{70} molecules are close-packed in with the direction parallel to the reconstruction lines on gold surface. Therefore, the molecules' close-packing direction makes a 30° angle to the close-packing direction of Au atoms. This C_{70} structure is called R30° phase. Fig. 4-3 (b) shows another area of Au(111) covered by close-packed C_{70} monolayer which is called R0° phase. Different from (a), islands with this structure have sharp zigzag edges, and the close-packing direction of C_{70} molecules is the same as that of Au atoms underneath. The inset of the image shows a magnified view of the islands' edge, where C_{70} molecules form several pieces of straight chains. Molecules in these chains also pack in the same direction as in the main body of islands. Thus, it can be concluded that, vapour deposited C_{70} on the Au(111) surface can form at least two types of phases with different azimuthal orientations, which is similar to C_{60}.

4.4 R0°, R30° and R14° Close-packed C_{70} Structures

The R0°, R30°, and R14° C_{70} phases can coexist on Au(111) and are separated by domain boundaries. The R0° C_{70} phase demonstrated in Fig. 4-3 (a) has its similarity to the R0° C_{60} phase having been introduced in the second chapter. Fig. 4-3 (a) also shows a high-resolution image of the R0° C_{70} phase, where all the C_{70} molecules are close-packed perpendicular to the direction of the DLs. However, compared with the R0° C_{60} phase, the nearest neighbour distance of C_{70} is measured as ~ 1.05 nm, which is 0.05 nm larger than that of the R0° C_{60} phase [6]. Also, the herringbone reconstruction remains unchanged after deposition of C_{70}. According to our observation, the R0° C_{70} phase appears most frequently at room temperature. It is mainly because the preferential attachment of C_{70} molecule to the close-packed Au steps during the initial phase of the growth.

The R14° C_{70} phase is observed in the lower part of Fig. 4-3 (a), which is from the R0° phase by a sharp and irregular boundary. In this structure, the close-packing direction of C_{70} is 13.9° rotated from the close-packing direction of gold atoms. It was observed by Guo *et al*. in 2004 after the confirmation of the R14° C_{60} phase by Sakurai and by Zhang *et al*. [6-9]. Due to the technique limitation, it is difficult to judge if a unit cell of the R14° C_{70} phase also includes the same (7×7) superlattice as the R14° C_{60} phase [10].

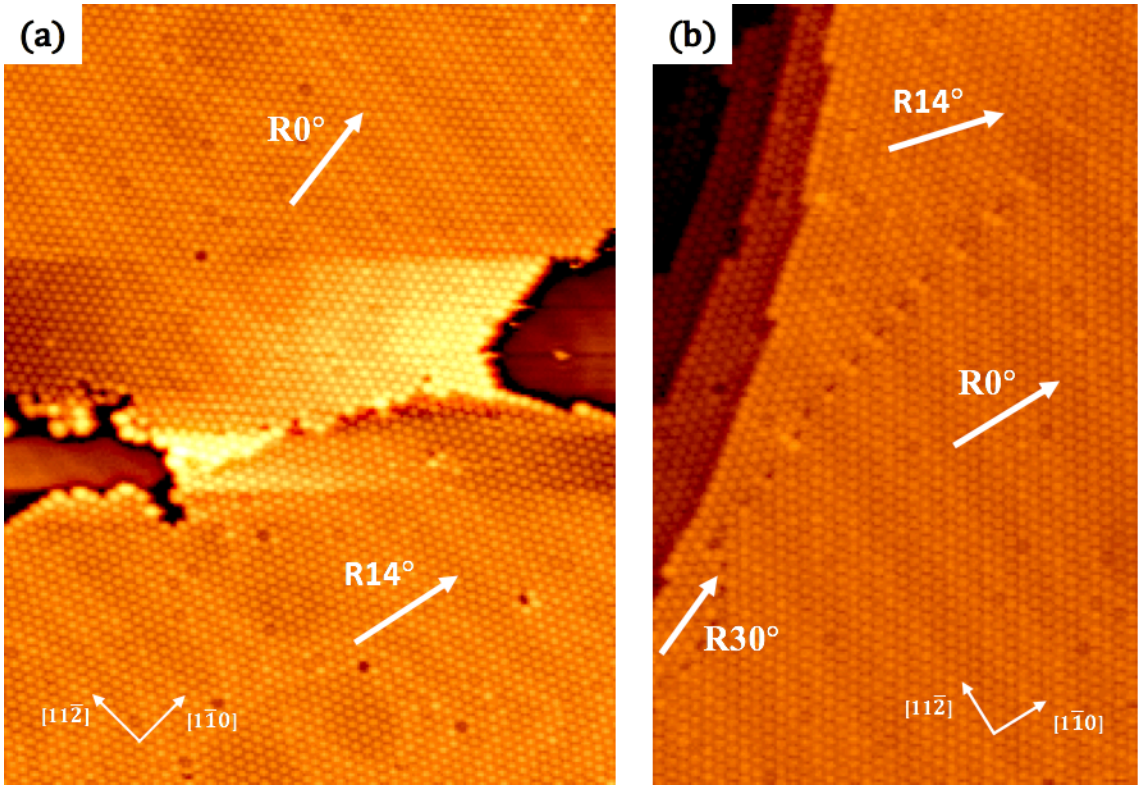


Fig. 4-3 (a) STM images of the R0°, and 14° C_{70} packing phases. There is an irregular sharp boundary separating the two types of domains. (b) STM image of one domain boundary growing from the bottom-left part to the top-right part of the image, which separates the R0°, R30°, and R14° C_{70} phases. The white arrows in the two images show the close-packing directions of C_{70} molecules (40 nm × 65 nm, -2.5 V, 100 pA).

In Fig. 4-3 (b), the majority of the gold substrate is covered by the R0° C_{70} domain. A narrow C_{70} domain with the R30° structure can be seen in the image. As described earlier, in the $(2\sqrt{3} \times 2\sqrt{3})$R30° C_{60} phase, all the molecules sit on

three-fold hollow sites, and the nearest neighbour distance of molecules is $\sim 2\sqrt{3}$ times the nearest neighbour distance of gold atoms in Au(111) [6]. However, the structure of the C_{70} domain here cannot be named $(2\sqrt{3} \times 2\sqrt{3})$R30°, because the substrate below remains its reconstructed form. From the bottom to the top of Fig. 4-3 (b), molecules' packing direction gradually rotates 16°. Thus an R14° C_{70} phase is formed on the top left side of the image, which does not form any obvious boundary with the R30° phase. However, the boundary between the R0° phase and R30° (R14°) phase can be observed clearly, which passes across the image and contains several uniform triangular gaps. It is due to the mismatch of the close-packing directions of molecules.

4.5 Changes of the Close-packed Fullerene Layer Due to Thermal Annealing

In this section, we examine how the C_{70} layer is affected by thermal annealing. Fig. 4-4 illustrates an STM image from (a) a C_{60} layer (R30°) and (b) a C_{70} layer (R30°). These two images are both acquired after thermally annealing the sample to 573 K for one hour. In the R30° C_{60} monolayer, some of the molecules appear 0.05 nm higher than others and form bright short-chain patterns. These brighter C_{60} molecules have weaker bonding with the gold below and are easier to be replaced by other incorporated molecules. The herringbone reconstruction is fully lifted.

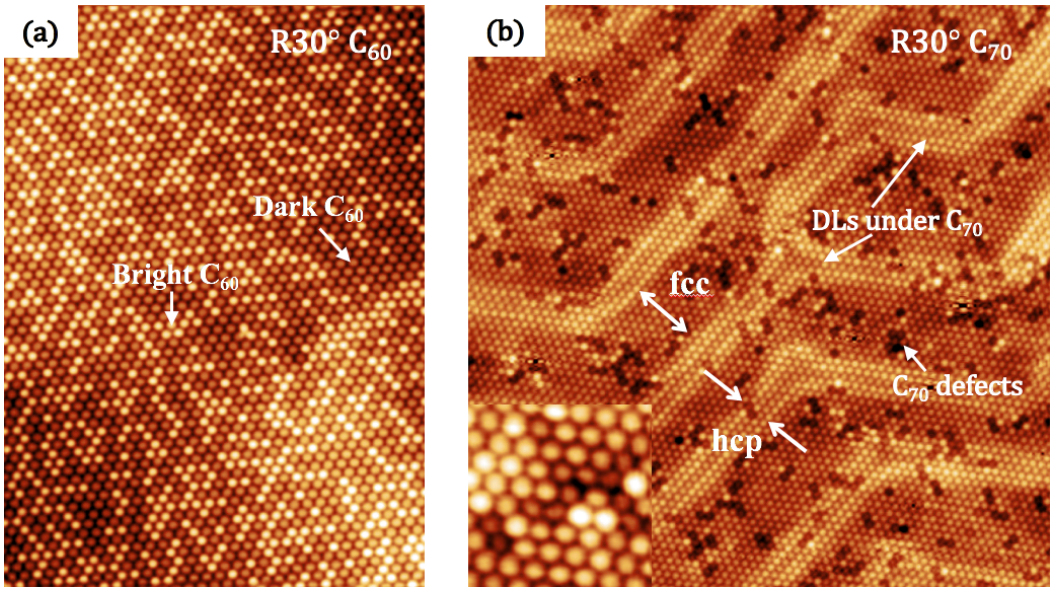


Fig. 4-4 (a) A compact layer of 30° C_{60} (33 nm × 45 nm, +2.5 V, 50 pA). (b) A compact layer of 30° C_{70}. Both C_{60} and C_{70} molecules are deposited on Au(111) at room temperature (75 nm × 75 nm, +2.5 V, 50 pA). Inset in (b) manifests the defects of 30° C_{70} result from some C_{70} molecules lying down and rotating. Most C_{70} molecules stand upright with their long axis perpendicular to the substrate surface.

R30° C_{70} monolayer shows a different morphology compared with R30° C_{60}. After sample annealing, the underlying gold substrate below the close-packed C_{70} molecules is still in its reconstructed form, and the width of HCP regions doesn't have obvious changes. However, compared with clean Au(111) surface, the average width of FCC regions have broadened and become 2.5 times of the original ones. It could be treated as an initial sign of lifting surface reconstruction. Compared with the sample surface before annealing, though most of the C_{70} molecules take an upright orientation, some others can still rotate or lie down on the gold surface with their long axis parallel to the sample surface, forming irregular shaped dim defects. Depths of these defects range from 0.05 nm to 0.15 nm. Inset in Fig. 4-4 (b) shows one group of these molecular defects with higher resolution. C_{70} molecules in these defects tilt or lie down with their long axis parallel to the gold surface. Under these molecules, there are probably various

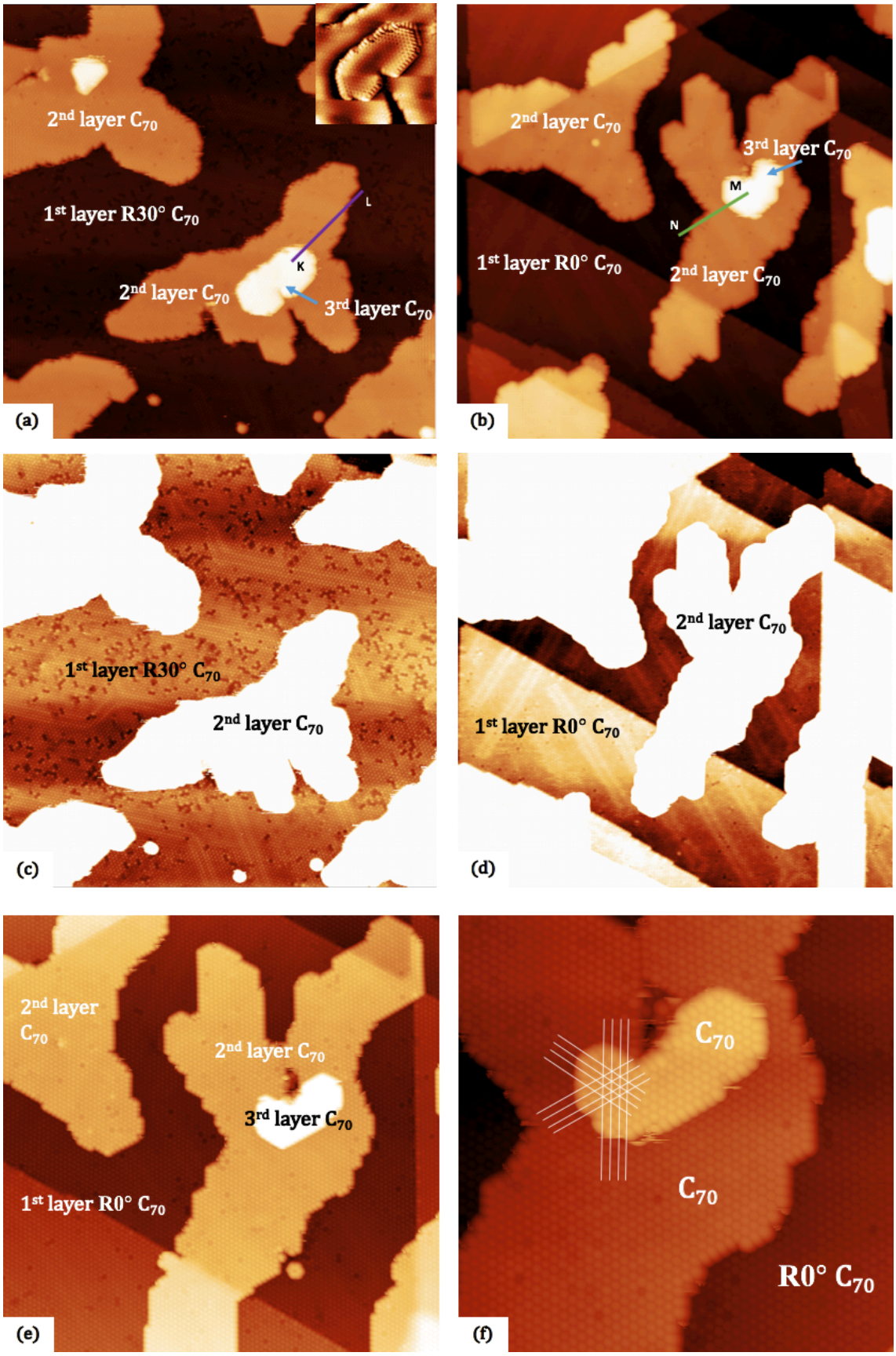
sizes of atomic defects in Au(111) substrate. These atomic defects are attributed to the interface strain.

4.6 Multi-layer C_{70} Islands

In this section, I study changes to C_{70} multilayers as a result of thermal annealing. In this work, 1 ML C_{70} was firstly deposited on top of the gold substrate at room temperature. Some areas show the R30° structure while some others show R0° structure. Then, 0.65 ML C_{70} was deposited on this full monolayer at room temperature. It leads to the growth of C_{70} multilayers: mainly two layers and three layers. The sample was then annealed progressively to 423 K, 473 K and 523 K, for one hour at each temperature. The STM images were obtained after each annealing step.

The first layer of C_{70} in Fig. 4-5 (a) has an R30° structure and the first layer of C_{70} in Fig. 4-5 (b) has the R0° structure. Each C_{70} molecule stands up with long axis perpendicular to the metal substrate, which is affected by both the van der Waals forces from adjacent molecules and the chemical interactions from the gold substrate below.

C_{70} in the second layer choose to grow as isolated islands. The molecular defects with different depths only exist in the first layer, while all the molecules in the second and third layers pack densely and appear as the same brightness. Therefore, in the first layer C_{70}, the defects cause a switch from freely orientating to uniform upright standing. The third layer forms well before the completion of the second layer. It shows that C_{70} on Au(111) does not take a layer-by-layer growth mode.


2nd layer C70
1st layer R30° C70
L
K
2nd layer C70
3rd layer C70
(a)
2nd layer C70
3rd layer C70
M
N
1st layer R0° C70
2nd layer C70
(b)
1st layer R30° C70
2nd layer C70
(c)
2nd layer C70
1st layer R0° C70
(d)
2nd layer C70
2nd layer C70
3rd layer C70
1st layer R0° C70
(e)
C70
C70
R0° C70
(f)

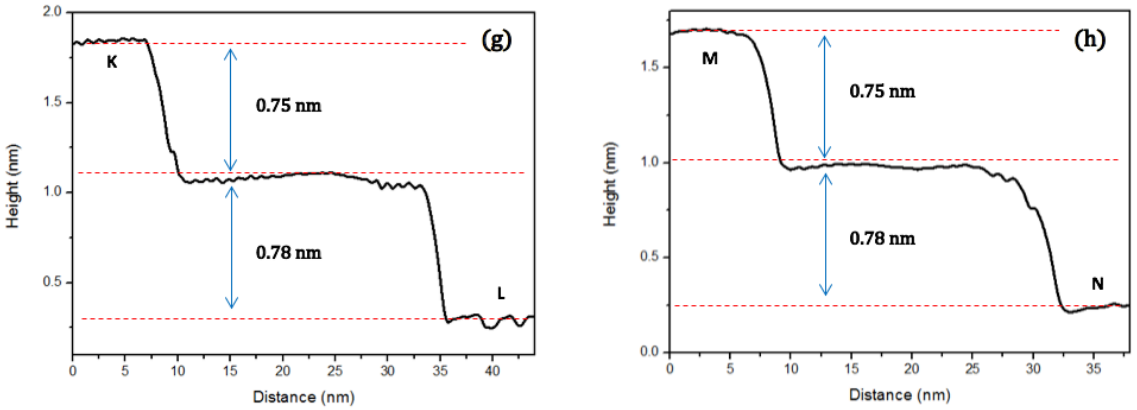


Fig. 4-5 0.65 ML C_{70} deposited onto one C_{70} monolayer on Au(111). Sitting on the first layer with (a) the R30° and (b) the R0° structures, the second and the third layers of C_{70} show similar shapes and sizes. Molecules in the two layers form close-packed structures with single dim defects. Both (a) and (b) are scanned under the same bias voltage and tunnelling current (150 nm × 150 nm, -2.5 V, 100 pA). Inset in (a) shows the close-packed molecules in the third layer with a higher resolution. (c) and (d) show the first layer of C_{70} in (a) and (b) with colour contrast, respectively. (e) Magnified view showing one of the second layer islands sitting on the R0° C_{70} monolayer. A third layer island with quasi-hexagonal shape sits on top of the second layer (80 nm × 80 nm, -2.5 V, 100 pA). (f) A further enlarging of the third layer island shown in (c). Each molecule occupies a three-fold hollow site in the lower layer (40 nm × 40 nm, -2.5 V, 100 pA). (g) Line profiles demonstrating the second layer and the third layer of C_{70} deposited on the R30° C_{70} monolayer with the heights of 0.78 nm and 0.75 nm respectively. (h) Line profiles demonstrating the same heights of the second and the third layer C_{70} deposited on R0° C_{70} monolayer [11].

With increasing temperature, some C_{70} molecules in the second layer can overcome the potential barrier and jump upwards, leading to further growth of the third layer. The third layer C_{70} islands are mostly found in the middle of second layer islands, well away from the edges of the second layer islands. Fig. 4-5 (c) and (d) show the high resolution C_{70} first layer of (a) and (b) with high resolution. By comparing Fig. 4-5 (a) and (c), a large number of molecular defects are found forming irregular dim groups and existing in R30° C_{70} phase in the first layer. In the second layers, on the contrary, these dim groups are not found at all.

It indicates that the molecules under the second layer have been driven by the second layer molecules to stand upright and form close-packed R0° phases. When the adding C_{70} form multilayer islands on R0° C_{70} phase, as shown in Fig. 4-5 (b) and (d), they follow the clos-packing structure of the first layer and also form R0° phase. Line profiles shown in Fig. 4-5 (g) and (h) indicates that, the second, third layer C_{70} sitting on the first layer are measured with ~ 0.75 nm and ~ 0.78 nm, which are very similar and not affected by the packing structure of the first layer.

As demonstrated in Fig. 4-5 (e) and (f), both the upper and lower C_{70} layers have numbers of the same single, dimeric and trimeric defects which have depths ranging from 0.05 nm to 0.10 nm. The solid white lines are shown in Fig. 4-5 (f) are used to measure the close-packing directions of C_{70} in the second and third layers, while the crossing points of lines mark the positions of C_{70} in the third layer. It illustrates that in both the two layers, all the molecules share the same close-packing directions, and each of them occupies a three-fold hollow site on the layer below. The growth of C_{70} on Au(111) also follows the ABCABC stacking mode, which is similar to the stacking of C_{70} in crystals. However, the nearest-neighbour distance (NND) of the molecules here is 0.02 nm to 0.05 nm wider than in crystals, due to the interaction between the first layer C_{70} and the gold substrate [12].

As shown in Fig. 4-6 (a), after annealing at 423 K for one hour, most close-packed C_{70} domains in the first layer have switched from the R0° phase to $(2\sqrt{3} \times 2\sqrt{3})$R30° phase. The first, second, third and fourth layer of C_{70} molecules are marked, respectively. On the flat terrace of Au(111), C_{70} islands in the second layer grow in size as a result of ripening. As shown in Fig. 4-6 (a), one of the islands includes a large main body. Molecules in the body stack with the R30° phase. The later deposited C_{70} molecules adsorb to the edges, nucleate and homoepitaxially grow as the finger-shape islands. There is no domain boundary between the main body and the finger-like islands. The shape of islands is due to

the aggregation of small islands. Around step edges of the gold substrate, there are also some smaller sized second layer islands, most of which grow along the step edges and do not have finger-like islands. Inside the second layer islands, all the C_{70} molecules take an upright configuration and form the close-packing structures.

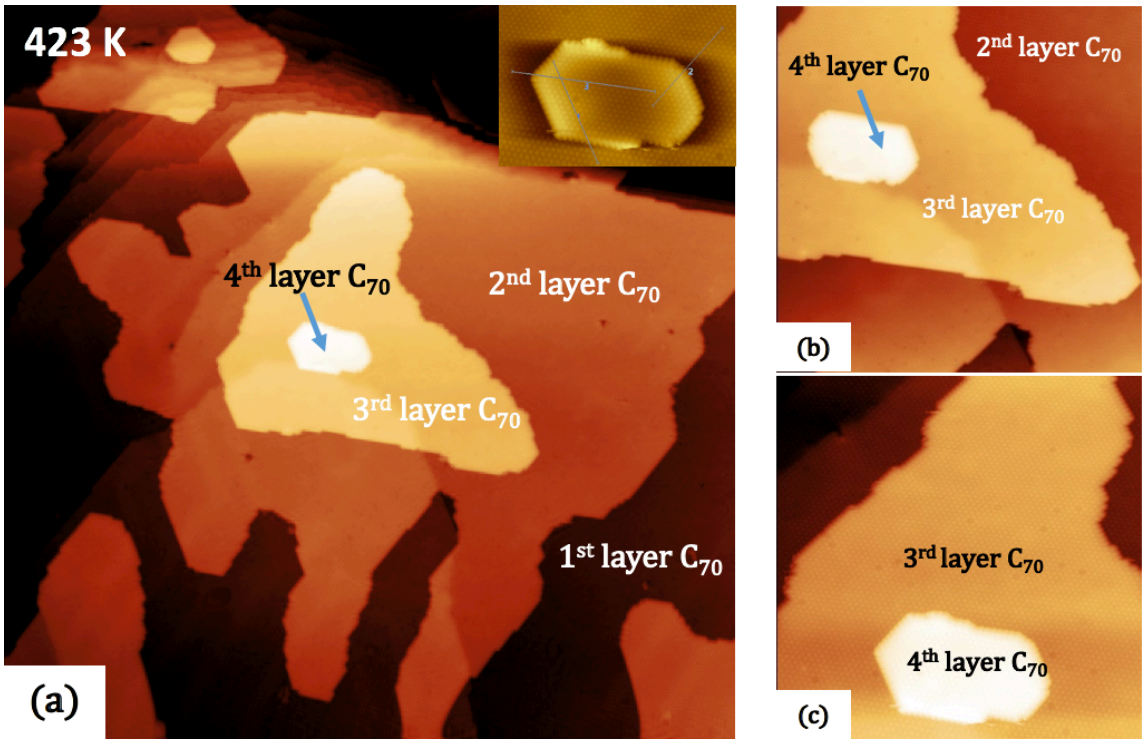


Fig. 4-6 (a) STM images of 1.65 ML C_{70} on Au(111) after being annealed at 423 K for one hour. The gold substrate is covered by a closed-packed C_{70} monolayer with R30° structure. There is a significant increase in the average size of the second and third layer islands. On top of some third layer islands, fourth layer islands with tiny sizes have appeared (270 nm × 270 nm, -2.5 V, 100 pA). Inset shows the fourth layer of C_{70} with a higher resolution. All the molecules in this layer are close-packed and sit on the hollow sites of the third layer. (b) Indication of a third and a fourth layer C_{70} island with high resolution (100 nm × 100 nm, -2.5 V, 100 pA). (c) Magnified view of the quasi-hexagonal fourth layer island already shown in (b). All the molecules in the island occupy the hollow sites in the third layer (65 nm × 65 nm, -2.5 V, 100 pA) [11].

On top of the second layer islands, the coverage of the third layer islands has increased from 0.04 to 0.12 ML. It suggests that a significant number of C_{70} molecules have moved upwards from the second layer. In addition, there are newly formed fourth layer small islands observed, most of which sit on the middle of the third layer islands and have quasi-hexagonal shapes. C_{70} molecules in this layer are dominated by the van der Waals force and grow epitaxially.

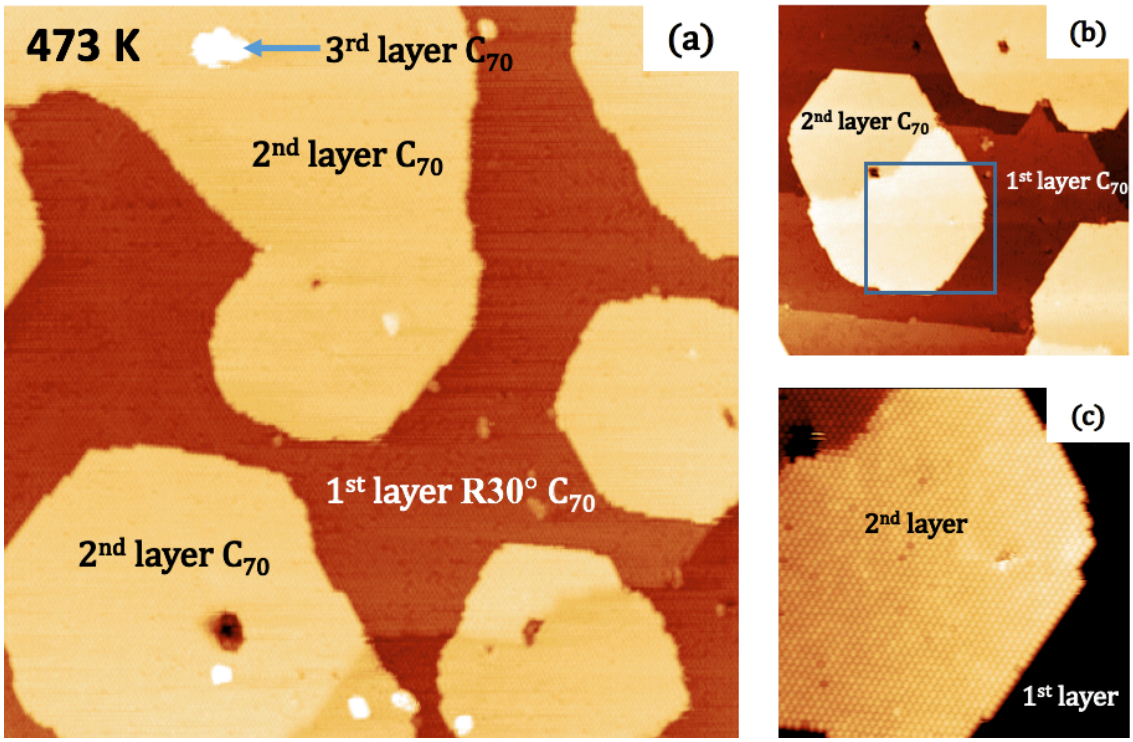


Fig. 4-7 STM image showing C_{70} on Au(111) after annealing for one hour at 473 K. (a) The fourth and most of the third layer islands have disappeared (165 nm × 165 nm, -2.5 V, 100 pA). (b) Image showing the magnified morphology of C_{70} islands in the second layer (150 nm × 150 nm, -2.5 V, 100 pA). (c) Magnified view showing the area marked with the rectangle in (b). C_{70} Molecules in the close-packed island occupy the three-fold hollow sites in the first layer (50 nm × 50 nm, -2.5 V, 100 pA) [11].

Because all the four layers are formed by only one type of molecule, it is hard to judge if there is any molecular exchange between the adjacent layers. However, the appearance of the fourth layer, as well as the expansion of the second and third layer islands indicates that during annealing, molecules tend to jump from

lower layers to higher ones, triggered by a typical coarsening effect. As calculated, there is few difference in the total coverage of the C_{70} molecules on Au(111) before and after annealing at 423 K. It agrees the that thermal energy gained by C_{70} molecules during the process is smaller than the heat of sublimation per molecule (195 KJ/mol) from a C_{70} crystal [13,14].

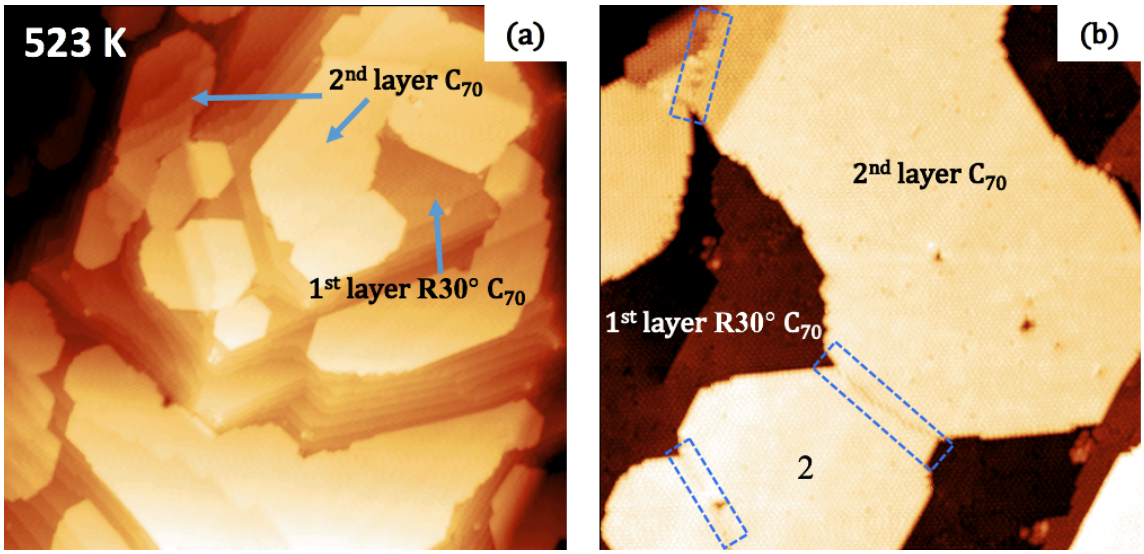


Fig. 4-8 STM images showing two layers of C_{70} on Au(111) after being annealed at 523 K for one hour. (a) The second layer C_{70} have reorganised as larger islands, and have covered most flat terraces of the substrate (260 nm × 260 nm, -2.5 V, 100 pA). (b) Magnified scanning image showing three domain boundaries on a newly formed second layer C_{70} island (120 nm × 120 nm, -2.5 V, 100 pA) [11].

Annealing at 473 K leads to a further ripening of the second layer C_{70}. All the fourth layers and most of the third layers have now disappeared, due to thermal desorption or diffusion. For the remaining C_{70} on the gold surface, higher temperature annealing gives molecules extra thermal energy to reorganise. In Fig. 4-7 (a), C_{70} islands in the second layer continue to ripen into larger sized ones. For large islands sitting on flat terraces, several finger-like islands attaching to the main bodies have merged and become thicker. For the smaller size islands sitting around the gold steps, their shapes have a tendency to be six-fold symmetric, which is due to the homoepitaxial growth mode of molecules. These

second layer islands have continuous growth when passing over gold step edges. The region in the blue rectangle has been magnified and shown in Fig. 4-7 (c), in which all the C_{70} molecules maintain in an upright orientation and form the close-packed structure. Driven by thermal annealing, island's edges have been modified by the moving of C_{70} molecules and become smoother.

Fig. 4-8 (a) shows an image acquired after annealing the sample to 523 K. The large islands sitting on flat terraces have incorporated with the small sized ones sitting at step edges, showing a tendency to form close-packed monolayers on the Au(111) surface. DLs lying under C_{70} layers haven't been fully lifted, proving the weak bonding condition between C_{70} and Au(111) substrate. A domain boundary can exist when two adjacent islands with different molecular orientations merge as one. As shown in Fig. 4-8 (b), there is a boundary between the C_{70}-R30° phase and C_{70}-R0° phase, which has the same morphology as the ones forming at room temperature. For achieving the average coverage of molecules each time deposited, fifty scanned with the sizes of $(50\ \text{nm} \times 50\ \text{nm})$, $(100\ \text{nm} \times 100\ \text{nm})$, $(200\ \text{nm} \times 200\ \text{nm})$ and $(400\ \text{nm} \times 40\ \text{nm})$ were selected after each round of scanning. Then, the total area of molecules covering gold substrate in each image were calculated. The covering area achieved in each image was then divided by the area of scanning image in order to get a ratio. In the end, all of these ratio numbers were averaged and the accurate coverage of C_{70} during experiment were achieved. Then I C_{70} molecules on Au(111) maintains a total coverage of 1.55 ML before and after annealing at 473 K and 523 K, respectively. Therefore, similar to C_{60} molecules, there is a much higher energy requirement for the desorbing of the second layer C_{70} molecules compared with the ones in the third or fourth layers [8].

4.7 Summary

At room temperature, vapour-deposited C_{70} can grow into the R30°, R0° (In-phase), R14° and R34° phases on the Au(111) substrates in an ultra-high vacuum system. The former two phases are more commonly observed during our scanning. In these phases, interactions between C_{70} molecules are optimized with the chemical interactions between the C_{70} and gold substrate. It drives all the C_{70} molecules to take an upright orientation and form close-packed structures.

At considerably lower coverage, C_{70} molecules on Au(111) firstly aggregate at gold steps or grain boundaries. In our scanning, most of the C_{70} islands grow along the lower side of gold step edges and form single layer islands. As the coverage of molecules increases, C_{70} monolayers grow out of the gold step edges and sit on both the upper and lower flat terraces. Islands at the two sides of one step edge keep the same packing structures. A further increase in the coverage of molecules leads to the appearance of larger sized islands, and domain boundaries due to merging growth fronts are observed. Domain boundaries separating domains with different packing structures have different shapes. When the coverage of molecules is higher than 1 ML, the second layer start to appear before the gold surface is fully covered by the first layer C_{70}, due to the weak interaction between gold and absorbed C_{70} molecules. All the molecules in the upper layers occupy the three-fold hollow sites in the lower layer and form perfect close-packed structures.

Multilayer C_{70} molecules on the Au(111) surface can be achieved by massive deposition. By annealing over 1 ML C_{70} at 423 K for one hour, most of the molecules in the first layer pack in the R30° phase. The molecules in lower layers achieve enough thermal energy to jump upwards in order to form the third or fourth layer islands. In these upper layers, molecules are dominated by van de Waals force while interaction coming from the substrate can be roughly ignored. After being annealed at 473 K or a higher temperature, only the first and part of

the second layer C_{70} remain due to their stronger interaction with the gold substrate below.

References

[1] G. Dresselhaus, M. S. Dresselhaus, P. C. Eklund, Science of Fullerenes and Carbon Nanotubes: Their Properties and Application (Academic Press, San Diego, 1995).

[2] W. Kratschmer, L. D. Lamb, K. Fostiropoulos, and D. R. Huffman. Nature **347**, 354 (1990).

[3] C. S. Yannoni, P. P. Bernier, D. S. Bethune, G. Meijer, and J. R. Salem. J. Am. Chem. Soc. **113**, 3190 (1991).

[4] S. Rousset, V. Repain, G. Baudot, Y. Garreau, and J. Lecoeur, J. Phys-Condens. Matter. **15**, 3363 (2003).

[5] E. I. Altman and R. J. Colton, Surf. Sci. **279**, 49 **(**1992).

[6] P. W. Murray, M. Ø. Pedersen, E. Lægsgaard, I. Stensgaard and F. Besenbacher, Phys. Rev. B **55**, 9360 (1997).

[7] S. Guo, D. Fogarty, P. Nagel, and S. A. Kandel, J. Phys. Chem. C **5513**, 185 (2004).

[8] E. I. Altman and R. J. Colton, Surf. Sci. **279**, 49 **(**1992).

[9] T. Sakurai, X. D. Wang, T. Hashizume, V. Yurov, H. Shinohara and H. W. Pickering, Appl. Surf. Sci. **87**, 405 (1995).

[10] J. A. Gardener, G. A. D. Briggs, and M. R. Castell, Phys. Rev. B **80**, 235434 (2009).

[11] Y. Wang, L. Guo, and Q. Guo, J. Phys. Chem. C **123**, 7776 (2019).

[12] M. A. Verheijen, H. Meekes, G. Meijer, P. Bennema, J. L. De Boer, S. Van Smaalen, G. Van Tendeloo, S. Amelinckx, S. Muto, and J. Van Lan-duyt, Chem. Phys. **166**, 287, (1992).

[13] J. Abrefah, D. R. Olander, M. Balooch, and W. J. Siekhaus, Appl. Phys. Lett. **60**, 1313 (1992).

[14] G. B. M. Vaughan, P. A. Heiey, D. E. Luzzi, D. A. Ricketts-Foot, A. R. Mcghie, J. E. Fischer, Y. W. Hui, A. L. Smith, D. E. Cox, W. J. Romanow, B. H. Allen, N. Coustel, J. P. Mccauley, A. B. Smith III, Science **254**, 1350 (1991).

5. Two-component Molecular Layers (C_{60}/C_{70}) Assembled on Au(111)

5.1 Introduction

In this chapter, we mainly study the mixing of C_{60} and C_{70} molecules on the Au(111) substrate with STM. The two types of molecules were deposited on Au(111) sequentially and annealed at various temperatures in order to study the structural interactions. To analyse the packing structure of fullerene molecules on Au(111), a "hard ball" model was used by considering a spherical and ellipsoidal shape for C_{60} and C_{70} molecules, respectively. The aspect ratio of the ellipsoidal C_{70} molecules is ~ 0.89, with the shorter axis of the oval cross section the same as the diameter of C_{60} [1-3]. Moreover, the adsorption of fullerene molecules on Au(111) has been studied in details, where molecules tend to assemble into large, close-packed layers due to the weaker chemical interaction between fullerene and Au(111) substrate than between two fullerene molecules. Also, different annealing temperatures change the azimuthal orientations of C_{70} and lead to the formation of different structures [4-14]. By depositing the two types of molecules onto the Au(111) surface, rows of dislocations appear at the C_{60} and C_{70} domain boundaries. The mixing of the two types of molecules in the same layer is only favoured at elevated temperatures. When C_{60} are deposited onto a C_{70} layer, C_{60} molecules can push their way into the C_{70} layer and force the C_{70} molecules below to sit with their long axis perpendicular to the C_{60}/C_{70} interface. Significant interlayer diffusion also takes place beyond a certain temperature. If the deposition sequence is reversed, C_{60} before C_{70}, the second layer C_{70} take the upright orientation in order to reduce the lattice constant to match the C_{60} in the first layer [15].

5.2 Experimental Procedure

The experiments are performed using an Omicron variable-temperature scanning tunnelling microscope (VT-STM) with a working pressure of 5×10^{-10} mbar. A clean Au(111) surface was obtained with a thermal deposition of gold thin films in UHV on HOPG and cleaned by repeated exposure to Argon ions of 1.5 keV in energy. C_{60} and C_{70} molecules are deposited on Au(111) sequentially at room temperature. Afterwards, the sample was annealed at a series of temperatures for one hour and was then scanned at room temperature.

In the first experiment, 0.3 ML C_{60} and 0.3 ML C_{70} molecules were deposited on the Au(111) surface at room temperature with C_{60} being deposited first. The sample was then heated at 573 K for one hour and the surface topography was scanned by STM at room temperature. In the second experiment, 1.2 ML C_{70} molecules were firstly deposited on Au(111) and annealed at 523 K for one hour, in order to form a close-packed monolayer film. Then 0.65 ML C_{60} molecules were added on to the C_{70} monolayer. The multilayer sample was then annealed at 423 K, 473 K and 523 K respectively for an hour to achieve the interlayer diffusion of C_{60} or C_{70} molecules while preventing the two types of molecules desorbing from the Au substrate. In the third experiment, 0.65 ML C_{60} molecules were deposited on top of the 1 ML C_{60}. The sample was also annealed at 423 K, 473 K and 523 K for an hour, respectively, in order to provoke the merging of the two layers' molecules. All the STM scanning were performed after the sample has been cooled to room temperature.

5.3 Results and Discussion

5.3.1 Mixed C_{60} and C_{70} on Au(111) At Room Temperature

0.3 ML C_{60} molecules and 0.3 ML C_{70} molecules were successively deposited onto Au(111) at room temperature. Fig. 5-1 (a) shows an image from the sample

with only 0.3 ML C_{60}. Both the close-packed periodic R30° and uniform R0° (In-Phase) phases form on the gold substrate. In the domains with uniform R0° structure, C_{60} molecules stack in the same direction as the gold atoms underneath. As shown in the white rectangle, boundaries of the this type of domains and include scratch-like lines and look fuzzy. It is due to the continuous freely moving of molecules around the island's edges during scanning. As for the R30° domains, C_{60} molecules in this type of phase pack in one of the <112> directions, and there is an 30° angle between the packing directions of molecules and gold atoms [9]. The R30° phase can be divided as the uniform and periodic phases, which are separated by the white dashed lines. In the uniform phase, C_{60} molecules form close-packed structure and are in the same brightness. It looks similar to the R0° phase. In the periodic R30° phase, there are two types of C_{60} molecules with different brightness. The darker molecules sit on the three-fold sites on the gold surface while the brighter molecules sit on random sites. As marked in the green rectangle, most boundaries of the R30° phase are sharp and are parallel to the DLs on the herringbone reconstructed Au(111) surface [9].

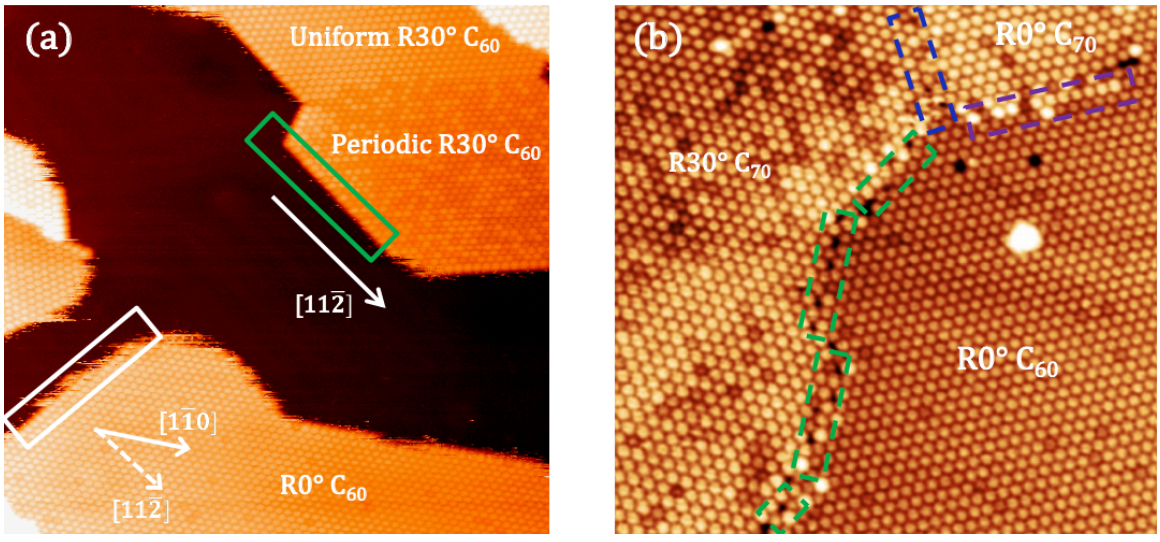


Fig. 5-1 (a) STM image of close-packed 0.3 ML C_{60} molecules sitting on the Au(111) surface at room temperature. The $\left(2\sqrt{3} \times 2\sqrt{3}\right)$R30° and R0° structures are formed by molecules. One of the close-packing directions of the C_{60} molecules in R30° structure is parallel to the discommensurate lines (65 nm × 65 nm, -2.5 V, 100 pA). (b) STM image of 0.3 ML C_{60}

molecules and 0.3 ML C_{70} molecules successively deposited on the Au(111) surface. The uniform R0° C_{60}, the uniform R0° and the periodic R30° C_{70} domains have been found. Between the R30° C_{70} and R0° C_{60} domains, there are a series of voids. Each voids has the size of single molecule and exists in the centre of a pentagon. Voids at the boundary between R30° C_{70} and R0° C_{60} domains have the shape of an acute triangle. There are no voids between the R0° C_{70} and R0° C_{60} domains. It has the same boundary shape as the one separating the R30° C_{70} and R0° C_{60} domains. The dashed lines highlight the boundary gap separating the R0° C_{70} and R30° C_{70} domains (60 nm × 60 nm, -2.5 V, 100 pA).

As illustrated in Fig. 5-1(b), when 0.3 ML C_{70} molecules are deposited onto the C_{60} monolayer in the presence of pre-deposited C_{60}, they form close-packed domains with R30° and R0° structures and attach to the existing C_{60} domains. The height difference between single C_{60} and C_{70} molecules is measured as around 0.10 nm. It indicates that in the close-packed domains on Au(111), C_{70} molecules are assumed to have approximately an upright configuration with their long axes perpendicular to the substrate. There are very few molecular voids existing at the boundary between the R0° C_{70} and R0° C_{60} phases, marked by the dashed purple lines. It is due to the perfect lattice match of molecules in the two domains. The boundary between R30° phase of C_{70} and R0° phase of C_{60} includes a series of voids, which are marked by the green dashed lines. Each of the voids has the size of a single molecule and is surrounded by five C_{60} molecules. The boundary between the R30° phase of C_{70} and R0° phase of C_{70} exist on top of the Fig. 5-1 (b). Voids at the boundary have the acute triangle shapes and the sizes smaller than single molecules. The stacking voids are mainly caused by the mismatch between the two structural phases. The NND of C_{70} in the close-packed domains is measured 0.05 nm larger than the C_{60}. Before annealing, both C_{60} and C_{70} molecules remain in their phases with no mixing, and there are only few C_{70} molecules observed crossing the boundary and trapped in the C_{60} domains.

5.3.2 Mixed C_{60} and C_{70} on Au(111) at 573 K

Annealing the sample at 573 K for one hour desorbs all the molecules except those in the first layer [4]. During annealing, molecules can move across the boundary leading to mixing of C_{60} with C_{70}. As demonstrated in Fig. 5-2 (a), during the cooling process, the two types of molecules do not form a homogeneous layer. Instead, they are phase separated into C_{60}-rich (C_{70}-rich) domains with trapped C_{70} (C_{60}) molecules. In the R30° C_{60} domains, most of the C_{70} molecules present aggregate into single, dimeric or trimeric bright spots. The height difference between the C_{70} and C_{60} is measured as 0.10 nm, which is in accordance with the C_{60}-C_{70} height difference when C_{70} molecules take an upright configuration on Au(111) [16].

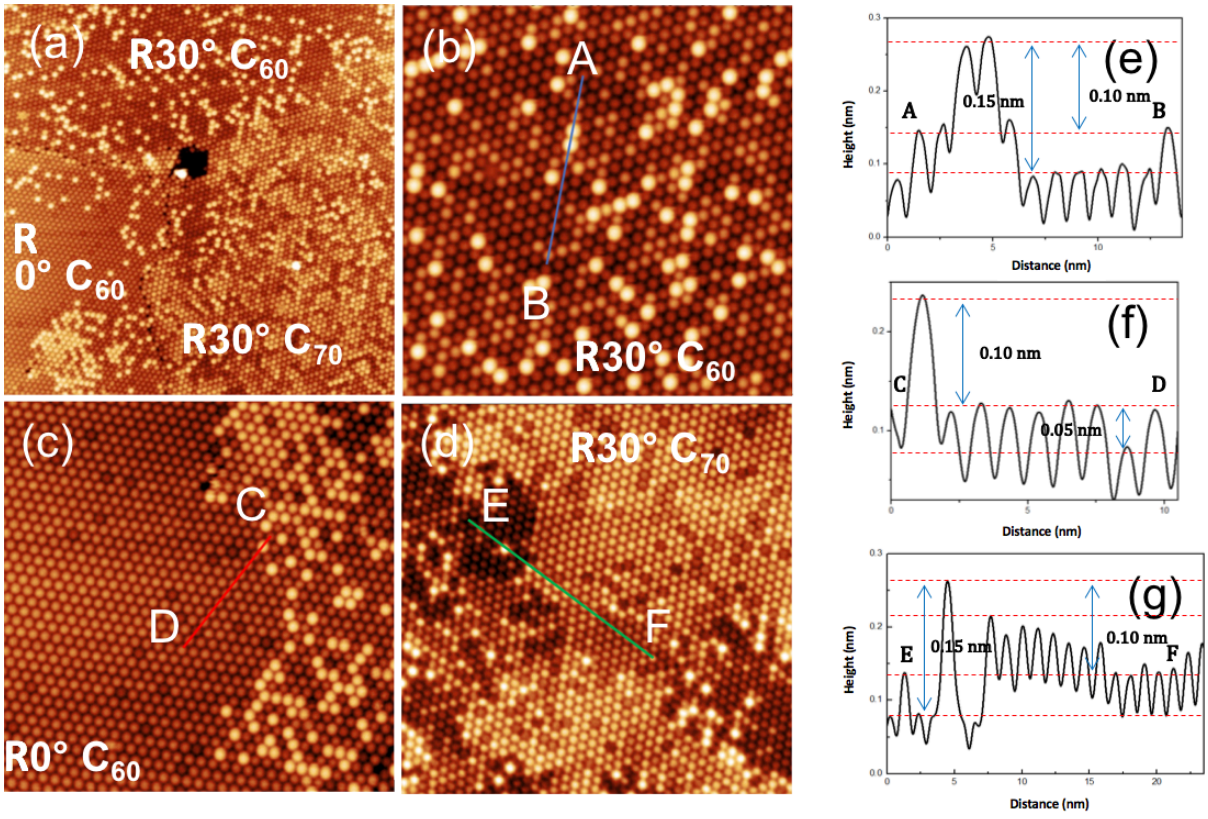


Fig. 5-2 (a) STM image demonstrating the co-existing C_{60} and C_{70} phases on Au(111) after being annealed at 573 K for one hour, where there is no obvious change of the boundaries between R30° C_{60}, R0° C_{60} and R30° C_{70} phases. The two types of C_{60} molecules in an R30° C_{60} domain can be distinguished. Some single C_{70} molecules are seen in C_{60} regions, appearing as bright spots measured 0.10 nm higher than all the C_{60} molecules in the R0° domains and the

brighter C_{60} molecules in R30° domains. C_{60} molecules mixing into C_{70} domains aggregate to small islands. (b) Most C_{70} molecules penetrate in $\left(2\sqrt{3} \times 2\sqrt{3}\right)$R30° C_{60} islands and aggregate to monomers or dimers. These trapped C_{70} molecules prefer to sit next to the bright C_{60} molecules as they have weaker interactions with the gold substrate. (30nm × 30nm, -2.5 V, 100 pA) (c) C_{70} molecules joining R0° C_{60} islands aggregate to larger molecular islands which sit close to the domain boundaries. (35nm × 35nm, -2.5 V, 100 pA) (d) A large number of C_{60} molecules penetrate R30° C_{70} domains and form islands with different sizes. In these regions, C_{60} molecules show the same packing structure as the surrounding C_{70}. (40nm × 40nm, -2.5 V, 100 pA) (e) Line profile along A-B line showing the mixed C_{70} molecules are 0.10 nm higher than the brighter C_{60} in R30° domains and 0.15 nm higher than the darker ones. The height difference between the bright and dark C_{60} in R30° domains is measured as ~ 0.05 nm. (f) Line profile along C-D line showing the height difference between C_{60} in R30° domains and trapped C_{70} as 0.10 nm. The depth of the molecular defects in this domain is greater than 0.05 nm. (g) C_{70} surface shows fluctuation. Line profiles along E-F line showing large size C_{60} islands squeezed in R30° C_{70} domains. C_{60} molecules are measured to be 0.15 nm lower than the surrounding C_{70} molecules [17].

Fig. 5-2 (b) indicates that most C_{70} molecules trapped in the R30° C_{60}-rich domains commonly sit next to one or two bright C_{60} molecules. It implies that the guest C_{70} molecules take over the positions used to be occupied by the brighter C_{60} molecules. However, inside R0° C_{60} domains, molecular spacing are smaller and all the molecules are equal, making it less favourable for C_{70} molecules to penetrate the structure. To the contrary, guest C_{70} molecules may migrate from C_{70}-rich domains to the C_{60}-rich domains and aggregate to islands at the boundary (Fig. 5-2(c)). The R30° C_{70}-rich domains with guest C_{60} molecules are observed in Fig. 5-2(d). After being annealed, C_{60} molecules aggregate into islands or irregularly shaped chains and sit in R30° C_{70} domains. In these domains, the joined C_{60} molecules also form the R30° structure and show the bright and dark patterns. The presence of the two types of C_{60} suggests a nonuniform bonding between molecules and Au(111), which could be caused by the varieties of

surface atomic vacancies. Squeezing of R30° C_{60} islands in C_{70}-rich domains results in a more complicated condition of the atomic vacancies below fullerene molecules. Thus, as shown in Fig. 5-2 (g), the C_{70} monolayer between two C_{60} islands has a fluctuated surface. Due to the height difference of C_{60} and C_{70} in scanning image, boundaries between the C_{60} islands and C_{70} around are sharp and easy to recognise.

The incorporating of the two types of molecules can be explained in three aspects: (i) C_{60} molecules have a relatively long diffusion length due to their perfect sphere shape, resulting in a higher mobility than C_{70} on Au(111) surface, making them more favourable to aggregate into large islands [18]. (ii) Gold atoms in the substrate have stronger interactions with the darker C_{60} in the R30° phases compared with C_{70} [19]. It triggers some C_{70} to move away from their original sites and leaves enough space for the guest C_{60} molecules to form small islands. Meanwhile, after being heated at the same temperature, the C_{70} molecules can also mix into the R30° C_{60} domains and mainly replace the brighter molecules with weaker bonding to the gold substrate. The arrangement of the bright and dark C_{60} forces these C_{70} to sit as single ones or only aggregate into dimmers. (iii) Another possible explanation is that van der Waals force between two adjacent C_{60} molecules is stronger than the one between two C_{70} molecules, thus it is more difficult for C_{60} molecules in the close-packed domains to be replaced.

Fig. 5-3 (a) shows a very straight and sharp boundary between R30° C_{60} and R30° C_{70} domains. It appears after the sample has been annealed at 573 K for one hour and then cooled down to room temperature. The boundary between C_{60} and C_{70} phases are straight, while the two types of molecules having been found passing across the boundary.

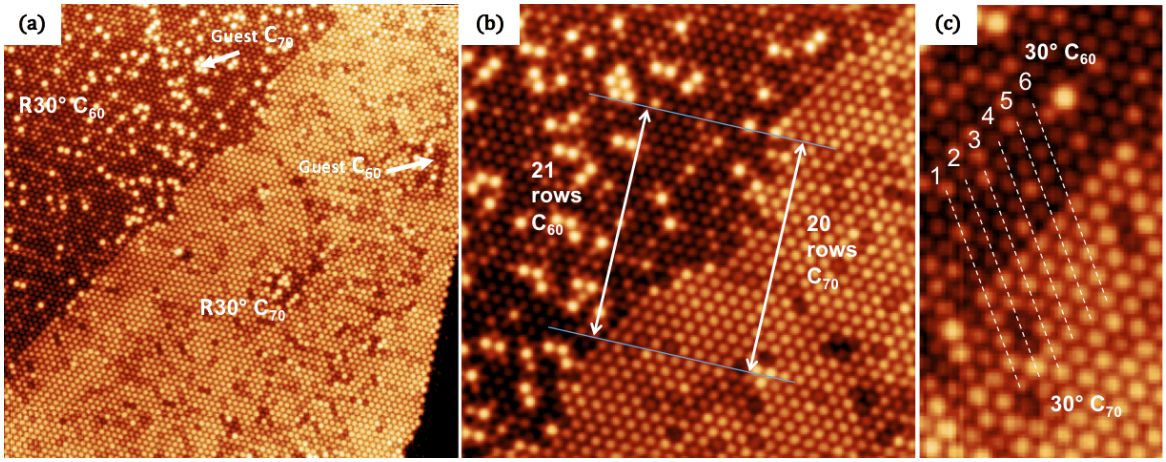


Fig. 5-3 (a) STM image showing the adjoining C_{70}-R30° and C_{60}-R30° domains with straight domain boundary. (85 nm × 85 nm, -2.5 V, 100 pA) (b) Higher resolution image of the domain boundary. The total length of 21 rows of close-packed C_{60} is equal to the length of 20 rows C_{70}, indicating a larger nearest neighbour distance of close-packed C_{70}. (c) Lattice mismatch at the C_{60}-rich and C_{70}-rich domain boundary. C_{60} and C_{70} molecules have weak coupling across the boundary [17].

A magnified view of this boundary is demonstrated in Fig. 5-3 (b) where we find that for the same distance that is covered by 20 rows of C_{70} can accommodate 21 rows of C_{60} molecules. There is an extra row of C_{60} molecules that terminates at the boundary between C_{70}-R30° and C_{60}- R30° domains, which gives rise to an edge dislocation. The NND of C_{70} is measured to be 1.05 times of that for C_{60}, and the C_{60} molecules in R30° phase are observed having a larger nearest neighbour distance than in R0° phase. Fig. 5-3 (c) demonstrates a small piece of an R30° oriented C_{60}-C_{70} domain boundary. Six white dashed lines are used to mark the packing directions of molecules and to show the positional relationship between the C_{60} and C_{70} rows separated by the boundary. As one moves from line 1 to line 6, the distance offset between the rows of C_{60} and C_{70} gradually increases, indicating the lattice mismatch between the two types of molecules.

5.3.3 0.65 ML C_{60} Deposited on 1 ML C_{70}

The STM image in Fig. 5-4 (a) exhibits the formation of a second layer C_{60} on top of a C_{70} monolayer. ~ 1.2 ML C_{70} molecules are first deposited on Au(111) annealed at 623 K for one hour to create close-packed C_{70} monolayers. Afterwards, ~ 0.65 ML of C_{60} molecules are deposited onto the C_{70} monolayer and form isolated C_{60} islands. The C_{60} forms quasi-hexagonal shaped, isolated islands, most of which attach to the step edges of the sample or domain boundaries in the first layer.

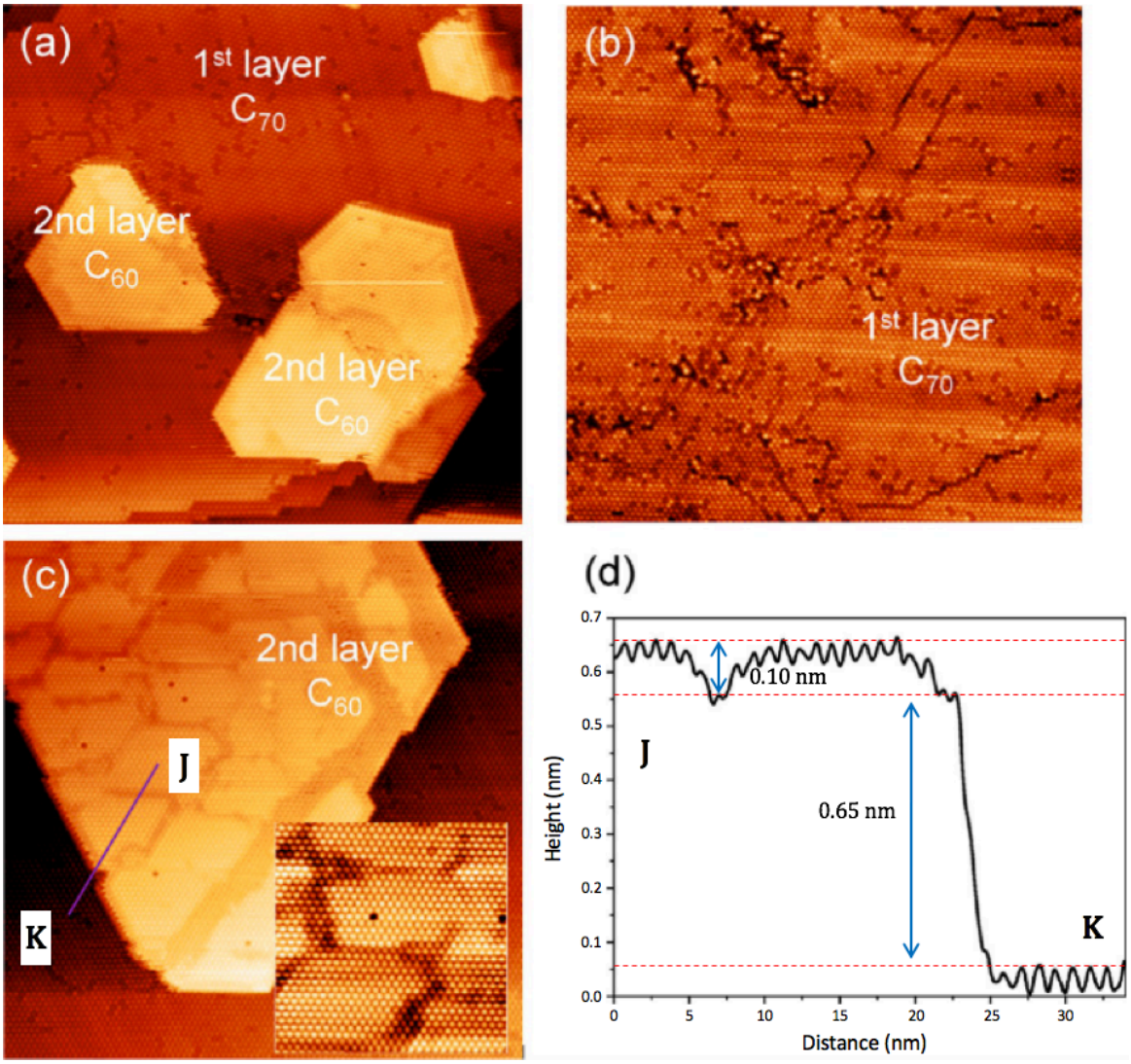


Fig. 5-4. (a) STM images showing 0.65 ML C_{60} on a compact R30° C_{70} monolayer (95 nm × 95 nm, -2.5 V, 100 pA). (b) C_{60} molecules trapped in the first layers of R30° C_{70} forming dark rows or small size islands (35 nm × 35 nm, -2.5 V, 100 pA). (c) STM images

5gshowing C_{60} islands with quasi-hexagonal shapes on C_{70} monolayer. The dark bands and single molecular defects on the second layer C_{60} islands. The inset (40 nm × 50 nm) enlarges the dark bands inside the C_{60} islands. (100 nm × 100 nm, -2.5 V, 100 pA) (d) Line profile along J-K line showing the depth of the dark bands of 0.08 nm to 0.10 nm. The heights of the C_{60} in the island are averagely 0.65 nm taller than the C_{70} molecules in the first layer [17].

In the second experiment, about 1.2 ML C_{70} molecules are firstly deposited on Au(111) and annealed at 623 K for one hour in order to form compact C_{70} monolayer. Then, ~ 0.65 ML of C_{60} molecules are deposited onto the C_{70} monolayer. The later deposited C_{60} either form isolated islands or incorporate into the C_{70} monolayer. Fig. 5-4 (b) shows a region where C_{60} mixing into R30° C_{70} domains on an Au(111) substrate. It can be seen in the figure that some molecules appearing darker than surroundings, which can be associated with C_{60} molecules (as height lower than C_{70}) or C_{70} defects. From the packing structures, it is possible to identify the dimmer molecules, since most of C_{60} in the first layer packs as rows or small islands, while C_{70} defects appear as singlets, dimers and trimers.

A case of C_{60} islands sitting on C_{70} monolayer is demonstrated in Fig. 5-4 (c), in which the long and narrow dark bands have the depth of ~ 0.10 nm and the width of one to two molecules. These bands are magnified in the inset image. Most of these dark bands share the same packing direction as C_{60} molecules. It is triggered by the intrinsic lattice mismatch between C_{60} and C_{70}. Inside close-packed domains, C_{60} has a smaller nearest-neighbour distance compared with that of C_{70} (Introduced in chapter 1). As a layer of C_{60} is placed on a layer of C_{70}, both the two layers of molecules are affected by interface strain, which causes the compression of C_{70} and tension in C_{60}. Apart from the dark band networks, there are also few molecular defects on the islands with the depth ranging from 0.02 nm to 0.30 nm.

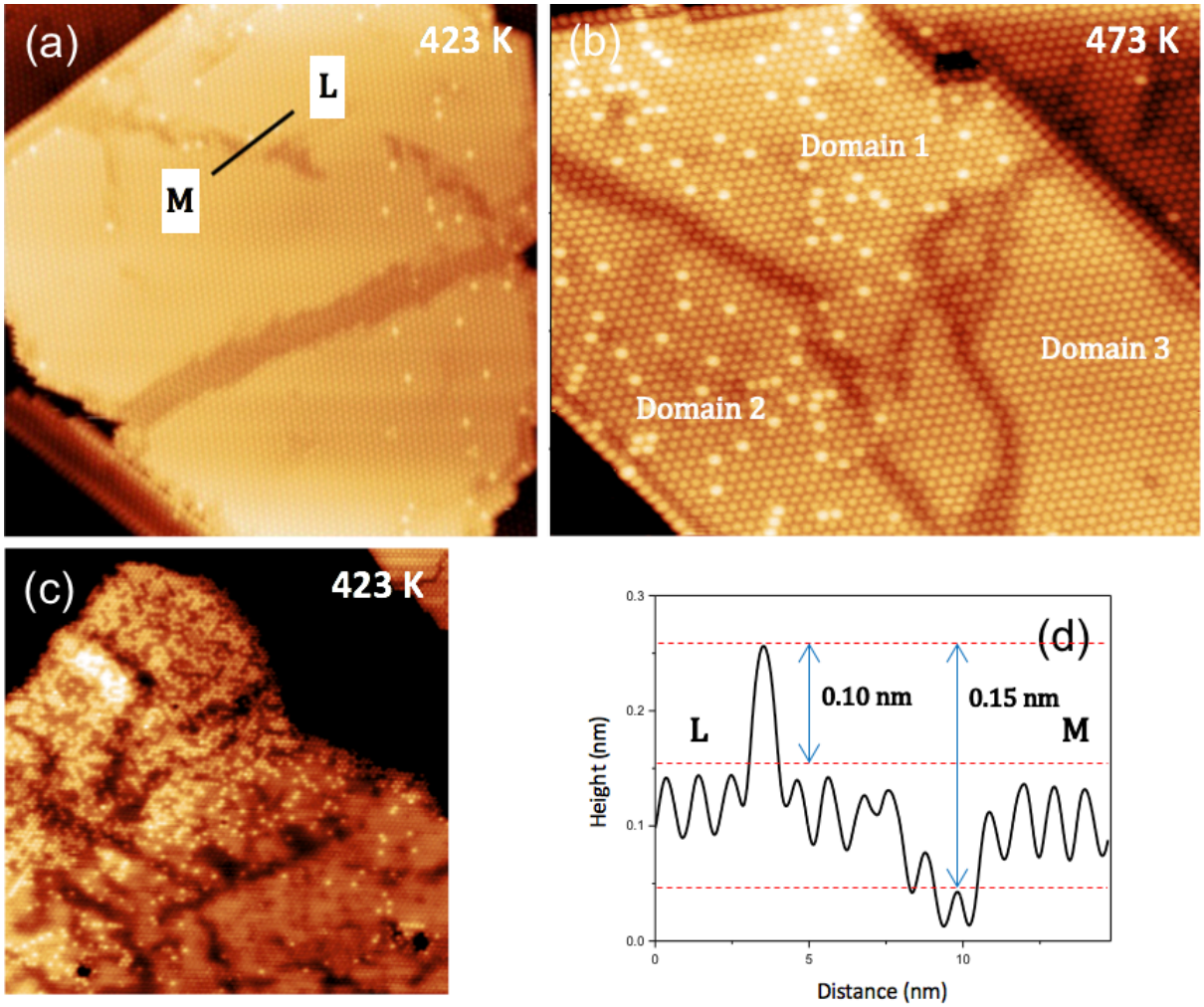


Fig. 5-5 (a) STM image (75 nm × 75 nm, -2.5 V, 100 pA) showing the C_{60} islands sitting on monolayer of C_{70} after one-hour annealing at 423 K. The Dark band networks separate the C_{60} islands into different sized domains. The bright spots identified as C_{70} molecules appear on the islands which are measured to be 0.10 nm higher than the surrounding C_{60} molecules. (b) After one hour annealing at 473 K, the larger size C_{60} islands are formed at step edges. C_{70} prefer to enter certain domains instead of others (55 nm × 45 nm, -2.5 V, 100 pA). (c) After being annealed at 523 K for one hour, there are super-large irregular C_{60} islands appearing. C_{70} molecules join in C_{60} islands and form a close-packed structure (90 nm × 90 nm, -2.5 V, 100 pA). (d) Line profile along L-M line showing the characteristic height of a single C_{70}, which is measured 0.10 nm higher than the surrounding C_{60} molecules and 0.15 nm higher than the dark bands.

In Fig. 5-5 (a), the sample has been annealed at 423 K for one hour. The dark bands tend to grow in random directions instead of following the orientation of the second layer of C_{60}. This indicates that after being annealed, the interfacial strain between the first layer C_{70} and the second layer C_{60} has changed, which triggers the reformation of the second layer C_{60} islands. Annealing also accelerates the molecules translocation between the upper and lower layers, leading to isolated guest C_{70} molecules merging into the upper layer of C_{60}. In the recorded STM images, most of these C_{70} molecules appear as bright spots and are 0.10 nm taller than the C_{60} molecules around. Most of these C_{70} molecules sit far from the islands' edges and the dark bands mentioned above. Compared with Fig. 5-4 (c), there is no C_{60} defect appearing in the second layer after annealing. These defects are thus attributed to the vacancies which are occupied by guest C_{70} molecules after annealing.

After being annealed at 473 K for one hour, the small isolated C_{60} islands in the second layer have aggregated to larger ones with sharper boundaries. The dark bands growing in random directions remain and separate C_{60} islands into several sized irregular domains. Molecules in these domains maintain the same orientation. There are more C_{70} molecules from the first monolayer merging as bright dimers or trimers inside the covering C_{60} islands. These C_{70} molecules prefer to sit in certain domains and leave the others empty. As shown in Fig. 5-5 (b), there is a greater number of C_{70} molecules in domain 1 and 2 compared within domain 3. It is probably due to the variation in the stress in these domains.

Some C_{70} molecules in the first layer are observed passing over the interface and join the islands in the second layer, some molecular vacancies in the first layer have been created. However, these vacancies are not observed in the scanning images, and there is almost no change in the coverage of islands during annealing. It implied that once a C_{70} jumped up, the vacancy it left might have been occupied quickly by other C_{70} molecules in the same layer.

Fig. 5-5 (c) illustrates the sample at room temperature after being annealed at 523 K for one hour. Most C_{60} from the sample have desorbed or dropped into the vacancies on the first layer. Thus there is a dramatic decrease in the number of the second layer C_{60} islands while the remaining C_{60} islands have a further aggregation. At the same time, there are more C_{70} below squeezing into these C_{60} islands. Remarkably, there are few narrow dark bands formed by rows of C_{70} molecules appearing on the islands, which separate an island into several irregular domains. In these domains, self-assembled structures of the transferred C_{70} molecules in the upper C_{60} layers are observed after annealing. While in other C_{60} domains, C_{70} molecules are hard to be found.

Here we can conclude that C_{70} molecules in the first layer can pass across the interface and join the C_{60} islands in the second layer during the process of annealing at 423 K, 473 K and 523 K. These C_{70} molecules take an upright configuration in second layer islands and keep their spacing with the adjacent ones same as lattice of close-packed C_{60}. In addition, annealing at higher temperatures increases thermal energy of the molecules, which can both accelerate the intra-layer transfer of the two types of molecules and trigger a rearrangement of C_{60}/C_{70} mixture in the same layer.

5.4 0.65 ML C_{70} Deposited on 1 ML C_{60}

Here we switch the molecular species in the first and the second layers. As shown in Fig. 5-6 (a) and (b), one compact ML C_{60} are firstly deposited on Au(111), followed by 0.65 ML C_{70} molecules. As shown in Fig. 5-6 (d), the height of one layer of C_{70} sitting on top of an R30° C_{60} monolayer is measured as 0.88 nm, which is ~ 0.2 nm higher than sitting on a C_{70} monolayer also with the R30° packing structure. It indicates that in the close-packed domains, the interaction of

a C_{60} and its adjacent C_{70} is weaker than that of two C_{70} with a standing up orientation.

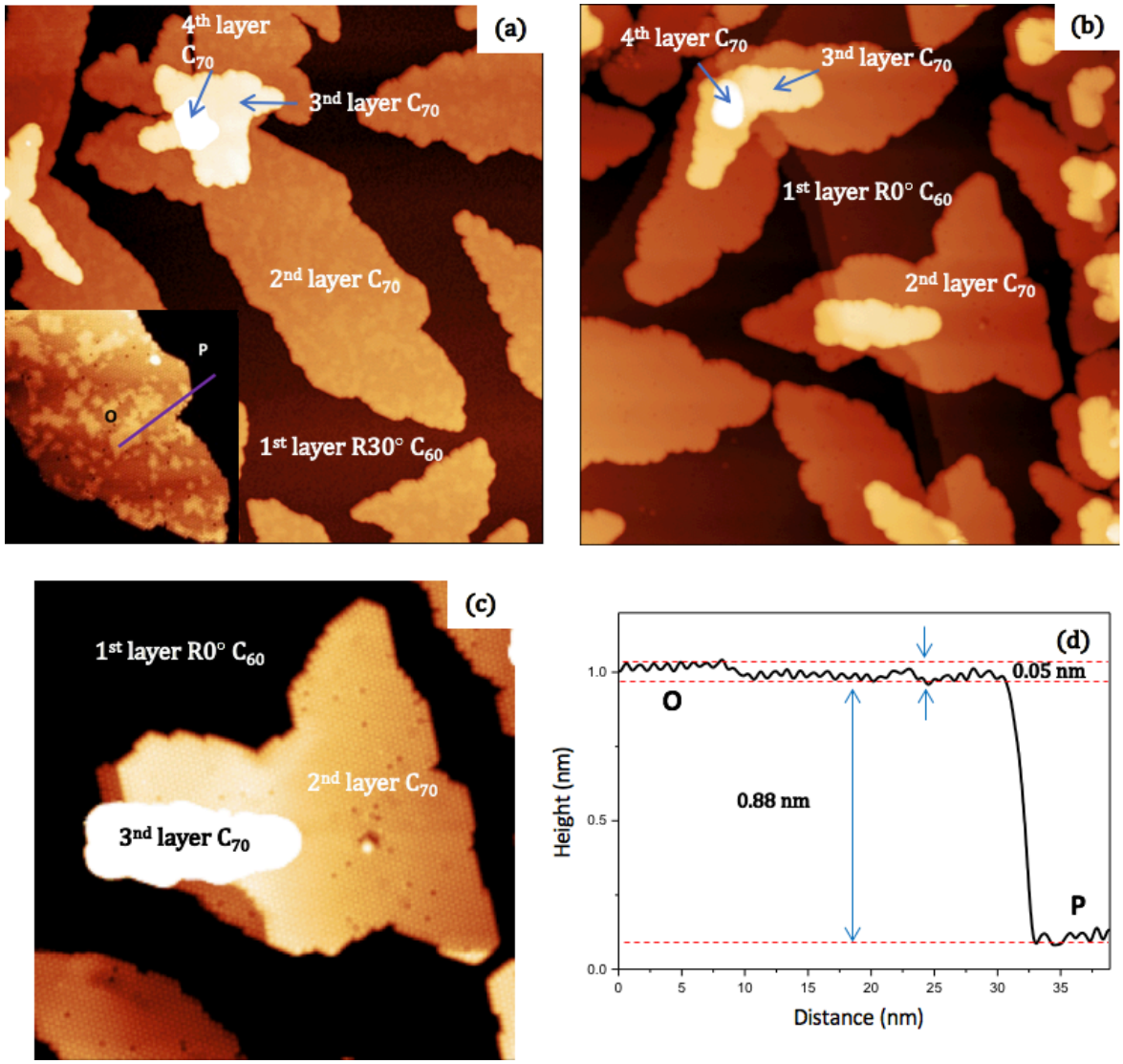


Fig. 5-6 (a) and (b) showing 0.65 ML C_{70} molecules deposited on a close-packed monolayer of C_{60} with the R30° and R0° structures, respectively. (a) C_{70} molecules on R30° C_{60} domains form dendritic shaped islands. On these islands, some brighter molecules are 0.02 nm - 0.03 nm higher than the darker ones in the background. C_{60} islands in the third and the fourth layers have smaller sizes and irregular shapes, in which all the molecules demonstrate uniform heights. Bright and dark molecules are magnified and shown in the insert. (80 nm × 80 nm, -2.5 V, 100 pA) (b) C_{70} sitting on R0° C_{60} domains also grow into three layers which have similar shapes compared with sitting on R30° C_{60} domains. C_{70} in all of these layers pack closely. (120 nm × 120 nm, -2.5 V, 100 pA) (c) Higher resolution image showing the second and the third layer C_{70} islands on monolayer R0° C_{60} domains. (d) Line profile along O-P line

showing one layer of C_{70} deposited on top of an R30° C_{60} monolayer with a height of 0.88 nm. The height difference between the bright and dark C_{70} is measured as ~ 0.05 nm [17].

Sitting on both R30° and R0° C_{60} domains, C_{70} aggregate to two to three layers of close-packed islands with similar dendritic shapes. On the R30° C_{60} domains, some bright patches appear in C_{70} islands with various shapes and sizes. As indicated in Fig. 5-6 (d), C_{70} molecules in these patches are measured ~ 0.05 nm taller than the dim molecules around, which is equivalent to the height difference between the bright and dim C_{60} in the layer underneath. It implies that the uneven surface of the C_{70} islands results from the bonding between the C_{70} and C_{60} layers. In reverse, the close-packed C_{70} molecules in the second layer are also possible to affect the packing structure of the C_{60} layer underneath [20]. Compared with the ones in the first layer, bright molecules in the second layer tend to aggregate. When C_{70} are added on top of the first layer C_{60}, the interaction between the two layers weakens the interaction between molecules in the first layer and gold substrate, which allows the atomic vacancies to change positions. On top of the R0° C_{60} domains, all the C_{70} molecules take an upright configuration and form close-packing structures to reduce interfacial strain [21]. Thus most of the C_{70} molecules in the islands demonstrate uniform brightness. The Insert in Fig. 5-6 (a) and (b) enlarge highlights two C_{70} islands landing on the R30° and R0° phases, respectively.

Fig. 5-7 (a) indicates that C_{70} islands merge and form larger ones with sharp and straight boundaries after being heated at 473 K for one hour. The top-left part of this island appears darker than the other regions because they stand on the lower terraces of the gold step. The brighter C_{70} molecules in the island remain 0.5 nm higher than the dim ones and are marked by the red triangles. Moreover, these special C_{70} molecules further aggregate into large bright patches and tend to attach to the edge of islands, which are marked in the blue rectangular box. After

heat treatment, darker molecular defects with a depth greater than 0.08 nm in the C_{70} islands occurs on the islands.

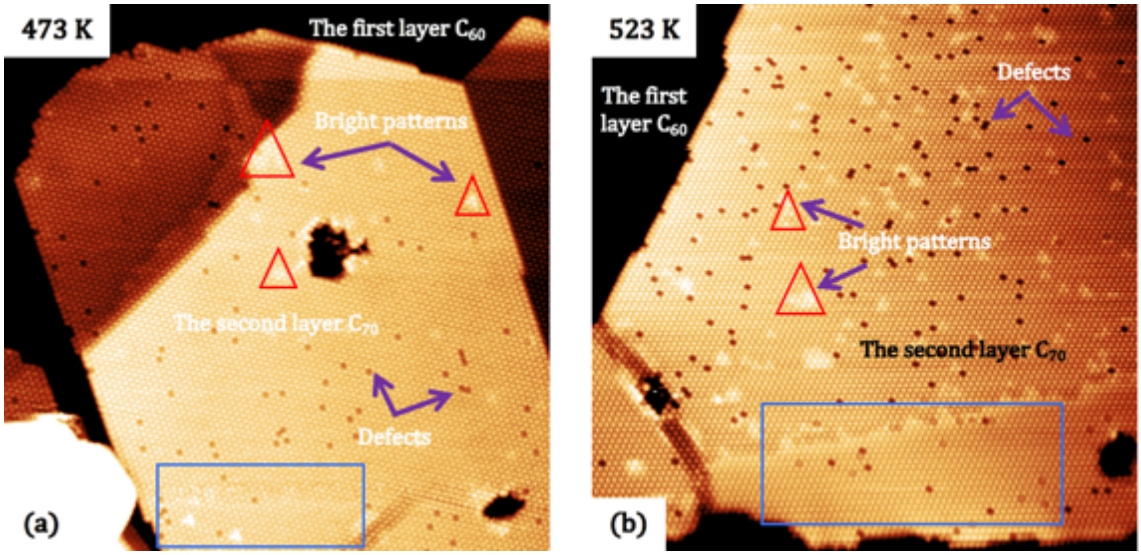


Fig. 5-7 STM images showing a C_{70} island sitting on C_{60} monolayer molecules after being annealed at (a) 473 K and (b) 523 K for one hour. (90 nm × 90 nm, -2.5 V, 100 pA). (a) C_{70} molecules sitting on top of C_{60} monolayer formed larger islands with straighter and sharper boundaries. Dark defects with a depth of 0.10 nm appear randomly on C_{70} islands. The bright C_{70} molecules aggregate and move to the edges of the islands (90 nm × 90 nm, -2.5 V, 100 pA). (b) C_{70} molecules forming large islands with irregular shapes on C_{60} monolayer. There is a noticeable increase in the number and density of monomer and dimer defects in the second layer. Bright patterns tend to move towards and gather at the islands' edge (80 nm × 80 nm, -2.5 V, 100 pA) [17].

When the sample was further annealed at 523 K, as demonstrated in Fig. 5-7 (b), most of the islands have agglomerated, and a higher density of the molecular defects are observed in the C_{70} islands. In between these defects, there are small protruding C_{70} trimers formed by C_{70} molecules, and the bright patches at the edge of C_{70} islands have ripened. A recessed, incomplete boundary separates the two islands which have merged after being annealed. The defects appear due to the orientation difference of the two C_{70} phases with a packing structure of R30° and R0° before merging. In conclusion, (i) During the process of annealing, C_{70}

islands sitting on top of C_{60} thermally aggregate. (ii) The second layer of C_{70} can affect the packing of C_{60} in the first layer. (iii) When supporting C_{70} islands above, C_{60} molecules do not jump up to the second layer islands during annealing due to their strong bonding with the gold substrate.

5.5 Change of Bias Voltage for The Mixed C_{60} and C_{70}

Charge state information of the fullerene molecule-gold interlayer and gold substrate are convoluted as the STM tip scans over the surface with certain bias voltages. Fig. 5-8 shows a series of STM images scanning the same area scanned with a bias voltage of $+2.0$ V, $+0.7$ V, -0.7 V and -2.0 V respectively. The tunnelling current is fixed at 100 pA. In the selected region, some isolated C_{70} molecules are found squeezing in 1 ML periodic $(2\sqrt{3} \times 2\sqrt{3})$R30° C_{60} phase on the Au(111) surface and keeping their positions unchanged. The guest C_{70} molecules are shown as the brightest spots in the scanning images. In the R30° phase, C_{60} molecules sitting close to and far from the guest C_{70} molecules show the same brightness. As the bias voltage sweep from $+2.0$ V to -2.0 V, the C_{60} molecules are found having a stronger voltage dependence compared with C_{70}.

The highest occupied molecular orbital (HOMO) and the lowest unoccupied molecular orbital (LUMO) of C_{60} for monolayer are -1.7 eV and $+1.0$ eV on Au(111) surface [22]. Previous research has shown that, for the close-packed C_{60} in the periodic R30° phase, if assuming all the molecules face the gold substrate with their carbon hexagons, the adsorption energy difference of molecules on hollow sites and bridge sites is ~ 0.05 eV [23]. By applying the bias voltage of $+2.0$ V ($> +1.0$ V) to the gold sample during scanning, electrons transfer from both the occupied orbitals of C_{60} molecules as well as the gold substrate to the scanning tip. The variety of adsorption energy leads to different charge distributions of C_{60} molecules, which make some of them brighter than the others

in the scanning images. When the bias voltage decreases to $+0.7$ V ($< +1.0$ V), the contribution from molecular orbitals is minimized. Therefore, the tunnelling current detected from each C_{60} molecule is similar, which makes their brightness tending to be uniform.

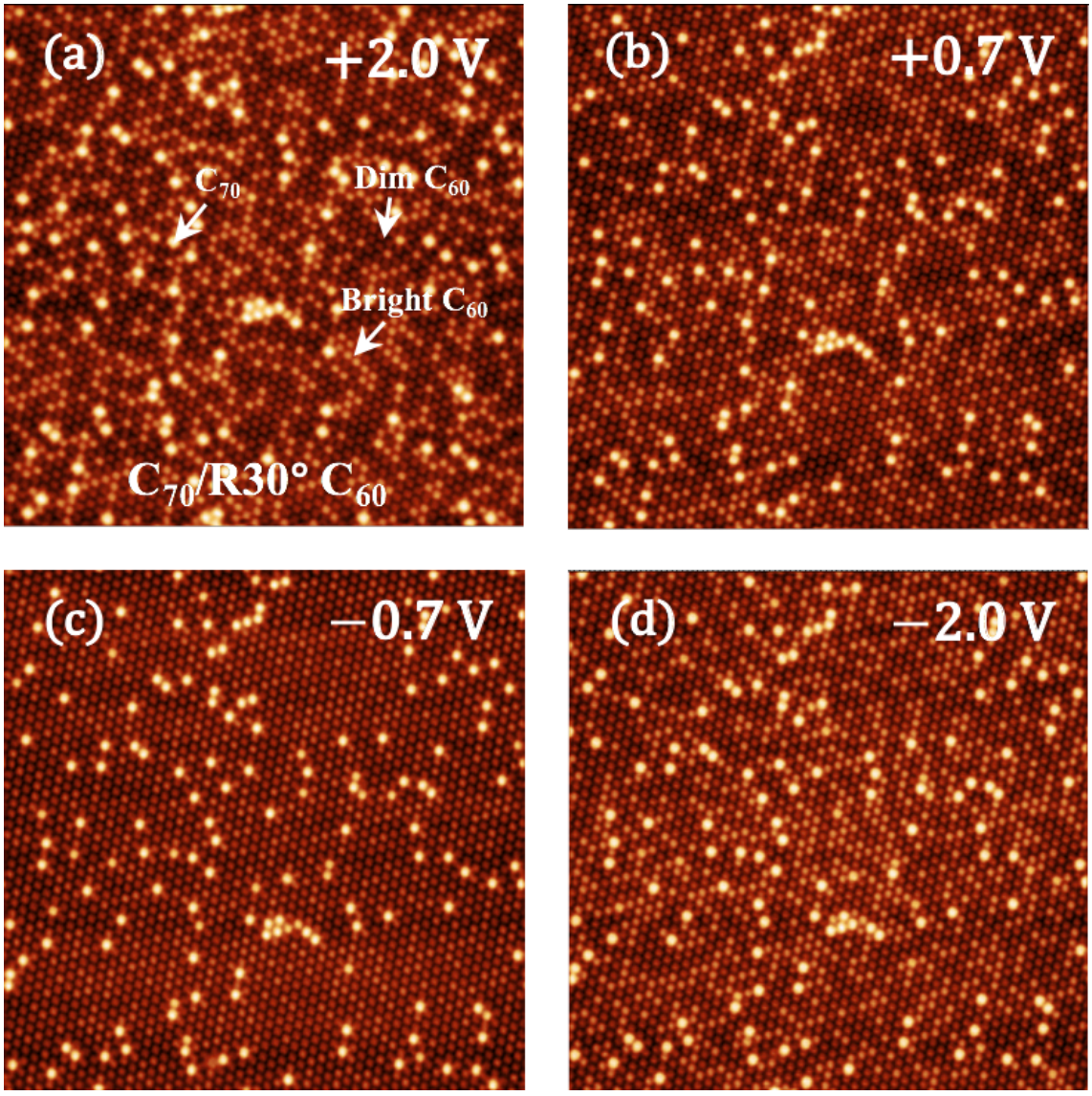


Fig. 5-8 STM images showing bias-dependent contrast of the R30° C_{60} domains with trapped C_{70} molecules (35 nm × 35 nm, I= 100 pA). The bias voltages are set as (a) $+2.0$ V, (b) $+0.7$ V, (c) -0.7 V and (d) -2.0 V, respectively.

When the bias voltage is set as minus values, electrons transfer from the scanning tip to the sample. When -2.0 V is applied to the sample, both the unoccupied

orbitals of C_{60} and the gold substrate below receive the elections, making an obvious brightness contrast for the C_{60} sitting on the hollow and random sites. When the bias voltage changes to -0.7 V, there are very few elections transferring from tip to the unoccupied orbitals of molecules. The image then shows a contrast reduction for the bright and dim C_{60} molecules. It is similar to the condition where $+0.7$ V is applied.

Height of the guest C_{70} molecules in Fig. 5-8 are measured larger than C_{60} and do not change even the bias voltage value decreases to 0.7 V. The main reason behind this is the different geometric shapes of C_{60} and C_{70}. All the guest C_{70} stand upright with their long axes perpendicular to the substrate, and are ~ 0.05 nm taller than the surrounding C_{60}. What's more, weak interaction between gold and C_{70} also contributes to this phenomenon. According to the previous research, For monolayer the average bonding energy of C_{70}-Au is smaller than that of C_{70}-Au (1.9 eV) [24]. This different spectroscopic response can be used to differentiate the two types of molecules.

For the periodic R30° C_{70} phases with C_{60} mixed in, the two types of molecules are harder to be distinguished compared with the conditions C_{70} trapped in C_{60} phases. It is due to the existing of molecular defects in the R30° C_{70} phases, which has already been introduced in Fig. 4-4. These defects result from the complicated interface between molecules and gold atoms as well as the tilting or even lying down of C_{70} molecules on the gold substrate. It has been found, the C_{70} molecules around C_{60} islands do not show the uniform brightness, which is probably due to the change of gold-fullerene interface. In this type of mixture, both the guest C_{60} as well as the C_{70} defects appear as dim spots in the scanning image. As shown in Fig. 4-4, most C_{70} defects in R30° phases appear as single dim spots or nucleate as small dim islands with the sizes smaller than 10 molecules, while most guest C_{60} tend to form single chains or merge as large islands with the sizes of more

than 10 molecules. However, it is hard to judge whether these C_{60} islands include one or few C_{70} defects without the help of spectroscopic test.

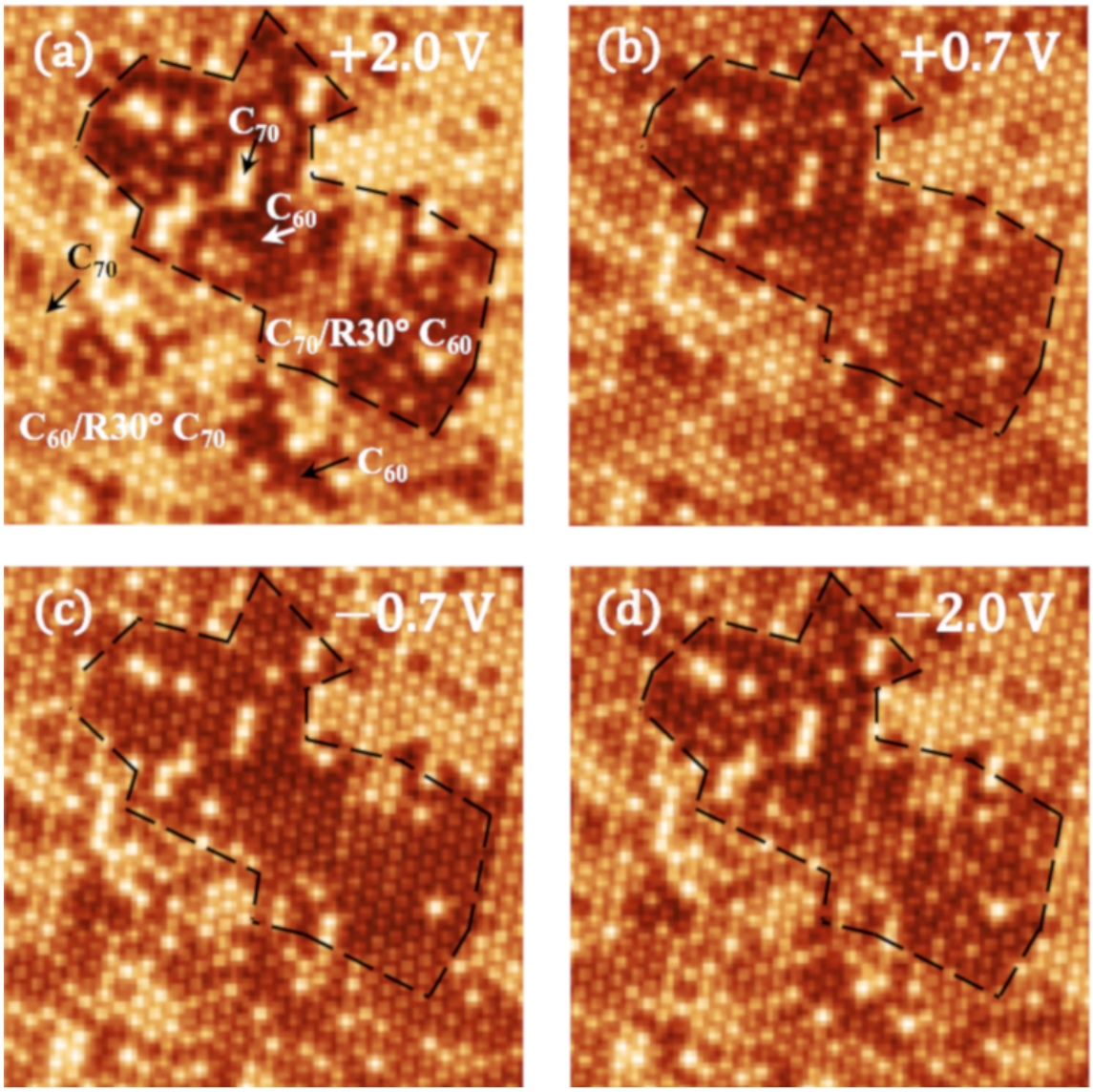


Fig. 5-9 STM images showing bias-dependent contrast of the R30° C_{70} phases with trapped C_{60} molecules (20 nm × 20 nm, I = 100 pA). The bias voltages are set as (a) +2.0 V, (b) +0.7 V, (c) −0.7 V and (d) −2.0 V, respectively. The black dashed lines highlight the contours the C_{60} island trapped in the R30° C_{70} phase.

Fig. 5-9 shows the 1 ML periodic R30° C_{70} phase on the Au(111) surface with C_{60} molecules squeezing in, where rough contours of an imbedding C_{60} island is highlighted by the black dashed lines. C_{60} in these islands pack with the periodic

$(2\sqrt{3} \times 2\sqrt{3})$R30° structure. Once small C_{60} islands appear in the R30° C_{70} domain, the single C_{70} molecules are also able to penetrate through these C_{60} islands and show as the brightest spots. When $+2.0$ V (or -2.0 V) is applied to the sample, C_{70} standing upright have an obvious colour contrast with the C_{60} in the figure. Under this condition, the electronic contribution of both C_{60} and C_{70} molecules can be detected by the STM tip, which are more influential compared with that of gold substrate. Hence the C_{60} molecules can be distinguished from the C_{70} molecules as well as molecular defects in R30° C_{70} phase.

Thus the individual C_{60} islands can be distinguished easily from the brighter C_{70} molecules nearby. By changing the bias voltage to $+0.7$ V (or -0.7 V), most electrons only transfer from the gold substrate to the unoccupied orbitals of C_{70} (Or from the occupied orbitals of C_{70} to the tip). Therefore, brightness of molecules mainly depends on their geometric sizes as well as the molecule-atom interface, while the contribution from molecular orbitals has been filtered out. Some C_{70} outside of the dashed lines gradually become as dark as the trapped C_{60} molecules, which makes the contours of C_{60} island not clear anymore. Compared with the isolated C_{70} mixed in R30° C_{60} phase, the close-packed C_{70} with guest C_{60} islands are more voltage dependent. In other words, the guest C_{60} molecules strongly change the molecule-gold interface in this system. It could be explained by the strong electron affinity of C_{60} molecules, 2.65 ± 0.05 eV [25]. However, by applying high bias voltage, differences in molecular spectroscopic response can always leads to a comparable clear contrast between C_{60} and C_{70} in the two types of binary systems.

5.6 Summary

We found that C_{70} molecules are not as mobile as C_{60} after being deposited on Au(111). With sufficient thermal energy, C_{60} molecules can pass across domain

boundaries and transfer from C_{60}-rich domains to C_{70}-rich domains. These transferred C_{60} molecules aggregate into different sized islands. The larger nearest-neighbour distance between C_{70} molecules in close-packed domains and the weak Van der Waals bonding between C_{60} molecules also accelerate this transfer process. Moreover, the stronger bonding with the gold substrate makes C_{60} harder to desorb or jump onto molecules around. Thus inside the close-packed C_{60} domains, there are fewer molecular vacancies left for C_{70} to occupy.

C_{60} molecules deposited on a close-packed C_{70} monolayer can form isolated single layer islands. Triggered by the lattice mismatch between the two layers, dark bands develop on the second layer and separate C_{60} islands into various sized domains. Under heat treatment, C_{70} molecules can desorb from the first layer and join the C_{60} islands as "guest" molecules. All these guest C_{70} form close-packed structures with their long axis perpendicular to the surface.

C_{70} molecules on the surface of C_{60} monolayer remain in an upright configuration and occupy the three-fold hollow sites on the first layer. During the process of annealing, C_{70} molecules can also merge and reform as larger islands. Compared with C_{70} islands landing on C_{70} monolayer in chapter three, when C_{70} islands sit on a C_{60} monolayer, molecules in the first layer cannot jump up and enter the second layer islands under the same annealing conditions. The extent of molecular exchange is strongly limited, indicating that the close-packed C_{60} sitting on Au(111) are more stable than C_{70}. At high temperature, C_{70} molecules in the second layer are also able to affect the packing of C_{60} molecules in the first layer. Driven by the van der Waals force, C_{60} molecules with weaker interaction to the gold substrate are forced to aggregate together and sit underneath the edge of the second layer islands in order to keep the lattice constant in the upper and lower layers matched.

References

[1] M. S. Dresselhaus, G. Dresselhaus, P. C. Eklund, Science of fullerene and carbon nanotubes: their properties and applications (Elsevier, 1996).

[2] K. Hedberg, L. Hedberg, D. S. Bethune, C. A. Brown, H. C. Dorn, R. D. Johnson, M. De Vries, Science **254**, 410 (1991).

[3] D. R. McKenzie, C. A. Davis, D. J. H. Cockayne, D. A. Muller, A. M. Vassallo, Nature **355**, 622 (1992).

[4] E. I. Altman, R. J. Colton, Surf. Sci. **295**,13 (1993).

[5] G. Schull, R. Berndt, Phys. Rev. Lett. **99**, 226105 (2007).

[6] J. A. Gardener, G. A. D. Briggs, M. R. Castell, Phys. Rev. B: Condens. Matter Mater. Phys. **80**, 235434 (2009).

[7] S. Guo, D. Fogarty, P. Nagel, S. A. Kandel, J. Phys. Chem. B **108**, 14074 (2004).

[8] C. Rogero, J. I. Pascual, J. Gomez-Herrero, A. M. Baro, J. Chem. Phys. **116**, 832, (2002).

[9] X. Zhang, F. Yin, R. E. Palmer, Q. Guo, Surf. Sci. **602**, 885 (2008).

[10] L. Tang, X. Zhang, Q. Guo, Y. N. Wu, L. L. Wang, H. P. Cheng, Phys. Rev. B 82, 125414 (2010).

[11] L. Tang, Y. C. Xie, Q. Guo, J. Chem. Phys. **135**, 114702 (2011).

[12] Y. C. Xie, L. Tang, Q. Guo, Phys. Rev. Lett. **111**, 186101 (2013).

[13] D. Kaya, D. Bao, R. E. Palmer, S. Du, Q. Guo, Nano Lett. **17**, 6171 (2017).

[14] Y. C. Xie, M. Rokni Fard, D. Kaya, D. Bao, R. E. Palmer, S. Du, Q. Guo, J. Phys. Chem. C **120**, 10975 (2016).

[15] Y. T. Wang, L. Guo, Q. Guo, J. Phys. Chem. C **123**, 7776 (2019).

[16] T. Chen, S. Howells, M. Gallagher, D. Sarid, L. D. Lamb, D. R. Huffman and R. K. Workman, Phys. Rev. B **45**, 14411 (1992).

[17] Y. Wang, L. Guo, and Q. Guo, J. Phys. Chem. C **123**, 7776 (2019).

[18] J. A. Gardener, G. A. D. Briggs, and M. R. Castell, Phys. Rev. B **80**, 235434 (2009).

[19] S. Guo, D. Fogarty, P. Nagel, and S. A. Kandel, J. Phys. Chem. C **5513**, 185 (2004).

[20] L. Tang, Q. Guo, Phys. Chem. Chem. Phys. **14**, 3323 (2012).

[21] L. Guo, Y. T. Wang, D. Kaya, R. E. Palmer, G. D. Chen, and Q. Guo, Nano Lett. **18**, 5257 (2018).

[22] C. T. Tzeng, W. S. Lo, J. Y. Yuh, R. Y. Chu, and K. D. Tsuei, Phys. Rev. B **61**, 2263 (2000).

[23] L.-L. Wang, and H.-P. Cheng, Phys. Rev. B **69**, 165417 (2004).

[24] F. Rossel, M. Pivetta, F. Patthey, E. Cavar, A. P. Seitsonen and W.-D. Schneider, Phys. Rev. B **84**, 075426 (2011).

[25] L. S. Wang, J. Conceicao, C. Jin, and R. E. Smalley. Chem. Phys. Lett. **182**, 5 (1992).

6. Orientational Epitaxy of Van der Waals Molecular Heterostructures

6.1 Introduction

Van der Waals force is a general term defining the weak and short-range electrostatic forces existing between molecules [1]. It results when electrons in the two adjacent molecules form temporary dipoles [1]. Dipole-dipole forces and London dispersion forces are the two most typical van der Waals forces. The London dispersion force is the weakest intermolecular force with the bonding energy ranging from 0.02 eV to 0.1 eV [2]. In this chapter, I report findings from a recent study of the intermixing of C_{60} and C_{70} on the HOPG substrate using STM under ultrahigh-vacuum (UHV) conditions. We study the mixing process with different fullerene deposition sequences and investigate temperature influences on the mixing. Due to the different lattice parameters, a C_{60}-C_{70} bilayer is expected to be strained with tensile stress in the C_{60} layer and compressive stress in the C_{70} layer. We also report findings on the orientation switching of the C_{70} molecule and the detailed structure of the C_{60}-C_{70} interface.

6.2 Experimental Procedure

Highly oriented pyrolytic graphite (HOPG) (purchased from Goodfellow, 99.99% purity) was used as the substrate. It was firstly annealed in UHV at 475 K for 30 min to remove surface contamination. Afterwards, C_{60} and C_{70} molecules (purchased from MER, 99.5% purity) were sublimed onto the HOPG substrate by home-built effusion cells. The effusion cells are degassed at 500 K for 5 min before sublimation. The C_{60} and C_{70} molecules were deposited on the surface with a rate of 0.12 and 0.10 ML/min, respectively. During the deposition, the background pressure in the UHV system does not exceed 10^{-9} mbar, thus STM

imaging was performed with a room temperature Beetle-type 400 RHK UHV STM and also with an Omicron UHV VT STM. Electrochemically etched tungsten tips were used after high-temperature annealing in UHV chamber. Images were collected using the constant current mode with the tunnelling current set at 0.1 nA and bias voltage in the range between +2.00 V and +2.58 V. Gwyddion [3] software was used to analyse the raw data acquired by the RHK-XPM Pro 2.1.6 and the Omicron MATRIX 3.3.

For the investigation of molecular mixing, we prepared two samples with sequentially deposited molecules. i) The first sample was deposited with 1.2 ML of C_{60} with an extra 0.2 ML of C_{70} added afterwards. ii) The second sample was deposited with 1.2 ML of C_{70} with an extra of 0.2 ML of C_{60} added afterwards. In each case, the sample was gradually heated up to higher temperatures. After heating up to each temperature, STM imaging was performed to examine the mixing of C_{60} with C_{70} molecules.

6.3 1.2 ML of C_{60} (C_{70}) on HOPG

After the deposition of 1.2 ML C_{60} molecules on the surface at room temperature, we observed two incomplete layers of C_{60}. The first layer formed directly above HOPG covers ~ 60 % of the substrate. The second layer C_{60} consists of islands sitting on top of the first layer. Although the total coverage is greater than one monolayer, there is still a small fraction of bare graphite because the second layer starts to form before the first layer is completed.

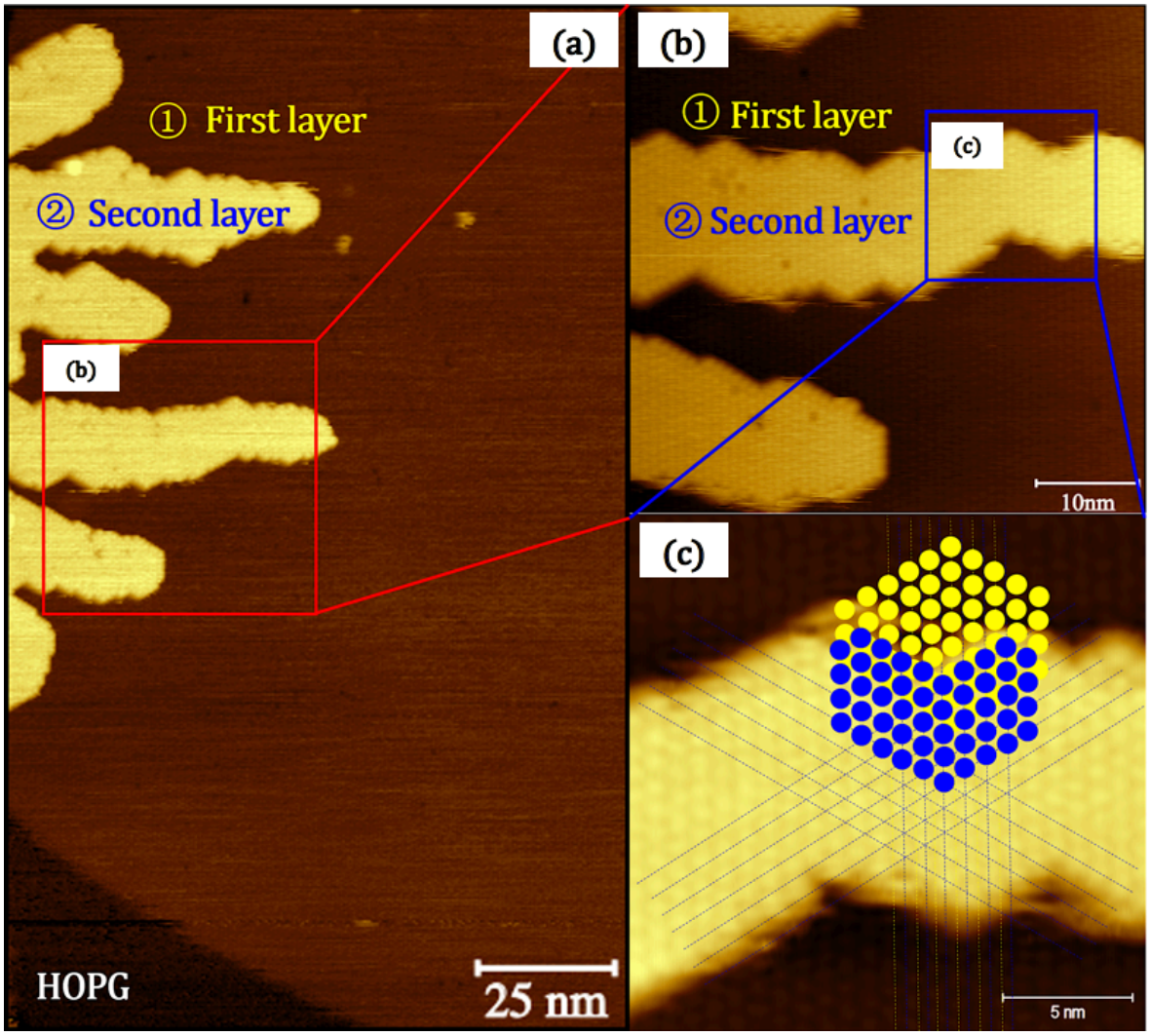


Fig. 6-1 1.2 ML of C_{60} sitting on HOPG at room temperature. (a) An area of HOPG showing a large fraction of the surface covered by a single layer of C_{60}, the existence of the second layer C_{60} and a small area of bare HOPG. (b) A selected area in (a) showing the details of the step edge structure of the C_{60} fingers. (c) Ball model superposed on top of the STM image for illustrating the positioning of the second layer molecules. (d) Close-packed blue and yellow spheres representing the positions of molecules in the second and first layer and showing the relationship of their positions.

Fig. 6-1 (a) shows an STM image of the sample with 1.2 ML C_{60}. At the bottom-left corner of the image, there is a small area of uncovered HOPG. The rest of the image shows a smooth first layer with finger-like structures in the second layer. The adsorption energy of C_{60} on top of a C_{60} layer is calculated to be 968 meV which is slightly higher than the 813 meV adsorption energy of C_{60} on HOPG.

The diffusion barrier for C_{60} on HOPG is only 12 meV, which is much lower than the 168 meV barrier for C_{60} on top of a C_{60} layer [4,5]. Therefore, C_{60} molecules are mobile on HOPG at RT and the first layer of C_{60} is expected to adopt a thermodynamic equilibrium shape. The finger-like structure of the second layer C_{60} is a result of diffusion-limited growth due to the much higher diffusion barrier. Applying simple triangulation on high-resolution images, we can identify that the second layer molecules occupy the three-fold hollow site of the first layer. Inset in Fig. 6-1 (a) is a ball model illustrating the positional relationship between the first two C_{60} layers assuming that further layers added would create an FCC crystal. Fig. 6-1(b) shows that the edges of the fingers are faceted exposing close-packed molecular rows. The azimuthal orientation of the C_{60} molecular rows relative to the HOPG is not analysed here. This is because of the difficulty in imaging the C_{60} layer and the HOPG substrate simultaneously with high resolution [6].

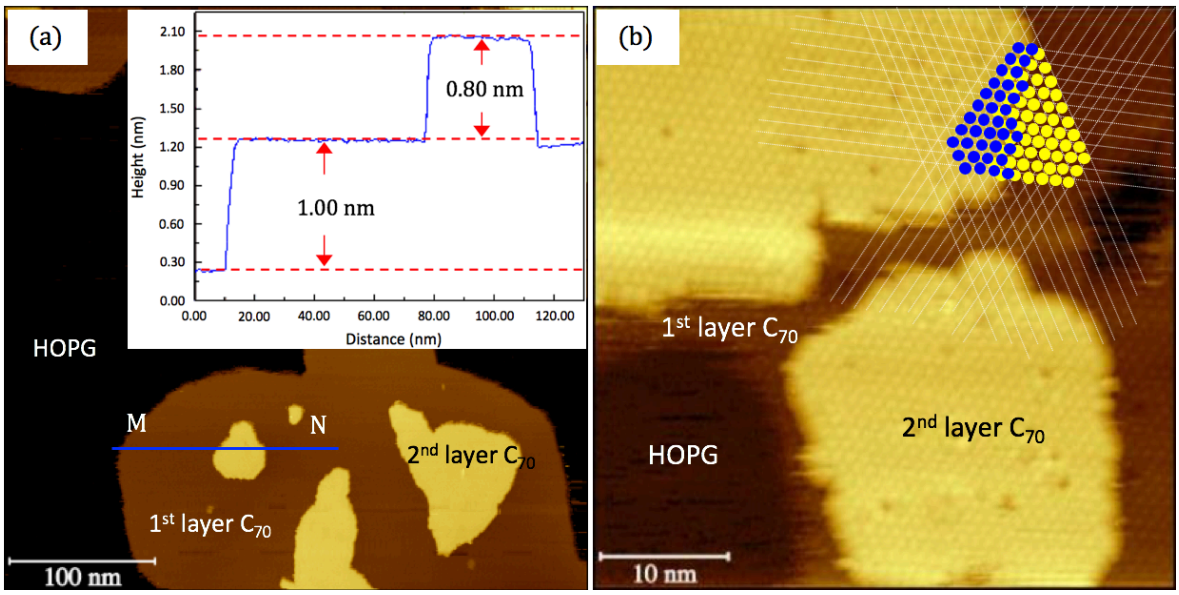


Fig. 6-2 1.2 ML of C_{70} on HOPG at room temperature. (a) A large area STM image shows the co-existence of bare HOPG, first layer C_{70} and second layer C_{70}. Inset graph shows the height profile of the first and second layers. (b) Ball model superposed on the top of an STM image. Yellow coloured circles represent the first layer molecules and blue circles are for the second layer molecules. The dashed lines help to determine the occupation site of the second layer molecules.

Fig. 6-2 shows STM images acquired from an HOPG substrate covered by 1.2 ML of C_{70}. Similar to what is already seen with C_{60}, the second molecular layer is formed before the first layer is completed. The edges of the second layer C_{70} island are ragged. Finger-like structures are also observed for second layer C_{70}. Due to the weak van der Waals interaction between molecules and the effect of electric field at the tip apex [7], C_{70} molecules are found to move around on the surface and the shape of the second layer islands gradually changes in time while the surface is being imaged under the STM. Inset in Fig. 6-2 (a) shows a height profile measured along the blue line M-N. Based on this height profile, the first layer measured from the HOPG surface is 1.00 nm tall. The second layer is 0.80 nm above the first layer. These values are approximately consistent with two layers of close-packed hard spheres with the second layer spheres sitting in the three-fold hollow sites. For C_{60} on HOPG, the first layer is 0.80 nm above the HOPG substrate, and the second C_{60} layer is 0.70 nm above the first layer. As will be discussed later, the C_{70} molecule rotates freely within the molecular layer at RT. For a free rotating ellipsoidal molecule, it has an effective diameter. The 1.00 nm height measured thus corresponds to such an effective diameter. In fact, a C_{70} molecule standing on HOPG with its long axis permanently perpendicular to the substrate appears taller than 1.00 nm. Moreover, from the ball model in Fig. 6-2 (b), it can be concluded that the C_{70} molecules within the second layer occupy the three-fold hollow site of the first layer.

6.4 Deposition of 0.2 ML C_{70} (C_{60}) on 1.2 ML C_{60} (C_{70}).

Fig. 6-3 shows STM images acquired from the sample after adding 0.2 ML of C_{70} molecules on the HOPG substrate which has already been covered by 1.2 ML of C_{60}. Structures similar to that in Fig. 6-3 have been reported previously [8,9]. As can be seen in Fig. 6-3 (a), the C_{70} molecules are attached to the edges of the pre-formed C_{60} island. For the second layer, each C_{60} island is enclosed by a rim with

a fairly uniform width of C_{70} molecules. The C_{70} rim follows exactly the contour of the existing C_{60} island. Hence, the addition of C_{70} does not affect the shape of the C_{60} island and a sharp boundary between the C_{60} island and the C_{70} rim can be recognized easily. For the first layer, the additional C_{70} molecules also form a rim, but the width of the rim is rather non-uniform. In some places, the rim is just one or two molecules wide, whereas in other places, it is more than 10 molecules wide. The non-uniform width of the rim in the first layer is consistent with the high mobility of the two types of molecules on HOPG. That is, molecules already captured by the C_{60} island still can move via edge diffusion. While for the second layer, it is more like a capture and stick situation. In addition, it can be seen that the boundary between C_{60} island and C_{70} rim is fuzzy on the first layer, which suggests that the mixture of the two molecules has taken place. This is an expected phenomenon since the edge of the C_{60} island on HOPG is rather fluidic at RT with molecules constantly leaving and joining. Fig. 6-3 (b) shows a height profile measured along line P-Q in Fig. 6-3 (a). The C_{70} rim in the first layer is 0.95 nm above the HOPG substrate, which is 0.15 nm taller than C_{60} molecules within the same layer. Besides, the C_{70} rim in the second layer is also 0.15 nm taller than the C_{60} molecules in the same layer.

Fig. 6-3 (c) is a magnified view of an area on the second layer which illustrates the C_{70} molecules seamlessly attach to the boundary of C_{60} island. Fig. 6-3 (d) is a height profile measured along line R-S. This line profile confirms that the C_{70} molecules form a natural extension from the existing C_{60} layer with no lateral defect in between except that the C_{70} is taller. It also shows that the nearest neighbour distance is the same for both C_{60} and C_{70} within the second layer. Therefore, C_{60} and C_{70} molecules in the second layer occupy the same type of hollow site. This further suggests that C_{70} molecules sitting above a C_{60} layer have their molecular axis perpendicular to the surface in order to fit the lattice parameters of the underlying C_{60} layer. From high resolution images shown later,

we find that for the first C_{70} layer, the nearest neighbour distance is 1.14 nm whereas for the first layer C_{60}, the nearest neighbour distance is 1.05 nm. These nearest neighbour distances are consistent with the lattice parameters for C_{70} and C_{60} crystals at room temperature.

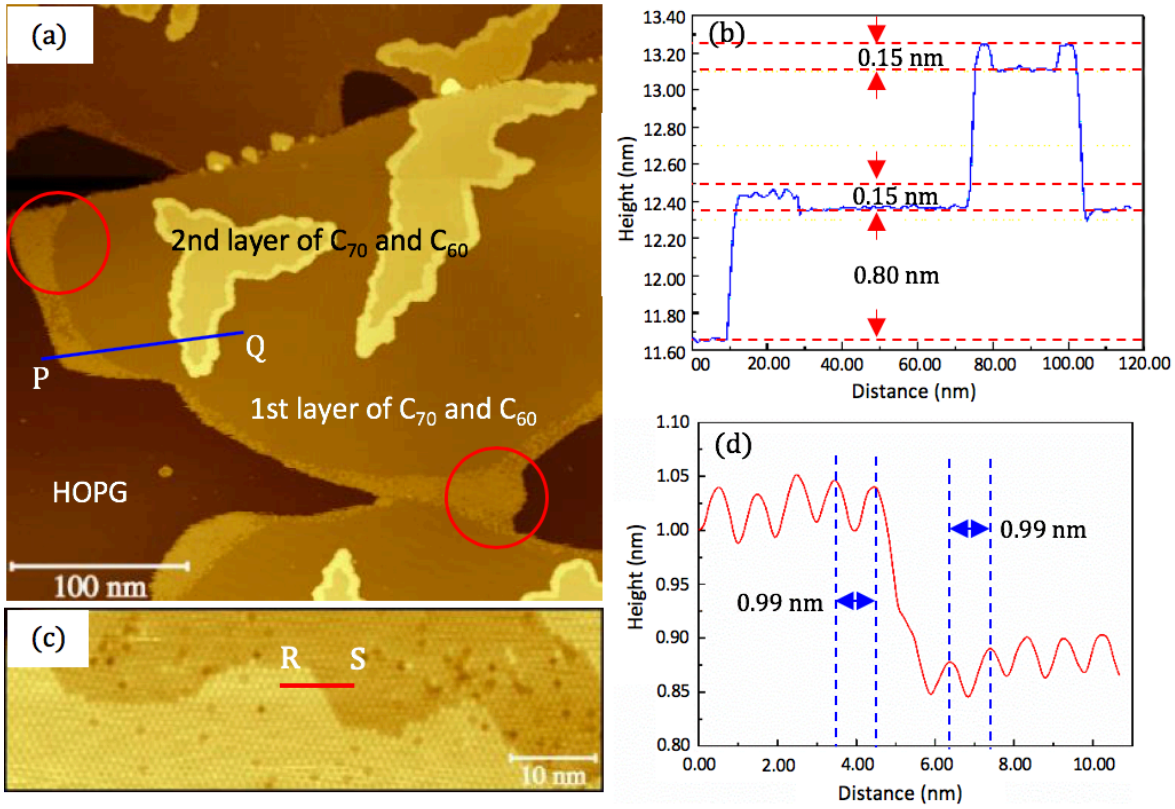


Fig. 6-3 0.2 ML of C_{70} added onto a pre-existing 1.2 ML of C_{60} on HOPG at room temperature. (a) C_{70} molecules attach to the edges of the C_{60} island forming rims in both the first and the second layer. (b) The height profile measured along line P-Q in (a). (c) Magnified view of a C_{60}-C_{70} boundary in the second layer. (d) Height profile measured along line R-S in (c).

After completing the experiment described above, we changed the deposition sequence. 1.2 ML of C_{70} on HOPG was primarily deposited on HOPG and 0.2 ML of C_{60} was added afterwards. As shown in Fig. 6-4 (a), the C_{60} molecules form close-packed layers, enclosing the pre-existed C_{70} islands on both the first and the second layers. Besides, a small patch of C_{60} is formed on top of the second layer of C_{70} molecules. Fig. 6-4 (b) shows the structure of a boundary between C_{60} and C_{70} in the first layer. Intermixing has clearly taken place at the boundary.

Formation of such a combined boundary is expected since the C_{70} molecules on the edges of the initial island have relatively high mobility. As a result, a significant number of C_{70} molecules detach from the edges and mix with the newly added C_{60} molecules at room temperature. Therefore, the final structure consists of a pure C_{70} and C_{60} region with a narrow region of mixed C_{60} and C_{70} sandwiched in between. From the image in Fig. 6-4 (b), one can estimate the distance that a C_{70} molecule can travel when it manages to escape from the edge of the C_{70} island. Here the average distance is about 5-6 nm. In other words, a C_{70} island on HOPG is surrounded by its "vapour atmosphere" with a dimension of 5-6 nm at RT. The diffuse boundary is formed during the addition of C_{60} to the surface. Once the boundary is formed, no further diffusion across the boundary diffusion can take place at RT. For C_{60} molecules inside the C_{70} territory, there appears to be the tendency that C_{60} molecules group together and form a short row. Preferred directional bonding could be one of the reasons for explaining this phenomenon. However, considering that orientation ordering within C_{60} and C_{70} crystals are destroyed by thermal energy at RT, it is unlikely that the directional bonding drives the formation of the C_{60} rows. A more likely reason is associated with the strain induced by the insertion of C_{60} into the C_{70} layer. One single isolated C_{60} molecule inside a C_{70} layer disturbs the bonding of six C_{70} molecules. By forming a row, the number of affected C_{70} molecules per C_{60} molecule is minimised and therefore this structure is more favoured.

Unlike the first layer, the boundary between C_{60} and C_{70} in the second layer is sharp as shown in Fig. 6-4 (c). This indicates the edges of the C_{70} islands in the second layer are more stable. The edge diffusion might still exist, but no C_{70} molecules can escape from the edges of the island.

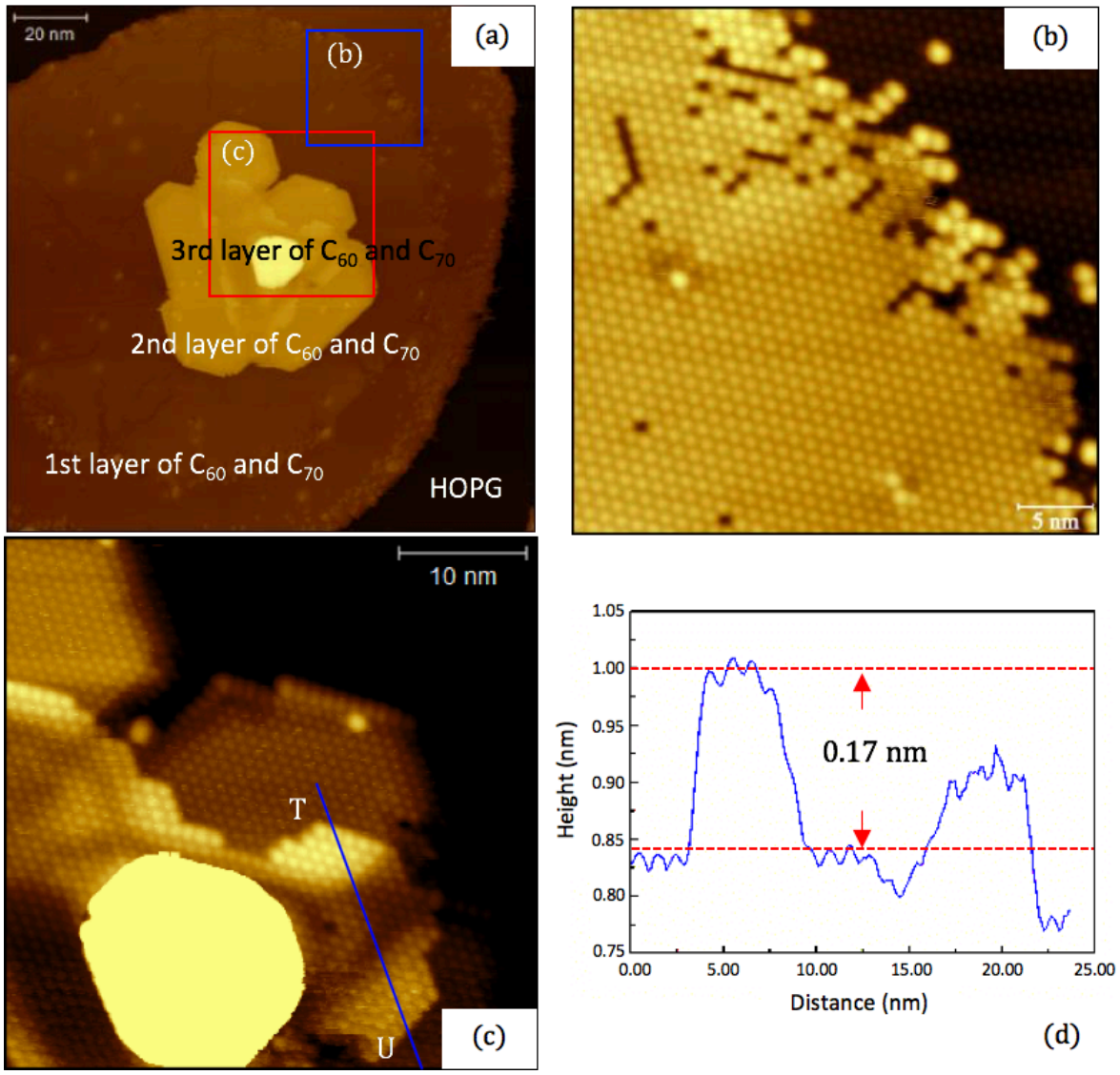


Fig. 6-4 Close-packed C_{60} island as the second layer on C_{70} islands on HOPG at RT. (a) STM image of a large area illustrating different island orientation and grain boundaries between C_{60} and C_{70} molecules. (b) and (c) Close section image of (a) which show different grain boundaries and occupied structure with centre molecules, respectively. (d) The height profile following the blue line T-U shown in (c).

The post-deposited 0.2 ML of C_{60} seems to have the ability to attack the preformed 1.2 ML C_{70}. It is noticed that some "cracks" formed within the first C_{70} layer suggesting the possibility that C_{60} molecules squeezing into the first layer C_{70} layer upon landing. The second layer C_{70} is also affected showing the appearance of dark "wrinkles" or "bands" after the addition of C_{60}. This is in

contrast with the preformed C_{60} layer when C_{70} molecules are added. Individual C_{70} molecules cannot break the dense C_{60} layer and thus mixing is mainly restricted to the first layer boundaries.

As a mismatch on the right side has been observed in Fig. 6-4 (b), we can conclude that molecules at the outside of the island occupy the hollow site of the first layer of C_{70} molecules. This feature is different from the location of C_{70} molecules on top of the first layer of C_{70}, as shown in Fig. 6-2 (b). As we carefully check the height profile following the blue line T-U in Fig. 6-4 (c) which shows some unusual height distribution, the maximum height is about 0.17 nm, which reduces gradually as approaching to the valley between wrinkles. The outside of wrinkle has a perfect packing structure consisting of C_{60} molecules. Hemantkumar *et al*. [8,9] report that there was some orientation disorder in the C_{70} packing structure on HOPG which is quite different compared with our observation, there is no any other elements was introduced except the carbon. It is very unusual that a defect-free C_{70} packing structure shows here even though there is a lattice mismatch between C_{60} and C_{70} in the close-packed phases. It implies a kind of local strain-free structures existing close to the boundary of C_{60} and C_{70} islands.

6.5 Thermally Activated Structural Evolution

In this section, we examine how the structure of the C_{60}/C_{70} layers respond to different sample temperatures. The sample was annealed for 30 minutes at a fixed temperature and then cooled down to RT for STM imaging. The annealing temperature was increased in several steps from 375 K to 475 K.

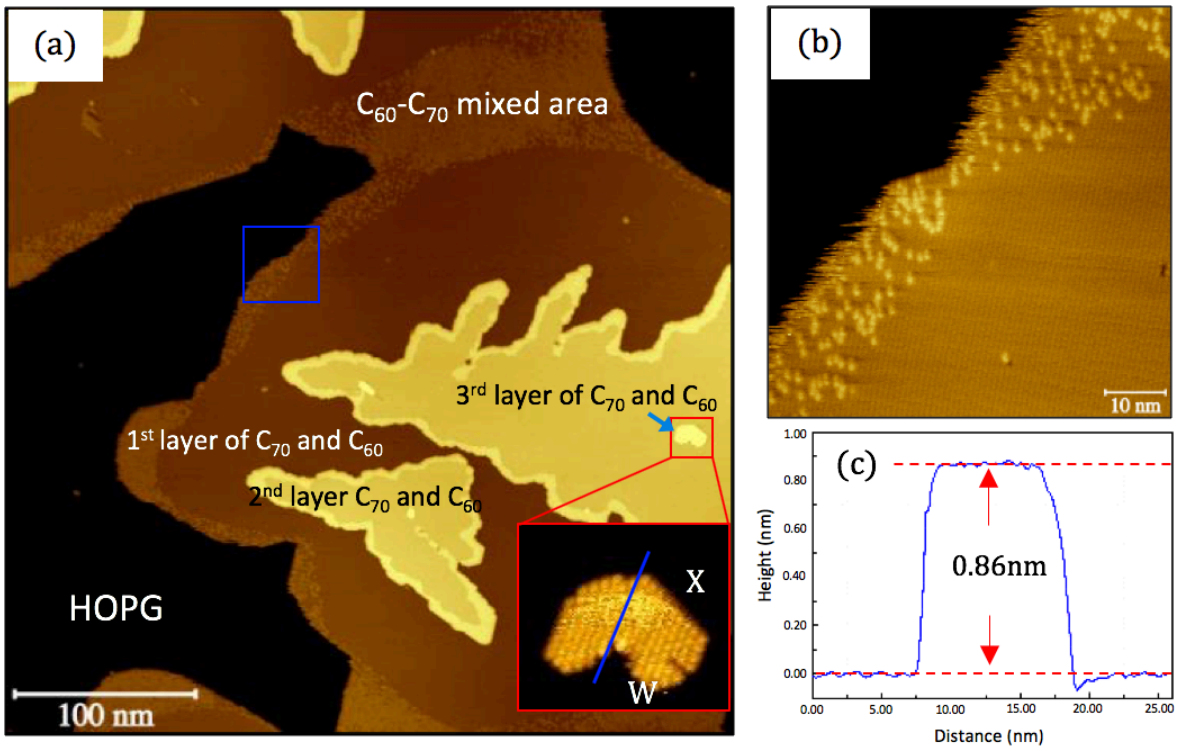


Fig. 6-5 The morphology of C_{70}-C_{60} on C_{60}/HOPG after annealing at 373 K for 30 min. (a) The morphology of packing structure at low resolution. The insert showing the high-resolution image of the third layer of C_{60} molecular is marked in the red rectangle. (b) The packing structure high-resolution image of the area in the blue rectangle showing in the (a). (c) Line profile along the line X-W showing the height of molecules in the fourth layer islands, which is measured as 0.86 nm.

Fig. 6-5 shows the morphology of the 0.2 ML C_{70} on 1.2 ML C_{60} sample after annealing at 375 K for 30 min. The C_{70} rim in the first layer is broken due to the inward movement of the C_{70} molecules. Some C_{70} molecules have moved by more than 10 nm into the C_{60} layer, which can be seen in Fig. 6-5 (b). In the second layer, the boundary between C_{60} and C_{70} is still sharp. As mentioned before, there is a "vapour" atmosphere in equilibrium with the "solid" first layer. Annealing to 375 K provides the opportunity for C_{60} and C_{70} to mix in this vapour phase. After annealing, the vapour condenses into a "solid". From Fig. 6-5, it can be concluded that the vapour phase at 375 K covers a distance of ~ 10 nm. Bulk of the first layer remains in the solid phase and hence the second layer in Fig. 6-

5 (a) retains its shape at the end of the annealing. A third layer island is formed showing in the inset of Fig. 6-5 (a). The height of this island alone the line W-X illustrated in Fig. 6-5 (c) is measured as 0.86 nm, which is consistent with the height of C_{70} on the second layer. Therefore, during annealing, some C_{70} molecules have managed to climb up the step edge and aggregated into a third layer island.

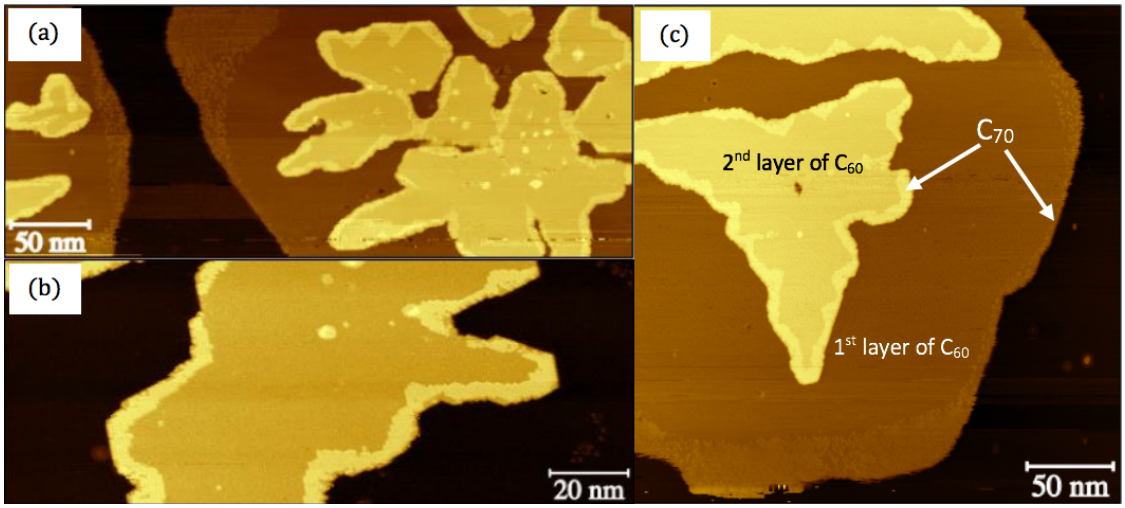


Fig. 6-6 The morphology of C_{70}-C_{60} on C_{60}/HOPG after annealing at 425 K for 30 min. (a) The low-resolution image of packing structure. (b) and (c) The high-resolution image of packing structure.

Fig. 6-6 shows the STM images acquired after annealing the sample to 425 K. In comparison with images shown in Fig. 6-5, the morphology of the molecular layers has barely changed by increasing the annealing temperature from 375 K to 425 K. Substantial variations of the morphology of the molecular layers are observed after annealing the sample to 475 K. Most remarkable changes are the appearance of molecular islands in the third layer and the erosion of the C_{70} rim in the second layer. Two third-layer islands appeared as can be seen in Fig. 6-7 (a). The formation of the third layer islands requires vertical upwards transportation of molecules. Since the binding of molecules to the HOPG substrate is weaker than that in between two layers of molecules, thermally

induced molecular transport from the first layer into the higher layers is expected to take place. The stronger inter-layer binding hence favours the growth of multilayers.

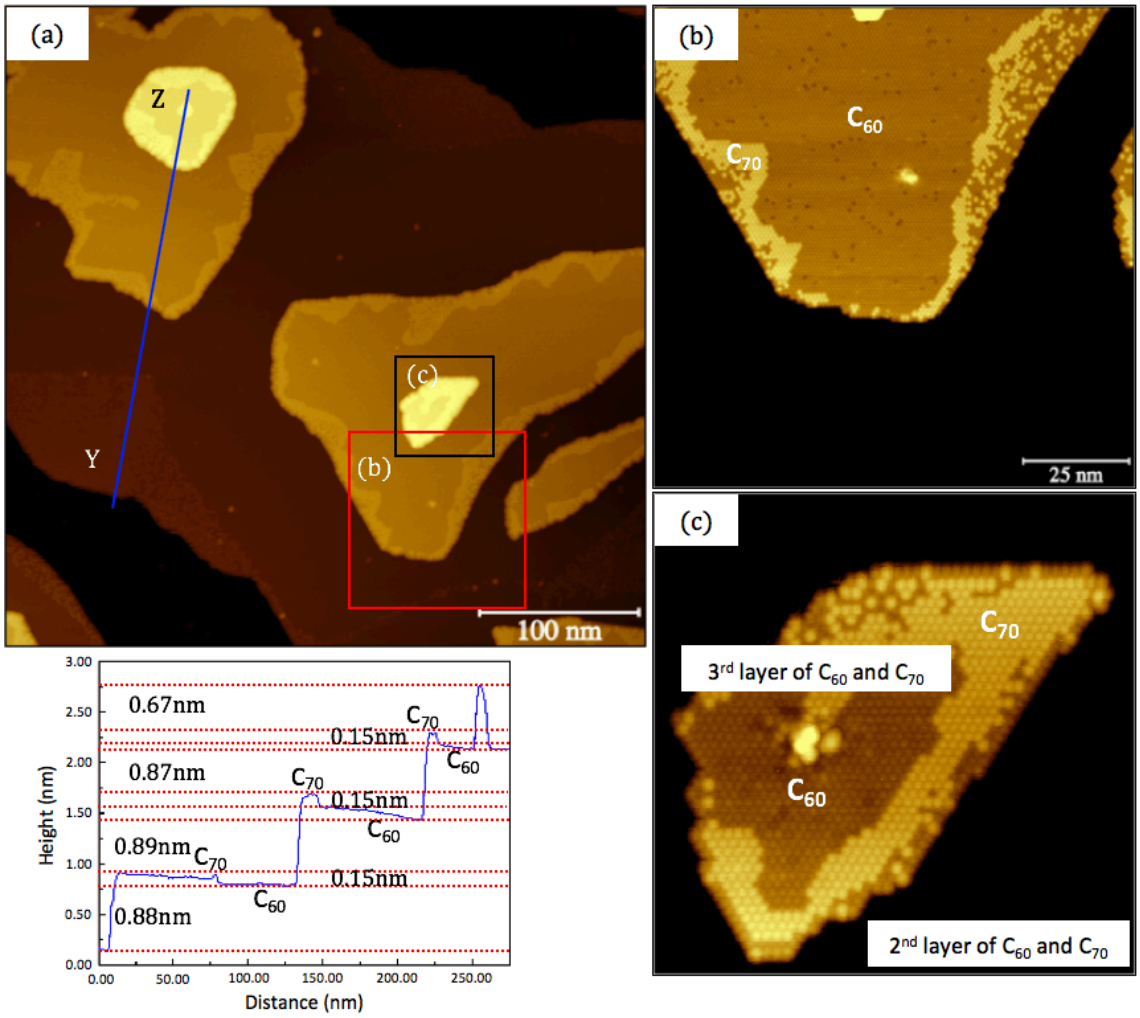


Fig. 6-7 The morphology of mixed C_{70}-C_{60} on C_{60}/HOPG after annealing at 475 K for 30 min. (b) and (c) is the high-resolution image of makers in the (a). Line profile showing the measured height along Y-Z line in (a).

Another significant observation is that the newly formed third layer consists of a C_{60} core and a C_{70} shell, as shown in Fig. 6-6. We did not image the surface during heating of the sample, and thus there is no direct observation of how the third layer island is formed. However, the structure of the island is consistent with the following speculation. During thermal annealing, both C_{60} and C_{70} molecules

climb up to a higher level. Nucleation starts with C_{60} and C_{70} molecules join the C_{60} island at a later stage to form the shell. Furthermore, the shape of the second layer islands becomes more regular with smoother edges. The C_{70} rim has gone through some reorganization as well and there is clearly intermixing of C_{70} and C_{60} molecules around the rim.

In Fig. 6-7 (a), we found that the packing structure on the second layer is surrounded by C_{70} molecules with smooth edges. Also, the C_{70} molecules tend to melt into the C_{60} molecules during the annealing, and branches of the third layer islands have disappeared. Along the line Y-Z in Fig. 6-7 (a), the height profile shows that the height of C_{70} on these three layers are sharing the same value of ~ 1.00 nm, which agrees with the previous studies [12-14]. In addition, the molecules located at the edge of the molecular islands gain enough energy to diffuse and "run away" from the island during annealing. The diffusion distance of the C_{60} and C_{70} molecules are different due to their different interactions with HOPG substrate [10]. With the cooling down to RT process, the molecules gather together again, resulting in the mixture of the C_{60} and C_{70} molecules. On the other hand, the molecules gain enough energy to overcome the inter-molecules interaction and reshape into a perfect closed-pack structure. As mentioned before, the third layer of C_{70}-C_{60} packing structures were formed when annealed at 475 K, we didn't observe any C_{70} molecules on top of the third layer.

In the following, consider structural changes responding to annealing temperature for a sample prepared by deposition of 0.2 ML of C_{60} on top of a pre-formed 1.2 ML C_{70} are discussed. Fig. 6-8 illustrates the expected multilayer structure. As mentioned earlier, the C_{70} layer on HOPG is not as robust as the C_{60} layer. During the deposition of C_{60}, C_{60} molecules are found to be able to mix into the preformed C_{70} layer when the sample is at RT.

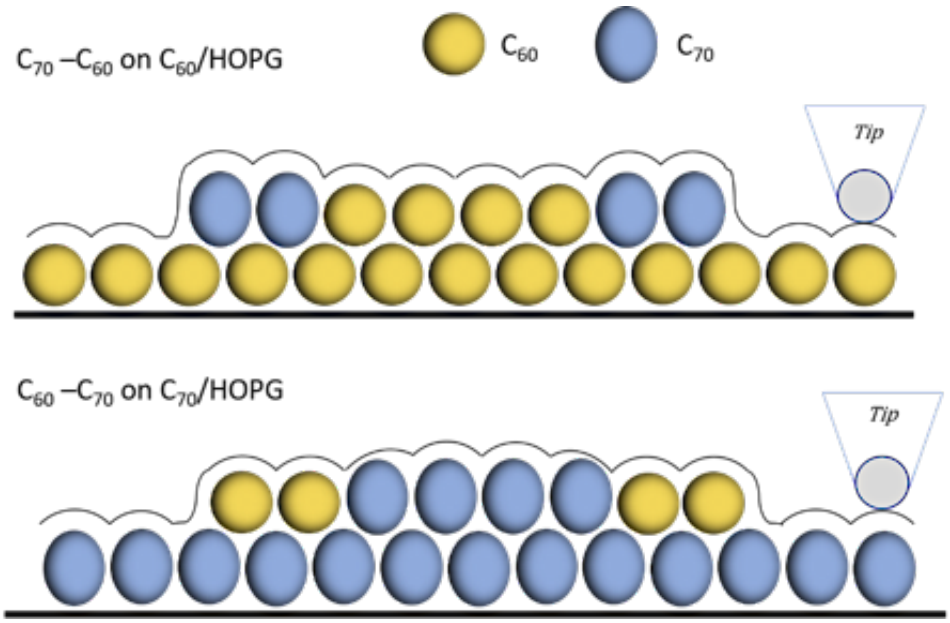


Fig. 6-8 schematic diagram showing the expected multilayer structure of C_{70}-C_{60} on C_{70}/HOPG.

Fig. 6-9 (a) shows the structure of the molecular layers observed with the STM after annealing the sample to 375 K. In Fig. 6-9 (b), one can see the incorporation of C_{60} into the first layer of C_{70}. However, the structures of the second molecular layer are demonstrated in Fig. 6-9 (c), is somewhat unexpected. Although the boundary between C_{70} and C_{60} can be identified, the height difference between C_{70} and C_{60} is well below the expected value.

A possible explanation for the apparent diminishing height difference between the two molecules is the re-organization of the C_{70} layer beneath the C_{60}. When the second layer C_{60} is formed above a C_{70} layer, there is a lattice mismatch. If the C_{60} molecule sits in the three-fold hollow site of the C_{70} layer, the C_{60} layer would be under tensile stress. The tensile stress can be relieved if the underlying C_{70} layer rearranges by making the C_{70} molecules standing up with their long molecular axis perpendicular to HOPG. In such a standing up orientation, the nearest neighbour distance between C_{70} molecules would be the same as the nearest neighbour distance between C_{60} molecules. Fig. 6-9 (d) shows a schematic

diagram which explains the reason of the second layer C_{60} molecules have a similar height as the second layer C_{70}. As for C_{70} on C_{70}, the molecules in both layers are free to rotate. Therefore, the C_{70} molecule can be regarded as flipping between the lying down and standing up configurations in STM scanning. The effective diameter of the molecule, shorter than the length of the long axis but longer than the length of the short axis, is measured. For C_{60} on C_{70}, the first layer C_{70} molecules are oriented vertically in order to lattice match the C_{60} layer above. The C_{70} underneath C_{60} has lost its rotational degree of freedom.

To summarize, the first layer of C_{70} can have different heights depending on what molecules are placed on top of it. For C_{70} on C_{70}, molecules in both layers are free to rotate at RT and are in a relaxed configuration. For C_{60} on C_{70}, the first layer C_{70} molecules are forced to stand up due to the influence of the C_{60} layer above.

In Fig. 6-9 (c), there are also some C_{70} molecules appear to be taller than the rest. These tall C_{70} molecules are found mostly around the C_{60}/C_{70} boundaries. It is likely that the C_{70} molecules underneath these tall C_{70} molecules are vertically oriented. Length covering a certain distance inside image is shown by two double-headed arrows, following which 16 rows of C_{60} pack within the C_{60} domain. However, the same distance is occupied by 15 rows of C_{70} molecules inside the C_{70} domain. The nearest neighbour distance (NND) of C_{60}-C_{60} here was measured to be 1.0 nm, corresponding to the lattice distance in C_{60} crystal [15] and the nearest neighbour distance of C_{70} is 1.07 nm as indicated by the scanning image. Thus, the ratio of the nearest neighbour C_{70}-C_{70} distance to that of the C_{60}'s is 1.07. These values are identical to the reported studies on the fullerene crystals by means of X-ray diffraction (XRD) [18].

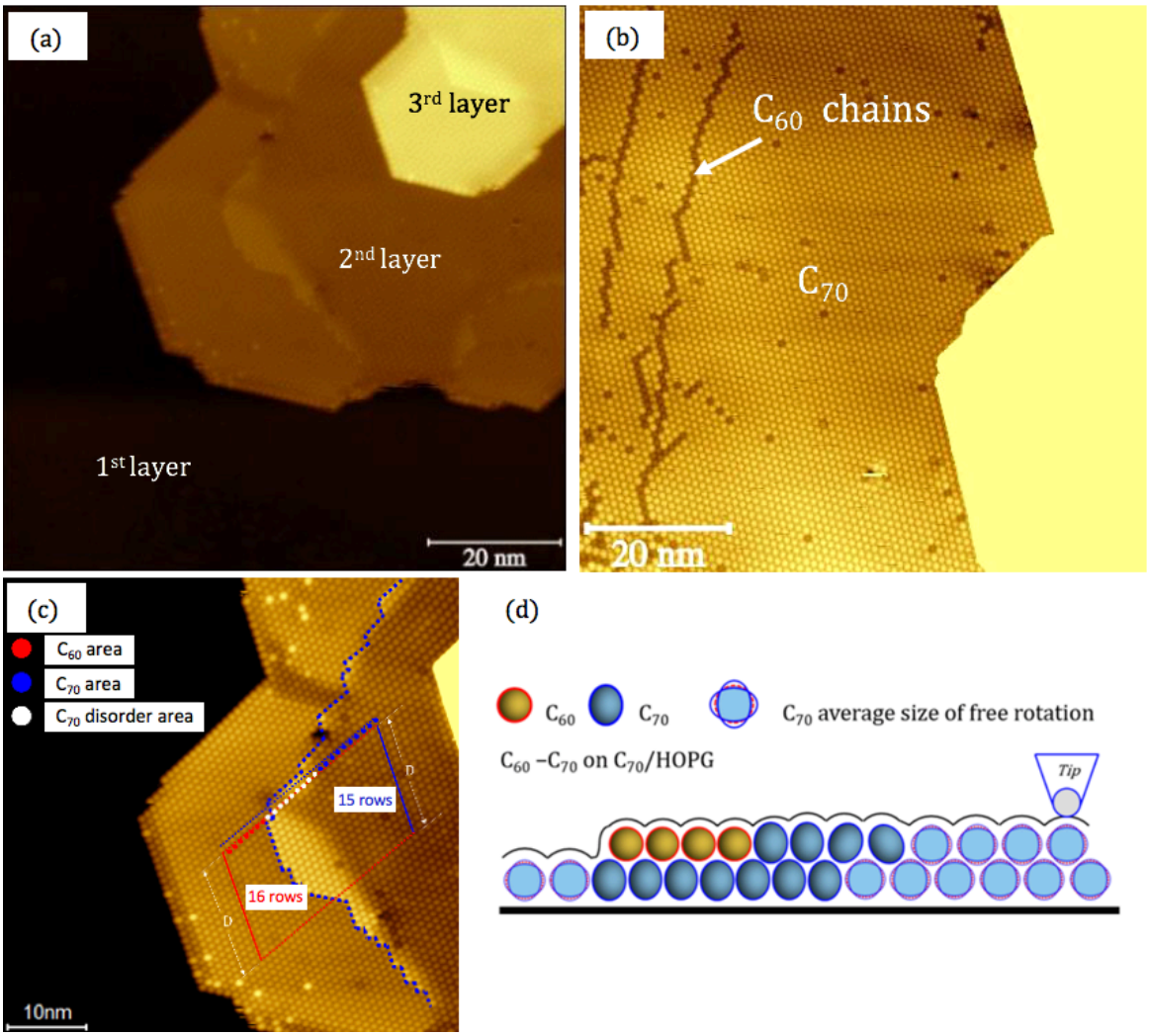


Fig. 6-9 The morphology of C_{70}-C_{60} on C_{70}/HOPG after annealing at 375 K for 30 min. (b) and (c) is the high-resolution image of an area in the (a). (b) is the high-resolution image of the first layer packing structure. (c) is the magnified image of the second layer packing structure. (d) schematic diagram showing C_{70} molecules beneath the C_{60} layer taking the upright configuration at RT, while C_{70} molecules beneath C_{70} freely rotating. It results in some C_{70} flipping.

Fig. 6-10 shows STM images acquired after the sample has been heated to 425 K. In the first layer, there are C_{60}-rich and C_{70} rich regions. Within the C_{60} rich region, we observed isolated C_{70} molecules. These isolated C_{70} molecules take the upright configuration. Such a configuration is preferred due to it causes little distortion of the C_{60} lattice. Within the C_{70} rich region, there are individual C_{60}

molecules as well as chains of C_{60} as shown earlier in Fig. 6-9 (b). The C_{60} molecules simply substitute the C_{70} molecules without causing any local lattice distortion. For the second layer, the boundary between C_{60} and C_{70} becomes less clear.

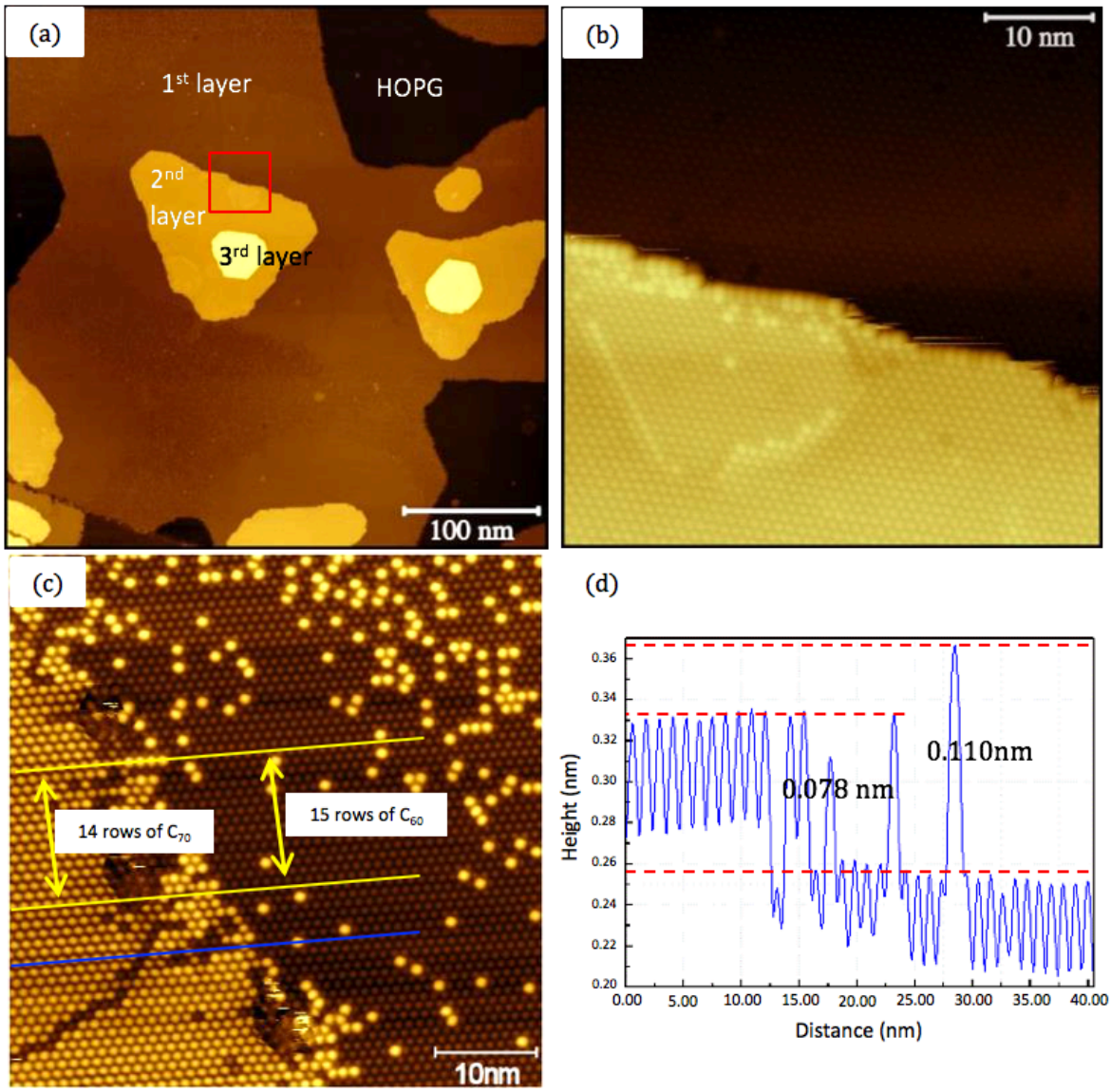


Fig. 6-10 The morphology of C_{70}-C_{60} on C_{70}/HOPG after annealing at 425 K for 30 min. (b) and (c) is the magnified image of the maker in the (a). (b) is the high-resolution image of the first layer packing structure. (c) is the high-resolution image of the second layer packing structure. (d) showing the height profile following the blue arrow in (c).

Further changes appear after increasing the annealing temperature to 475 K. As can be seen in Fig. 6-11 (b), the second layer island consists of C_{70} molecules only. According to the schematic diagram of Fig. 6-9 (d), C_{70} molecules beneath the C_{60} layer take the upright configuration at RT. During the annealing process, thermal energy might be sufficient to trigger these upright C_{70} molecules to rotate, which cause the mismatch of the lattice. As a consequence, C_{60} molecules in the second layer become destabilised and further diffuse to their locations. However, the C_{70} molecules remain as scattered molecules inside the C_{60} layer.

By comparing Fig. 6-2, Fig. 6-4, Fig. 6-8, Fig. 6-9 and Fig. 6-10, there was a clear evolution from the original structure to the newly formed structure. Here, we propose a mechanism to illustrate the molecules lattice at the wrinkle area. Fig. 6-9 (d) shows the model occupation site of C_{60} on C_{70}/HOPG. We have observed that C_{70} molecules in the second layer prefer to occupy the hollow sites of the first C_{70} molecules with a perfect ordering structure. This finding is quite different from previous researches [10,17-19]. Moreover, the nearest-neighbour distance alone all the direction of lattice are measured having the same value, which indicates that the C_{70} molecules take upright orientation on the second layer as well as on the first layer. This is an unstable status that can be easily disturbed by later introduced guest molecules. If C_{60} molecules were introduced, they prefer to occupy the hollow sites. The equilibrium bond distance of C_{60} molecule is 9.84 Å (centre to centre) in FCC structure whereas for C_{70} is 9.94 Å. The ratio between them is about 1% of the bond distance of C_{70}, such a small mismatch on the lattice could cause several changes. For example, the upright orientated C_{70} molecules on the grain boundary will tilt to a small angle to adapt the mismatch of lattice. This would lead to a series of disorder of the neighbouring C_{70} molecules. Moreover, the cohesive energy of C_{60} and C_{70} is about 43.9 kal/mol and 49.5 kal/mol, respectively [14].

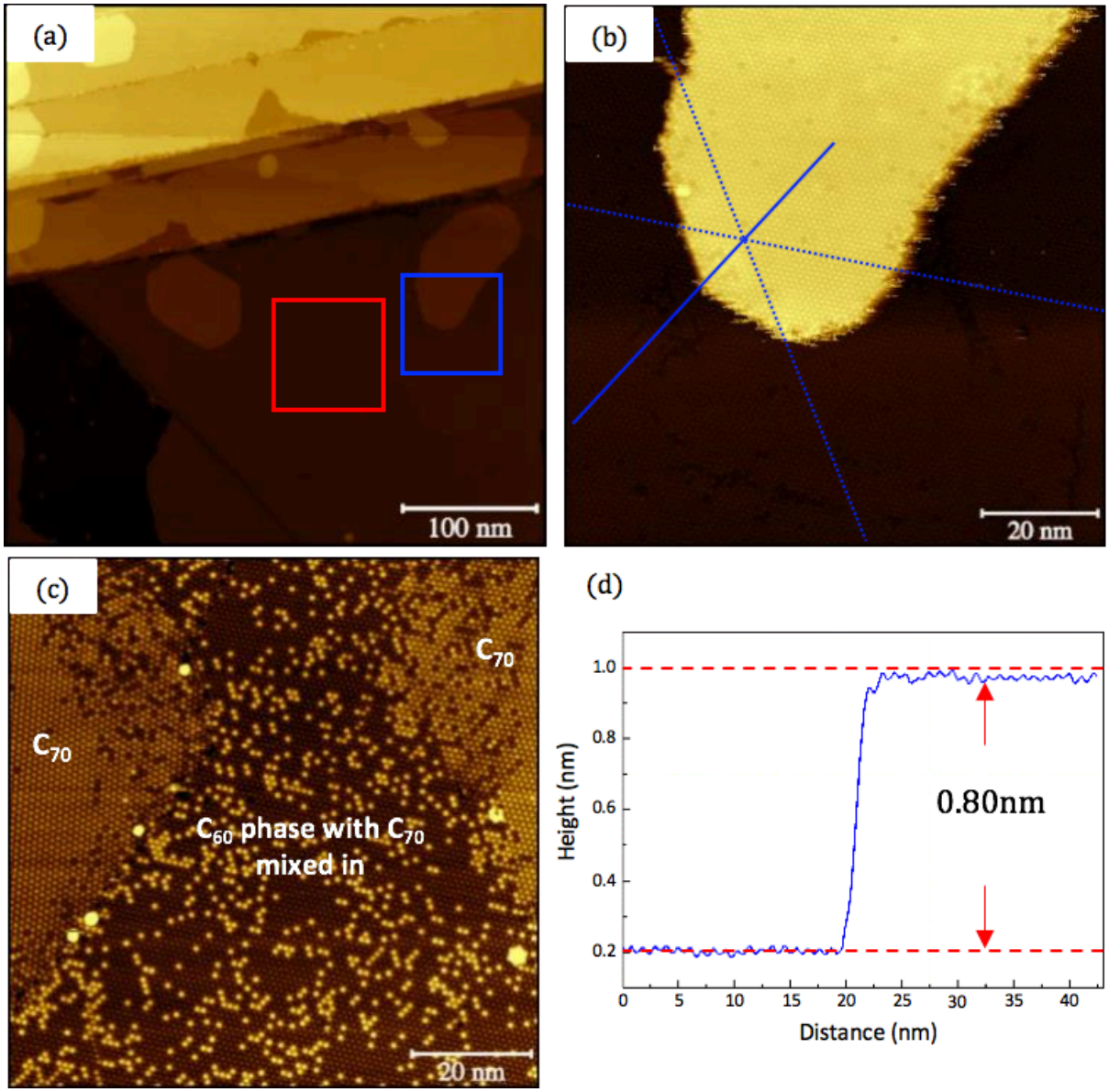


Fig. 6-11 The morphology of C_{70}-C_{60} on C_{70}/HOPG after annealing at 475 K for 30 min. (b) and (c) is the high-resolution image of the maker in (a). (b) is the high-resolution image of the second layer packing structure (marked by the blue rectangle). (c) is the high-resolution image of the first layer packing structure (marked by the red rectangle). (d) showing the height profile following the solid blue line in (b).

At the same temperature, the C_{60} molecules are thus more mobile than C_{70} molecules. The distance defined by the two double-headed arrows in Fig. 6-10 (c) indicating that 15 rows of C_{60} molecules and 14 rows of C_{70} have the same length. This 16/15 ratio is roughly the same as the ratio of the first layer molecules

as measured from Fig. 6-9 (c). It indicates the packing structure of the monolayer fullerenes on HOPG is similar to the bulk projection of the corresponding fullerite's (111) plane. As shown in Fig. 6-10 (c), the bright features inside the C_{60} domain are the trapped C_{70} molecules. C_{60} molecules inside the C_{70}-rich domain seem to have aggregated into zigzag rows.

From the above investigations, it is clear that how the packing structures of C_{60} and C_{70} molecules evolve as temperature increases. When C_{70} molecules are deposited on defect-free and HOPG surface, these molecules prefer to take an upright orientation and form close packing structure to each other. When the C_{60} molecules are introduced later, C_{70} molecules of the second layer will tilt on the grain boundary in order to adapt the difference on the lattice. There is no mismatching between the graphene and C_{60} (C_{70}) molecule, these two kinds of molecules will form a perfect lattice without defect. The C_{60} molecules located at the outside of C_{70} island on the second layer start to diffuse to the first layer while the temperature increases. When the temperature reaches 475 K, most of the C_{60} molecules diffuse to the first layer. During the annealing, the second layer of C_{70} molecules gain enough energy to overcome the diffusion barrier and packing into a perfect closed-packed structure. The wrinkle area disappeared after the C_{60} molecules moved to the first layer.

Such a reversible structure creates defects and adsorption position, which enables potential applications on producing templates for nano-devices and catalyst system. Such behaviours were different from the case of C_{70} on C_{60}/HOPG, are already shown in Fig 5-3. During the annealing, the introduced C_{70} molecules act as a "barrier" and restrict the C_{60} molecules' thermal motion. This also explains the phenomenon with the C_{60} on C_{70}/HOPG. The introduced C_{60} molecules on the second layer diffuse around during the annealing at sufficient temperature whereas the C_{70} molecules are much more stable than C_{60} molecules except the shape variation from fracture to round, as shown in Fig. 6-10. When the

temperature is cooled down to RT, the shape of C_{70} molecules remain the same while the C_{60} molecules have diffused to the first layer.

6.6 Summary

Packing structure of C_{60} and C_{70} molecules have been studied on different deposition sequences and annealing temperature. C_{70} pack closely with C_{60} molecules on C_{60} surface and molecules in the second layer sits on the hollow sites of the first layer of C_{60}. In the mixed domains of C_{60} and C_{70}, C_{70}'s ellipsoidal shapes are able to significantly change the structure of C_{60}-C_{70}'s interface. A strain-free heterostructure appears in the mixture when C_{70} choose an upright orientation and make their lattice matches the close-packed C_{60} layer. By changing the order of deposition, C_{60} can also form close-packed domains with C_{70} molecules on the C_{70} monolayer, where C_{70} molecule sitting on the hollow sites and take an upright orientation, and C_{60} molecule sits on the hollow sites of the first layer of C_{70}. Due to the lattice mismatch and space limitation, some C_{70} molecules in the second layer are observed flipping instead of totally lying down on the first layer. Even though giving up some degrees of rotational freedom results in a reduced entropy of the C_{70} layer. The entropy reducing is overcompensated by the reduced interfacial energy. At higher temperatures, some C_{60} and C_{70} molecules can pass over the domain boundaries. The difference is, the guest C_{70} molecules are trapped in the C_{60}-rich domains as isolated ones, while the guest C_{60} molecules can form molecular chains in the C_{70}-rich domains.

References

[1] J. Visser, Powder Technol. **58**, 1 (1989).

[2] F. Rossel, M. Pivetta, F. Patthey, E. Cavar, A. P. Seitsonen and W.-D. Schneider, Phys. Rev. B **84**, 075426 (2011). [1] D. Nečas, P. Klapetek, Open Phys. **10**, 181 (2012).

[2] D. A. Olyanich, V. V. Mararov, T. V. Utas, A. V. Zotov, A. A. Saranin, Surf. Sci. **653**, 138 (2016).

[3] P. Gravil, M. Devel, P. Lambin, X. Bouju, C. Girard, A. Lucas, Phys. Rev. B **53**, 1622 (1996).

[4] S. Szuba, R. Czajka, A. Kasuya, A. Wawro, H. Rafii-Tabar, S. S, C. R, K. A, W. A, R.-T. H, Appl. Surf. Sci. **144**, 648 (1999).

[5] T. T. Tsong, Phys. Rev. B **44**, 13703 (1991).

[6] H. Liu, P. Reinke, J. Chem. Phys. **124**, 164707 (2006).

[7] H. Liu, Z. Lin, L. V Zhigilei, P. Reinke, J. Phys. Chem. C **112**, 4687 (2008).

[8] H. N. Aiyert, A. Govindaraj, C. N. R. Rao, Philos. Mag. Lett. **72**, 185 (1995).

[9] J. Koepke, Bull. Mater. Sci. **17**, 563 (1997).

[10] D. R. R. McKenzie, C. A. A. Davis, D. J. H. J. H. Cockayne, D. A. A. Muller, A. M. M. Vassallo, Nature **355**, 622 (1992).

[11] P. Dietz, K. Fostiropoulos, W. Krätschmer, P. K. Hansma, P. D. Fostiropoulos, W. Krätschmerpaul, K. Hansma, P. Dietz, K. Fostiropoulos, W. Krmschmer, P. K. Hansma, Appl. Phys. Lett. **60**, 62 (1992).

[14] Y. Guo, N. Karasawa, W. A. Goddard III, Nature **351**, 464 (1991).

[15] M. S. Dresselhaus, G. Dresselhaus, P. C. Eklund, Science of Fullerenes and Carbon Nanotubes (Academic, New York 1996).

[16] G. B. M. Vaughan, P. A. Heiney, D. E. Cox, J. E. Fischer, A. R. McGhie, A. Smith, R. M. Strongin, M. A. Cichy, A. B. Smith III, Chem. Phys. **178**, 599 (1993).

[17] G. B. M. Vaughan, P. A. Heiey, D. E. Luzzi, D. A. Ricketts-Foot, A. R. Mcghie, J. E. Fischer, Y. W. Hui, A. L. Smith, D. E. Cox, W. J. Romanow, B. H. Allen, N. Coustel, J. P. Mccauley, A. B. Smith III, Science **254**, 1350 (1991).

[18] M. C. Valsakumar, N. Subramanian, M. Yousuf, P. C. Sahu, Y. Hariharan, A. Bharathi, V. Sankara Sastry, J. Janaki, G. V. N. Rao, T. S. Radhakrishnan, C. S. Sundar, Phys. Rev. B, **48**, 9080 (1993).

[19] A. K. Callebaut, K. H. Michel, Phys. Rev. B **52**, 15279 (1995).

7. $(C_{70})_m$-$(Au)_n$ Hybrid Magic Number Clusters

7.1 Introduction

Clusters combining molecules and atoms are an important class of materials which exhibit size-dependent properties [1-4]. Great effort has been devoted to the fine tailoring of clusters, including size-selection [5,6], shape control [7] and surface passivation [8,9]. In this chapter, we create magic number $(C_{70})_m$-$(Au)_n$ clusters by successively depositing gold and C_{70} molecules on Au(111) in |UHV system. Then we select and focus on scanning some magic clusters with different sizes for several hours at room temperature. The overall property of the $(C_{70})_m$-$(Au)_n$ cluster is similar to that of $(C_{60})_m$-$(Au)_n$. Metal core in one $(C_{60})_m$-$(Au)_n$ cluster consisting of *n* Au atoms is protected by the molecular "shell", and thus both of its Ostwald and Smoluchowski ripening are affected and hinted. Due to the weak interaction between gold and C_{70} molecules, magic clusters such as $(C_{70})_{10}$-$(Au)_{35}$, $(C_{70})_{12}$-$(Au)_{49}$ change their azimuthal orientations all of a sudden after keeping still for many hours on gold surface.

7.2 Experimental Procedure

The experiment was performed with a variable temperature STM (VT-STM). The substrates used for holding clusters were made by depositing thin gold films, ~ 200 nm, onto highly oriented pyrolytic graphite (HOPG) with the method of physical vapour deposition in high vacuum. On the surface of HOPG, the deposited gold films were preferentially oriented by exposing the (111) crystal plane. The flat clean Au(111) terraces were obtained by cleaning the sample in an ultra-high vacuum (UHV) chamber with cycles of Ar^+ ion bombardment and thermal annealing at 870 K for one hour.

For forming $(C_{70})_m$-$(Au)_n$ magic number clusters, the Au(111) sample was firstly cooled down to 110 K, and ~ 0.15 ML gold atoms were deposited onto the sample surface, forming irregular islands at the elbow sites on the reconstructed gold substrate. It was followed by the deposition of ~ 0.05 ML C_{70} molecules, which decorated the existing gold islands. The sample was then annealed to room temperature gradually, which was sufficient to create magic number $(C_{70})_m$-$(Au)_n$ clusters via a complete self-organisation process. In our experiments, the gold atoms were over-deposited in order to create the higher density of diffusing gold atoms on the substrate at room temperature, making the clusters being attacked more often and thus the azimuthal orientation of clusters more obvious.

7.3 Structure of $(C_{70})_m$-$(Au)_n$ Magic Number Clusters on Au(111)

Fig. 7-1(a) shows several types of clusters, mostly sitting close to elbow sites: i) planar clusters; ii) ring clusters; and iii) joined clusters. The hybrid cluster is featured by a group of close-packed "bright" C_{70} molecules surrounded by "dim" C_{70} molecules. The hybrid cluster has a regular shape with a specific number of C_{70} molecules and hence known as magic number cluster. Some magic number clusters sitting closely are bridged by a number of C_{70} molecules forming joined clusters. The ring cluster is characterized by a ring of C_{70} molecules.

Fig. 7-1(b) shows two height profiles: one across a 10 molecule hybrid cluster and the other across a ring cluster. According to the red curve, the area inside the molecular ring is ~ 0.2 nm taller than the Au(111) substrate. Thus, a single atomic layer Au island occupies this area. The molecules within the ring, measured from the Au(111) substrate are ~ 0.7 nm tall. This is the same as the height of the dim molecules in the hybrid cluster. The bright molecules in the cluster is ~ 0.9 nm tall. It suggests that there is an atomic layer Au island beneath the bright C_{70}

molecules. All the molecules take the orientation that the long axis is perpendicular to the substrate.

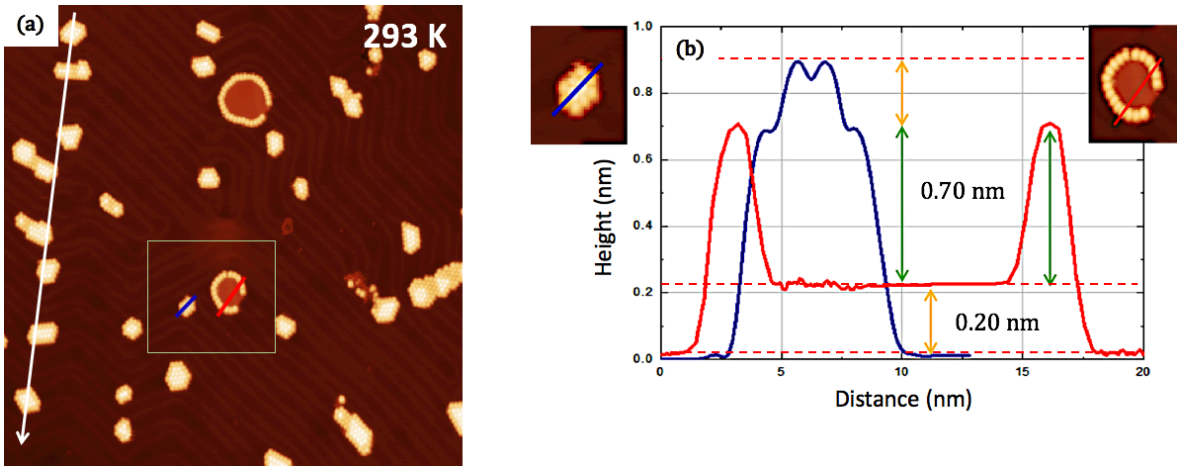


Fig. 7-1 (a) STM image of the C_{70}-Au magic number clusters, ring clusters and joined clusters sitting at elbows on Au(111) (130 nm × 130 nm, -2.0 V, 0.05 nA); (b) Line profiles showing the height of one hybrid magic number cluster and one ring cluster.

Based on the above analysis, we come up with the following proposed structural models for the three smallest magic number clusters: $(C_{70})_7$-$(Au)_{19}$, $(C_{70})_{10}$-$(Au)_{35}$ and $(C_{70})_{12}$-$(Au)_{49}$ as shown in Fig. 7-2. For the $(C_{70})_7$-$(Au)_{19}$ cluster, a hexagonal gold island consisting of 19 gold atoms are closely surrounded by six C_{70} molecules, which are shown as dim spots in the STM image. Considering the lateral distance between two neighbour C_{70} molecules inside clusters, C_{70} inside clusters take the same configuration as in the $\left(2\sqrt{3} \times 2\sqrt{3}\right)R30°$ phase, which is formed by close-packed C_{70} on Au(111) introduced in the former chapters, each C_{70} occupies one three-fold hollow site of Au(111) substrate with its pentagon ring. Gold atoms directly contacting C_{70} are marked with red colour, in Fig. 7-2 (a). There is one C_{70} molecule sitting on the Au_{19} island. This molecule appears bright in the image. This C_{70} molecule interacts with all ~~the~~ other molecules with van der Waals force, and bonds to the Au atoms via charge transfer. Charge transfer and van der Waals forces are combined and make the whole cluster stable.

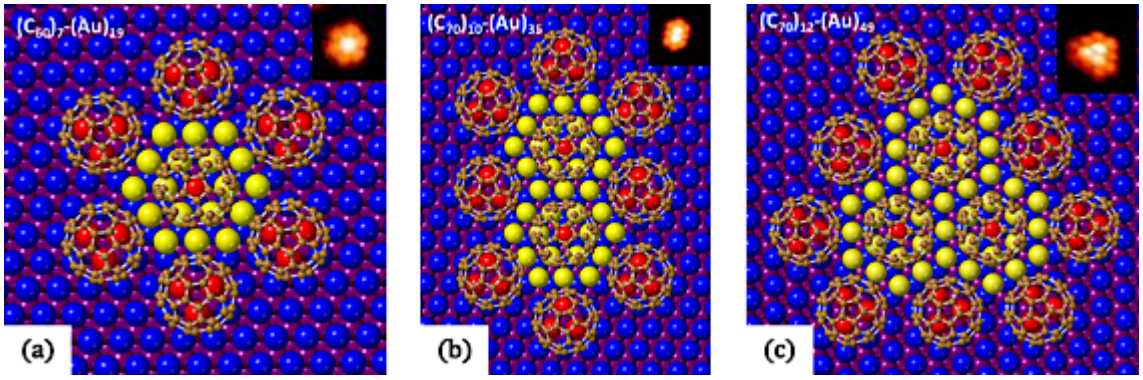


Fig. 7-2 Schematic showing the proposed structural models of $(C_{70})_7$-$(Au)_{19}$, $(C_{70})_{10}$-$(Au)_{35}$ and $(C_{70})_{12}$-$(Au)_{49}$ clusters. (a) Blue and purple spheres represent the gold atoms in the first and second layer of Au(111), respectively. Yellow spheres are the 19 Au atoms within the monolayer gold island. Six C_{70} molecules stand around the gold island while one C_{70} molecule stands on its top. Red spheres represent the gold atoms in the top-most layer of the substrate and in the monolayer island which directly interact with the pentagon rings of C_{70} molecules. Inset is an STM image of one $(C_{70})_7$-$(Au)_{19}$ cluster. The bright spot is the C_{70} molecule sitting on top of the gold island. (b) $(C_{70})_{10}$-$(Au)_{35}$. Inset shows one of this type cluster scanned by STM. Two C_{70} molecules sit on the gold island side by side. (c) $(C_{70})_{12}$-$(Au)_{49}$. Inset is one of this type of cluster.

The $(C_{70})_{10}$-$(Au)_{35}$ and the $(C_{70})_{12}$-$(Au)_{49}$ clusters are natural extensions of the $(C_{70})_7$-$(Au)_{19}$ cluster, with two and three edge-sharing hexagonal Au islands, respectively. Larger clusters can be constructed based on the same mechanism. The standing up configuration is favourable for intermolecular interactions at the specified molecule-molecule distances. However, the standing up configuration is achieved by the C_{70} molecule contacting the Au(111) surface with a pentagonal ring. From previous studies, C_{60} molecules prefer to contact the Au(111) surface with a hexagonal ring. Thus, the C_{70}-Au(111) interaction is not optimised, and this is likely due to the compromise between molecule-substrate interaction and the molecule-molecule interaction.

7.4 Branching Ratio of $(C_{70})_m$-$(Au)_n$ Clusters

In the previous section, we have introduced the formation of three types of $(C_{70})_m$-$(Au)_n$ clusters: magic number clusters, ring clusters and joined clusters. In the following section, we will examine how the branching ratios of these clusters can be controlled by changing the depositing amounts of Au and C_{70} molecules.

Coverage of gold atoms	Coverage of C_{70} molecules	Magic number clusters/Total clusters	Rings clusters/Total clusters	Joined clusters/Total clusters	Clusters far from elbows/Total clusters
0.02 ML	0.04 ML	32 % ± 3 %	48 % ± 4 %	20 % ± 2 %	2 %
	0.08 ML	36 % ± 3 %	35 % ± 3 %	29 % ± 3 %	4 %
	0.16 ML	19 % ± 2 %	20 % ± 2 %	61 % ± 4 %	3 %
0.04 ML	0.08 ML	28 % ± 3 %	3 % ± 1 %	69 % ± 4 %	4 %

Table. 7-1 The different branching ratio of magic number, ring and joined clusters in the three independent experiments. Ratios of the clusters sitting far from elbows are shown in the last column. In the former three groups of experiments, depositing amount of gold atoms is fixed at 0.02 ML, while depositing amount of C_{70} molecules increases from 0.04 ML to 0.08 ML and 0.16 ML orderly. In the last experiment, 0.04 ML gold atoms and 0.08 ML C_{70} molecules are co-deposited. In each experiment, total 376 clusters have been calculated.

For investigating how the C_{70}/Au ratio affects the branching ratio of magic number clusters, Au atoms and C_{70} molecules were co-deposited on the gold substrate with three different ratios. In the experiments, Au and C_{70} were co-deposited on Au(111) at 110 K. The amount of gold atoms deposited is fixed to 0.02 ML while the amount of C_{70} deposited was varied from 0.04 ML to 0.08 ML and then to 0.16 ML by heating the source to 600 K, 620 K and 643 K, respectively. After each deposition, we count the numbers of clusters and sort them into the three types: i) compact, ii) ring and iii) joined. In each of the three experiments, 376 clusters have been counted and divided into different groups.

The branching ratios of the compact, ring and joined clusters are shown in Table. 7-1. Although most clusters prefer to occupy elbow sites, there are still a small number of magic number clusters found within the FCC domain far away from elbows. In Figs. 7-3. 7-4, 7-5, this type of clusters are marked in a solid blue circle.

In the first experiment, 0.02 ML gold atoms and 0.04 ML C_{70} molecules were co-deposited on Au(111) at 110 K. When the sample was heated up to room temperature, the ring clusters are found taking up ~ 48 % of the total counted 376 clusters. The number of this type clusters is 1.5 times of the magic number clusters and even more than twice of the joined clusters. It indicates that gold atoms have aggregated into large size monolayer gold islands before combining with diffusing C_{70} molecules and form magic number clusters. The abundance of ring clusters is an implication that the Au/C_{70} ratio is too high. In the second experiment, 0.02 ML gold atoms and 0.08 ML C_{70} molecules were co-deposited onto the gold substrate at 110 K. Compared with the first experiment, there is a significant decrease in the number of ring clusters here. Meanwhile, both the numbers of magic number and joined clusters have an increase, and the increasing amplitude of joined clusters is larger. In the third experiment, total amount of the gold atoms deposited remained as 0.02 ML, and the amount of C_{70} molecules was further increased to 0.16 ML. On the Au(111) surface, over half of the clusters appear as joined ones at room temperature. When the Au/C_{70} ratio approached 1∶2, number of all the three types of clusters distribute averagely on the substrate. Therefore, by changing the Au/C_{70} ratio, we are able to select the specific types of clusters to form on the gold substrate. Besides, among the three groups of experiments, it is found that with the fixed coverage of gold atoms at 0.02 ML, the fraction of clusters sitting far from elbow sites is always less than 5%. In other words, with deficient gold atoms deposited, all the three types of clusters prefer to occupy the elbow sites on Au(111).

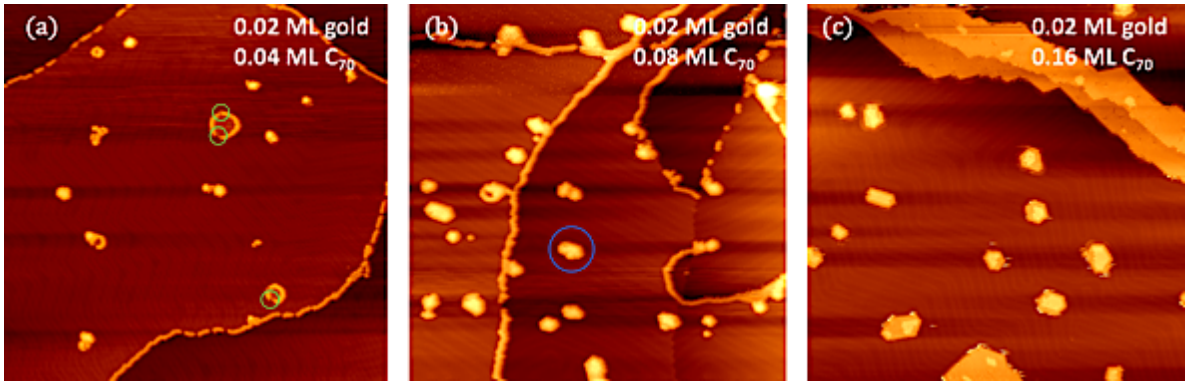


Fig. 7-3 STM image of the C_{70}-Au clusters forming on the Au(111) substrate by co-depositing 0.02 ML gold atoms and (a) 0.04 ML, (b) 0.08 ML and (c) 0.16 ML C_{70} molecules at 110 K. After deposition, the sample was heated to room temperature and then scanned by STM. (a) Large ring clusters and small magic number clusters observed occupying more than one elbow sites. Several green circles are used to mark the empty HCP regions around the large gold islands of ring clusters, indicating the C_{70} molecules surrounding gold islands have a preference of sitting in the FCC regions instead of the HCP ones (200 nm × 200 nm, -1.23 V, 0.04 nA). (b) The clusters on the gold surface belonging to the closed-shell type, which are magic number clusters. One cluster sitting in the FCC regions far from elbow sites is marked by a blue solid circle (159 nm × 159 nm, -2.84 V, 0.04 nA). (c) Most clusters on the gold surface are joined clusters and large magic number clusters (145 nm × 145 nm, -1.54 V, 0.04 nA).

Fig. 7-3 indicates the sample after the Au and C_{70} were co-deposited with different ratios. It was scanned at room temperature after deposition of 0.02 ML gold atoms and 0.04 ML C_{70} molecules at 110 K. Step edges on Au(111) are decorated by single rows of C_{70} molecules. Most clusters on flat terraces are observed having large single layer gold islands, of which the edges are decorated by C_{70} molecules. The gold islands inside relatively small ring clusters are completely enclosed by C_{70} molecules. However, for larger sized ring clusters, the gold islands occupy three or even more elbow sites simultaneously on the substrate, under which the reconstructions are not lifted. As shown in the green circles in Fig. 7-3 (a), most C_{70} molecules decorating large gold islands prefer to occupy FCC regions instead of HCP ones or herringbone reconstructions.

Compared with FCC regions, HCP regions provide a comparable narrow accommodation space, which prevent C_{70} molecules from packing closely around gold islands and keeping a constant spacing with their adjacent ones. In Fig. 7-3 (a), one cluster is observed containing two single layer gold islands. The larger gold island is fully covered by molecules, while the other is not.

Then, 0.02 ML Au and 0.04 ML C_{70} were co-deposited on the gold surface at 110 K. The Au islands were already surrounded by sufficient C_{70} molecules and form closed-shell clusters before ripening as large size ones. Therefore, a significantly higher density of clusters on Au(111) was obtained. As shown in Fig. 7-3 (b), some gold islands grow out from step edges and sit beneath the bright C_{70} molecules. Almost all the elbow sites on the flat terraces have been occupied by clusters, most of which are the magic number and joined clusters. We found that in the image, there is one cluster, marked with a sold blue circle, sitting in the FCC region far from elbow sites. It indicates that the Au atoms can aggregate in the FCC region and form a cluster which is then quickly decorated by diffusing C_{70} molecules. Then a closed-shell cluster is formed and does not move to any elbow site. As mentioned above, only ~ 3% of the total clusters sit far from elbow sites. It thus proves that the elbow sites play a crucial role in affecting the formation of clusters on Au(111). As shown in Fig. 7-3 (c), both the gold atoms and molecules were still co-deposited on Au(111) at 110 K. The coverage of gold atoms maintained as 0.02 ML, and the amount of C_{70} increased further to 0.16 ML. At room temperature, most of the C_{70} form wide molecular bands and attach to the gold steps. Under the molecules sit few small gold islands, which make several molecules brighter than the neighbour ones. On the gold substrate, there is no ring clusters observed. more than half of the clusters on the gold surface belong to the joined types. Moreover, the magic number clusters in Fig. 7-3 (c) are commonly larger than that in Fig. 7-3 (a) or (b).

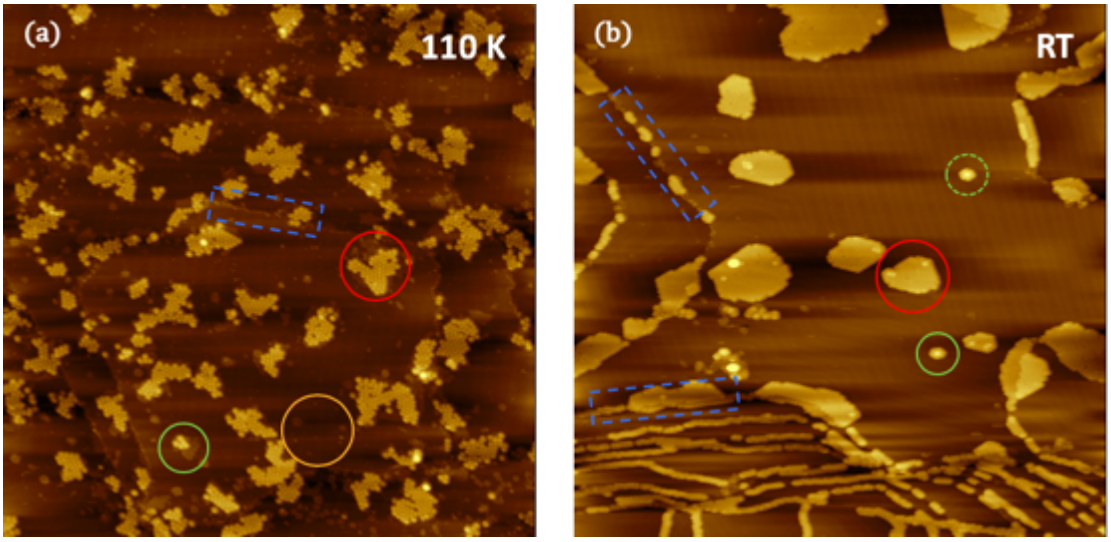


Fig. 7-4 (a) STM image of the C_{70}-Au clusters when the sample is cooled down to 110 K. 0.04 ML gold atoms and 0.08 ML C_{70} molecules are co-deposited onto Au(111) surface. The sample surface is scanned by STM at 110 K. On the Au(111) substrate, several small size gold islands appearing darker are marked in a solid orange circle. Atoms in these gold islands are fully exposed to scanning tip. In the bottom-left of the figure, a gold island with a slightly larger size is marked with a solid green circle. A small fraction of the island is covered by only four C_{70} molecules. Another gold island with a much larger size in the right side of image is marked with a solid red circle, more than half of which is covered by molecules. Around the island's edges, C_{70} form close-packed structure with irregular shapes. A piece of gold steps edges is shown in the dashed blue rectangle, which keeps clean at 110 K. (125 nm × 125 nm, -2.50 V, 0.15 nA); (b) STM image obtained by annealing sample from 110 K to room temperature. Steps edges of Au(111) shown in dashed blue rectangles are all decorated by closed-packed C_{70} rows. Gold islands remaining on flat terraces combine with C_{70} molecules and form super large clusters. A large joined clusters containing two individual gold islands is marked in a solid red circle. Two magic number clusters occupying an elbow site and sitting in FCC regions are marked with sold and dashed green circles respectively. (125 nm × 125 nm, -2.50 V, 0.15 nA).

In this experiment, 0.04 ML gold atoms and 0.08 ML C_{70} were deposited onto the Au(111) surface after the gold sample has been cooled down to 110 K. Fig. 7-4 (a) shows an image of clusters obtained at 110 K by STM. A large number of C_{70} clusters are found on the gold surface. Most of the C_{70} clusters attach or cover Au atoms. For example, one of the clusters marked in a red box has plenty of dark

vacancies, which are filled by Au atoms. At low temperature, diffusion of molecules are limited on the gold surface, which results in these islands with irregular shapes. Some molecules sitting on monolayer gold islands appear brighter than their neighbour ones. The gold steps are not decorated by C_{70} molecules at this temperature.

When the sample was heated to room temperature, the step edges are found partially decorated by C_{70} molecules, and most of the molecules prefer to occupy the FCC regions rather than the HCP ones. The C_{70} used to pack randomly around the gold islands form close-packed monolayer islands and connect two existing gold islands. Hence the super large joined clusters appear and occupy more than two elbow sites simultaneously. Apart from the large clusters, there are also two small magic number clusters shown in Fig. 7-4 (b), marked with blue and green circles, respectively. The magic number cluster in a solid blue circle sits in FCC region and is confined by a pair of DLs, while the other sits close to a pinched elbow site. However, these two types of clusters are still difficult to be found in our scanning images.

7.5 Stick-Sudden-Rotation of $(C_{70})_m$-$(Au)_n$ Magic Number Clusters

It has been discussed in the previous section that branching ratios of different type clusters are affected by changing the Au/C_{70} ratio. In the next experiment, we deposited excess gold atoms on Au(111)while keeping the amount of C_{70} molecules constant. When these atoms form magic number clusters with C_{70} molecules on the gold surface, some of the clusters are observed changing their orientations all of a sudden after keeping static for a long time.

The eight images in Fig. 7-5 demonstrate the rotation of clusters with various sizes. The large size clusters with more than six molecules sitting on top of gold

islands can be divided into two types. The first type cluster in Fig. 7-5 is marked with a yellow circle, where eight C_{70} molecules sit side-by-side on the gold island underneath. The whole cluster only occupies one elbow site and keeps still for a long time before changing its orientation all of a sudden. During the three hours scanning, this cluster only changes its orientation of ~ 10° twice, which are shown in the image 4 and 8 respectively.

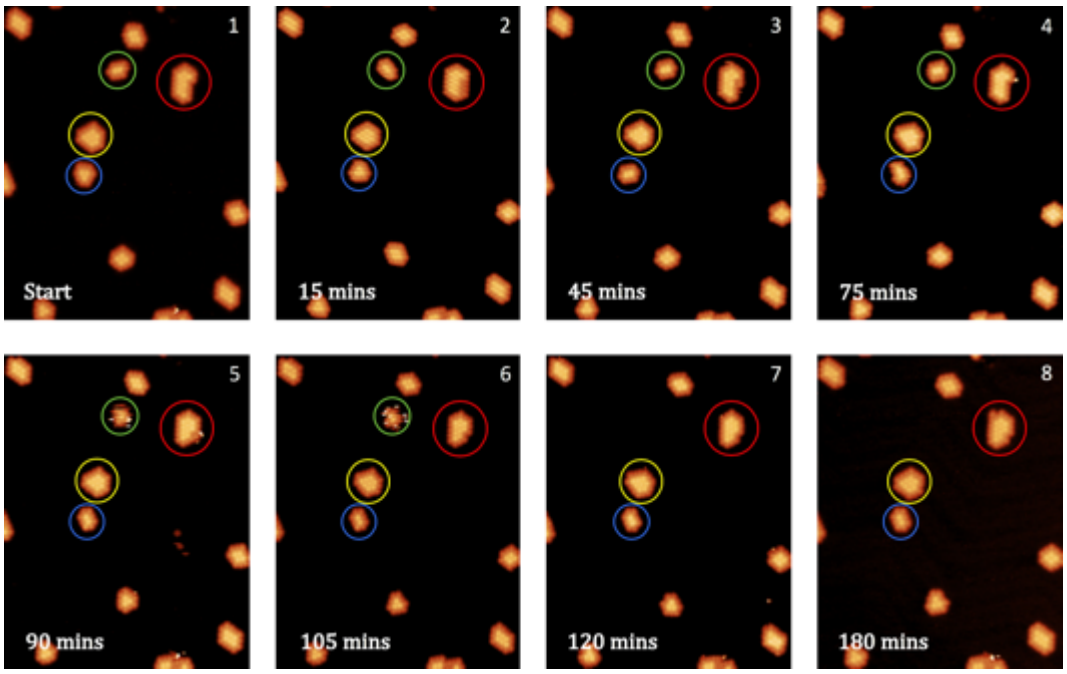


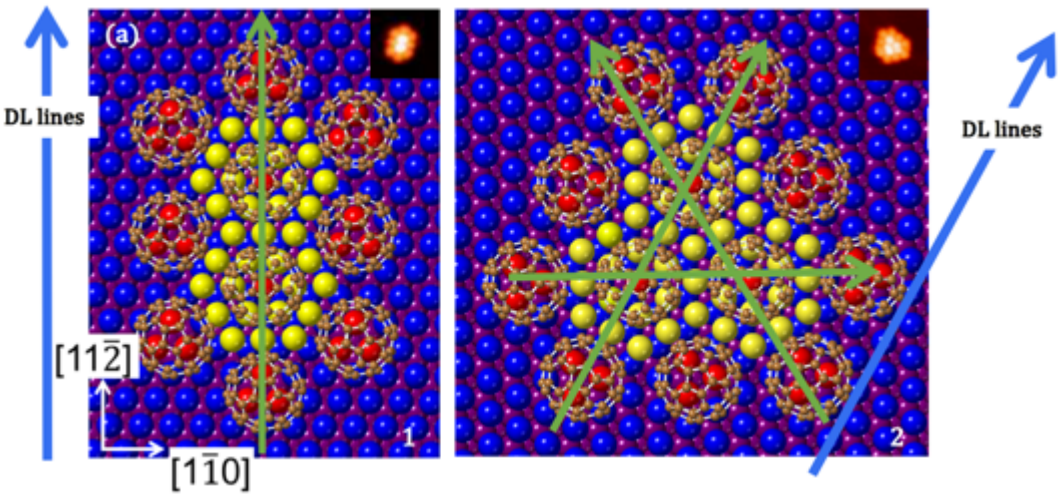
Fig. 7-5 Eight STM images of the rotation of $(C_{70})_m$-$(Au)_n$ clusters with different sizes on the Au(111) substrate (35 nm × 60 nm, -2.0 V, 50 pA). The clusters were being scanned continuously for 3 hours with the same bias voltage and tunnelling current. The image 1 to 8 showing clusters morphology after 0 mins, 15 mins, 45 mins, 75 mins, 90 mins, 105 mins and 180 mins respectively.

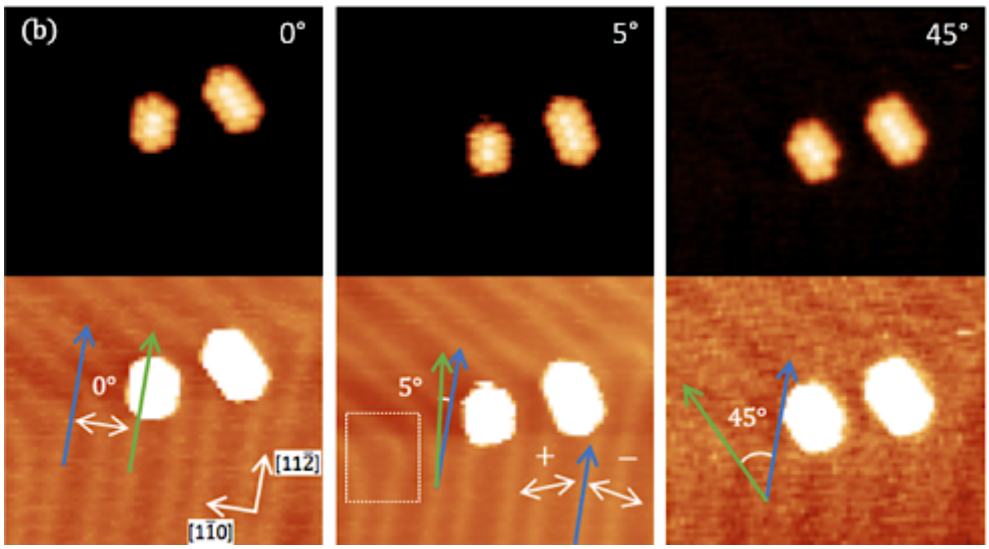
The second type large cluster marked with a red circle has an even larger size, in which the monolayer gold island occupies two elbow sites. Compared with image 4 and 5, we can see the cases that the total number of C_{70} on gold island maintains as 10, and only one molecule has a short distance diffusion after 90 minutes. It indicates that at room temperature, this gold island keeps a constant orientation and is too stable to have a significant change in its shape. C_{70} molecules indirectly

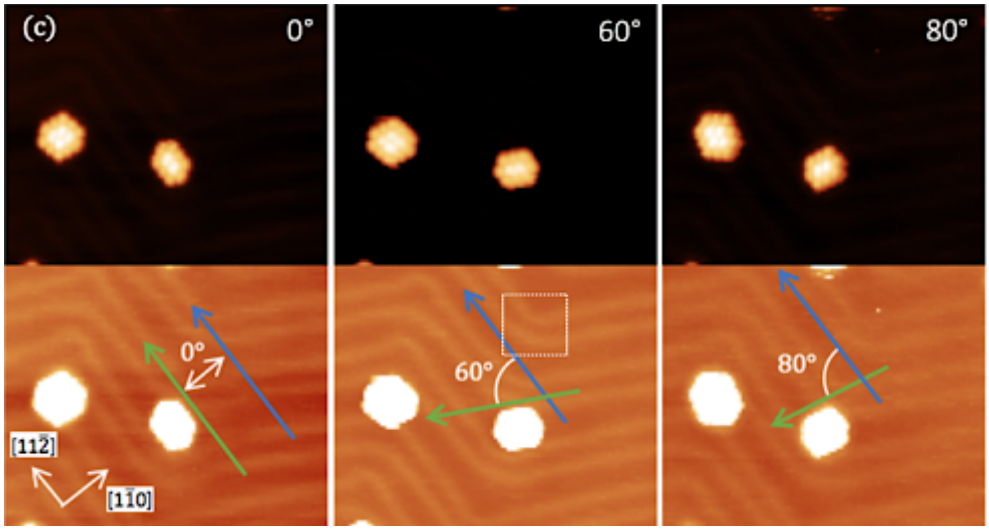
attaching to gold island keep diffusing around this cluster. It can be explained with the high thermal energy of C_{70} molecules at room temperature as well as a weak interaction between C_{70} molecules sitting perpendicular on Au(111).

7.5.1 Rotation of $(C_{70})_{10}$-$(Au)_{35}$ Clusters At Room Temperature

Compared with the larger ones, the smaller size magic number clusters have less stability and all rotate on the Au(111) surface. As shown in Fig. 7-5, the clusters with six or fewer than six molecules sitting on the top of gold islands can keep static for a short time and change their global orientations all of a sudden, behaving like rotation at their original positions. One $(C_{70})_{10}$-$(Au)_{35}$ cluster marked in the green ring changed its orientations all of a sudden. During the process of rotation, this $(C_{70})_{10}$-$(Au)_{35}$ cluster is observed directly decaying into a $(C_{70})_{7}$-$(Au)_{19}$ type one, as shown in the image 4 and 5. The newly formed small cluster is more fragile, in which molecules and gold atoms quickly diffusing and reorganizing. As shown in the image 6 and 7, the cluster looks quite blurry and disintegrates within 2 hours. Another $(C_{70})_{12}$-$(Au)_{49}$ cluster marked in a solid blue circle transformed into $(C_{70})_{10}$-$(Au)_{35}$ after 45 minutes. This newly formed cluster is hard to break due to the optimised interactions between gold atoms and C_{70} molecules. These two clusters are scanned by STM under the same circumstances. It implies that a perfect $(C_{70})_{10}$-$(Au)_{35}$ cluster is higher stabilised on Au(111) among all the small size magic number clusters. The shape of the $(C_{70})_{10}$-$(Au)_{35}$ cluster with its long axis makes it easier to identify its rotations on surfaces. Some other clusters such as $(C_{70})_{7}$-$(Au)_{19}$ have a centre symmetries and are thus not good candidates. For example, the rotation with 60° and 120° are difficult to be identified. Therefore, in the following paragraphs, the orientation changing of $(C_{70})_{10}$-$(Au)_{35}$ clusters sitting at or far away from elbow sites are mainly investigated.


(a)
DL lines
[11$\bar{2}$]
[1$\bar{1}$0]
1
2
DL lines


(b)
0°
5°
45°
0°
[11$\bar{2}$]
[1$\bar{1}$0]
5°
+
−
45°


(c)
0°
60°
80°
0°
[11$\bar{2}$]
[1$\bar{1}$0]
60°
80°

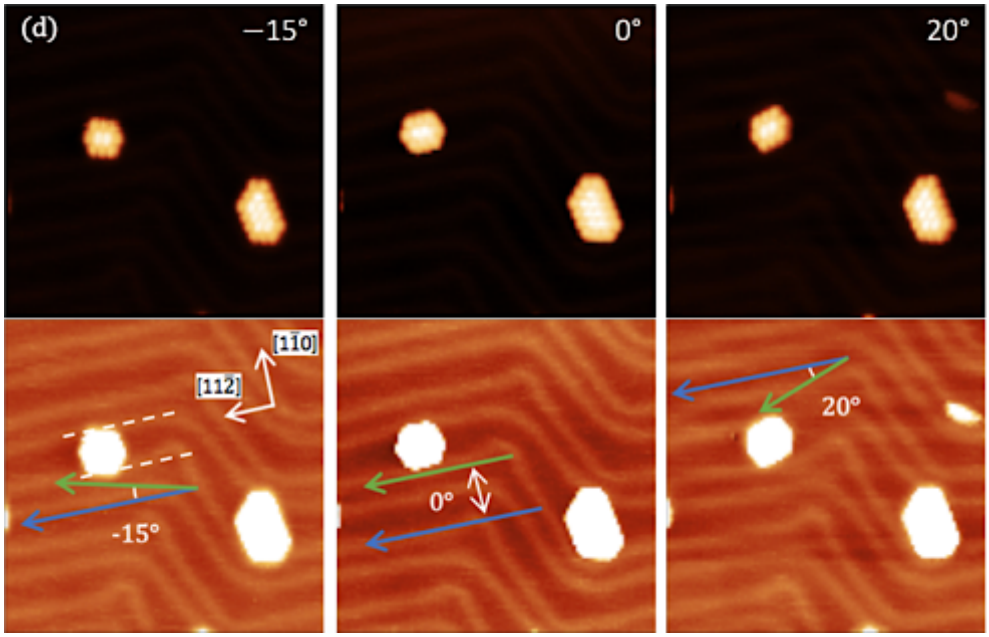


Fig. 7-6 (a) Models of $(C_{70})_{10}$-$(Au)_{35}$ and $(C_{70})_{12}$-$(Au)_{49}$. Yellow balls are the gold atoms forming the gold islands in clusters. A blue arrow is used to mark a discommensuration line (DL) near the cluster. In the image 1, a green arrow is aligned to the long axis of a $(C_{70})_{10}$-$(Au)_{35}$ cluster. In the image 2, three green lines are aligned along the three edges of a $(C_{70})_{12}$-$(Au)_{49}$ cluster, respectively. Each edge consists of three C_{70} molecules decorating the gold island. Three groups images demonstrated in (b), (c) and (d) introduce several rotating conditions of $(C_{70})_{10}$-$(Au)_{35}$ clusters sitting at a bulged elbow site, a pinched elbow site and far from elbows respectively. Each image is applied with contrast enhancement in order to highlight the reconstruction patterns on the substrate. (b) One $(C_{70})_{10}$-$(Au)_{35}$ cluster occupied at bulged elbow sites (30 nm × 30 nm, -2.0 V, 50 pA). (c) One $(C_{70})_{10}$-$(Au)_{35}$ cluster occupied at pinched elbow sites (40 nm × 33 nm, -2.0 V, 50 pA) and (d) one $(C_{70})_{10}$-$(Au)_{35}$ cluster occupying FCC regions (40 nm × 37 nm, -2.0 V, 50 pA). Molecules and gold atoms in the clusters can reorganise and show as a global rotation at these different adsorption sites. A pair of white dashed lines are used to mark the DLs on the two sides of the cluster. Each image in (c) and (d) takes 15 mins to scan.

When a cluster rotates, the atoms in the single layer island reorganise and then form a new single layer island. At room temperature, there is a large number of free gold atoms diffusing quickly on the substrate. When these atoms move close to a magic cluster, some of them can join and change the shapes of its gold island.

It leads to broken of the already formed global balance between van der Waals force and weak chemical Au-C_{70} interactions existing in the cluster. Therefore, for rebuilding clusters' equilibrium, the same number of atoms have to leave the island again. The atoms joining or leaving the cluster are not necessarily sitting in the same positions. Thus the newly formed gold island inside cluster may have a different azimuthal orientation.

Fig. 7-6 (a) illustrates the packing model of one $(C_{70})_{10}$-$(Au)_{35}$ cluster. The herringbone reconstruction on the gold substrate is not drawn in the substrate for simplifying. However, according to the vertical relationship between DLs and gold atoms' packing directions, a blue arrow can be used to represent a discommensuration line (DL) near the cluster. For measuring orientations, the longer axis of the cluster is marked with a green arrow. In Fig. 7-6, the green and blue arrow can overlap, indicating the alignment of the longer axis of the cluster and one of the discommensuration lines (DLs) nearby. With this orientation, gold atoms both in cluster and substrate pack in the same direction. When the cluster changes orientations of its long axis, the green arrow may point to different directions and thus has a series of angles with the blue arrow. By measuring and comparing these angles, it is possible to dope out the packing structure of gold atoms and molecules inside the newly formed magic clusters on Au(111).

As introduced in the first chapter [10-12], there are two kinds of elbow sites on the Au(111) substrate. An extra row of gold atoms inserts into its turning point of a bulged elbow, creating a single gold atom dislocation at its turning point. Compared with pinched elbows, bulged elbows also offer narrower accommodation space to the clusters. On Au(111), most $(C_{70})_{10}$-$(Au)_{35}$ clusters occupy these two types of elbows, while there are also few clusters sitting in FCC regions and staying far from elbows. Fig. 7-6 (b), (c) and (d), as well as their contract enhancement demonstrate several examples of three $(C_{70})_{10}$-$(Au)_{35}$ clusters rotating at the three types of positions. The clusters are observed having

their orientations changed all of a sudden after keeping static for a while. During the process of rotation, all of these clusters are also found having a short distance shifting around elbows or along DLs.

It has been found that the clusters' rotation angles are not continuous. On the contrary, some of these angles appear repeatedly, which means these orientations are more preferred by the clusters than the others. It is probably because the clusters have comparatively lower energy with these orientations. At a bulged elbow site, a pinched elbow site and in the FCC regions far from elbows, the rotation angles of a $(C_{70})_{10}$-$(Au)_{35}$ cluster appearing most frequently are shown in Fig. 7-7, 7-8 and 7-9, respectively.

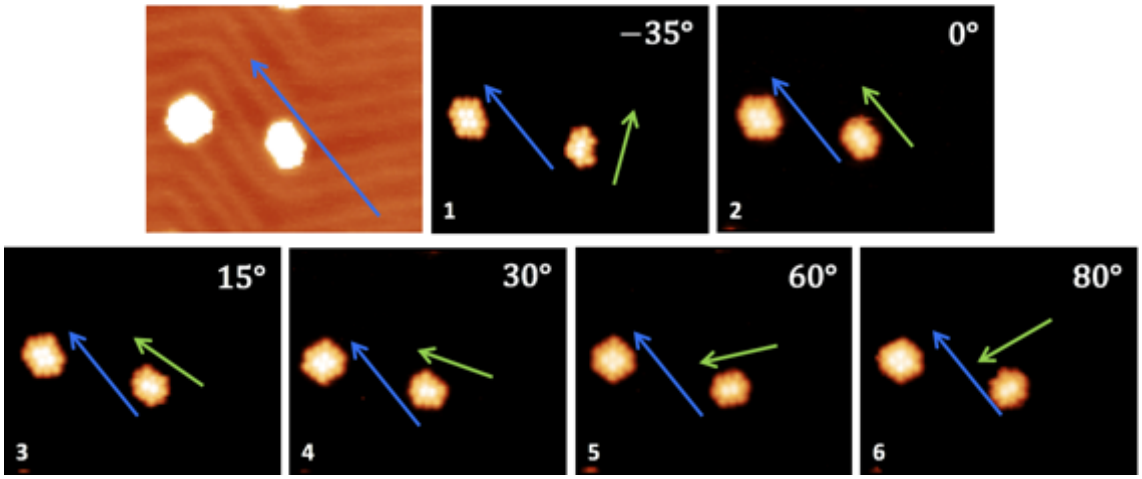


Fig. 7-7 STM images showing the most observed orientations of one $(C_{70})_{10}$-$(Au)_{35}$ cluster sitting at a pinched elbow site. The cluster with the rotation angles of -35°, 0°, 15°, 30°, 60° and 80° are demonstrated in the six images, respectively. Here the positive and minus signs only represent rotating directions of this cluster.

Fig. 7-7 shows the rotation angles of a $(C_{70})_{10}$-$(Au)_{35}$ cluster appearing most often at a pinched elbow in 72 hours. The cluster is scanned by a STM tip with the same bias voltage and tunnelling current. This type of elbow sites do not include single atom dislocations and offer larger accommodation space to clusters compared with the other two occupation sites. Close to the $(C_{70})_{10}$-$(Au)_{35}$ cluster, a $(C_{70})_{12}$-

$(Au)_{49}$ cluster with a larger size is taken as a reference. During scanning, merging of gold islands inside the two clusters is hindered by C_{70} molecules even though Ostwald growth is preferred by bare gold islands here.

With different rotation angles, gold island inside the $(C_{70})_{10}$-$(Au)_{35}$ cluster is always large enough for holding up two C_{60} molecules. When this cluster rotates either 0° or 60°, its long axis is parallel to one of the DLs, and thus packing structure of atoms and molecules inside the cluster suits the model shown in Fig. 7-6 (a). When rotating with other angles, the cluster keeps intact in most cases while having its shape changed slightly when the monolayer gold island inside achieve or lose atoms. The long axis of the cluster shown in the image 1 rotates 35° anti-clockwise from being parallel to a discommensuration line. After rotation the total number of C_{70} molecules doesn't change, but the gold island sitting below C_{70} molecules loses some atoms and becomes smaller. The newly formed cluster thus have a narrower "waist", and molecules on the two sides of its long axis do not pack as straight rows. In the images 2 to 8, cluster rotates clockwise with angles from 0° to 80°. With a rotation angle of 30°, two terminals of the cluster become unequal. It is because one terminal of the gold island under C_{70} have absorbed some more atoms and thus has a larger size. The extra space around the island's edge allows the accommodation of an extra C_{70} molecule. The later joined C_{70} also stands with its long axis perpendicular to the substrate and sit side by side with its neighbouring molecules. When the cluster continued to take other orientations, it changed back to the original shape and lost this extra C_{70} again.

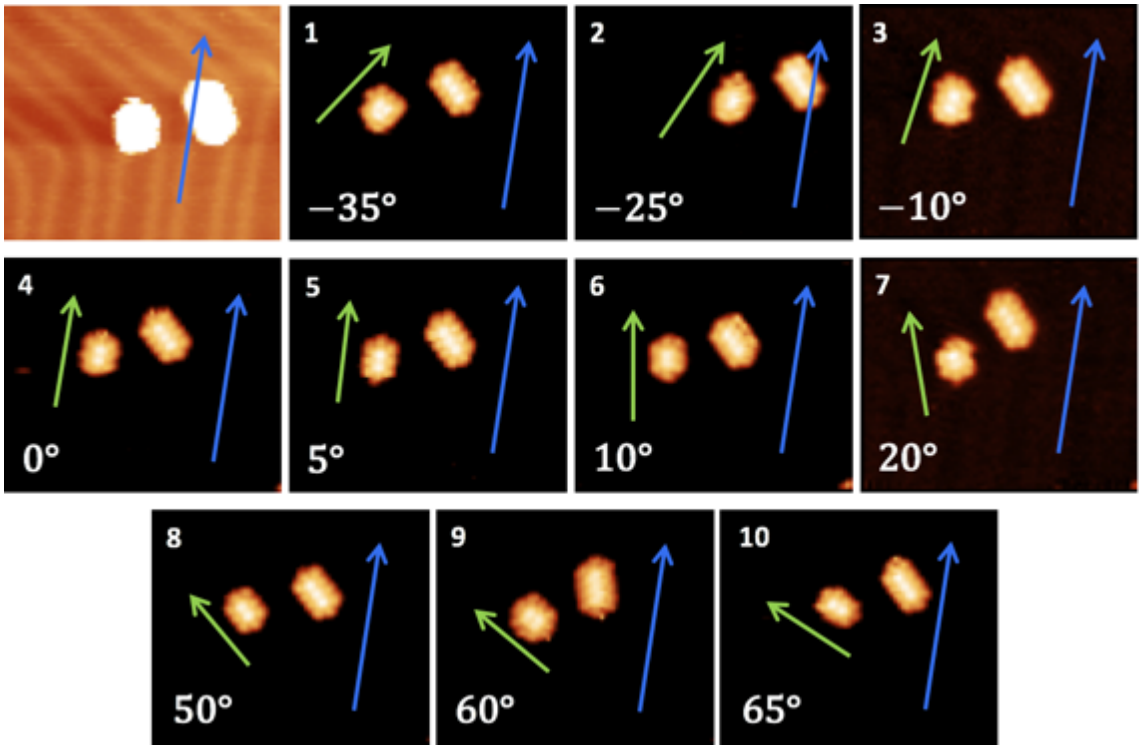


Fig. 7-8 STM images showing the most observed rotation angles of one $(C_{70})_{10}$-$(Au)_{35}$ cluster sitting at a bulged elbow site. The cluster with the rotation angles of -35°, -25°, -10°, 0°, 5°, 10°, 20°, 50°, 60° and 65° are shown in the image 1 to 10, respectively. The positive and minus signs represent rotating directions of this cluster.

Compared with pinched elbows, bulged elbows provide narrower occupation space for magic clusters. As shown in the ten images of Fig. 7-8, most common rotation angles of a $(C_{70})_{10}$-$(Au)_{35}$ cluster at a bulged elbow site is more diversified. Most of these angles are equal or very close to the ones already shown in Fig. 7-7, but none of them is bigger than 65°. Moreover, the single atom defect existing at the bulged elbow site can change gold atoms packing in the substrate and slightly enhances the interaction between the clusters and substrate. It thus makes the rotation mechanism of a cluster here more complicated. For example, with the same rotation angle of -35°, the cluster sitting at a bulged elbow site has a much larger gold island compared with the one sitting close to a pinched elbow site, which allows three C_{70} molecules instead of two sitting on its top.

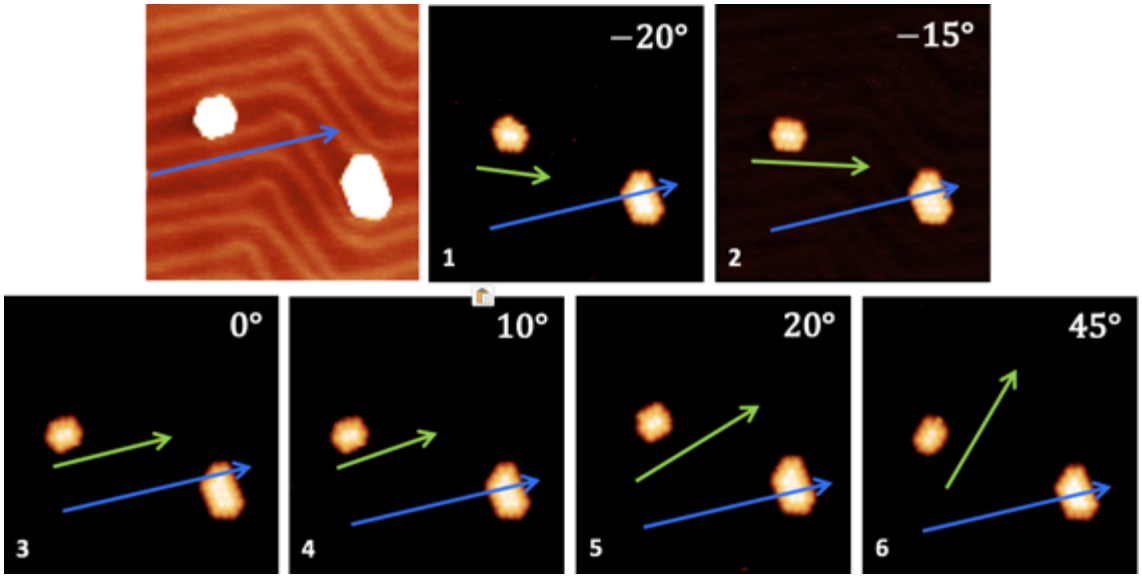


Fig. 7-9 STM images showing the rotation angles of one $(C_{70})_{10}$-$(Au)_{35}$ sitting in the FCC regions appearing most often. The cluster with the rotation angles of -20°, -15°, 0°, 10°, 20°, 45° are demonstrated in the image 1 to 6 respectively. The positive and minus signs represent rotating directions of this cluster [2].

Limited by parallel DLs, the maximum rotation angle of a $(C_{70})_{10}$-$(Au)_{35}$ cluster far from elbow sites observed in the scanning images is much smaller compared with occupying elbow sites. Apart from packing with its long axis parallel to DLs (0°), the cluster in Fig. 7-9 prefers to have rotation angles of $\pm 10°$, $\pm 15°$ and $\pm 20°$. Here, the positive and minus signs only represent rotating directions. All of these angles are similar to the angles shown in both Fig. 7-7 and Fig. 7-8, the clusters sitting far from elbows maintain their basic shapes during rotation in most cases. For this cluster, the rotation angles with the same values but different directions appear with almost equal possibilities according to our statistics due to an axisymmetric environment the cluster existing in. The first image in Fig. 7-9 showing the cluster with a rotation angle of -20°. Similar to the phenomenon shown before, the gold island under C_{70} molecules expand, and another C_{70} molecule joins the cluster and occupies the vacancy left by other molecules surrounding the island. The cluster can also change back to the original shape

after taking other orientations. Therefore, no matter approaching elbow sites or not, magic number clusters always have the ability of "self-healing" during rotation. Edge diffusing of gold atoms and molecules play dominant roles in this process.

The clusters sitting on the Au(111) surface prefer to orienting with certain angles more frequently than the others. Hence three $(C_{70})_{10}$-$(Au)_{35}$ clusters occupying a bulged elbow, a pinched elbow and far away from elbows were scanned simultaneously for a long duration. The same bias voltage and tunnelling current were applied during scanning. Then, we counted the occurrence number of each rotation angle and classified these angles depending on their occupation sites.

Statistics results are shown in Fig. 7-10, in which a total of 206 images were counted. The $(C_{70})_{10}$-$(Au)_{35}$ cluster occupying pinched elbows has the richest category of rotation angles, most of which are in the range of $-85°$ to $90°$. For the clusters sitting at bulged elbows or far from elbows, all of their rotation angles have the values within $-65°$ to $65°$. At both the two types of elbows, a $(C_{70})_{10}$-$(Au)_{35}$ cluster prefer to have the rotation angles such as $-25°$, $0°$, $5°$, $10°$, $50°$ and $60°$, among which, rotation angles of $0°$, $10°$, $50°$ and $60°$ occur more than 10 times at bulged elbows. However, the rotation angles such as $10°$ and $50°$ are less preferred by the cluster at pinched elbows. However, for the cluster sitting far from elbow sites, their rotation angles are limited in a smaller range. Fig. 7-10 illustrates that most values of these angles are smaller than $30°$. It is because the cluster is trapped more tightly by a pair of parallel DLs. Once the cluster rotates, C_{70} molecules and gold atoms it includes are expected to lift part of the DLs nearby, which requires extra energy. The larger angles cluster rotates, the higher energy is demanded. Therefore, we can draw a conclusion that clusters' orientation can be strongly affected and limited by the herringbone reconstruction on the gold substrate.

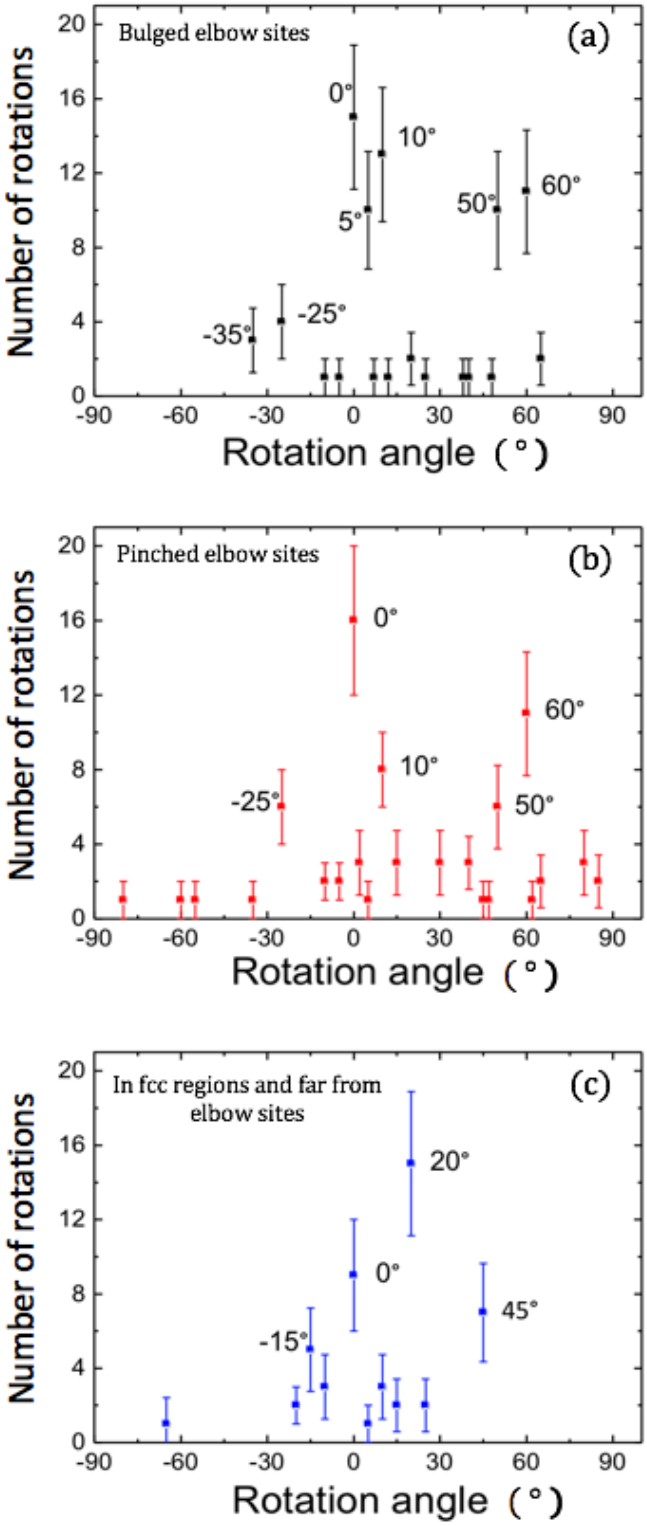


Fig. 7-10 Pointed profile showing the distribution of rotation angles for the $(C_{70})_{10}$-$(Au)_{35}$ clusters sitting at the bulged elbow sites, pinched elbow sites and far from elbow sites. A total number of 206 rotation angles are recorded.

As mentioned above, 0°, 10°, 50° and 60° are the four most common rotation angles of $(C_{70})_{10}$-$(Au)_{35}$ clusters sitting at elbows. It indicates that at these positions, the $(C_{70})_{10}$-$(Au)_{35}$ clusters are with lower energy and stronger stability compared with orienting with other angles. In Fig. 7-11 (a), only the monolayer gold island of a $(C_{70})_{10}$-$(Au)_{35}$ cluster is left on the substrate while all the C_{70} molecules are removed. Thirty-five close-packed atoms forming the single layer island are coloured in yellow. The long axis of this cluster is marked with a green arrow, which can be obtained by connecting the gold atoms (coloured red) sitting in the centre of two hexagons. When a $(C_{70})_{10}$-$(Au)_{35}$ cluster changes its orientation from 0° to other angles, the number of corner atoms in the islands' centre has to be minimized because of the lower coordination of these atoms. Also, for keeping the cluster's size and shape unchanged, only one or two diffusing atoms are expected to be captured or lost by the gold island during rotation.

Possible models of the monolayer gold island rotating 10°, 30° and 50° inside a $(C_{70})_{10}$-$(Au)_{35}$ cluster have been put forward in Fig. 7-11 (b), (c) and (d). All of these islands have enough size for holding up two C_{70} molecules. However, by allowing the joining of extra gold atoms, the cluster has its energy increase. When other eight C_{70} molecules surround these islands, neighbour distances between them are difficult to be uninformed. It explains why clusters could not maintain stability with these azimuthal orientations for such a long time.

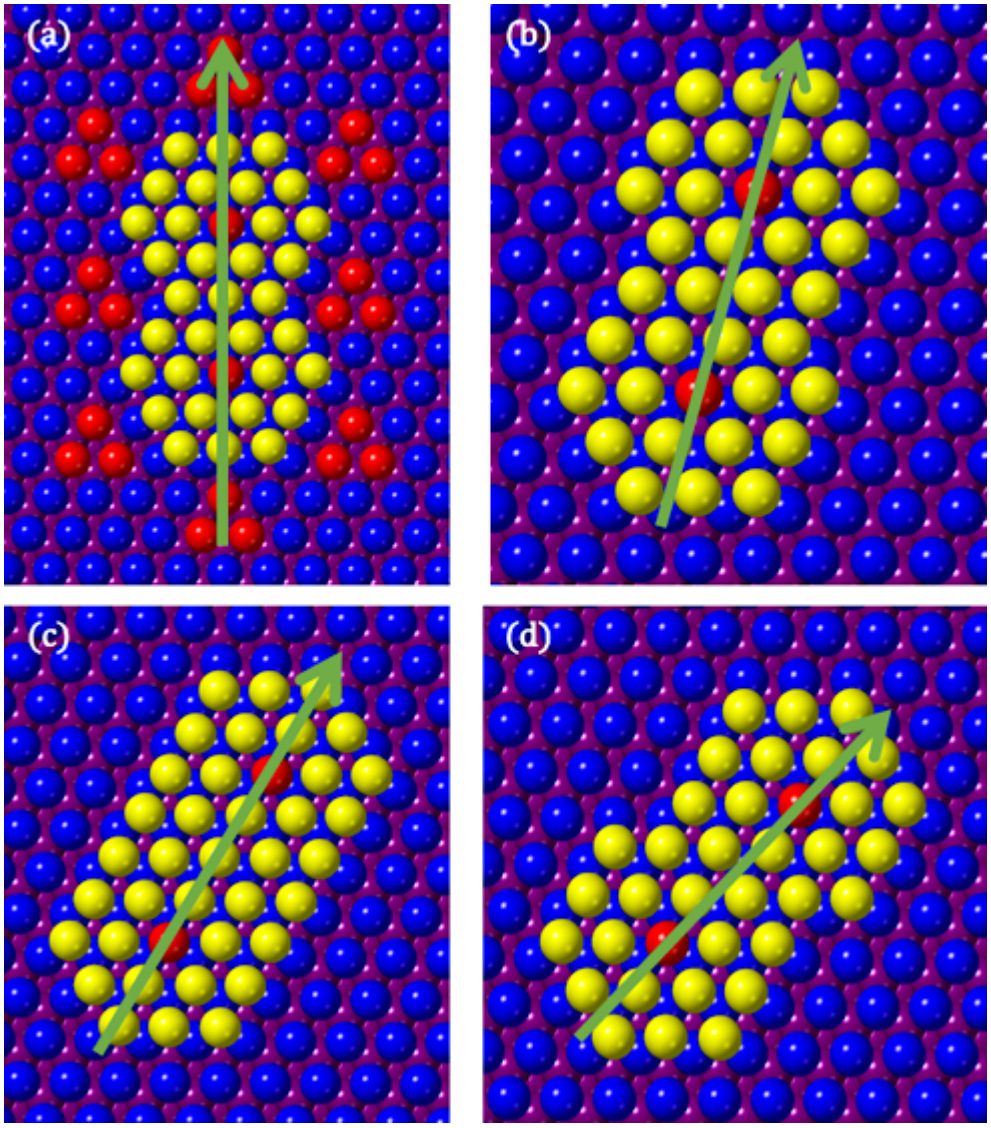


Fig. 7-11 Structural models proposed for single atomic layer Au islands consisting of ~ 35 Au atoms. (a) The ideal packing structure of the $(C_{60})_{10}$-$(Au)_{35}$ cluster. (b) Au island with 36 Au atoms. The red spheres indicate where the two "bright" C_{70} molecules sit. (c) Au island 39 Au atoms. (d) Au island with 36 Au atoms. When ten C_{70} molecules are added to the four different shaped Au islands, we can see the formation clusters with their longer axis rotating 0°, 10°, 30° and 50° from $[11\bar{2}]$, respectively.

When a cluster's long axis rotates 10° or 50° from being parallel to a DL, gold atoms inside the cluster occupy three-fold hollow sites and form a new island. During this period, one extra gold atom adds in and cooperates with the original 35 atoms. The general shapes of both the two newly formed gold islands are kept

as quasi twin-hexagonal, in which the fewest atoms sitting at islands' corners can be found.

Fig. 7-11 (c) puts forward a possible model of the gold island with the rotation angle of 30°, in which there is even fewer number of gold atoms sitting at island's corner compared with the models of 10° and 50°. However, this type of orientation is only preferred by $(C_{70})_{10}$-$(Au)_{35}$ clusters sitting at rounded elbows. Either sitting at bulged elbows or far from elbow sites, this type of clusters always refer to rotate with 20°, which is close but still has ten degrees to 30°. It indicates that herringbone reconstruction (DLs) nearby can slightly affect the packing of atoms and molecules sitting on the gold surface and thus change clusters' rotation angles.

7.5.2 Rotation of $(C_{70})_{10}$-$(Au)_{35}$ Clusters At Low Temperatures

At 110 K, the diffusion of gold atoms and C_{70} molecules on Au(111) are suppressed. Rotation of a magic cluster is dominated by the thermal activation of its gold atoms and molecules. In Fig. 7-12 (a), a magic cluster and a ring cluster sitting on the substrate are marked in a blue and a yellow circle respectively. Scanned by the STM tip with a fixed bias voltage and tunnelling current for four hours, both the two clusters kept static, and none of their C_{70} molecules changed its position. A small size gold island is marked in a green circle, which can also maintain stability for a long time even though it is not surrounded by C_{70} molecules.

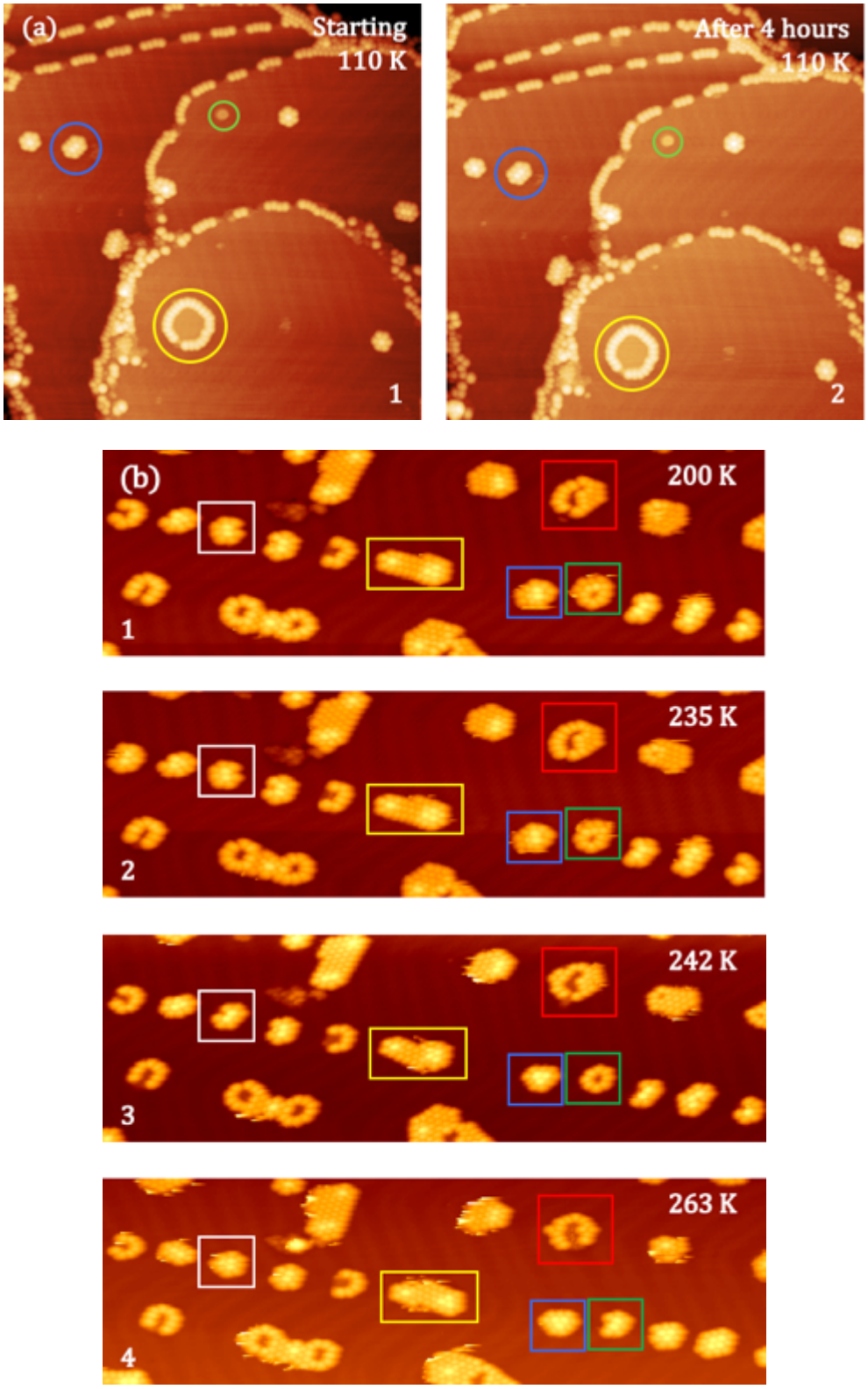


Fig. 7-12 (a) STM images showing the magic number and ring clusters at 110 K. Before being cooled to 110 K again, these clusters have been formed at 110 K firstly and then annealed to room temperature. Both the clusters and gold islands marked in circles remain unchanged at elbow sites on the Au(111) surface after being scanned for four hours (-2.0 V, 50 pA,

65 nm × 65 nm). (b) The clusters formed at 110 K and then increased to room temperature. The gold atoms and C_{70} molecules of clusters start to reorganise at 242 K. The gold islands inside clusters can rotate and nucleate as larger ones before being fully covered or surrounded by C_{70} molecules. (-2.0 V, 50 pA, 91 nm × 28 nm). At higher temperatures, most of the clusters tend to form closed-shell magic number clusters, ring clusters and joined clusters.

Then the clusters were then annealed from 110 K to room temperature. The clusters were observed maintaining static until 242 K. As shown in Fig. 7-12 (b), all the size clusters start to change orientations and tend to have compact structures. It is because the C_{70} molecules have enough energy to overcome the potential barrier and jump onto the top of gold islands at this temperature. A cluster having a shape similar to $(C_{70})_{10}$-$(Au)_{35}$ but lacking one C_{70} molecule is highlighted by a white box. From the image 2 to 3, it rotates 60° and keeps its basic shape unchanged. When temperature increases to 263 K, a gold island inside the cluster ripens large enough for accommodating three C_{70} molecules on its top. Some more diffusing C_{70} molecules also join the cluster and form a new $(C_{70})_{12}$-$(Au)_{49}$ cluster. One joined cluster and one ring cluster are marked in yellow and red boxes, respectively. At 242 K, C_{70} molecules around the two clusters start to move on top of the gold islands or diffuse away. However, the gold islands inside the two clusters do not have a noticeable change in their sizes before the temperature reaches 263 K. It indicates that, the gold islands play a dominant role in changing the orientations of clusters, while the surrounding C_{70} molecules mainly work as a shell and limit ripening of the gold islands.

7.5.3 Rotation of Other Hybrid Clusters

Azimuthal orientations of the large magic number clusters such as $(C_{70})_{12}$-$(Au)_{49}$ have also been studied. As shown in Fig. 7-6, if we continue to use the same method of measuring the rotation of $(C_{70})_{10}$-$(Au)_{35}$ clusters, there are three green

arrows used to represent the packing conditions of one $(C_{70})_{12}$-$(Au)_{49}$ cluster due to its property of centre symmetry. It is thus more difficult for us to judge the exact orientation angles of clusters on Au(111). Therefore, for distinguishing the orientation of a $(C_{70})_{12}$-$(Au)_{49}$ cluster, we firstly connect every two of the three C_{70} molecules sitting on top of gold islands and then draw the corresponding three green arrows. For simplify, one of the DLs near the cluster is still marked with a blue arrow. The angles between this blue arrow and all the three green arrows are measured. The smallest acute angle is then chosen to represent the rotation of a $(C_{70})_{12}$-$(Au)_{49}$ cluster. The clusters belonging this type are observed changing orientations at a bulged elbow site and a pinched elbow site respectively, which are demonstrated in Fig. 7-13 (a) and (b). These clusters are scanned by STM with the application of the bias voltage of -2.0 V and the tunnelling current of 50 pA. Similar to $(C_{70})_{10}$-$(Au)_{35}$, a $(C_{70})_{12}$-$(Au)_{49}$ cluster can also maintain its basic shape during rotation.

At the bulged elbow sites, rotating angles of the $(C_{70})_{12}$-$(Au)_{49}$ clusters range from 0° to 60°. The positive and negative signs represent clockwise rotation and anti-clockwise rotation, respectively. In our STM images, this $(C_{70})_{12}$-$(Au)_{49}$ cluster also prefers to take the rotation angles such as 10°, 20°, 25°, 50° and 60°. According to our scanning images, the $(C_{70})_{12}$-$(Au)_{49}$ cluster keeps static with these orientations for a longer time compared with a $(C_{70})_{10}$-$(Au)_{35}$ cluster. It is because this cluster contains a larger number of gold atoms and C_{70} molecules and requires higher energy to rotate. However, when a $(C_{70})_{12}$-$(Au)_{49}$ cluster rotates between 0° and 10°, the C_{70} molecules surrounding gold island tend to pack along the DLs and then slightly change the island's shape, as shown in the sixth image of Fig. 7-13 (a).

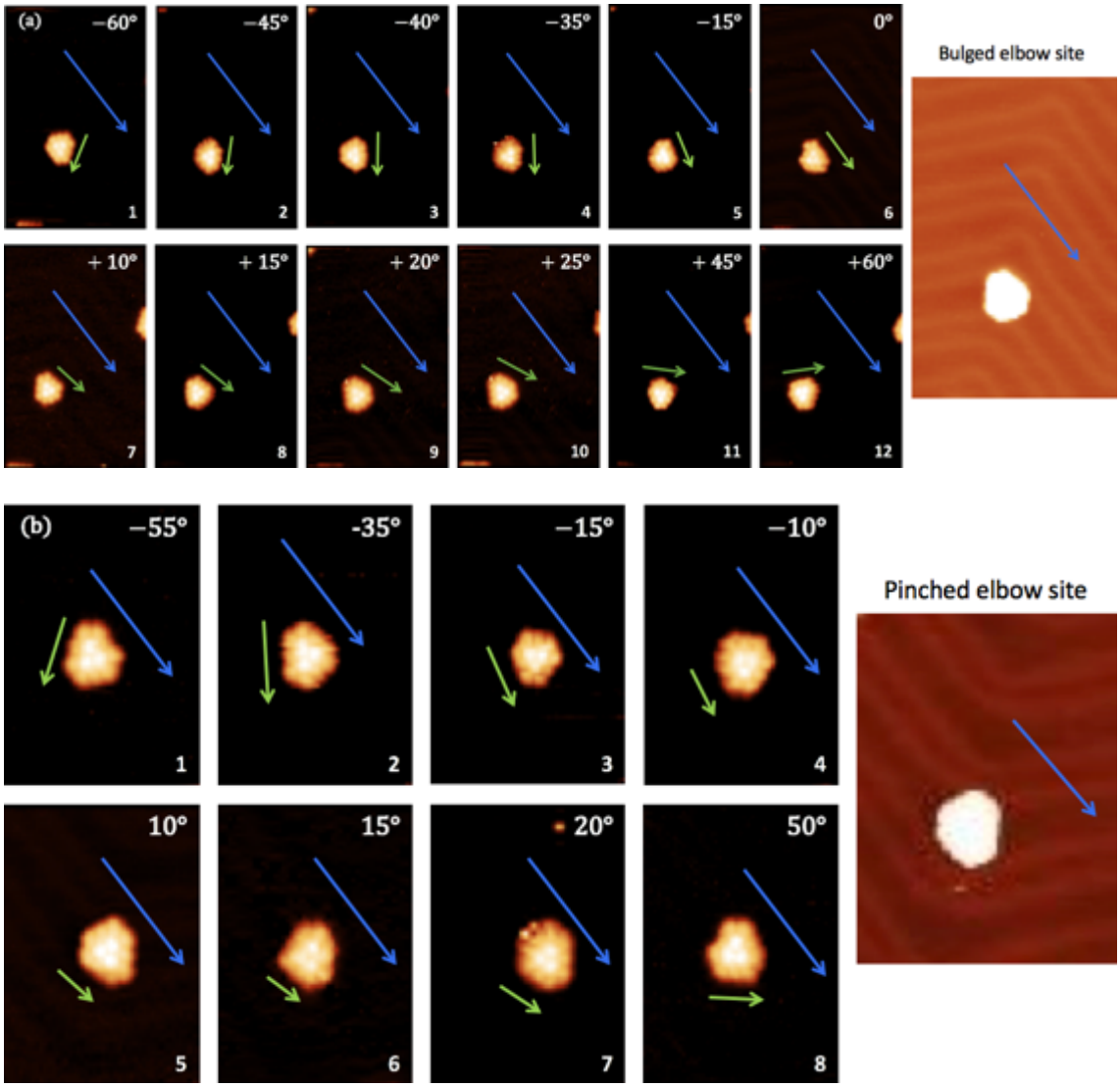


Fig. 7-13 The main orientations of a $(C_{70})_{12}$-Au_{49} cluster sitting at (a) a bulged elbow site and (b) a pinched elbow site on Au(111) $(-2.0\ \mathrm{V}, 50\ \mathrm{pA})$. The blue arrows represent DLs near the clusters. The green arrows are always parallel to one edge of the $(C_{70})_{12}$-Au_{49} cluster.

When a $(C_{70})_{12}$-$(Au)_{49}$ cluster sits on a pinched elbow site, fewer categories of orientations are found in our scanning, and the values of these angles are limited within 55°. Apart from 0° and 10°, the rotation angles such as 25° and 45° are also less observed. Instead, rotation angles of 20° or 50° appear more frequently. The larger space offered by pinched elbow sites enables atoms and molecules inside the cluster to find their most preferable and stable occupying positions.

Fig. 7-14 (a) shows an ideal structure of single atomic layer gold island inside one $(C_{60})_{12}$-$(Au)_{49}$ cluster. Atoms in this island are represented by yellow colour spheres which all sit on three-fold hollow sites, while the red spheres represent the gold atoms directly contacting with C_{70} molecules. When cluster rotates, size and position of both the gold islands and C_{70} molecules around are required to change. If the island is too large, another C_{70} molecule can attach to one edge of the new island for filling the vacancy left by other molecules.

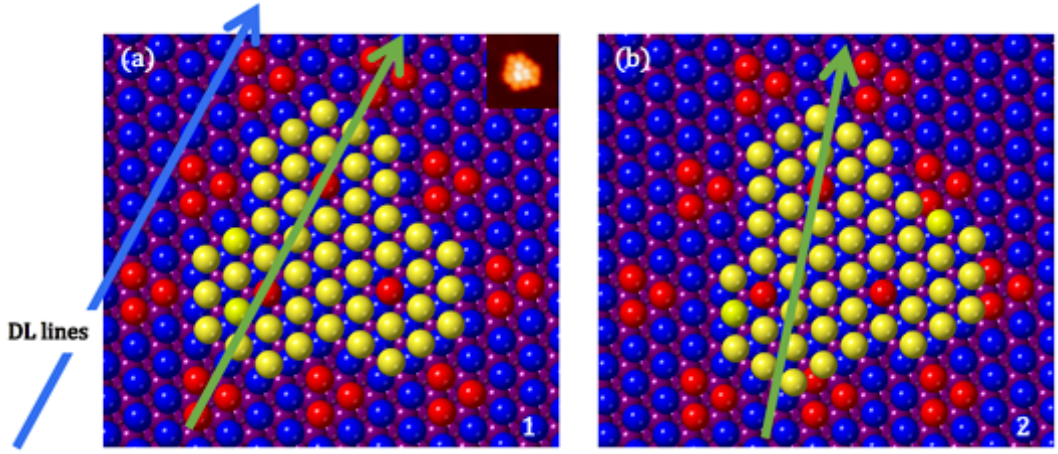


Fig. 7-14 Structural models proposed for single atomic layer Au islands consisting of ~ 49 Au atoms inside a $(C_{60})_{12}$-$(Au)_{49}$ cluster. The red spheres mark the occupation sites of three C_{70} molecules on the island's top. (a) Island structure when the $(C_{60})_{12}$-$(Au)_{49}$ cluster has 0° orientation. (b) The newly formed cluster rotating 10°, where the gold island consisting of 51 atoms.

Fig. 7-14 (b) indicates a possible model, where the $(C_{60})_{12}$-$(Au)_{49}$ cluster rotates about 10°, and the newly formed gold island is observed consisting of 51 gold atoms. A green arrow is used in Fig. 7-14 (b) to mark the new orientations of this cluster, which is drawn by connecting the atoms sitting in the centre of two hexagons. The angle between the green and blue arrow 10°. The original positions of C_{70} molecules are coloured in red. Taking these red atoms as a reference, we find all the C_{70} molecules have to change their positions during rotation. The newly formed island consists of 51 gold atoms, marked in yellow. Some gold

atoms on the left side of the island disappeared while some others appeared on the right side. It leads to a slight shift of the whole island. There are two assumptions can explain it. One explanation is that the original 49 atoms in the islands reorganised and formed a new island with extra two atoms, which has already been discussed above. The other explanation is based on dynamic equilibration. The gold island captured some diffusing atoms on the right side but lost gold atoms on the left side at the same time.

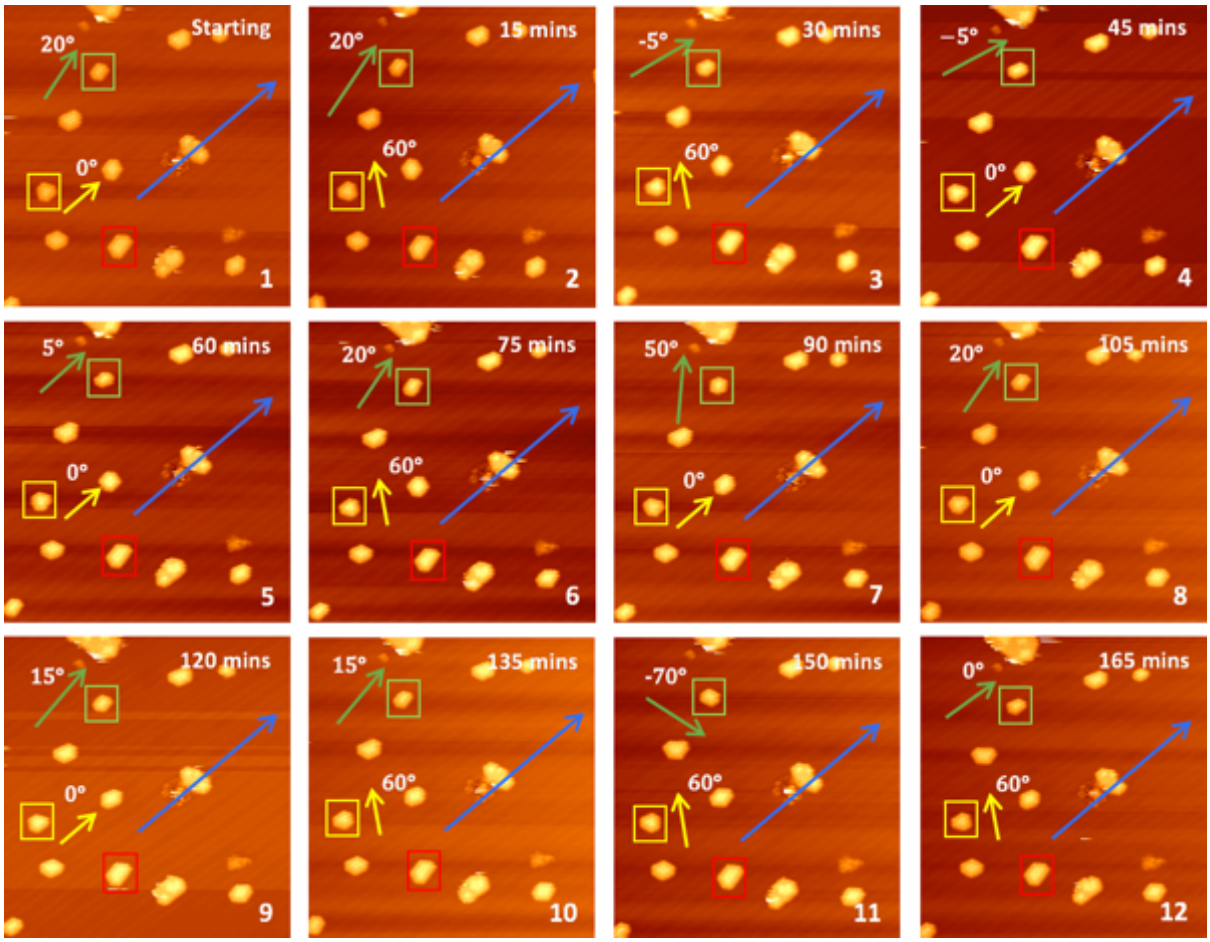


Fig. 7-15 Rotation of various size magic number clusters on a region of Au(111) where there is no elbow site demonstrated in 12 images (-2.0 V, 50 pA). All the clusters sit in FCC regions far from elbows. The packing direction of surface gold atoms is perpendicular to the blue arrow. A green arrow and a yellow arrow is used to mark the orientations of a $(C_{70})_{10}$-$(Au)_{35}$ cluster and a $(C_{70})_{12}$-$(Au)_{49}$ cluster on gold substrate, respectively.

An area where various sizes of magic number clusters and joined clusters sit in FCC regions far from elbows is shown in Fig. 7-15. All these clusters are confined tightly by their adjacent discommensuration lines. However, the clusters with smaller sizes are still able to change azimuthal orientations in the total 165 mins scanning. A $(C_{70})_{10}$-$(Au)_{35}$ cluster existing in the top-left of the images is marked in the green boxes. It still prefers to change orientations with angles such as 0°, 15° and 20°, which are similar to the ones already demonstrated in Fig. 7-9. As shown in the yellow boxes, rotation of a $(C_{70})_{12}$-$(Au)_{49}$ cluster is more strongly affected by the DLs nearby due to its larger size. It can be observed from the 12 images, the cluster is observed only rotating 0° or 60°. Therefore, during the whole process of scanning, gold atoms in the cluster always pack in the same directions with the ones in the top layer of the substrate.

Comparing two continuous images (e.g., 3 and 4 or 9 and 10), we find that under the same scanning conditions, the two clusters marked are found rotating out of sync. When the $(C_{70})_{10}$-$(Au)_{35}$ cluster keeps one orientation of either -5° or 15°, the $(C_{70})_{12}$-$(Au)_{49}$ cluster can change its orientation from 60° (0°) to 0° (60°), and vice versa. As shown in the red box, the cluster with a larger size keeps static for more than two hours. It indicates that the orientation change of magic clusters is determined by their sizes and reconstruction on Au(111).

The joined clusters can also change orientations on Au(111) even though they commonly consist of more of gold atoms and C_{70} molecules. The Two joined clusters are shown in Fig. 7-16. Inside the cluster on the right, there are two gold islands with unequal sizes, which occupy two independent pinched elbow sites. One of its gold islands is large enough to hold up ten C_{70} molecules while the other one is too small to accommodate more than one molecule on its top.

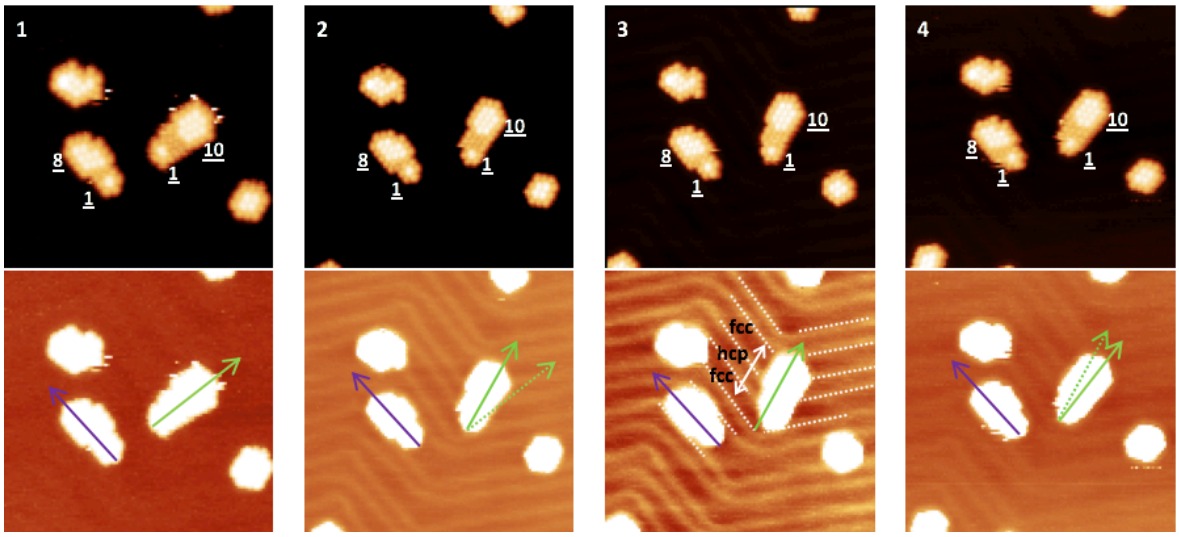


Fig. 7-16 Rotation of the two joined clusters on the Au(111) substrate. One occupies two FCC regions and one HCP region. Two gold islands in one cluster have unequal sizes and sit at two pinched elbow sites, respectively (-2.0 V, 50 pA). The other joined cluster consisting of a large and a small gold island sits in the FCC regions entirely on the gold substrate.

As marked in the image 3, this cluster occupies two FCC regions and one HCP region. One of its terminal shifts along one DLs for a very short distance after being scanned for 4 hours, while the other terminal of the cluster keeps still during this time. After being scanned for 18 hours, the larger gold island of the cluster in the image 4 moves a short distance again, and the small island still keep static. It could be also treated as a global rotation of the joined cluster. Therefore, once after rotation, a joined cluster can maintain stability for a longer time.

The joined cluster on the left side lies entirely in the FCC regions. One of its gold islands is large enough to hold up eight C_{70} molecules, while on the other one can only accommodate one C_{70} molecule on its top. Confined by the reconstruction on the two sides, this cluster doesn't rotate or move at all during scanning.

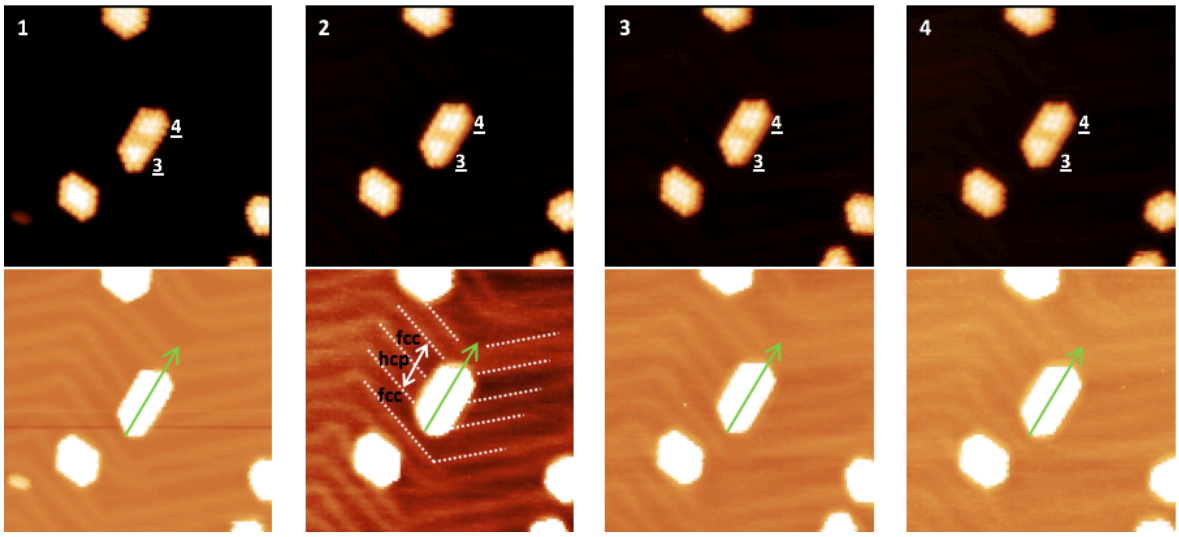


Fig. 7-17 Rotation of a joined cluster on the Au(111) substrate. It occupies an FCC and an HCP region. The gold islands in the cluster have similar sizes and also occupy two pinched elbow sites, respectively (-2.0 V, 50 pA).

Fig. 7-17 puts forward another joined cluster containing two single layer gold islands on Au(111). The cluster occupies one FCC and one HCP region, and its two terminals just touch two pinched elbows, respectively. Inside the cluster, one gold island is observed lifting three C_{70} molecules while the other island lifting four. It indicates the two gold islands of this cluster have similar sizes. this cluster is being scanned. The cluster keep static totally for more than 18 hours and does not show any rotation.

7.6 Cluster Shifting and Merging At Room Temperature

The small size magic clusters are also observed changing their positions on Au(111) due to the effect of Ostwald ripening. A $(C_{70})_{10}$-$(Au)_{35}$ cluster sitting between a bulged elbow site and a large ring cluster is shown in Fig. 7-18, where the cluster kept changing positions and had size transformation in a total of 14 hours. During scanning, -2.0 V and 50 pA are respectively used as the bias voltage and tunnelling current. The cluster moves back and forth slowly along the DLs

on its two sides, which are marked with a pair of white dashed lines. Either tip scanning or the diffusing atoms offered by the large ring cluster on the left could be the reason triggering position shifting of the cluster.

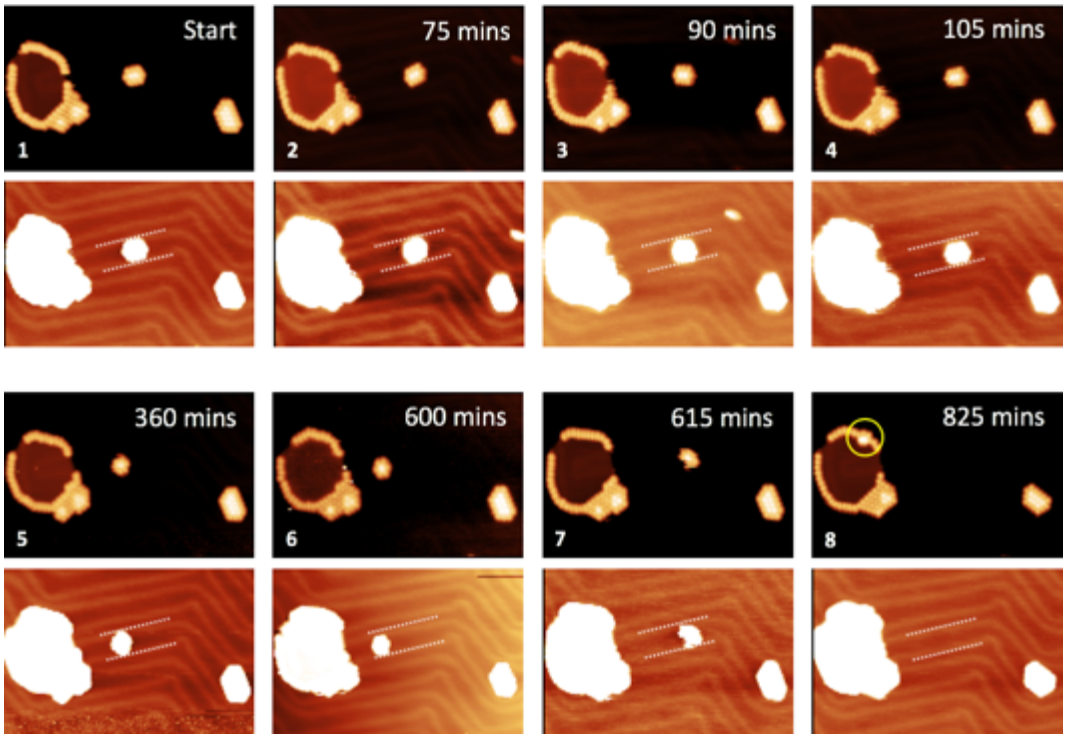


Fig. 7-18 The shifting as well as the transforming of one $(C_{70})_{10}$-$(Au)_{35}$ cluster trapped in FCC regions between a ring cluster with large gold island and a bulged elbow site (-2.0 V, 50 pA). Two parallel dashed white lines highlight the DLs on the two sides of the cluster.

From the image 2 to 3, the cluster doesn't change its positions but rotates ~ 15°. However, taking the white lines as reference, the cluster in the image 4 continues to rotate and meanwhile shifts slightly to the right side. It makes the DLs on the two sides of this cluster bend a bit. After being scanned for 6 hours, the $(C_{70})_{10}$-$(Au)_{35}$ cluster has transformed into a $(C_{70})_7$-$(Au)_{19}$ type one, which continues shifting along DLs for another 7 hours before finally breaking up. The newly formed cluster consists of a fewer number of gold atoms and C_{70} molecules and has a smaller size. It thus makes the cluster move in the narrow FCC region more smoothly. When the same bias voltage and tunnelling current are applied to the

scanning tip, the $(C_{70})_7$-$(Au)_{19}$ cluster in the FCC region is observed moving farther distances compared with a $(C_{70})_{10}$-$(Au)_{35}$ one.

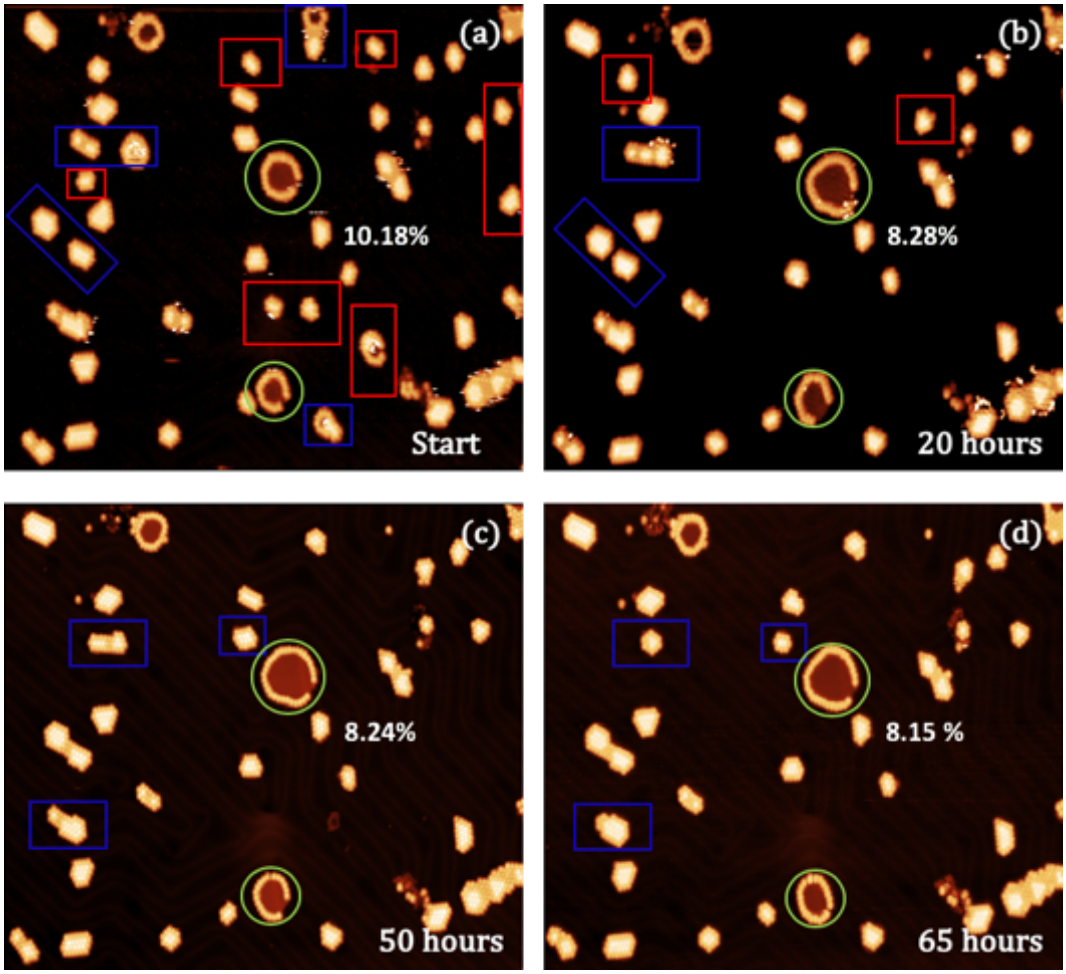


Fig. 7-19 STM images showing the effect of tip scanning to the transformation of magic clusters on Au(111) (-2.0 V, 50 pA, 137 nm × 123 nm). The red and blue boxes in one figure are used to mark the clusters breaking up or transforming into smaller size ones in the next image, respectively. Two large ring clusters are marked with green circles, of which the sixes increase gradually during scanning. (a) The original topography of various sizes of clusters sits at elbow sites on the Au(111) substrate. (b) The same clusters after being scanned uninterruptedly for 20 hours by a tungsten tip with a constant bias voltage of -2.0 V and tunnelling current of 50 pA. (c) The same clusters on the gold substrate without being scanned for 30 hours. (d) Clusters after being scanned sequentially for 15 hours with the bias voltage of -2.0 V and the tunnelling current of 50 pA.

When this $(C_{70})_7$-$(Au)_{19}$ cluster finally breaks up, its atoms and molecules move again and quickly diffuse away. One of these C_{70} molecules is found joining the edge of the ring cluster on the left, marked in a yellow circle. On the right side of the image 8, the large magic number cluster occupying a pinched elbow site is found rotating 30° all of a sudden. It is probably triggered by the gold atoms of the missing $(C_{70})_7$-$(Au)_{19}$ cluster.

For investigating the effect of the bias voltage to the clusters, an area on Au(111) is chosen for scanning, where a series of clusters with different sizes occupy elbow sites. These clusters are kept being scanned by a tungsten tip with a constant bias voltage of -2.0 V and a tunnelling current of 50 pA. As demonstrated in Fig. 7-19 (a) and (b), after being scanned for 20 hours, some small size clusters marked in the red boxes disintegrated. The large joined clusters marked in the blue boxes have transformed to smaller ones, and the aggregation of two or more clusters is also observed. Since the total coverage of all the clusters drops significantly from 10.18 % to 8.28 %, most of molecules and atoms in these missing and transforming clusters have diffused away to gold steps on the substrate. Triggered by Ostwald ripening, ring clusters in solid green circles ripen as larger ones by catching a small quantity of these diffusing atoms and molecules.

Then these clusters are kept in UHV without being scanned by scanning tip for ~ 30 hours. The same clusters are then scanned when the same bias voltage and current are applied. Compared with image 7-19 (b) and (c), a continuous ripening of the ring clusters in green circles is observed, while there are fewer closed-shell clusters transforming or disintegrating on the gold substrate. In addition, there is no obvious change in the total coverage of clusters in the 30 hours. In the next 15 hours, there is no obvious change in the number and sizes of the magic number and ring clusters. Comparing the clusters in all the four figures, we can conclude

that with or without tip scanning, rotation of small size clusters can always happen. It indicates the limited impact scanning tip puts on these clusters.

7.7 Summary

We have provided an approach for creating and controlling the morphological evolution of metal-organic coordinates on metal substrates. Most of the small size magic clusters sit close to the bulged or pinched elbow sites, while there are also few clusters found sitting in the FCC regions far from elbow sites. In UHV, gold atoms and C_{70} molecules were co-deposited on Au(111) at 110 K and then annealed to room temperature, C_{70} molecules are observed surrounding or sitting on top of the single layer gold island and forming the closed-shell $(C_{70})_m$-$(Au)_n$ magic number clusters. At room temperature, these clusters are able to adsorb the diffusing gold atoms on the Au(111) surface and become unstable. Therefore, the gold atoms and C_{70} molecules have to reorganise and form a new cluster. The interesting thing is, the newly formed clusters are observed keeping basic shapes the same as the old ones but having different azimuthal orientations. In the STM images, these magic number clusters look like rotating once after keeping static for a while. On the same flat terraces of the gold substrate, the magic number clusters with large sizes are harder to change their orientations compared with the smaller ones. As time goes on, some of these large-sized clusters transform into the smaller ones gradually by losing atoms and molecules .

The herringbone reconstructions on the (111) gold surface can put an effect on the rotation of clusters. Compared with the bulged elbow sites, the pinched elbow sites offer comparable large accommodation spaces, which enables the clusters to rotate with larger amplitudes. The clusters sitting far from elbow sites are trapped by their adjacent DLs and thus have the smallest rotation angles. Moreover, the electric field created by the applied tunnelling current can also

change the stability of the magic number clusters can accelerate clusters transformation.

References

[1] B, Palpant, B. Prevel, J. Lerme, E. Cottancin, M. Pellarin, M. Treilleux, A. Perez, J. L. Vialle, and M. Broyer, Phys. Rev. B: Condens. Matter Mater. Phys. **57**, 1963 (1998).

[2] G. M. Pastor, J. Dorantes-Davila, and K. H. Bennemann, Phys. Rev. B: Condens. Matter Mater. Phys. **40**, 7642 (1989).

[3] E. L. Muetterties, Science **196**, 839 (1977).

[4] W. Wernsdorfer, and R. Sessoli, Science **284**, 133 (1999).

[5] M. F. Jarrold, Science **252**, 1085 (1991).

[6] U. Buck, F. Huisken, Chem. Rev. **100**, 3863 (2000).

[7] X. Peng, L. Manna, W. Yang, J. Wickham, E. Scher, A. Kadavanich, and A. P. Alivisatos, Nature **404**, 59 (2000).

[8] X. Huang, E. Lindgren, and J. R. Chelikowsky, Phys. Rev. B: Condens. Matter Mater. Phys. **71**, 165328 (2005).

[9] Yitao Wang, Dogan Kaya, Jianzhi Gao and Quanmin Guo, Stick-Sudden Rotation and Structural Polymorphism of $(C_{70})_m$-$(Au)_n$ Hybrid Nanoclusters, J. Phys. Chem. C **123**, 12791 (2019).

[10] D. D. Chambliss, R. J. Wilson, J. Vac. Sci. Technol. B **9**, 928 (1991).

[11] D. D. Chambliss, R. J. Wilson, S. Chiang, Phys. Rev. Lett. **66**, 1721 (1991).

[12] D. D. Chambliss, R. J. Wilson, S. Chiang, J. Vac. Sci. Technol. B **9**, 933 (1991).

8. Summary and Future Work

In this work, several two-dimensional structures formed by fullerene molecules (C_{60} and C_{70}) and gold atoms have been studied on the substrates such as Au(111) and highly oriented pyrolytic graphite (HOPG). The chemical interaction between gold atoms and molecules as well as the van der Waals force between molecules play crucial roles in forming and maintain these structures. Depending on the difference in the molecules' categories, the properties of the structures vary from each other.

As the simplest fullerene molecules, both C_{60} and C_{70} molecules tend to form close-packed molecular layers on the gold substrate. Similar to C_{60}, close-packed C_{70} on the Au(111) substrate can orient into different packing directions and form angles of 14°, 30° and 34° relative to that of the surface gold atoms. Each C_{70} stands with their long molecular axis perpendicular to the gold surface with the domain lattice of 1.05 nm. By annealing more than one layer C_{70} molecules at 423 K, some of them can overcome the potential barrier of islands' steps and form the third or even fourth layers with quasi-hexagonal shapes on top of the first layer. The interaction between the gold substrate and the molecules in these upper layers are rather weak, the molecules' packing structures are thus determined by the van der Waals forces. When the annealing temperature reaches 473 K, most of the third and fourth layers disappear, leaving the C_{70} in the first and second layers on the gold substrate. The second layer islands merge as larger ones and tend to have hexagonal shapes.

Several experiments have been conducted to study the possibility of growing "molecular alloys" on the gold surface. When 0.3 ML C_{60} and 0.3 ML C_{70} are co-deposited on Au(111) at room temperature, the two kinds of molecules form sharp boundaries and do not mix in the absence of thermal treatment. Due to the lattice mismatch, edge-dislocations can be observed at the boundaries between the C_{60}-rich and C_{70}-rich domains. After being annealed at 573 K for 30 minutes, both

the two types of molecules in the first layer can pass across domain boundaries and mix into each other. Since C_{70} molecules have lower diffusion ability and weaker interaction with gold substrate compared with C_{60} molecules, Single C_{70} molecules can be trapped in the C_{60}-rich domains. In contrast, C_{60} molecules squeezing into C_{70}-rich domains are able to nucleate as small groups or chains. The mixed C_{60}/C_{70} in the first layer has a high density with the lattice approximately equal to that of a close-packed C_{60} layer on the Au(111) surface. The 0.65 ML C_{60} are deposited on monolayer C_{70} form close-packed structures and nucleate as small islands in the second layer. The C_{70} molecules beneath C_{60} islands tend to stand upright uniformly and make the molecular spacing matching that of C_{60}. The lattice of the first layer C_{70} becomes more complex, and hence some strain relieve patterns can be observed in the C_{60} islands. As shown in the STM images, one C_{60} island is separated into multiple regions by the patterns.

Substantial molecular transport between the first layer C_{70} and the second layer C_{60} happens at elevated temperatures. To summarise, annealing sample at 423 K for 30 minutes some C_{70} molecules in the first layer can pass across the interface, join in the second layer and appear as isolated bright spots. The vacancies left by these missing molecules in the first layer could be either occupied by other C_{70} in or C_{60} molecules. After being annealed at 473 K, the number of guest C_{70} in the second layer C_{60} has a dramatic increase, and these molecules prefer to sit in some regions instead of the others. None of the C_{70} molecules is found in the strain relieve patterns. When the sample is further heated at 523 K, the C_{60} islands in the second layer merge as larger ones. In some regions of these islands C_{70} almost replace C_{60} totally, while in some other regions C_{70} are still scarce.

On the surface of highly oriented pyrolytic graphite, interactions between the substrate and the adsorbed molecules are much weaker compared with on the gold substrate. Hence the packing structure of C_{60} and C_{70} are determined by the molecular interactions. At room temperature, either C_{60} or C_{70} on the graphite

surface are observed forming close-packed structure and growing layer by layer. In the close-packed domain of C_{70}, all the molecules stand with their long axes perpendicular to the substrate. When C_{70} are added onto the monolayer of C_{60} and nucleate as the second layer islands, C_{70} molecules stand upright at the hollow sites with the lattice matching that of C_{60} beneath. This type of two-molecular heterostructure is free of strain on the graphite surface. By changing the order of deposition, C_{60} are also found sitting on the hollow sites on the monolayer of C_{70} and form close-packed structures. Driven by the interlayer force, the lattice of the C_{70} domain below C_{60} molecules reduces slightly, which leads to the lattice mismatch in the C_{70} layer. Some C_{70} in the second layer flip and form wave-like patterns close to the boundaries of C_{60}-rich and C_{70}-rich domains. Though the lower rotational freedom results in a reduced entropy of the C_{70} layer, the entropy reduction is overcompensated by the reduced interfacial energy of C_{60} and C_{70}. When the two types of heterostructures are annealed to higher temperatures, some C_{70} molecules are observed passing over the domain boundaries and appear as isolated bright spots in the C_{60} domains, while some C_{60} molecules can nucleate and form molecular chains in the C_{70} domains.

At 110 K, both C_{60} and C_{70} molecules can combine with gold atoms and form stable planar metal-organic clusters on Au(111). After being heated to room temperature, the closed-shell clusters with specific ratios of atoms and molecules are called magic number clusters. Due to the weak interaction between C_{70} and gold substrate and the edge diffusing of gold atoms on the substrate, the $(C_{70})_m$-$(Au)_n$ magic number clusters are more easily to be observed rotating with a series of angles at their positions after keeping static for a short time. The DLs as well as their elbow sites on the Au(111) surface, provide limited accommodation space for these magic number clusters and thus have a great influence on their rotation. The large clusters occupying two or even more elbow sites simultaneously do not rotate at all and only allow the C_{70} molecules to move around their gold islands.

The small-sized clusters (e.g. $(C_{70})_{10}$-$(Au)_{35}$) sitting close to bulged or pinched elbow sites can rotate with larger amplitudes compared with the same type ones sitting far from elbow sites.

Based on the experimental results, there are numerous work can be done in the future for a deeper understanding of the self-assembly of binary molecular systems and two-dimensional metal-organic complexes. E.g., for studying the mixture of C_{60} and C_{70} on the Au(111) and HOPG substrate, most of the STM images in this thesis were obtained at room temperature. It is hence hard for us to know the continuous moving paths of molecules. In the future, we are going to scan the substrates with C_{60} and C_{70} co-deposited when it's temperature is maintained at 423 K, 473 K and 523 K. Moreover, with the help of low-temperature STM (LT-STM), the samples can be cooled down to 4 K or even lower temperature in ultrahigh vacuum. It enables us to achieve stable electronic characteristics of C_{60} and C_{70} in the close-packing domains.

For the $(C_{70})_m$-$(Au)_n$ magic number clusters we have studied, rotation of the clusters haven't been scanned higher than room temperature yet. At high temperatures, both the amplitude and frequency of the clusters' rotation could differ widely from that at room temperature. However, if the substrate's temperature is too high, some clusters could disassemble quickly, while the orientations of the remaining clusters could be changed too fast to be fully recorded by STM. Therefore, we are going to study the rotation of magic number clusters in UHV at a series of temperatures, which are going to be set between 273 K and 373 K. Moreover, we are also planning to investigate how the variable-strength electric fields resulting from different bias voltage and current affects clusters' rotation.

Appendix

- **Yitao Wang**, Dogan Kaya, Jianzhi Gao and Quanmin Guo, Stick-Sudden Rotation and Structural Polymorphism of $(C_{70})_m$-$(Au)_n$ Hybrid Nanoclusters, J. Phys. Chem. C **123**, 12791 (2019).
- **Yitao Wang**, Lu'an Guo and Quanmin Guo, Two-Component Fullerene Molecular Layers Assembled on the Au(111) Substrate, J. Phys. Chem. C **123**, 7776 (2019).
- Lu'an Guo, **Yitao Wang**, Dogan Kaya, Richard Palmer and Quanmin Guo, Orientational Epitaxy of Van der Waals Molecular Heterostructures, Nano Lett. **18**, 5257 (2018).
- Jianzhi Gao, Haiping Lin, Xuhui Qin, Xin Zhang, Haoxuan Ding, **Yitao Wang**, Mahroo Rokni Fard, Dogan Kaya, Gangqiang Zhu, Qing Li, Youyong Li, Minghu Pan and Quanmin Guo, Probing Phase Evolutions of Au-Methyl-Propyl-Thiolate Self-Assembled Monolayers on Au(111) at Molecular Level, J. Phys. Chem. B **122**, 6666 (2018).

THE JOURNAL OF PHYSICAL CHEMISTRY C

Article

Cite This: J. Phys. Chem. C 2019, 123, 12791−12796

pubs.acs.org/JPCC

Stick-Sudden-Rotation and Structural Polymorphism of $(C_{70})_m$−$(Au)_n$ Hybrid Nanoclusters

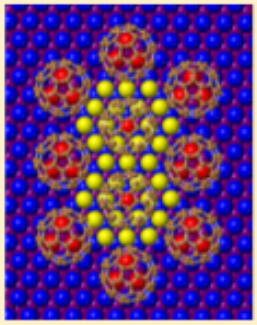
Yitao Wang,[†] Dogan Kaya,[‡] Jianzhi Gao,[§] and Quanmin Guo*[,†]

[†]School of Physics and Astronomy, University of Birmingham, Birmingham B15 2TT, U.K.

[‡]Department of Electronics and Automation, Vocational School of Adana, Cukurova University, Cukurova 01160, Adana, Turkey

[§]School of Physics and Information Technology, Shaanxi Normal University, Xi'an 710119, China

ABSTRACT: We fabricated magic number $(C_{70})_m$−$(Au)_n$ clusters on the Au(111) substrate. These clusters are stable at room temperature but display unpredictable rotational movement. The time duration between two successive rotations is in the order of ~hour. The cluster rotation is a thermally activated process due to energy fluctuation, which is more significant for small clusters. We followed the rotational movement of $(C_{70})_{10}$−$(Au)_{35}$ clusters using scanning tunneling microscopy. Our observation suggests that thermal fluctuation leads to rapid diffusion of Au atoms at the edges of the cluster and the cluster has many metastable configurations associated with structural polymorphism.



INTRODUCTION

Atomic and molecular clusters are an important class of materials exhibiting size-dependent properties.[1−4] A great amount of effort has been devoted to the fine tailoring of clusters, including size-selection,[5,6] shape control,[7] and surface passivation.[8] Metal clusters passivated with a molecular layer have demonstrated superior stability against sintering and degradation[9] and are thus potentially useful in aggressive environments such as electrolytes or biological systems.

Recently, we succeeded in making magic number fullerene−metal hybrid clusters, $(C_{60})_m$−$(Au)_n$.[10] These clusters are self-assembled on the Au(111) substrate with the smallest cluster being $(C_{60})_7$−$(Au)_{19}$.[10] The clusters are stable up to 400 K as a result of effective interaction between the molecules and the Au atoms in the cluster. Here, we investigate thermally induced cluster transformation with a view to understanding how the hybrid clusters diffuse, coalesce, and ripen on the Au(111) surface.

Ostwald ripening and Smoluchowski ripening are the two dominant pathways for coarsening and growth.[11] As the most common ripening pathway, Ostwald ripening is characterized by shrinking of small-sized clusters and growth of the large ones driven by the tendency to minimize the total free energy.[12−14] Smoluchowski ripening, on the other hand, is featured by whole cluster displacement and merger of clusters as a result of cluster collision.[15] Both the ripening pathways aim at reducing the system's total free energy with the help of mass transport.

For two-dimensional (2D) clusters supported on a substrate, the clusters tend to have a regular shape.[16] Adatoms on the surface of the substrate can act as a medium for mass transport between different clusters.[17,18] Research about coarsening and positional change of 2D nanoclusters in homoepitaxial systems has been conducted on different metal surfaces such as Ag and Cu,[19−22] in which the same type of adlayer islands ripen in different pathways. For the $(C_{60})_m$−$(Au)_n$ cluster, the metal core consisting of n Au atoms is protected by the molecular "shell", thus affecting both Ostwald and Smoluchowski ripening. In the work presented here, we have replaced C_{60} with C_{70} and created $(C_{70})_m$−$(Au)_n$ clusters. The overall property of the $(C_{70})_m$−$(Au)_n$ cluster is similar to that of $(C_{60})_m$−$(Au)_n$.

Experimental Methods. The experiments were performed using an Omicron variable-temperature scanning tunneling microscopy (VT-STM) system. The substrates were thin gold films grown on highly oriented pyrolytic graphite (HOPG) with physical vapor deposition. The Au films are about 200 nm thick and have a preferred orientation to expose the (111) planes. The Au films were treated with cycles of argon ion sputtering and thermal annealing to obtain clean and atomic smooth terraces. To grow $(C_{70})_m$−$(Au)_n$ magic number clusters, the Au/HOPG sample is first cooled down to 110 K, and ~0.15 ML gold atoms are deposited. This forms irregular Au islands at the elbow sites on the reconstructed gold substrate. We subsequently deposit ~0.05 ML of C_{70} molecules. The molecules become attached to the pre-existing Au islands. The sample is then slowly annealed to room temperature (RT), leading to the formation of $(C_{70})_m$−$(Au)_n$ magic number clusters.

Received: February 11, 2019
Revised: April 11, 2019
Published: May 2, 2019

ACS Publications © 2019 American Chemical Society

DOI: 10.1021/acs.jpcc.9b01349
J. Phys. Chem. C 2019, 123, 12791−12796

THE JOURNAL OF PHYSICAL CHEMISTRY C

Article

Cite This: J. Phys. Chem. C 2019, 123, 7776−7785

pubs.acs.org/JPCC

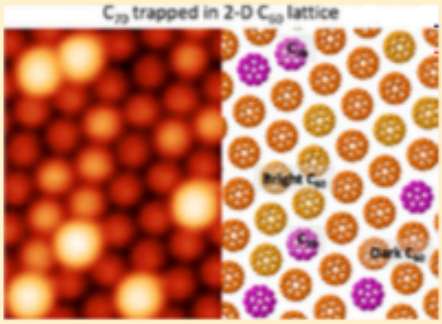
Two-Component Fullerene Molecular Layers Assembled on the Au(111) Substrate

Yitao Wang,[†] Lu'an Guo,[†,‡] and Quanmin Guo*[,†]

[†]School of Physics and Astronomy, University of Birmingham, Birmingham B15 2TT, United Kingdom

[‡]Department of Applied Physics and Key Laboratory for Quantum Information and Quantum Optoelectronic Devices of Shaanxi Province, Xi'an Jiao-Tong University, Xi'an, Shaanxi 710049, People's Republic of China

ABSTRACT: Self-assembly of binary and multicomponent colloidal crystals is an effective approach for the fabrication of structured new materials. The formation of colloidal crystals in most cases is controlled by optimized space occupation by the particles. C_{60} and C_{70} molecules, when treated as the smallest "colloidal particles", can be used as model systems to study the formation of multicomponent molecular crystals in which the intermolecular forces are mainly of the van der Waals type. By deposition of C_{60} and C_{70} molecules onto Au(111), the mixing of the two molecules has been investigated. Both C_{60} and C_{70} form close-packed layers on Au(111), but with different lattice constants. At room temperature, the molecules within the molecular layer have complete freedom to rotate. The boundary between the C_{60} and the C_{70} domains consists of row dislocations. Adding C_{60} onto a C_{70} layer has an interesting effect in that C_{60} molecules can push their way into the C_{70} layer and force the C_{70} molecules to take a fixed upright configuration where the long axis of the molecule is perpendicular to the interface. Significant interlayer diffusion takes place at elevated temperatures. When C_{70} is added to a C_{60} layer, there is little evidence of C_{70} getting into the C_{60} layer. The second layer C_{70} forms a lattice-matched structure by taking the upright orientation.



1. INTRODUCTION

Multicomponent materials with two or more constituent building blocks have great potential technological applications.[1−4] In contrast to single-component materials, multicomponent materials such as metallic glasses[5] and metal organic frameworks[6,7] have a clear advantage that their properties can be fine-tuned by varying the composition, structure and synthesis procedure. One interesting class of multicomponent materials are soft solids formed by close-packing of the constituent particles; for instance, photonic crystals assembled with colloidal particles[8] and binary nanoparticle superlattices (BNSL).[9] The structure of the solid depends on the size and shape of the building blocks.[10] Being the simplest multicomponent materials, the binary system has attracted a high level of attention. By drying a suspension containing two kinds of particles with poly(methyl methacrylate) (PMMA) as cores and different radii, Bartlett et al.[11,12] have studied the binary mixtures of hard sphere colloids and found complex ordered structures such as AB_2 and AB_{13}. The stoichiometry and stability of the BNSL depend on a number of factors including the electrical charge on the colloidal particle and the van der Waals forces.[13] By changing the stoichiometry, two A_3B structures with packing densities higher than that of the phase-separated face-centered cubic crystals have been found with simulation.[14] Kiely et al. have studied the assembly of superlattices from alkanethiol-passivated gold nanoparticles of different radii.[15] With a radius ratio of the two particles at 0.47, the small and large particles form phase-separated domains. A relatively stable AB_2 phase is formed with a radius ratio in the range from 0.48 to 0.62. A random alloy of gold particles can appear if the size difference is less than 15% as explained by the Hume−Rothery rule.[10]

Recently, there has been growing interest in the precise control of the binary superlattices[9,15] as well as the assembly of more complex structures using more than two building blocks.[16−18] A layer-by-layer assembly method was introduced by Denkov et al. and modified by Singh et al. for creating binary and ternary colloidal crystals.[19,20] With the method developed by Denkov et al., it is possible to grow colloidal crystals by depositing alternating A and B layers with a high degree of accuracy.[21−23] The complexity increases if two particles with not just different sizes, but also different shapes are mixed. In the case of nanorods and nanospheres, it is found that phase separation is favored.[24,25] In a study of a mixture of Fe_3O_4 nanospheres and $NaYF_4$ nanorods, Ye et al.[26] observed a bulk separating phase, a lamellar phase and an AB_2 binary nanocrystal shape alloy (BNSA). The BNSAs are stabilized mainly with the help of short-range attractions.[26]

Special Issue: C: Hans-Joachim Freund and Joachim Sauer Festschrift

Received: July 5, 2018
Revised: August 8, 2018
Published: August 20, 2018

ACS Publications © 2018 American Chemical Society

DOI: 10.1021/acs.jpcc.8b06420
J. Phys. Chem. C 2019, 123, 7776−7785

NANO LETTERS
Letter
Cite This: Nano Lett. 2018, 18, 5257−5261
pubs.acs.org/NanoLett

Orientational Epitaxy of van der Waals Molecular Heterostructures

Lu'an Guo,[†,‡] Yitao Wang,[‡] Dogan Kaya,[§] Richard E Palmer,[∥] Guangde Chen,[†] and Quanmin Guo*[,‡]

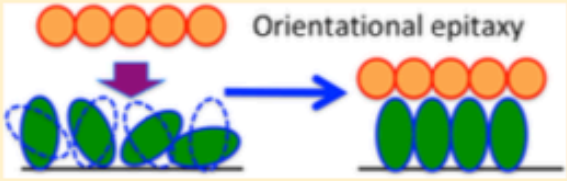
[†]Department of Applied Physics and Key Laboratory for Quantum Information and Quantum Optoelectronic Devices of Shaanxi Province, Xi'an Jiaotong University, Xi'an 710049, China

[‡]School of Physics and Astronomy, University of Birmingham, Edgbaston, Birmingham B15 2TT, U.K.

[§]Department of Electronics and Automation, Vocational School of Adana, Cukurova University, 01160 Cukurova, Adana, Turkey

[∥]College of Engineering, Swansea University, Bay Campus, Fabian Way, Swansea SA1 8EN, U.K.

ABSTRACT: The shape of individual building blocks is an important parameter in bottom-up self-assembly of nanostructured materials. A simple shape change from sphere to spheroid can significantly affect the assembly process due to the modification to the orientational degrees of freedom. When a layer of spheres is placed upon a layer of spheroids, the strain at the interface can be minimized by the spheroid taking a special orientation. C_{70} fullerenes represent the smallest spheroids, and their interaction with a sphere-like C_{60} is investigated. We find that the orientation of the C_{70} within a close-packed C_{70} layer can be steered by contacting a layer of C_{60}. This orientational steering phenomenon is potentially useful for epitaxial growth of multilayer van der Waals molecular heterostructures.



KEYWORDS: *van der Waals heterostructures, epitaxy, self-assembly, fullerene, graphene, interface, scanning tunnelling microscopy*

Epitaxial growth of thin films, a process extensively used in the semiconductor industry for fabricating electronic and optoelectronic devices,[1−4] has recently found applications in a number of emerging fields such as van der Waals heterostructures,[5−7] metal−organic frameworks (MOFs),[8] organic semiconductors,[9,10] and colloidal assembly.[11,12] In a typical heteroepitaxy process, a thin film of element A is grown on a crystalline substrate of element B. The thin film of A is normally under some stress, which arises from lattice mismatch between the two elements,[13] and consequently, there has been much interest in fabricating strained layers by deliberately introducing stress into the grown layers.[14−16] The structure of the interface depends not only on the lattice mismatch but also on the type of bonding involved.[17] For van der Waals epitaxy[17] where a layered material grows on top of another layered material such as the stacking of transition metal dichalcogenides (MoS_2, WSe_2, etc.), multilayer stacks of high quality 2D materials can be formed in the presence of very large lattice mismatch.[17] For such 2D materials, the formation of an epitaxial layer is mainly controlled by the strong atomic bonding within the layer, with the weak van der Waals interaction between the layers playing a much less significant role.

The term "van der Waals epitaxy" should not be restricted to the epitaxial growth of the conventional van der Waals heterostructures.[5−7] By introducing organic molecules, for example, hybrid organic/inorganic van der Waals heterostructures have been made.[18] The self-assembly of organic molecules on top of 2D materials opens up new avenues for fabricating hybrid functional materials.[18] Layered materials can also be produced by stacking organic molecules based completely on van der Waals interactions. One can take the layer-by-layer approach[19] to synthesize a molecular material consisting of alternating layers of two molecules (A and B). Molecules within both the A and B layers are bonded via van der Waals interaction. The bonding between the A and B layers is also van der Waals in nature. Without any specific interaction such as hydrogen bonding or ionic bonding, controlling the interfacial structure between two van der Waals molecular layers can be a real challenge. Here, we investigate the structure of the C_{60}/C_{70} interface. By depositing C_{60} and C_{70} sequentially onto highly oriented pyrolytic graphite (HOPG) at room temperature, a van der Waals bilayer is produced. There are two interesting aspects of this bilayer system. (i) Both molecules are significantly larger than typical atoms, but much smaller than colloidal particles. The system serves as a good example to understand size scalability in nucleation and growth.[20] (ii) The different shapes of the two molecules offer a good example to study the packing of objects with different geometric forms.[21,22]

C_{60} is a useful component in organic solar cells[23,24] and in molecular p−n heterojuctions.[10] When combined with gold atoms, C_{60} molecules are able to assemble into hybrid magic number clusters[25,26] or nanorings.[27] The assembly of C_{60} on various atomically flat solid substrates has been extensively studied.[28−35] It has been found that C_{60} molecules have strong

Received: June 2, 2018
Revised: July 12, 2018
Published: July 12, 2018

ACS Publications © 2018 American Chemical Society

DOI: 10.1021/acs.nanolett.8b02238
Nano Lett. 2018, 18, 5257−5261